DISSERTATION

MECHANISTICALLY-GUIDED ADVANCEMENT OF PHOTOINDUCED

ORGANOCATALYZED ATOM TRANSFER RADICAL POLYMERIZATION

Submitted by

Bonnie Leigh Buss

Department of Chemistry

In partial fulfillment of the requirements

For the Degree of Doctor of Philosophy

Colorado State University

Fort Collins, Colorado

Spring 2020

Doctoral Committee:

    Advisor: Garret Miyake

    Travis Bailey
    Yian Shi
    Margarita Herrera-Alonso

ABSTRACT

MECHANISTICALLY-GUIDED ADVANCEMENT OF PHOTOINDUCED

ORGANOCATALYZED ATOM TRANSFER RADICAL POLYMERIZATION

Photoinduced organocatalyzed atom transfer radical polymerization (O-ATRP) is a promising polymerization methodology which leverages radical reactivity to afford macromolecular products with a high degree of control over polymer molecular weights and molecular weight distributions, paired with the added benefit of spatial and temporal control over polymerization. This process, a metal-free approach, relies on photoexcitation of an organic photoredox catalyst which stringently mediates the radical activation and deactivation steps of an oxidative quenching catalytic cycle. To successfully operate this cycle, and thus control the polymerization, the rate of deactivation must be faster than both the rates of radical activation and monomer propagation. Central to the initial development of O-ATRP has been the design and study of strongly reducing organic photocatalysts, particularly in the context of methacrylate monomer polymerizations. However, as a burgeoning methodology, the full scope of O-ATRP has not yet been established.

In this dissertation, efforts in addressing three key challenges in O-ATRP, including reaction scalability, complex architecture synthesis, and polymerization of challenging monomers, through manipulation of features of the oxidative quenching mechanistic cycle is presented. To address these challenges diverse approaches were employed, including adaptation to continuous-flow reactors, implementation of multifunctional initiating systems, and rational design of a new

family of organic photocatalysts, ultimately facilitating progression of O-ATRP to a scalable and efficient approach in the well-defined synthesis of industrially-relevant materials.

ACKNOWLEDGEMENTS

My work on three published articles is detailed in this dissertation. However, I did not do this work alone and would like to expressly thank my collaborators and to specifically define their contributions, as well as acknowledge the appropriate funding sources.

Chapter 2: This dissertation chapter contains the manuscript of an article [Ramsey (Buss), B.L.; Pearson, R. M.; Beck, L. R.; Miyake, G. M. "Photoinduced Organocatalyzed Atom Transfer Radical Polymerization Using Continuous Flow" *Macromolecules* **2017,** *50,* 2668-2674]. R.M.P synthesized and characterized photocatalyst 4 and assisted with experimental design. B.L.B. synthesized photocatalysts 2 and 3, constructed the photo-flow reactor, and performed polymerization experiments with assistance from L.R.B..

Chapter 3: This dissertation chapter contains the manuscript of an article [Buss, B. L.; Beck, L. R.; Miyake, G. M. "Synthesis of star polymers using organocatalyzed atom transfer radical polymerization through a core-first approach" *Polymer Chemistry* **2018,** *9,* 1658-1665.] L.R.B. synthesized the multifunctional initiators and B.L.B. performed polymerizations and polymer characterizations.

Chapter 4: This dissertation chapter contains the manuscript of an article [Buss, B. L.; Lim, C.-H.; Miyake, G. M. "Dimethyl Dihydroacridines as Photocatalysts in Organocatalyzed Atom Transfer Radical Polymerization of Acrylate Monomers" *Angewandte Chemie International Edition* **2020,** *59,* 3209-3217. C.H.L performed all density functional theory calculations in a partnership with *New Iridium.* B.L.B. synthesized and characterized all photocatalysts, designed and constructed various photoreactors, performed all polymerization experiments, and characterized all polymers.

TABLE OF CONTENTS

CHAPTER 1

Introduction

       This dissertation is written to follow the Journals Format as accepted by the Graduate School at Colorado State University and is based on three first-author peer-reviewed publications that have appeared in *Macromolecules, Polymer Chemistry,* and *Angewandte Chemie International Edition*. The central theme of this dissertation is to further develop, study, and expand organocatalyzed atom transfer radical polymerization (O-ATRP) through a fundamental mechanistically-guided approach.

General Motivations

       Polymeric materials have shaped the modern world, becoming integrated into all facets of society. While commodity plastics are undoubtedly important, advanced polymeric materials have also emerged to address challenges in applications requiring strict control over polymer structures and physical properties, including biomedical and electronic fields. These polymers can be synthesized using controlled radical polymerization (CRP) techniques, which impart precise control over polymer molecular weights, compositions, and functionalities. Atom transfer radical polymerization (ATRP), the most widely-studied CRP, relies on the reversible activation of an alkyl-halide bond, minimizing radical concentrations to prevent undesirable bimolecular termination events.[1] Traditionally, this ATRP equilibrium is mediated by a transition metal catalyst, which can contaminate polymeric products, making this approach problematic for biological or electronic applications.

       Photoinduced ATRP was first reported in 2012 using a photoredox-catalyzed oxidative quenching cycle mediated by an iridium-based photocatalyst.[2] In 2014, organocatalyzed atom

1

transfer radical polymerization (O-ATRP) was introduced as an approach which uses an organic photoredox catalyst (PC) to produce methacrylate based polymers using energy-efficient and mild reaction conditions.[3] Like traditional ATRP, in this approach, a strict maintanence of the activation and deactivation equilibrium by the PC is required in order to access well-defined polymers.
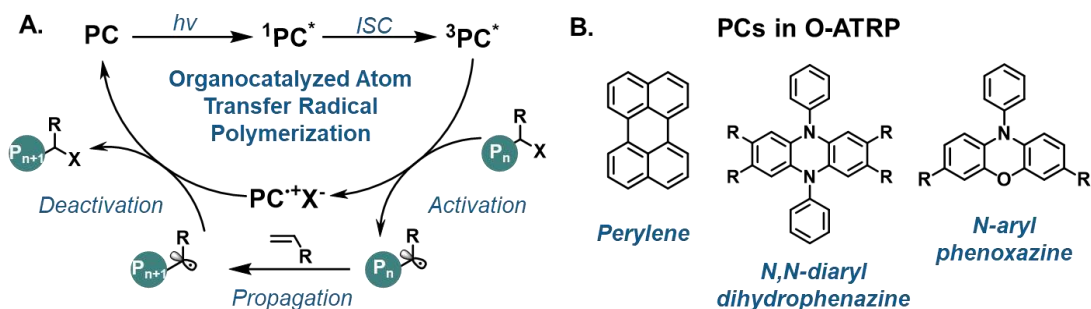
Figure 1.1: Overview of photoredox oxidative quenching catalytic cycle used for O-ATRP (a) and PCs developed by the Miyake group for O-ATRP (b).

As such, central to the development of O-ATRP has been the development and fundamental study of organic PCs, which must be sufficiently strongly-reducing to activate an alkyl-bromide bond, a feature that was previously rare for organic molecules. In the Miyake laboratory, PCs belonging to perylene, *N,N*-diaryl dihydrophenazine, and *N*-aryl phenoxazine families have been developed, which possess a wide range of redox, absorption, and photophysical properties, accessed through structural modifications.[4] Development of these PCs has primarily been in the context of O-ATRP of methacrylate monomers. However, as a burgeoning methodology, the full scope and capabilities of O-ATRP in the synthesis of industrially-relevant and advanced application materials has not yet been established.

Discussed Work

Addressing some of the unexplored challenges in O-ATRP, the following topics are discussed in detail in the following chapters:

2. Photoinduced organocatalyzed atom transfer radical polymerization in continuous flow

3. Synthesis of star polymers using organocatalyzed atom transfer radical polymerization through a core-first approach

4. Dimethyl dihydroacridines as photocatalysts in organocatalyzed atom transfer radical polymerization of acrylate monomers

In Chapter 2, adaptation of O-ATRP from batch photoreactor systems to a continuous flow system is presented. In batch photoreactor systems, the ability of light to uniformly penetrate the reaction media is constrained by the chromophore absorptivity, chromophore concentration, and path length of the system. Because of an increased surface-area-to-volume ratio, continuous flow reactor systems can provide more uniform irradiation and subsequently have an influence on photocatalyst performance and polymerization outcomes. The performance in continuous flow of four organic photocatalysts with diverse performance in batch reactor systems is discussed. The capabilities of this reactor system are also explored, finding the ability to apply this using low PC loadings, toward a broad methacrylate monomer scope, and in the scalable synthesis of well-defined block copolymers.
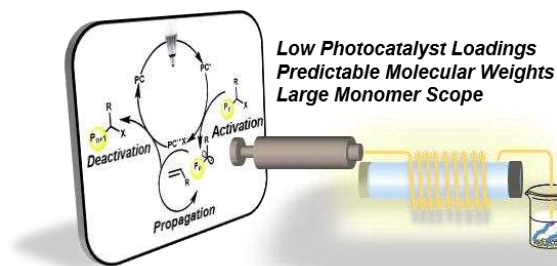
Figure 1.2: Table of Contents image for publication discussed in Chapter 2.

In Chapter 3, application of O-ATRP to the synthesis of star polymers using a core-first approach is presented. Synthetic routes to higher ordered polymeric architectures are important tools for advanced materials design and realization. Structurally similar multifunctional initiators possessing 2, 3, 4, 6, or 8 initiating sites were used in this study for the synthesis of linear telechelic polymers and star polymers, accessing products with dispersities typically lower than 1.5 while achieving also high initiator efficiencies and subsequent control over polymer molecular weight. In this approach, no evidence of undesirable star-star coupling reactions was observed, even at high monomer conversions and high degrees of polymerization. The utility of this system is further exemplified through the synthesis of well-defined diblock star polymers.
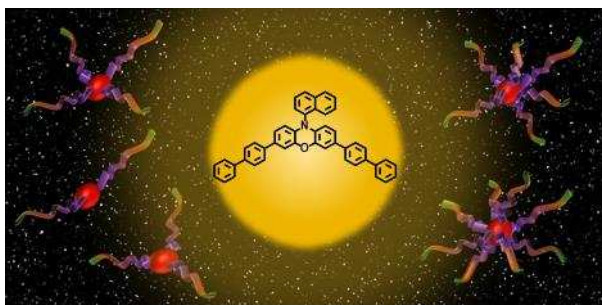
Figure 1.3: Table of Contents image for publication discussed in Chapter 3.

In Chapter 4, dimethyl-dihydroacridines are presented as a new family of organic PCs, for the first time enabling controlled polymerization of challenging acrylate monomers via O-ATRP. Structure-property relationships for seven PCs are discussed, demonstrating tunable photochemical and electrochemical properties and accessing a strongly oxidizing $^2\text{PC}^{\bullet+}$ intermediate for efficient deactivation. In O-ATRP, a combination of PC choice, implementation of continuous-flow reactors, and promotion of deactivation through addition of LiBr are critical to producing well-defined acrylate polymers with dispersities as low as 1.12. The utility of this approach is established through demonstration of the oxygen tolerance of the system and

4

application to diverse acrylate monomers, including the synthesis of well-defined di- and triblock copolymers.
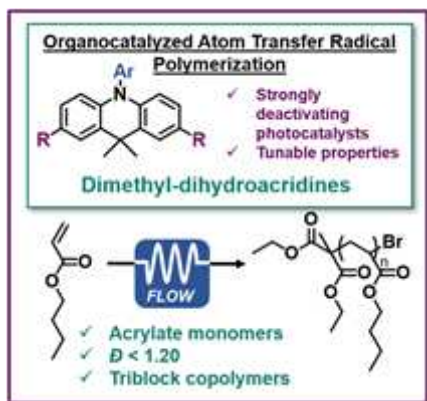
Figure 1.4: Table of Contents image for publication discussed Chapter 4.

In Chapter 5, a summary of the work discussed in this dissertation is given. Additionally, insights into the key remaining questions and challenges in O-ATRP and organic photoredox catalysis is presented.

References

1.   Matyjaszewski, K.; Xia, J. *Chem. Rev*. **2001**, *101*, 2921–2990.

2.   Fors, B. P.; Hawker, C. J. *Angewandte Chemie* **2012,** *51,* 8850-8853.

3.   Miyake, G. M.; Theriot, J. C. *Macromolecules* **2014,** *47,* 8255-8261.

4.   Corbin, D. A.; Lim, C. -H.; Miyake, G. M. *Aldrichimica Acta.* **2019,** *52,* 7-21.

Photoinduced Organocatalyzed Atom Transfer Radical Polymerization Using Continuous Flow

Overview

Organocatalyzed atom transfer radical polymerization (O-ATRP) has emerged as a metal-free variant of historically transition-metal reliant atom transfer radical polymerization. Strongly reducing organic photoredox catalysts have proven capable of mediating O-ATRP. To date, operation of photoinduced O-ATRP has been demonstrated in batch reactions. However, continuous flow approaches can provide efficient irradiation reaction conditions and thus enable increased polymerization performance. Herein, the adaptation of O-ATRP to a continuous flow approach using visible-light absorbing photocatalysts has been performed with multiple visible light absorbing photoredox catalysts. Using continuous flow conditions, improved polymerization results were achieved, consisting of narrow molecular weight distributions as low as 1.05 and quantitative initiator efficiencies. This system demonstrated success with photocatalyst loadings as low as 0.01 mole % and a diverse methacrylate monomer scope. Additionally, successful chain-extension polymerizations using 0.01 mole % photocatalyst loadings reveal continuous flow O-ATRP to be a robust and versatile method of polymerization.

Introduction

Photoinduced controlled radical polymerizations (CRPs) have become powerful tools for polymer synthesis to yield polymers with targeted molecular weights (MWs), low molecular

weight dispersities ($Đ$), and controlled compositions with the added potential for spatial and temporal control.[5,6,7,8,9] In the last two decades atom transfer radical polymerization (ATRP) has emerged as the most widely applied CRP.[10,11] The popularity of ATRP is largely due to use of readily available reagents, robust implementation, and functional group tolerance. The ability of ATRP to preserve a functional chain-end group makes this methodology well-suited for the synthesis of advanced architectures, such as block-co-polymers.[12] In ATRP, control over the polymerization relies on strict regulation over the equilibrium between a dormant alkyl halide and an active propagating radical species in order to maintain a low radical concentration and minimize undesirable bimolecular termination reactions.[13] Traditionally, ATRP has employed transition metal catalysts to mediate this equilibrium, which ultimately contaminates the polymer product and can restrict the application potential of the polymer, especially in electronic applications. Significant advancements have enabled the use of lower levels of transition metal catalysts[14,15,16,17] and increased ability for polymer purification,[18,19,20] while recently organocatalyzed ATRP (O-ATRP) has risen as an approach to entirely eliminate metal contamination of the polymer product.[21,22,23,24,25,26]

A proposed mechanism for O-ATRP proceeds through photoexcitation of the ground state photoredox catalyst (PC) to generate the singlet excited state ($^1PC^*$) and subsequent intersystem crossing to a highly reducing triplet excited state ($^3PC^*$) (**Figure 2.1-A**). The $^3PC^*$ activates an alkyl halide through reduction to simultaneously form the PC radical cation halide anion ion pair ($^2PC^{•+}X^-$) and the active carbon centered radical species for polymerization propagation. The $^2PC^{•+}X^-$ species deactivates the growing polymer chain *via* an oxidative event, generating a halide end-capped polymer. For CRPs, control over polymerization relies on a faster rate of deactivation than rate of activation. The irradiation of the PC plays an important role in the efficiency of PC

photoexcitation and thus relative concentrations of every PC species in the polymerization reaction, which culminates in control over the polymerization. As such, we hypothesized developing O-ATRP in continuous flow would enhance irradiation efficiency and facilitate the synthesis of well-defined polymers.

In 2014, perylene[21] and *N*-aryl phenothiazines[22] were presented as PCs able to orchestrate O-ATRP through an oxidative quenching pathway using visible and UV irradiation, respectively. Recently, our group has revealed *N,N*-diaryl dihydrophenazines[23] and *N*-aryl phenoxazines[24], as strongly reducing visible-light absorbing PCs efficient for O-ATRP. Mechanistic studies of O-ATRP mediated by *N*-aryl phenothiazine catalysts highlighted the necessity for fast activation and deactivation for controlled polymerizations.[27] Further studies have shown the importance of photoinduced charge transfer states of the PC and solvent stabilization of the resulting $^2PC^{\bullet+}X^-$ ion pair in *N,N*-diaryl dihydrophenazine catalysts for the synthesis of well-defined polymers using O-ATRP.[28] These studies reveal the free energy of $^2PC^{\bullet+}X^-$, which is influenced by solvent polarity, to play a key role in efficient deactivation and to achieve control over the polymerization.

As an alternative to traditional batch reactors, photo-mediated continuous flow reactors have materialized as an excellent approach in both small molecule[29,30,31,32] and macromolecular[33,34,35] syntheses to promote efficient and uniform irradiation conditions. According to the Beer-Lambert Law, in a photo-mediated batch reaction the ability for photons to travel in the reaction medium decreases exponentially with increasing path length, equating to non-uniform irradiation and limiting the efficiency of the reaction.[29,36] In particular, for photoinduced CRP reactions poor irradiation control leads to broad molecular weight distributions, slower reaction times, and limited scalability.[30,37] In contrast to batch reactors, continuous flow offers a high surface-area-to-volume ratio of reactor to solution, allowing uniform irradiation, fast reaction

times, efficient heat and mass transfer, reduction of batch-to-batch variations, and facile scalability (**Figure 2.1-C**).[30,32,38] Considering reaction design, reaction parameters can be easily adjusted during polymerization by modulating flow rates, irradiation intensity, and reaction stoichiometry.[39]
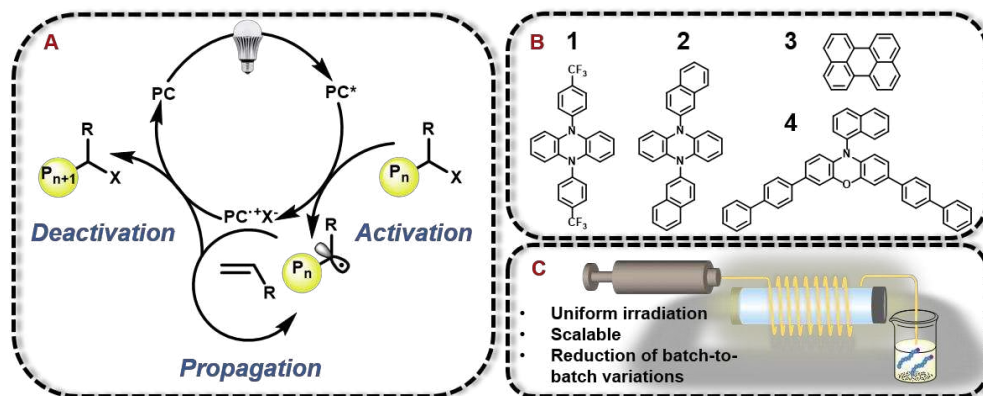
Figure 2.1: (a) The proposed mechanism for O-ATRP proceeding through an oxidative quenching pathway. (b) The visible light absorbing PCs used in this study include *N,N*-diaryl phenazines (**1** and **2**), perylene (**3**), and *N*-aryl phenoxazines (**4**). (c) Photo-mediated flow reactors offer significant advantages to batch systems.

To date, the scalability and irradiation efficiency of O-ATRP has been constrained by limitations inherent to batch reactor systems. Reports of continuous flow approaches have been presented for nitroxide mediated polymerization (NMP),[40,41] reversible addition-fragmentation chain-transfer (RAFT)[35,42], and metal-catalyzed ATRP[43,44]. This method has been further extended to photoinduced RAFT,[45,46,47] and photoinduced metal-catalyzed ATRP,[48,49] but photo-induced O-ATRP in continuous flow has not yet been reported. With that in mind, we hypothesized that the favorable characteristics of photo-mediated continuous flow systems, namely control over irradiation, would facilitate further study of the capabilities of recently developed organic PCs through heightened control over activation and deactivation resulting in enhanced results of

polymerization. To that end, this work reports a thorough study of the integration of visible-light mediated O-ATRP into a continuous flow approach, improving and expanding the utility of the methodology while offering an energy-efficient method for producing polymers on scale.

Results and Discussion

   Synthesis of PMMA using visible-light absorbing PCs. To examine the performance of O-ATRP using a continuous flow reactor, we investigated multiple previously reported PCs studied in a batch reactor system for the polymerization of methyl methacrylate (MMA). The PCs used in this study were selected due to absorption profiles in the visible light regime and familial diversity (**Figure 2.1-B**). For a direct comparison of polymerization trends, similar reaction conditions were used to those reported in batch, including reaction stoichiometry and choice of alkyl bromide initiator. In batch conditions using broad spectrum white LEDs for irradiation for PC **1** and **2**, *Đ* typically ranged from 1.10-1.18 and 1.03, respectively, with initiator efficiency (*I**)[50] values reaching 66% and 46%.[23] For the earliest reported PC for O-ATRP, PC **3**, batch conditions gave *Đ* of 1.3-1.8, but low *I** (14-22%) and a lack of control over MW as polymerization proceeded.[21] In the case of PC **4**, in typical batch reactions *Đ* of 1.25-1.17 and *I** of ~100% was reported.[28] In all cases, *I** was observed to increase during low monomer conversion periods until reaching a maximum value, typically around 40-50% conversion, which depended on the PC catalyzing polymerization. A summary of key photophysical and redox properties of these PCs can be found in **Table 2.1**.

   The results for polymerizations using PCs **1, 2, 3,** and **4** in continuous flow all showed similar trends of enhanced polymerization performance in comparison to batch reactor conditions, as demonstrated by improved predictability in MW and lowered *Đ* (**Figure 2.2**). When employing

Table 2.1: A Summary of Redox and Photophysical properties for PCs **1-4**.[a]

PC	E° $(^2PC^{\cdot+}/^3PC^*)^a$	E° $(^2PC^{\cdot+}/^1PC)^a$	λ_{max} (nm)	ε_{max} $(M^{-1}cm^{-1})$
1[b]	-1.80	0.29	370	4,700
2[b]	-1.71	0.19	340	6,300
3[c]	-0.70	0.98	436	38,500
4[b]	-1.93	0.65	388	26,635

[a]Redox potentials are in V vs SCE. [b]Values are from referenced batch O-ATRP reports and were determined experimentally.[19,20] [c]Determined computationally as described in Reference 19.

1, Đ ranged from 1.10 to 1.18 over the course of polymerization, reaching 49% conversion after a 2 hour residence time. In the case of **2**, Đ ranged from 1.05-1.14 while reaching 64% conversion after a 1.5 hour residence time. Using PC **3** showed distinct improvement over batch reactions and was able to produce PMMA with a Đ as low as 1.10. Although inferior to the *N,N*-diaryl dihydrophenazine and *N*-aryl phenoxazine catalysts, **3** still exhibited a linear growth in MW, a marked change in comparison to reported batch reaction results. The performance of PC **4** in continuous flow is highlighted by near 100% *I**, a predictable increase in MW, and Đ ≤ 1.20 (**Figure 2.2-D**).

Most notably, for *N,N*-diaryl dihydrophenazine catalysts **1** and **2**, at low monomer conversion continuous flow demonstrated superior control in comparison to batch reactors, with experimentally measured MWs near theoretically predicted MWs resulting in nearly quantitative *I**. These results can be explained through analysis of the proposed mechanism of O-ATRP in the context of continuous flow. In the O-ATRP mechanism, the rate of deactivation must be higher than activation in order to maintain control over the propagating radical species.[27] This phenomenon is facilitated by the concentration, availability, and oxidation potential of the $^2PC^{\cdot+}X^-$ deactivator species. Low concentrations of $^2PC^{\cdot+}X^-$ hinder effective deactivation, limiting control

over propagation *via* reversible end-capping of the active polymer chain. However, in a photo-flow reactor, due to the Beer-Lambert law, a higher surface-to-volume ratio allows for more efficient irradiation and PC photoexcitation, subsequent activation, and therefore an indirect increase in deactivator concentrations. These conditions allow for control over propagation and result in enhanced control over MW at low polymer conversions for **1** and **2**.
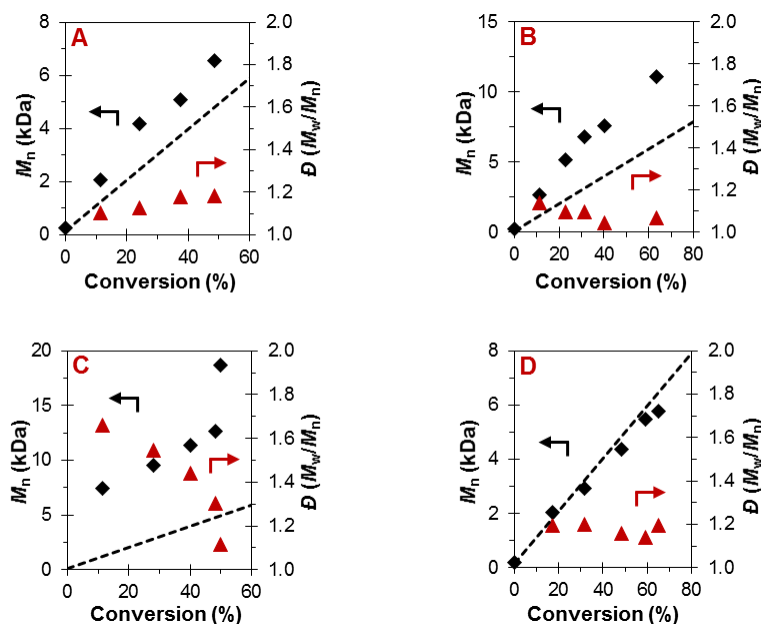
Figure 2.2: Plots of M_n (black diamonds) and $Đ$ (red triangles) with respect to monomer conversion during the polymerization of MMA catalyzed by **1** (a); **2** (b); **3** (c); or **4** (d) performed in continuous flow at steady-state conditions and under different residence times. Shown is the theoretical evolution of M_n (dashed line) with respect to monomer conversion. Conditions for all plots: [1000]:[10]:[1] of [MMA]:[Initiator]:[PC]; 3.73 mM PC; initiators are ethyl α-bromophenylacetate (EBP) when using **1**, **2**, **3** and diethyl 2-bromo-2-methylmalonate (DBMM) when using **4**; 2:3 MMA to DMA by volume; 160 cm of tubing reactor, irradiated by 3000 K fluorescent light. See experimental section for flow rates and residence times used.

In total, these results demonstrate that a continuous flow approach can provide significant improvements in polymerization metrics using a variety of PCs, especially regarding results at low monomer conversions. In a continuous flow system, the maximum I^* was reached at lower monomer conversions than in batch. This can be attributed to uniform irradiation resulting in

higher concentrations of ^{3}PC* and subsequent fast activation of the alkyl halide initiator. Due to low $Đ$ and consistently high I* values near 100%, **4** was chosen as PC for additional study of continuous flow techniques using O-ATRP.

The effect of relative solvent volume on results of polymerization was explored using PC **4** (**Table 2.11**). Polymerization results did not vary significantly with varying reaction solution concentrations. The conditions tested included 1:1, 2:3, 1:2, and 1:3 ratios of MMA to DMA by volume. For all conditions, $Đ$ remained relatively low, typically below 1.25, and MW predictability was conserved with I* near 100%. The most concentrated solution tested, a 1:1 ratio of MMA:DMA, exhibited the fastest reaction rate; however, remarkably increased viscosity upon reaching conversions above 70% posed issues with the continuous flow system. For fast reaction times and lower viscosities, a ratio of 2:3 MMA:DMA by volume was chosen for subsequent polymerizations.

As photo-flow reactors facilitate efficient and homogenous irradiation of the reaction solution due to increased surface-to-volume area of the reactor,[36] we hypothesized sufficient concentrations of excited state ^{3}PC* for successful polymerizations could be achieved using decreased PC loadings. To test this hypothesis, O-ATRP of MMA was performed using varying concentrations of **4**. For mol % levels spanning 0.1% to 0.01%, all loadings were well-controlled above 40% conversion (**Table 2.2, Runs 1-4**). However, for 0.04-0.01% (Runs 2-4), early stages of polymerization (< 40% conversion) showed slightly higher MW polymers in comparison to theoretical MWs (**Figure 2.11**). This is likely a consequence of an insufficient concentration of critical deactivating ^{2}PC$^{•+}$X$^-$ species at low monomer conversions. Lowering the PC loading to 0.005% (**Table 2.2, Run 5**) resulted in a loss of control over MW growth. A control experiment with no PC in the system resulted in low monomer conversions, $Đ \geq 1.85$ and I* below 8% (**Table**

2.8). To continue a comparison of general trends in batch reaction systems and continuous flow,

PC loadings of 0.1% were employed in further studies.

Table 2.2: Results of the O-ATRP of MMA Investigating PC **4** Loading.[a]

Run No.	[PC 4] mol %	Conv. (%)[b]	M_n (kDa)[c]	Đ (M_w/M_n)[c]	Theo. M_n (kDa)[d]	I^* (%)[e]
1	0.1	61	6.4	1.23	6.11	95
2	0.04	69	6.9	1.22	6.86	100
3	0.02	68	6.2	1.26	6.82	110
4	0.01	71	7.9	1.27	7.09	90
5	0.005	72	6.7	1.60	7.25	108

[a][MMA]:[DBMM]:[**4**] = [1000:[10]:[X]; 2:3 of MMA to DMA by volume and 160 cm tubing reactor irradiated by 3000 K fluorescent lamp. Results shown were achieved with a 90 minute residence time at a flow rate of 8.11 µL/min. [b]Determined by ^{1}H NMR. [c]Measured using GPC. [d]Calculated by $(Conv \times [Mon]/[Init.] \times Mw_{Mon})/1000$. [e]Initiator efficiency (I^*) calculated by $(Theo. M_n/Calc. M_n) \times 100$.

To validate that this system can be used to synthesize polymers with targeted MWs with a

high level of control, the O-ATRP of MMA was performed with the goal of synthesizing PMMA

with a range of MWs (**Figure 2.3**). These data showed well-controlled polymerizations through

conversions above 80%, first order kinetic behavior, nearly constant and relatively low Đ, and a

linear increase in MW paired with quantitative I^*.

To synthesize PMMA with tunable MWs in continuous flow, concentrations of either

monomer or initiator were adjusted while maintaining a constant [**4**] (**Table 2.3**). Through altering

the stoichiometry, predictable MWs and relatively low Đ were obtained for low MW polymers.

However, when targeting high monomer to initiator loadings, Đ increased above 1.5 and I^*

exceeded 100%, showing a loss of control over the polymerization. This loss of control in

continuous flow at high MW may be attributed to increased solution viscosities provided by high
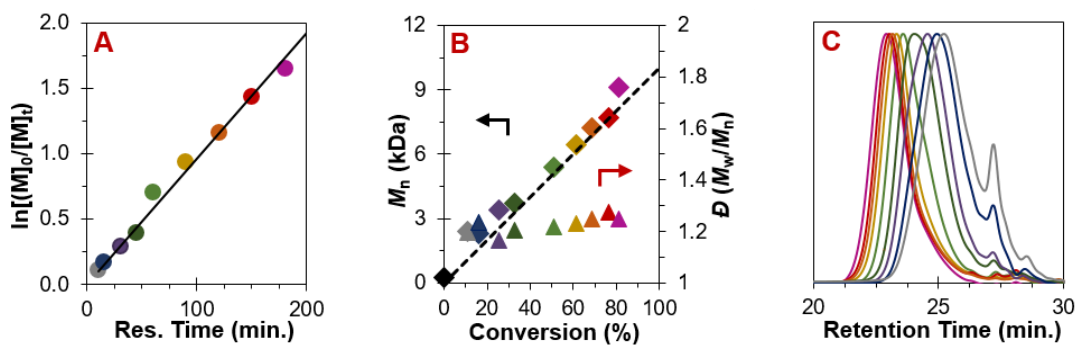
Figure 2.3: Results of the polymerization of MMA catalyzed by **4**: (a) first order kinetic plot; (b) plot of the molecular weight (♦) in comparison to theoretical molecular weight (dashed line) with respect to monomer conversion and dispersity (▲); and. (c) GPC traces of the polymers corresponding to points shown in (a) and (b), color coded. Conditions used are [MMA]:[DBMM]:[**4**] = [1000]:[10]:[1]; 3.73 mM of PC, 2:3 MMA:DMA by volume, irradiated by 3000 K fluorescent lamp. See Experimental Section for flow rates and residence time used.

MW polymers, which can cause increased shear rates within the reactor and poor diffusional mixing of the solution.[51] As such, even at uniform flow rates polymer chains become elongated and move through the reactor at varying rates, leading to broadened residence time distributions that likely contribute to a higher $Đ$.[39]

Application of O-ATRP for the polymerization of other monomers. The expansion of this polymerization to a diverse group of methacrylate monomers using O-ATRP in continuous flow was investigated (**Table 2.4**). Polymerizations of benzyl methacrylate and ethyl methacrylate produced polymers with $Đ$'s of 1.38 and 1.26, respectively, and linear increases in MW with monomer conversion (**Table 2.4, Runs 1 and 2**). Synthesis of poly(2-ethylhexyl methacrylate) resulted in polymer with 98% I^* and $Đ$ of 1.40 (**Table 2.4, Run 3**). The polymerizations of lauryl methacrylate and isodecyl methacrylate were well-controlled until reaching 60% and 66% conversion, respectively, although $Đ$'s increased at higher monomer conversions (**Table 2.3, Runs 4 and 5**). Applying this polymerization approach to diethylene glycol methyl ether methacrylate was controlled over MW throughout polymerization and a polymer with $Đ$ of 1.14 at 66%
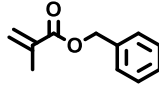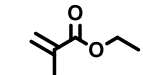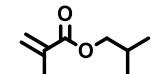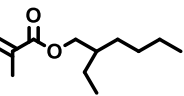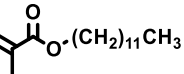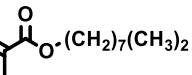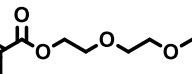
conversion (**Table 2.4, Run 7**). Highlighting the robustness of O-ATRP in continuous flow, no additional optimization was necessary in order to accomplish a well-controlled polymerization of methacrylate monomers possessing varying functionalities.

Table 2.3: Results of O-ATRP of MMA in Continuous Flow for the Synthesis of PMMA with Tunable Molecular Weights.[a]

Run No.	[MMA]:[DBMM]:[4]	Conv. (%)	M_w (kDa)	M_n (kDa)	$Đ$ (M_w/M_n)	Theo. M_n (kDa)	I^* (%)
1	[1000]:[20]:[1]	73	6.3	5.4	1.17	3.6	68
2	[1000]:[15]:[1]	48	3.7	3.0	1.24	3.2	108
3	[1000]:[10]:[1]	69	9.0	7.2	1.25	6.9	95
4	[1000]:[5]:[1]	76	25.2	19.3	1.30	15.3	79
5	[1000]:[2]:[1]	61	43.0	24.4	1.77	30.4	125
6	[250]:[10]:[1]	50	2.2	1.8	1.18	1.3	69
7	[500]:[10]:[1]	61	4.3	3.8	1.13	3.1	81
8	[1500]:[10]:[1]	85	18.9	13.6	1.39	12.7	94
9	[2000]:[10]:[1]	76	21.3	15.4	1.38	15.2	98
10	[3000]:[10]:[1]	79	29.9	20.5	1.46	23.6	115
11	[4000]:[10]:[1]	74	35.3	22.4	1.58	29.5	131
12	[5000]:[10]:[1]	65	37.0	22.2	1.67	32.6	147

[a][MMA]:[DBMM]:[**4**] = [X]:[Y]:[1]; 3.73 mM of **4,** with 2:3 of MMA to DMA by volume and 160 cm tubing reactor irradiated by 3000 K fluorescent tubular lamp. Results were achieved using a 120 minute residence time at a flow rate of 5.41 µL/min.

Table 2.4: Monomer Scope of O-ATRP of Methacrylate Monomers using Continuous Flow under Standard Conditions.[a]

Run No.	Monomer	Res. Time (min)	Flow Rate (µL/min)	Conv. (%)	M_w (kDa)	M_n (kDa)	Đ (M_w/M_n)	Theo. M_n (kDa)	$I*$ (%)
1		90	8.11	82	20.7	15.0	1.38	14.4	96
2		90	8.11	63	9.4	7.6	1.24	7.1	94
3		90	8.11	67	12.2	9.9	1.23	9.5	96
4		90	8.11	79	22.4	16.0	1.40	15.6	98
5		60	12.16	60	27.6	18.5	1.49	15.4	83
6		60	12.16	66	31.9	26.5	1.22	14.9	56
7		60	12.16	66	19.1	16.7	1.14	12.4	74

[a][Monomer]:[DBMM]:[PC **4**] = [1000]:[10]:[1] 3.73 mM of **4,** with 2:3 of MMA to DMA by volume and 160 cm tubing reactor irradiated by 3000 K fluorescent lamp.

Chain-extension of PMMA synthesized in continuous flow. To further demonstrate the controlled nature of O-ATRP in a continuous flow system, chain-end group fidelity was validated by chain-extension from a PMMA macroinitiator synthesized on large scale in continuous flow. The large-scale synthesis of the PMMA macroinitiator was carried out to obtain 3.3 g of purified PMMA macroinitiator in a 73% yield (see Experimental Section: Macroinitiator Synthesis and Chain-extension Experiments). Low PC loadings were implemented for all steps (0.01 mol % of **4**) and chain extensions were performed with isobutyl methacrylate or benzyl methacrylate. Macroinitiator chain-end fidelity was confirmed through successful chain-extension of macroinitiator to block copolymer, as shown by baseline resolved shifts in GPC traces from the PMMA macroinitiator to higher molecular weight block copolymers (**Figure 2.4-B**).
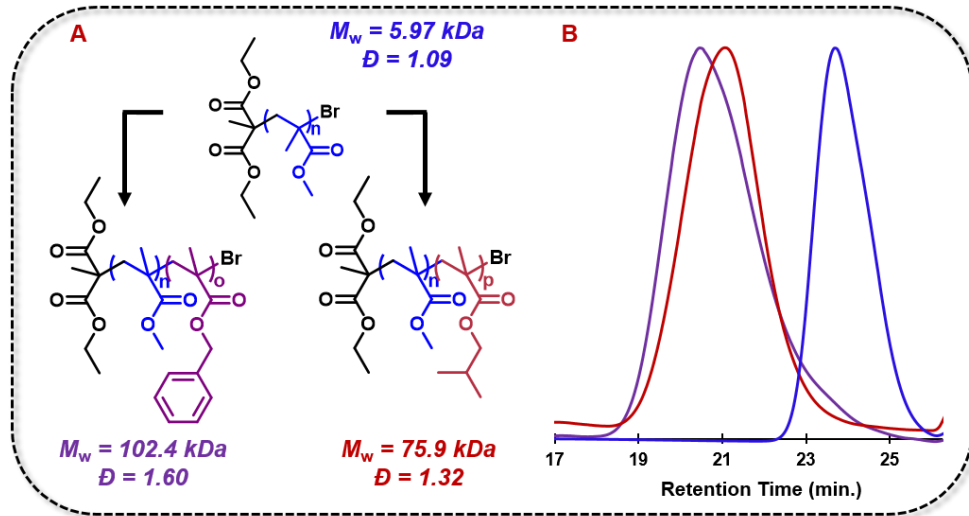
Figure 2.4: (A) Chain extension using O-ATRP from a PMMA macroinitiator extended with BzMA (purple) and iBuMA (red). (b) Gel permeation chromatography traces of the polymers are shown with corresponding color schemes.

Conclusion

Photoinduced O-ATRP performed in continuous flow has been established as a robust and efficient method of polymerization. For each photoredox catalyst tested, results show good control over all metrics of polymerization to produce polymers with relatively low Đ and high MW predictability. Control over the course of the polymerization was maintained when catalyst loadings were lowered to 0.01 mol %. Further, this technique has been successfully applied to the polymerization of a diverse scope of methacrylate monomers with no further optimization required and provides the capability for the scalable synthesis of well-defined block copolymers. The success of O-ATRP in this system is enhanced by the efficient irradiation characteristics offered by continuous flow.

Experimental

Materials and Methods

Methyl methacrylate (MMA) was purchased from VWR. Ethyl methacrylate (EMA), 2-ethylhexyl methacrylate (EHMA), benzyl methacrylate (BzMA), di(ethylene glycol) methyl ether methacrylate (DEGMA), isodecyl methacrylate (iDMA), lauryl methacrylate (LMA), N,N-Dimethylacetamide (DMA), ethyl α-bromophenylacetate (EBP), and diethyl 2-bromo-2-methylmalonate (DBMM) were purchased from Sigma-Aldrich. These reagents were purified by stirring overnight with calcium hydride, vacuum distillation, followed by 3 freeze-pump thaw cycles. The monomers were stored under inert nitrogen atmosphere in a -30 °C freezer. Monomers were allowed to warm to room temperature before use. Perylene 98% purity (**3**) was purchased from VWR and used as received. All other catalysts used were synthesized according to the procedures described below. All other reagents were used as received.

Nuclear magnetic resonance spectra were recorded on a Bruker Avance-III 300 MHz instrument, with chemical shifts referenced using internal solvent resonance, 7.26 ppm for $CDCl_3$ and 7.16 ppm for C_6D_6. Deuterated chloroform was purchased from Cambridge Isotope Laboratories. Analysis of polymer molecular weight and dispersity was performed using gel permeation chromatography (GPC) coupled with multi-angle light scattering (MALS), using an Agilent HPLC fitted with one guard column and three PLgel 5 µm MIXED-C gel permeation columns in series. The detectors used were a Wyatt Technology TrEX differential refractometer and a Wyatt Technology miniDAWN TREOS light scatter detector. The solvent used was THF with a flow rate of 1 mL/minute.

Synthesis of Catalysts

5,10-di(4-trifluoromethylphenyl)-5,10-dihydrophenazine

PC **1** was synthesized according to the already reported procedure.[23]
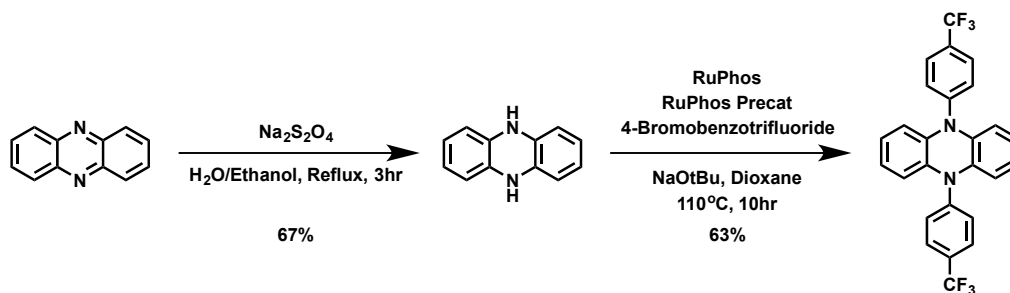
Figure 2.5: Synthetic scheme for PC **1**.

5,10-di(2-naphthalene)-5,10-dihydrophenazine

PC 2 was synthesized according to the already reported procedure.[19] The catalyst was further

purified by dissolving in benzene at 80°C and then passed through a 1 inch silica plug. The

catalyst was dried overnight under vacuum before use.
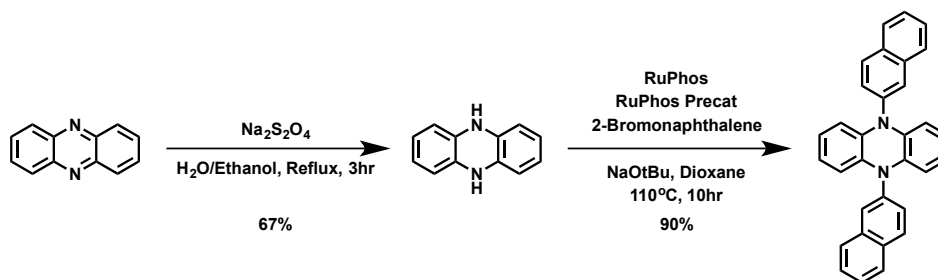
Figure 2.6: Synthetic scheme for PC **2**.

3,7-di(4-biphenyl)-1-naphthalene-10-phenoxazine

PC **4** was synthesized according to an already reported procedure.[24]
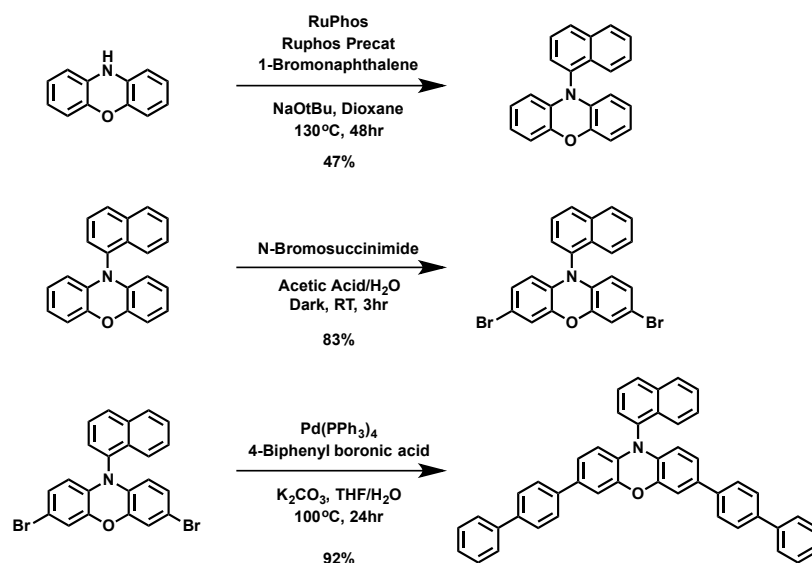
Figure 2.7: Synthetic scheme for PC **4**.

Flow Reactor Materials and Design

Flow polymerizations were carried out using a Pump 11 Elite Infusion Only Syringe Pump and either an 8 mL or 50 mL stainless steel syringe fitted with Chemraz O-rings and a 1/16" OD fitting, all purchased from Harvard Apparatus. The Halar tubing used was dimensions of 1/16" OD and 0.03" ID and purchased from IDEX Health & Science. Sections of the tubing reactor were connected using a PEEK Union Assembly, 0.020 thru hole, 1/16", purchased from IDEX Health & Science.

The reactor was assembled using 3 sections of tubing (see **Figure 2.8**). The first section connected the syringe to the irradiated second section. The second section was wrapped around the light source and connected to the third section, which was used for collection. The length of the second section was used to calculate residence time. The length of the third section was 10% of the irradiated (second) section's length. All sections of tubing were wrapped with aluminum foil to control irradiation.

The light source used was a Warm White 18" fluorescent tube light with a color temperature of 3000 K, wattage of 15, and lumen output of 745. Before beginning polymerization, the light source was turned on for 1 hour. At that time temperature of the light was measured at 55-60 ˚C. The temperature was monitored continuously during polymerization by placing a thermometer probe directly underneath the light bulb and reactor. The temperature remained constant during polymerization.
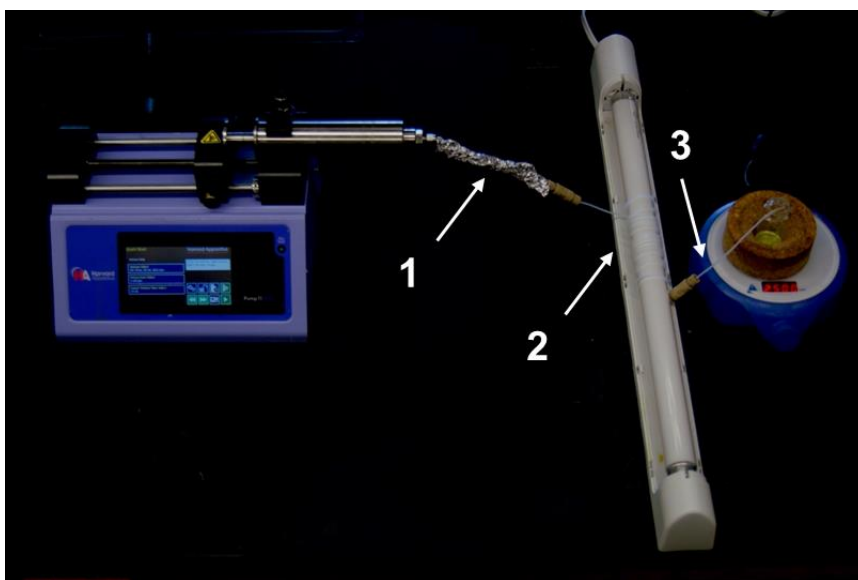
Figure 2.8: Flow Reactor set-up showing the position for each section of tubing.
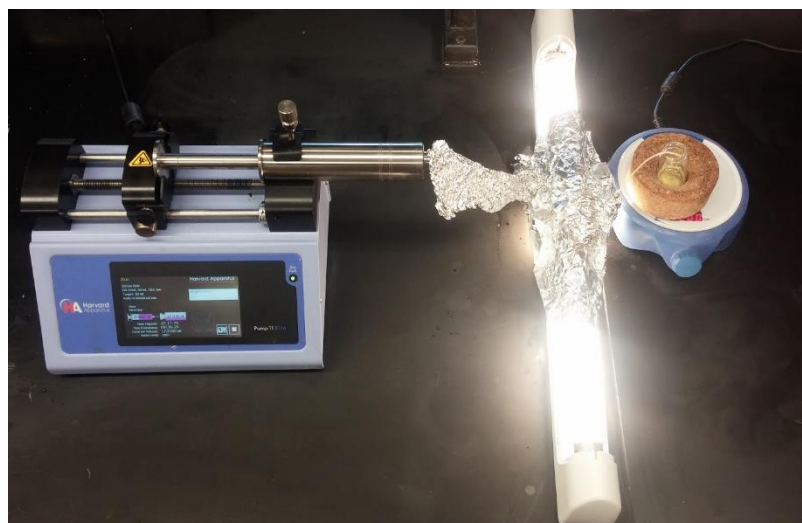
Figure 2.9: Flow reactor set-up showing placement of aluminum foil during polymerization.

Light Source Emission and PC Absorbance Profiles
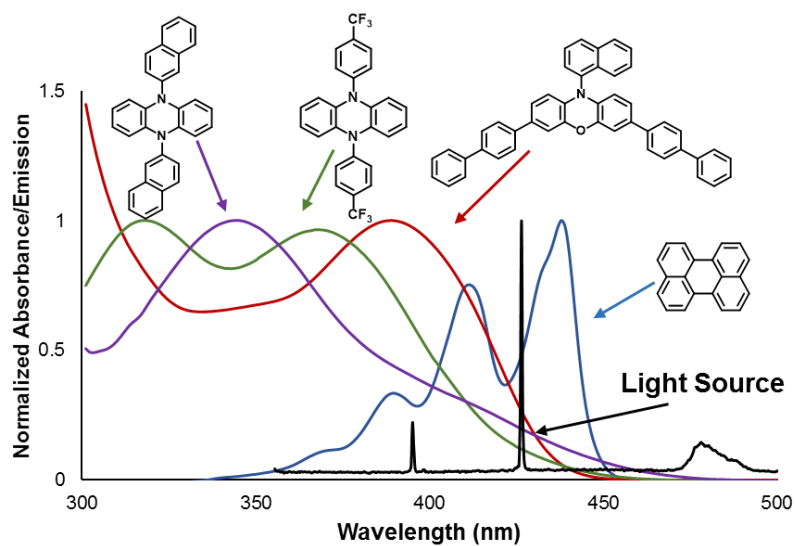
Figure 2.10: Normalized plot of light source emission (Black) and absorbance for PC 1 (Green), PC 2 (Purple), PC 3 (Blue), and PC 4 (Red). The emission spectrum of the fluorescent bulb was measured with an ocean Optics ADC1000 spectrometer. The light was attenuated as needed with a continuously variable neutral density filter to prevent saturation of the detector. The

light was then guided into the spectrometer with a fiber0optic cable. The data was processed with

a home-built LabView program. The PC absorbance was measured using UV-vis spectroscopy.

<u>Procedures</u>

Flow Reactor Calculations:

Determination of Reactor Volume:

$$Volume = \pi r^2 \; x \; Reactor \; Length$$

where *r* is the internal radius of the tubing.

Determination of Residence Time and Flow Rate:

$$Flow \; Rate = \frac{Reactor \; Volume}{Residence \; Time}$$

Determination of Equilibration Time:

$$Equil. Time = (1.5 Residence \; Time) + (0.1 Residence \; Time)$$

- The additional 0.1 residence time is to account for the third, outlet, section of tubing.

For more information depicting residence time and flow rate calculations, see **Table 2.5**.

Table 2.5: Flow reactor parameters commonly used in polymerization experiments.[a]

Flow Rate (mL/min)	Residence Time (min)	Equilibration (min.)	Collection (min.)
0.04864	15	24	3.75
0.02432	30	48	7.5
0.01216	60	96	15
0.00608	120	192	30

[a]Determination of flow rates, residence times, equilibration times, and collection times for 160 cm of irradiated tubing with an additional 16 cm of non-irradiated tubing in the last segment of the reactor.

General Polymerization Procedure in Continuous Flow

The catalyst was weighed into a vial, loaded with a Teflon coated stir-bar and brought into a Nitrogen filled glovebox. DMA was added to the vial and allowed to stir until the catalyst was fully dissolved. At that time the appropriate amount of monomer was added, followed by initiator. The reaction mixture was loaded into either an 8 mL or 50 mL stainless steel syringe. The syringe was fitted with the first section of tubing, which was attached while still inside the glovebox. The syringe with tubing was brought outside the glovebox and quickly attached to the tubing reactor. After starting the syringe pump the reaction was allowed to reach steady state by loading the tubing reactor with reaction mixture, then running for 1.5 residence times. The polymer product was collected, and the reaction quenched by placing the tubing into a 20 mL scintillation vial containing a mixture of deuterated chloroform with 50 ppm BHT as radical inhibitor. The tubing reactor was flushed with DMA after polymerization was complete.

Monomer conversion was determined by ^{1}H NMR analysis immediately following collection by comparison of the integrations of the monomer peak at 3.73 ppm to the polymer peak at 3.57 ppm. The collected sample was dried for molecular weight analysis using GPC.

To test the evolution of molecular weight and dispersity with respect to conversion the reactor flow rate was modulated to target increasing conversions. After each change in flow rate the system was allowed to equilibrate using the method described above. The product was collected for one-fourth of the residence time, then analyzed using the above-described methods. The fastest flow rate employed in these types of experiments was 73.0 µL/min (10 minute residence time) and slowest 4.05 µL/min (180 minute residence time).

Macroinitiator Synthesis
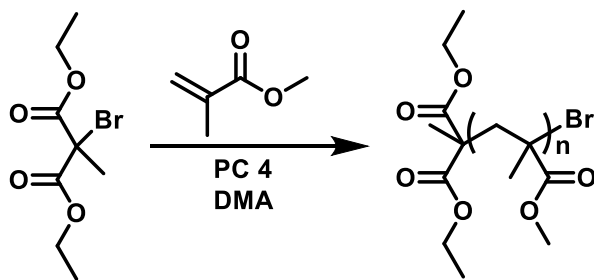
Macroinitiator synthesis was performed by setting up a standard polymerization as described above, using 10.0 mL MMA (940 mmol), 0.36 mL (1.88 mmol) DBMM, 11.5 mg PC **4** (0.188 mmol) and 15.0 mL DMA. Once the syringe was connected to the reactor and secured to the pump, the pump was started with a flow rate of 6.08 µL/min, giving a residence time of 2 hours. After equilibration, an aliquot was taken for ^{1}H NMR analysis to determine percent conversion. At that time the polymerization mixture was quenched by dropping directly from the reactor into 20 mL of stirring methanol. The polymerization was allowed to proceed until no reaction mixture remained in the syringe. At that time the polymer solution was concentrated on a rotary evaporator and redissolved by addition of 25 mL of dichloromethane followed by slow precipitation into an additional 200 mL of methanol at -78 °C. The precipitated polymer was isolated via vacuum filtration, washed with methanol, and redissolved in dichloromethane. The polymer was reprecipitated 2 more times and dried under vacuum at 50 °C overnight to isolate of PMMA as a colorless solid (3.3 g, 72%; M_n = 5.48 kDa; Đ = 1.09).

Chain-Extension Experiments

Synthesis of PMMA-b-PBzMA:
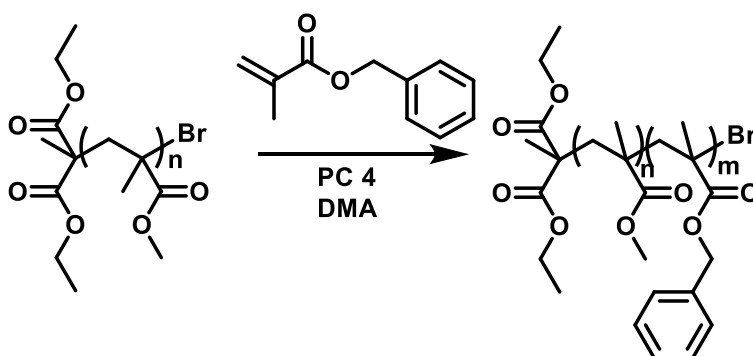
Chain-extension of the macroinitiatior with benzyl methacrylate was performed by dissolving 250 mg of PMMA macroinitiator (0.46 mmol) in 4.0 mL DMA, followed by the addition of 2.71 mL benzyl methacrylate (16.0 mmol) and 1.55 mg PC **4** (0.46 µmol). Continuous flow polymerization was set up according to standard procedures using a flow rate of 4.05 µL/min, for a 3 hour residence time. After equilibration an aliquot of the polymer solution was analyzed using ^{1}H NMR then collected. After collection the polymer was precipitated into methanol at -78 °C, dried, and analyzed using GPC. Conversion, 82.3%; M_n = 64.0 kDa; Đ = 1.60, I^* = 88%.

Synthesis of PMMA-b-PiBMA:
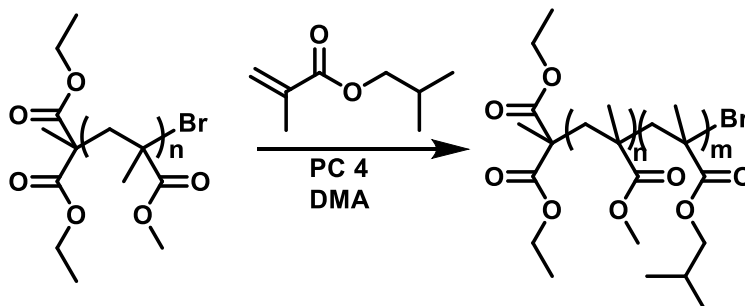
Chain-extension of the macroinitiatior with iso-butyl methacrylate was performed by dissolving 250 mg of PMMA macroinitiator (0.46 mmol) in 3.8 mL DMA, followed by the

addition of 2.56 mL isobutyl methacrylate (0.016 mol) and 1.47 mg PC **4** (0.46 µmol). Continuous

flow polymerization was set up according to standard procedures using a flow rate of 4.05 µL/min,

for a 3 hour residence time. After equilibration an aliquot of the polymer solution was analyzed

using ^{1}H NMR then collected. After collection the polymer was precipitated into methanol at -78

°C, dried, and analyzed using GPC. Conversion, 58%; M_n = 57.5 kDa; $Đ$ = 1.32, I^* = 60%.

Optimization Tables and Additional Experiments

Reactor Temperature Comparison:

Table 2.6: Results of O-ATRP of MMA in Continuous Flow Performed at Different Temperatures at Constant Residence Times.[a]

Run No.	Temperature (°C)[b]	Conv. (%)[c]	M_n (kDa)[d]	$Đ$ (M_w/M_n)[d]	Theo. M_n (kDa)[e]	I^* (%)[f]
1	28	52	4.5	1.16	5.2	116
2	39	61	6.5	1.12	6.1	94
3	60	69	7.2	1.25	6.9	95

[a][MMA]:[Initiator]:[PC] = [1000]:[10]:[1]; 3.73 mM of PC with, 2:3 MMA:DMA by volume, and irradiated by 3000 K fluorescent tubular lamp. [b]The temperature of the system was altered by blowing a fan on the system. [c]Determined by ^{1}H NMR. [d]Measured using GPC. [e]Calculated by $(Conv \times [Mon]/[Init.] \times Mw_{Mon})/1000$. [f]Initiator efficiency (I^*) calculated by $(Theo. M_n/Calc. M_n) \times 100$.

Tubing Length Optimization:

Table 2.7: Results of O-ATRP of MMA in Continuous Flow using Different Flow Rates at Constant Residence Times in Halar Tubing.[a]

Run No.	PC	Reactor Length (cm)	Flow Rate (µL/min)	Res. Time	Conv. (%)[b]	M_w (kDa)[c]	M_n (kDa)[c]	Đ (M_w/M_n)[c]	Theo. M_n (kDa)[d]	I^* (%)[e]
1	1	320	16.2	90	47	8.6	6.9	1.24	4.7	67
2	1	160	8.11	90	38	6.0	5.1	1.18	3.8	74
3	4	320	16.2	90	56	7.0	5.5	1.28	5.6	103
4	4	160	8.11	90	59	6.3	5.5	1.14	5.9	108
5	4	100	5.07	90	68	10.7	9.6	1.12	7.2	76

[a][MMA]:[Initiator]:[PC] = [1000]:[10]:[1]; 3.73 mM of PC with, 2:3 MMA:DMA by volume, and irradiated by 3000 K fluorescent tubular lamp. [b]Determined by ^{1}H NMR. [c]Measured using GPC. [d]Calculated by $(Conv \times [Mon]/[Init.] \times Mw_{Mon})/1000$. [e]Initiator efficiency (I^*) calculated by $(Theo. M_n/Calc. M_n) \times 100$.

Control Experiment with no PC:

Table 2.8: Results of Polymerization of MMA in a Continuous Flow Reactor with No PC.[a]

Residence Time (min.)	Flow Rate (µL/min)	Conv. (%)	M_n (kDa)	Đ (M_w/M_n)	Theo. M_n (kDa)	I^* (%)
15	48.64	4	95	1.85	0.4	0.4
30	24.32	7	100	2.06	0.7	0.7
60	12.18	13	47	3.33	1.3	2.8
120	6.08	20	27	5.97	2.0	7.4

[a][MMA]:[Initiator]:[PC] = [1000]:[10]:[0]; with 2:3 MMA:DMA by volume, and irradiated by 3000 K fluorescent tubular lamp.

Catalyst Screens:

Table 2.9: Results of O-ATRP of MMA in a Continuous Flow Reactor using PCs 1-4.[α]

Run No.	PC	Residence Time (min)	Flow Rate (µL/min)	Conv. (%)[b]	M_w (kDa)	M_n (kDa)[c]	Đ (M_w/M_n)[c]	Theo. M_n (kDa)[d]	I^* (%)[e]
1	1	30	24.32	12	2.3	2.1	1.10	1.2	56
2	1	60	12.16	24	4.7	4.2	1.13	2.4	58
3	1	90	8.11	38	6.0	5.1	1.18	3.8	74
4	1	120	6.08	49	7.8	6.6	1.18	4.9	74
5	2	15	48.64	12	3.0	2.7	1.14	1.2	43
6	2	30	24.32	23	5.6	5.1	1.10	3.2	45
7	2	45	16.21	32	7.5	6.8	1.10	3.2	46
8	2	60	12.16	40	7.9	7.6	1.05	4.0	53
9	2	90	8.11	64	11.8	11.1	1.07	6.6	57
10	3	5	145.9	12	12.3	7.4	1.66	1.2	16
11	3	15	48.64	28	14.8	9.5	1.55	2.8	29
12	3	30	24.32	40	16.4	11.4	1.44	4.0	35
13	3	60	12.16	48	16.4	12.6	1.30	4.8	38
14	3	90	8.11	50	20.9	18.9	1.10	5.0	26
15	4	15	48.64	17	2.5	2.1	1.19	1.7	85
16	4	30	24.32	32	3.5	2.9	1.20	3.2	108
17	4	60	12.16	48	5.0	4.3	1.16	4.8	111
18	4	90	8.11	59	6.3	5.5	1.14	5.9	108
19	4	120	6.08	65	6.9	5.8	1.19	6.5	112

[a][MMA]:[Initiator]:[PC] = [1000]:[10]:[1]; 3.73 mM of PC with, 2:3 MMA:DMA by volume, and irradiated by 3000 K fluorescent tubular lamp. [b]Determined by ^{1}H NMR. [c]Measured using GPC. [d]Calculated by $(Conv \times [Mon]/[Init.] \times Mw_{Mon})/1000$. [e]Initiator efficiency (I^*) calculated by $(Theo. M_n/Calc. M_n) \times 100$.
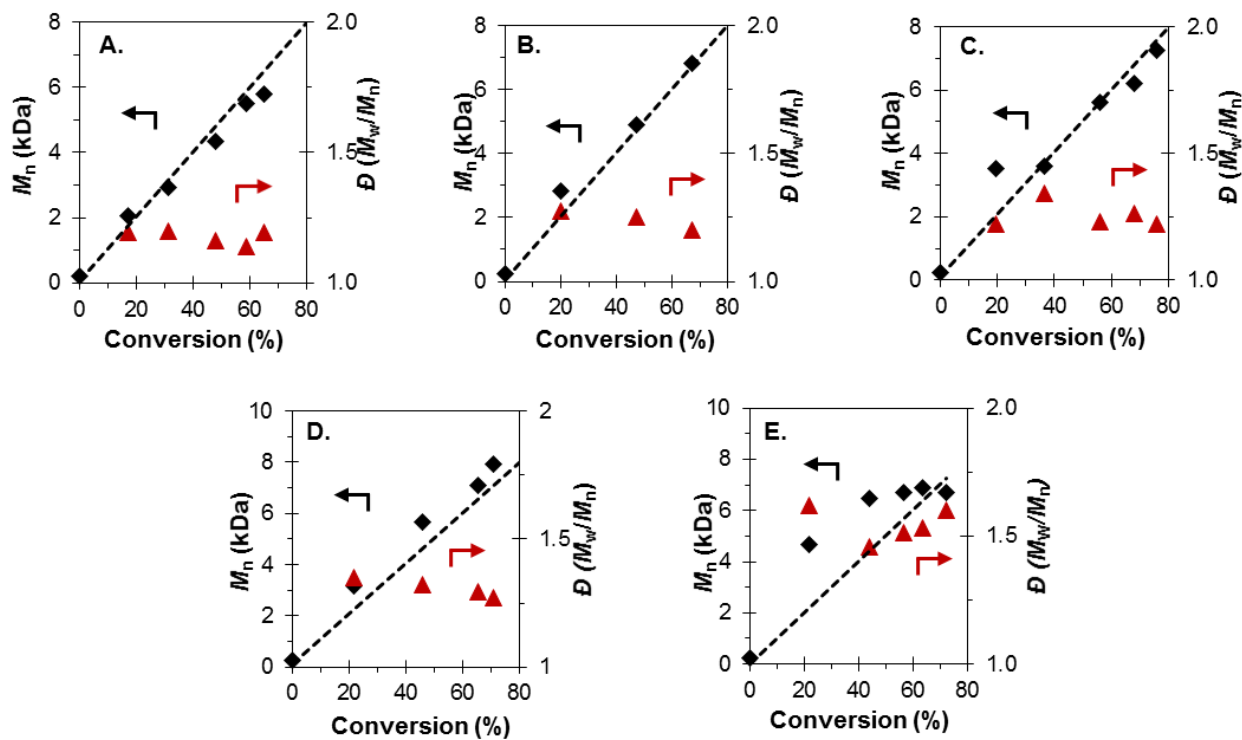
PC 4 Loading:

Figure 2.11: Plots of M_n (black diamonds) and $Đ$ *(red squares)* with respect to monomer conversion during the polymerization of MMA catalyzed by PC **4** using 0.1 (a), 0.04 (b), 0.02 (c), 0.01 (d) and 0.005 (e) mol % of **4**. Conditions for all plots: [1000]:[10]:[X] of [MMA]:[DBMM]:[4]; 160 cm of tubing reactor, irradiated by 3000 K fluorescent light.

Table 2.10: Detailed Polymerization Results for Experiments Testing the Effect of PC Loading on the O-ATRP of MMA in Continuous Flow.[a]

[4] mol %	Residence Time (min)	Flow Rate (μL/min)	Conv. (%)[b]	M_w (kDa)	M_n (kDa)[c]	Đ (M_w/M_n)[c]	Theo. M_n (kDa)[d]	I^* (%)[e]
0.1	15	48.64	17	2.5	2.1	1.19	1.74	85
0.1	30	24.32	32	3.5	2.9	1.20	3.15	108
0.1	60	12.16	48	5.0	4.3	1.16	4.82	111
0.1	90	8.11	59	6.3	5.5	1.14	5.90	108
0.1	120	6.08	65	6.9	5.8	1.19	6.49	112
0.04	15	48.64	20	3.6	2.8	1.28	2.0	71
0.04	60	12.16	47	6.1	4.9	1.25	4.7	97
0.04	90	8.11	67	8.2	6.8	1.20	6.7	98
0.02	15	48.64	19	4.3	3.5	1.22	1.9	55
0.02	30	24.32	36	4.8	3.6	1.34	3.6	101
0.02	60	12.16	56	6.9	5.6	1.23	5.6	100
0.02	90	8.11	68	7.9	6.2	1.26	6.8	109
0.02	120	6.08	76	8.9	7.2	1.22	7.6	105
0.01	15	48.64	22	4.3	3.2	1.35	2.2	69
0.01	30	24.32	46	7.5	5.7	1.32	4.6	80
0.01	60	12.16	65	9.2	7.1	1.30	6.5	92
0.01	90	8.11	71	10.1	7.9	1.27	7.1	90
0.005	15	48.64	22	7.6	4.7	1.62	2.2	47
0.005	30	24.32	44	9.5	6.5	1.46	4.4	68
0.005	45	16.21	57	10.2	6.7	1.52	5.7	84
0.005	60	12.16	64	10.6	6.9	1.53	6.4	93
0.005	90	8.11	72	10.7	6.7	1.60	7.3	108

[a][MMA]:[DBMM]:[**4**] = [1000:[10]:[X]; 2:3 of MMA to DMA by volume and 160 cm tubing reactor irradiated by 3000 K fluorescent lamp.
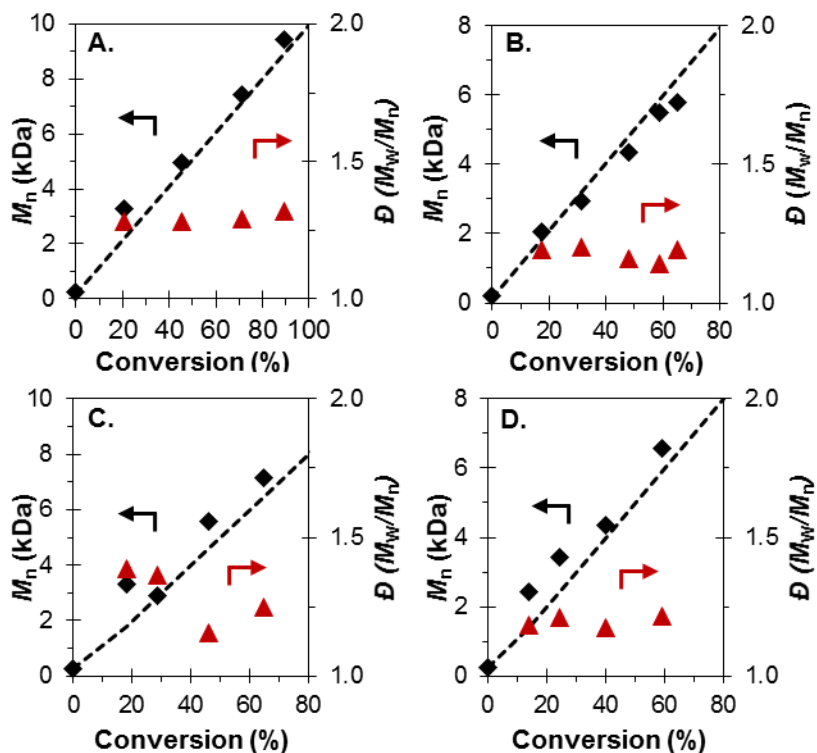
Solvent Volume Optimization:

Figure 2.12: Plots of M_n (black diamonds) and Đ *(*red squares*)* with respect to monomer conversion during the polymerization of MMA catalyzed by PC **4** using 1:1 (a), 2:3 (b), 1:2 (c), 1:3 (d) relative volumes of MMA:DMA. Conditions for all plots: [1000]:[10]:[1] of [Mon]:[Init.]:[PC]; 3.73 mM PC, 160 cm of tubing reactor, irradiated by 3000 K fluorescent light.

Table 2.11: Detailed Polymerization Results for Experiments Testing the Effect of Reaction Concentrations on the O-ATRP of MMA in Continuous Flow.[a]

MMA:DMA[b]	Residence Time (min)	Flow Rate (μL/min)	Conv. (%)	M_w (kDa)	M_n (kDa)	$Đ$ (M_w/M_n)	Theo. M_n (kDa)	I^* (%)
1:1	15	48.64	21	4.2	3.3	1.28	2.1	63
1:1	30	24.32	45	6.3	5.0	1.28	4.6	92
1:1	60	12.16	71	9.6	7.4	1.29	7.1	96
1:1	120	6.08	89	12.5	9.4	1.32	8.9	95
2:3	15	48.64	17	2.5	2.1	1.19	1.74	85
2:3	30	24.32	32	3.5	2.9	1.20	3.15	108
2:3	60	12.16	48	5.0	4.3	1.16	4.82	111
2:3	90	8.11	59	6.3	5.5	1.14	5.90	108
2:3	120	6.08	65	6.9	5.8	1.19	6.49	112
1:2	15	48.64	18	4.6	3.3	1.39	1.8	54
1:2	30	24.32	29	3.9	2.9	1.37	2.9	99
1:2	60	12.16	46	6.4	5.6	1.15	4.6	82
1:2	120	6.08	65	9.0	7.2	1.25	6.5	90
1:3	15	48.64	14	2.9	2.4	1.18	1.4	56
1:3	30	24.32	24	4.1	3.4	1.21	2.4	71
1:3	60	12.16	40	5.1	4.4	1.17	4.0	91
1:3	120	6.08	59	8.0	6.6	1.22	5.9	90

[a][MMA]:[DBMM]:[**4**] = [1000:[10]:[1]; 160 cm tubing reactor irradiated by 3000 K fluorescent lamp. [b]Relative volume ratios of DMA to MMA.
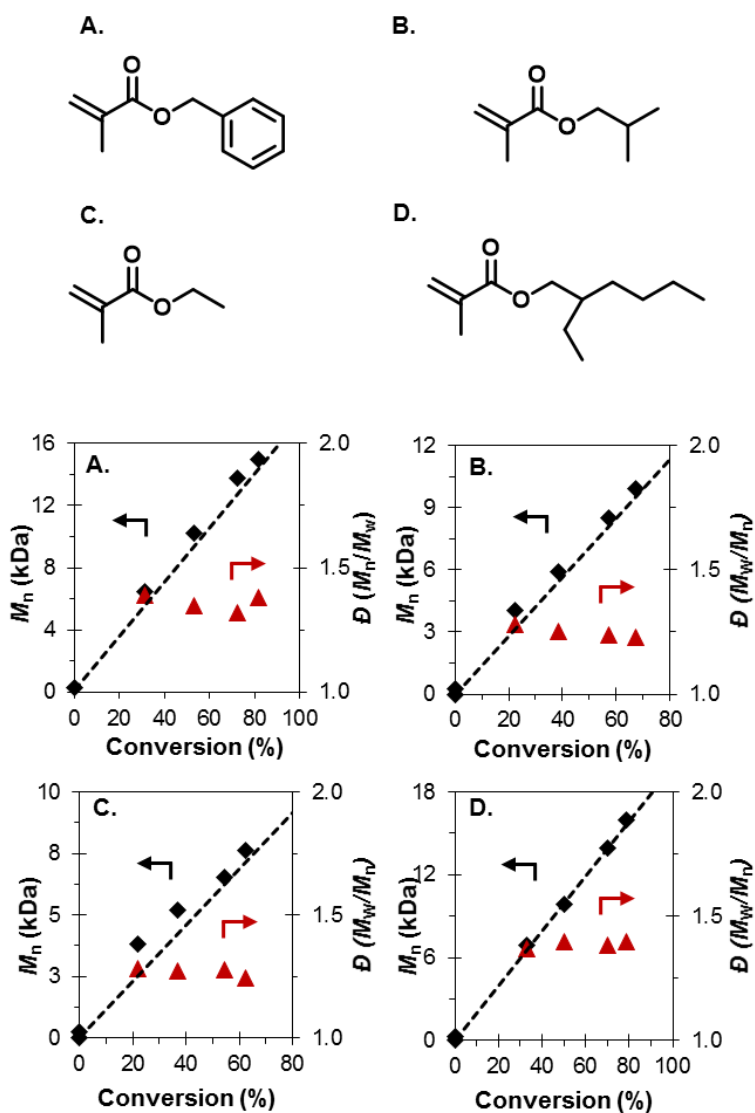
Expansion of Monomer Scope:

Figure 2.13: Plots of M_n (black diamonds) and $Đ$ *(*red squares*)* with respect to monomer conversion during the polymerization of benzyl methacrylate (a), isobutyl methacrylate (b), ethyl methacrylate (c), and 2-ethylhexyl methacrylate (d). Conditions for all plots: [1000]:[10]:[1] of [Mon]:[DBMM.]:[4]; 3.73 mM PC, 160 cm of tubing reactor, irradiated by 3000 K fluorescent light.

Table 2.12: Detailed Polymerization Results for O-ATRP of Methacrylate Monomers in Continuous Flow.[a]

Monomer[b]	Residence Time (min)	Flow Rate (μL/min)	Conv. (%)	M_w (kDa)	M_n (kDa)	$Đ$ (M_w/M_n)	Theo. M_n (kDa)	I^* (%)
BzMA	15	48.64	31	9.0	6.5	1.39	5.5	84
BzMA	30	24.32	53	13.8	10.2	1.35	9.4	91
BzMA	60	12.16	72	18.2	13.8	1.32	12.7	92
BzMA	90	8.11	82	20.7	15.0	1.38	14.4	96
iBMA	15	48.64	22	5.2	4.0	1.28	3.2	79
iBMA	30	24.32	39	7.4	5.9	1.25	5.5	93
iBMA	60	12.16	57	10.6	8.5	1.24	8.12	95
iBMA	90	8.11	67	12.2	9.9	1.23	9.53	96
EMA	15	48.64	22	4.9	3.8	1.28	2.5	65
EMA	30	24.32	37	6.6	5.2	1.27	4.2	81
EMA	60	12.16	55	8.4	6.5	1.28	6.2	95
EMA	90	8.11	63	9.4	7.6	1.24	7.1	94
EHMA	15	48.64	33	9.5	6.9	1.37	6.5	94
EHMA	30	24.32	50	13.8	9.9	1.40	10.0	101
EHMA	60	12.16	70	19.3	13.9	1.38	13.9	100
EHMA	90	8.11	79	22.4	16.0	1.40	15.6	98

[a][MMA]:[DBMM]:[**4**] = [1000:[10]:[1]; 2:3 of MMA to DMA by volume and 160 cm tubing reactor irradiated by 3000 K fluorescent lamp. [b]Polymerizations of benzyl methacrylate (BzMA), isobutyl methacrylate (iBMA), ethyl methacrylate (EMA), and 2-ethylhexyl methacrylate (EHMA).
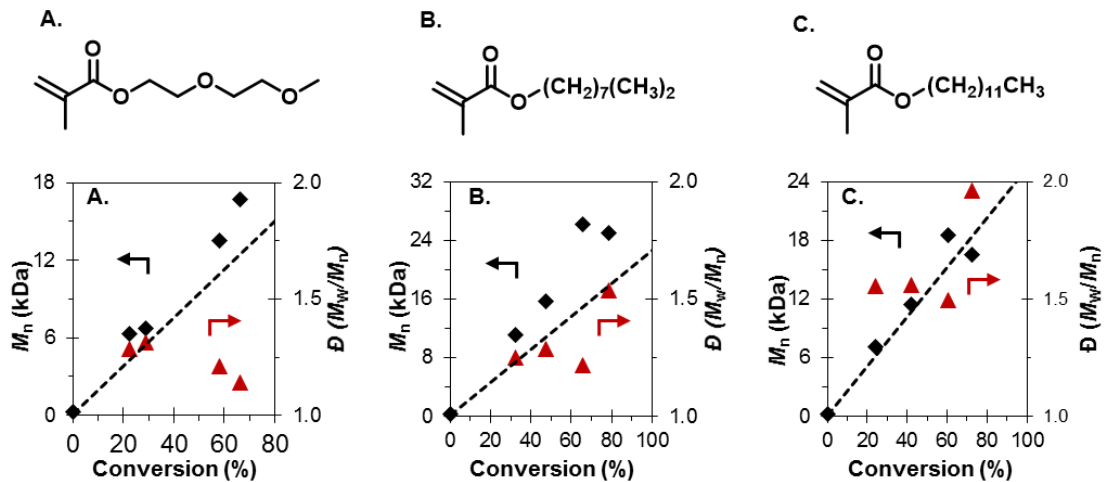
Figure 2.14: Plots of M_n (black diamonds) and $Đ$ (red squares) with respect to monomer conversion during the polymerization of diethylene glycol methyl ether methacrylate (a), isodecyl methacrylate (b), and lauryl methacrylate (c). Conditions for all plots: [1000]:[10]:[1] of [Mon]:[DBMM.]:[4]; 3.73 mM PC, 160 cm of tubing reactor, irradiated by 3000 K fluorescent light.

Table 2.13: Detailed Polymerization Results for O-ATRP of Methacrylate Monomers in Continuous Flow.[a]

Monomer[b]	Residence Time (min)	Flow Rate (μL/min)	Conv. (%)	M_w (kDa)	M_n (kDa)	$Đ$ (M_w/M_n)	Theo. M_n (kDa)	I^* (%)
DEGMA	10	73.0	22	8.1	6.3	1.29	4.2	67
DEGMA	15	48.64	29	8.8	6.7	1.31	5.5	82
DEGMA	45	16.21	58	16.4	13.5	1.21	11.0	81
DEGMA	60	12.16	66	19.1	16.7	1.14	12.4	74
iDMA	15	48.64	32	13.9	11.1	1.25	7.34	66
iDMA	30	24.32	47	20.1	15.7	1.29	10.7	69
iDMA	60	12.16	66	31.9	26.2	1.22	14.9	57
iDMA	90	8.11	79	38.3	24.9	1.54	17.8	71
LMA	15	48.64	24	11.0	7.1	1.55	6.17	87
LMA	30	24.32	42	17.9	11.5	1.56	10.7	94
LMA	60	12.16	60	27.6	18.5	1.49	15.4	83
LMA	90	8.11	72	32.5	16.5	1.96	18.4	111

[a][MMA]:[DBMM]:[**4**] = [1000:[10]:[1]; 2:3 of MMA to DMA by volume and 160 cm tubing reactor irradiated by 3000 K fluorescent lamp. [b]Polymerizations of di(ethyleneglycol) methyl ether methacrylate (DEGMA) isodecyl methacrylate (iDMA), and lauryl methacrylate (LMA).

References

1. Pan, X.; Tasdelen, M. A.; Laun, J.; Junkers, T.; Yagci, Y.; Matyjaszewski, K. *Progress in Polymer Science* **2016**, *62*, 73-125.

2. Corrigan, N.; Shanmugam, S.; Xu, J.; Boyer, C. *Chem. Soc. Rev.* **2016**, *45,* 6165-6212.

3. Chatani, S.; Kloxin, C. J.; Bowman, C. N. *Polym. Chem.* **2014**, *5*, 2187-2201.

4. Yagci, Y.; Jockusch, S.; Turro, N. J. *Macromolecules* **2010**, *43*, 6245-6260.

9. Zhou, y. N.; Guo, J. K.; Li, J. J.; Luo, Z. H. *Ind. Eng. Chem. Res.,* **2016,** *55,* 10235-10242.

10. Patten, T. E.; Xia, J.; Abernathy, T.; Matyjaszewski, K. *Science* **1996**. *272*, 866– 868.

11. Matyjaszewski, K.; Xia, J. *Chem. Rev*. **2001**, *101*, 2921–2990.

12. Matyjaszewski, K.; Tsarevsky, N. V. *J. Am. Chem. Soc.* **2014,** *136*, 6513–6533.

13. Matyjaszewski, K. *ACS Symposium Series* **2015**, *1187*, 1-17.

14. Konkolewicz, D.; Shröder, K.; Buback, J.; Bernhard, S.; Matyjaszewski, K. *ACS Macro Lett.* **2012**, *1*, 1219-1223.

15. Mosnaćek, J.; Ilčíková, M. *Macromolecules* **2012**, *45*, 5859-5865.

16. Jones, G. R.; Whitfield, R.; Anastasaki, A.; Haddleton, D. M. *J. Am. Chem. Soc.* **2016**, *138*, 7346-7352.

17. Zhou, Y. N.; Luo, Z. H. *AlChE* **2015,** *61,* 1947-1958.

18. Faucher, S,; Okrutny, P.; Zhu, S. *Macromolecules* **2006**, *39*, 3-5.

19. Zhang, H.; Abeln, C. H.; Fijten, M. W. M.; Schubert, U. S. *E-Polymers* **2006**, *6*, 90-98.

20. Matyjaszewski, K.; Pintauer, T.; Gaynor, S. *Macromolecules* **2000**, *33*, 1476-1478.

21. Miyake, G. M.; Theriot, J. C. *Macromolecules* **2014,** *47,* 8255-8261.

22. Treat, N. J.; Sprafke, H.; Kramer, J. W.; Clark, P. G.; Barton, B. E.; Read de Alaniz, J.; Fors, B. P.; Hawker, C. J. *J. Am. Chem. Soc.* **2014**. *136*, 16096-16101.

23. Theriot, J. C.; Lim, C.-H.; Yang, H.; Ryan, M. D.; Musgrave, C. B.; Miyake, G. M. *Science* **2016**, *352*, 1082.

24. Pearson, R. M.; Lim, C.-H.; McCarthy, B. G.; Musgrave, C. B.; Miyake, G. M. *J. Am. Chem. Soc*. **2016**, *138*, 11399-11407.

25. Allushim A.; Jockush, S.; Yilmaz, G.; Yagci, Y. *Macromolecules* **2016**, *49,* 7785-7792.

26. Huange, Z.; Gu, Y.; Liu, X.; Zhang, L.; Cheng, Z.; Zhu, X. *Macromol Rapic Commun.* **2016.** DOI: 10.1002/marc.201600461.

27. Pan, X.; Fang, C.; Rantin, M.; Maolhotra, N.; So, W. Y.; Peateanu, L. A.; Isee, A. A.; Gennaro, A.; Liu, P.; Matyjaszewski, K. *J. Am. Chem. Soc.* **2016**, *138,* 2411-2425.

28. Lim, C. H.; Ryan, M. D.; McCarthy, B. G.; Theriot, J. C.; Sartor, S. M.; Damrauer, N. H.; Musgrave, C. B.; Miyake, G. M. *J. Am. Chem. Soc.* **2016.** DOI: 10.1021/jacs.6b11022.

29. Tucker, J. W.; Zhang, Y.; Jamison, T. F.; Stephenson, C. R. J. *Angew. Chem. Int. Ed.* **2012**, *51,* 4144-4147.

30. Hook, B. D. A.; Dohle, W.; Hirst, P. R.; Pickworth, M.; Berry, M. B.; Booker-Milburn, K. I. *J. Org. Chem.* **2005,** *70,* 7558-7564.

31. Beatty, J. W.; Douglas, J. J.; Miller, R.; McAtee, R. C.; Cole, K. P.; Stephenson, C. R. J. *Chem* **2016,** *1,* 456-472.

32. Garlets, Z. J.; Nguyen, J. D.; Stephenson, C. R. J. *Isr. J. Chem.* **2014**, *54*, 351.

33. Steinbacher, J. L.; McQuade, D. T. *J. Polym. Sci, Part A: Polym. Chem.* **2006**, *44,* 6505-6533.

34. Natalello, A.; Morsbach, J.; Friedel, A.; Alkan, A.; Tonhauser, C.; Müller, A. H. E.; Frey, H. *Org. Process Res. Dev.* **2014**, *18,* 1408-1412.

35. Diehl, C.; Laurino, P.; Azzouz, N.; Seeberger, P. H. *Macromolecules* **2010**, *43,* 10311-10314.

36. Bou-Hamdan, F. R.; Seeberger, P. H. *Chem. Sci.* **2012**, *3*, 1612-1616.

37. Lu, H.; Schmidt, M. A.; Jensen, K. F. *Lab on a Chip* **2001**, *1*, 22-28.

38. Elliott, L. D.; Knowles, J. P.; Koovits, P. J.; Maskill, L. G.; Ralph, M. J.; Lejeune, G.; Edwards, L. J.; Robinson, R. I.; Clemens, I. R.; Cox, B.; Pascoe, D. D.; Koch, G.; Eberle, M.; Berry, M. B. Booker-Milburn, K. I. *Chem. Eur. J.* **2014,** *20,* 15226-15232.

39. Wu, T.; Mei, Y.; Cabral, J. T.; Xu, C.; Beers, K. L. *J. Am. Chem. Soc.* **2004**, *126*, 9880-9881.

40. Fukuyama, T.; Kajihara, Y.; Ryu, I.; Studer, A. *Synthesis* **2012,** *44,* 2555–2559.

41. Enright, T. E.; Cunningham, M. F.; Keoshkerian, B. *Macromol. Rapid Commun*. **2005**, *26*, 221-225.

42. Hornung, C. H.; Guerrero-Sanchez, C.; Brasholz, M.; Saubern, S.; Chiefari, J.; Moad, G.; Rizzardo, E.; Thang, S. H. *Org. Process Res. Dev.* **2011,** *15,* 593-601.

43. Muller, M.; Cunningham, M. F.; Hutchinson, R. A. *Macromol. React. Eng.* **2008,** *2,* 31-36.

44. Noda, T.; Grice, A. J.; Lever, M. E.; Haddleton, D. M. *Eur. Polym. J.* **2007,** *43,* 2321-2330.

45. Chen, M.; Johnson, J. A. *Chem. Commun.* **2015**, *51,* 6742-6745.

46. Gardiner, J.; Hornung, C. H.; Tsanaktsidis, J.; Guthrie, D. *European Polymer Journal* **2016,** *80,* 200-207.

47. Corrigan, N.; Rosli, D.; Jones, J. W. J.; Xu, J.; Boyer, C. *Macromolecules* **2016**, *49,* 6779-6789.

48. Melker, A.; Fors, B. P.; Hawker, C. J.; Poelma, J. E. *J. Polym. Sci., Part A: Polym. Chem.* **2015**, 53, 2693-2698.

49. Wenn, B.; Conradi, M.; Carreiras, A. D.; Haddleton, D. M.; Junkers, T. *Polym. Chem.* **2014**, *5,* 3053-3060.

50. Initiator efficiency (I^*) = theoretical number average molecular weight (Mn)/experimentally measured Mn × 100.

51. Parida, D.; Serra, C. A.; Gómez, R. I.; Garg, D. K.; Hoarau, Y.; Bouquey, M.; Muller, R. *J. Flow Chem.* **2014**, *4,* 92-96.

CHAPTER 3

Synthesis of Star Polymers using Organocatalyzed Atom Transfer Radical

Polymerization Through a Core-first Approach

Overview

Synthetic routes to higher ordered polymeric architectures are important tools for advanced materials design and realization. In this study, organocatalyzed atom transfer radical polymerization is employed for the synthesis of star polymers through a core-first approach using a visible-light absorbing photocatalyst, 3,7-di(4-biphenyl)-1-naphthalene-10-phenoxazine. Structurally similar multifunctional initiators possessing 2, 3, 4, 6, or 8 initiating sites were used in this study for the synthesis of linear telechelic polymers and star polymers typically possessing dispersities lower than 1.5 while achieving high initiator efficiencies. Furthermore, no evidence of undesirable star-star coupling reactions was observed, even at high monomer conversions and high degrees of polymerization. The utility of this system is further exemplified through the synthesis of well-defined diblock star polymers.

Introduction

Synthetic polymers have become indispensable, with applications integrated into all facets of modern society. Advanced polymeric materials can be designed and imbued with specific functionalities for precise applications through exploitation of synthetic methods to form chemical compositions and tune polymer architectures to influence the resulting properties.[1] Tailored materials are accessible through the use of complex polymeric architectures, one example of which is star polymers. Star polymers are macromolecules possessing three or more linear polymeric

chains, or "arms", radiating from a central branching point, or "core", and offer an avenue toward advanced materials design stemming from their higher-order architecture and unique properties.[2] In comparison to their linear analogues, star polymers exhibit unique rheological and physical properties stemming from a compact, globular structure.[3,4] Furthermore, star polymers are highly customizable, with tunable properties and numerous available applications through modification of arm and core sizes, functionalities, and compositions.[5]

There are 3 major methods for the synthesis of star polymers, each with their own advantages and disadvantages. These approaches include core-first, arm-first, and grafting-onto. Each set of synthetic approaches can be modulated for the synthesis of star polymers possessing desired properties and applications. The core-first approach relies on the use of a multifunctional initiator, which begins polymerization outward from the core. In this approach, the arm incorporation can be precisely controlled by the number of initiating sites on the initiator, which is best performed in systems with high initiator efficiencies. However, in these systems the core sizes are typically quite small and limited by the choice of multifunctional initiator. Furthermore, in radical polymerization methods star-star coupling reactions can occur, causing gelation, high dispersities, and uncontrolled properties.[6] These undesireable termination events occur from the reaction of two intramolecular arm chain-ends, forming high molecular weight (MW) stars that can be observed via gel permeation chromatography (GPC). The arm-first approach relies on crosslinking of linear polymer chain-end groups with a multifunctional monomer species. In this approach, high MW stars can be synthesized using well-defined linear arms. However, arm incorporation into the star can be difficult to regulate and is typically controlled by reaction stoichiometry, arm size, and reaction component compositions.[7,8,9] Star-star coupling reactions can also occur, resulting in star polymers with a high dispersity and unreacted polymer arms.

46

Moreover, incorporation of arms with high numbers of monomer repeat units can be limited due to steric effects.[10] The grafting-onto approach exploits post-polymerization modification steps to combine the chain-end group of a synthesized polymer with a core and is typically achieved through well-studied "click" reactions between polymer arm and core molecules with complementary functionality.[11] This method is advantageous in that it allows for complete characterization of both the arm and core molecules. Similar to the core-first approach, the core size is typically small and, as in the arm-first method, the incorporation of high MW arms can be challenging.[12]

Controlled radical polymerizations (CRPs) have emerged as powerful synthetic approaches for the synthesis of advanced materials with complex architectures due to robust monomer scope and reaction media compatibility to yield control over important polymerization metrics including dispersity ($Đ$), growth of MW, and retention of chain-end group functionality.[13,14] The most widely studied CRP, atom transfer radical polymerization (ATRP), historically operates by reversible activation of a dormant alkyl halide species by a transition metal catalyst to generate a propagating carbon centered radical, which is deactivated through end-capping by the halogen to return the growing polymer to the dormant state.[15,16] Control over polymerization is imparted through a higher rate of deactivation in comparison to rates of propagation and initiation, maintaining a low concentration of radicals and minimizing undesirable bimolecular termination events.[17]

The reversible activation mechanism orchestrated by ATRP results in retention of a functional halogen chain-end group. This functionality facilitates the synthesis of advanced materials, such as through chain-extension to form block copolymer structures or further reactivity for post-polymerization modifications.[18] ATRP has been employed for the synthesis of star polymers using all 3 of classes of synthetic approaches.[19,20,10,21,22] In particular, for the core-first

approach a variety of different catalytic systems have shown to be effective in star synthesis using a range of monomers and multifunctional initiators.[23,24,25,26] However, in some cases star-star coupling reactions have been observed, becoming more prevalent with increased number of arms and higher monomer conversion. This effect has been controlled through use of dilute systems and limiting polymerization to low monomer conversions in copper catalyzed ATRP systems. [27] Recently, photoinduced ATRP catalyzed by a copper catalyst synthesized star polymers containing, 4, 6, and 21 arms from a core-first approach, reaching above 80% conversion before star-star coupling reactions were observed.[28]

A newly developed variant of ATRP, organocatalyzed ATRP (O-ATRP) uses a photoredox catalyst to mediate the catalytic cycle through an oxidative quenching pathway and is proposed to proceed through 4 central steps (**Figure 3.1 A**).[29] First, irradiation of the ground state PC generates the excited state PC*. Next, PC* reduces an alkyl halide initiator during activation to simultaneously form an active carbon-centered radical species and $^2PC^{\bullet+}X^-$. The third step is polymerization propagation of the carbon centered radical to grow the polymer chain. Finally, the last step of the cycle is deactivation, which occurs through end-capping of the active polymer chain with the halide group, returning the polymer to the dormant state and the catalyst to the ground state PC. Analogous to ATRP, control over polymerization is imparted through a fast rate of deactivation in comparison to propagation and activation.
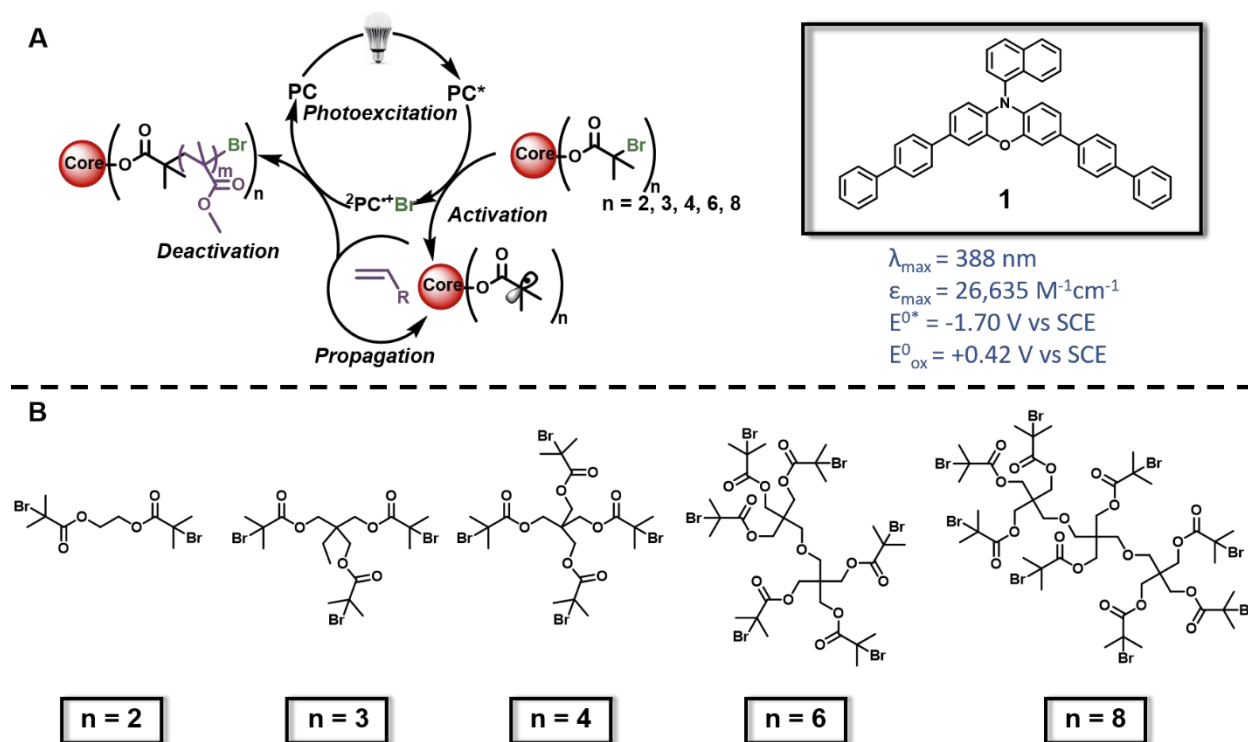
Figure 3.1: (a) Proposed catalytic cycle for core-first star synthesis using O-ATRP (left) and structure and properties of PC **1** used in this study (right). (b) Structures of multifunctional initiators used in this study containing *n* number of initiating sites.

Since 2014, research in our group has centered on the development of O-ATRP through the establishment of PC design principles gained from increased mechanistic understanding.[30,31,32,33,34] This progress has been achieved through a combined computational and experimental approach, largely studying the polymerization of methyl methacrylate (MMA) for the synthesis of linear poly(methyl methacrylate) (PMMA) to study PC success. Recently, we have reported on the use of 3,7-di(4-biphenyl)-1-naphthalene-10-phenoxazine (**1**) as a photocatalyst capable of operating a well-controlled O-ATRP under a variety of irradiation conditions[35] as well as in both batch and scalable continuous flow reactors.[36] Beyond O-ATRP, **1** also can be used as a PC in several small molecule transformations.[37] **1** possesses several desirable attributes of a PC for O-ATRP, including efficient visible light absorption, with a λ_{max} at 388 nm, ε_{max} of 26,635 M⁻

^{1}cm^{-1}, paired with a strong triplet excited state reduction potential of -1.70 V vs SCE, and oxidation potential of +0.42 V vs SCE. Furthermore, **1** has a high triplet quantum yield ($\Phi = 0.9$) with a sufficiently long excited state lifetime ($\tau = 480$ µs). Lastly, **1** is stable to reversible redox processes necessary for a PC. With these considerations in mind, we sought to expand the synthetic capabilities of this PC in O-ATRP to include well-defined star polymer synthesis through a core-first approach. 4 structurally similar multifunctional initiators, with number of initiating sites (*n*) ranging from 3-8, were employed in the synthesis of PMMA star polymers. To fully understand the capabilities of O-ATRP and a core-first approach, a similar initiator with 2 initiating sites was also employed to produce a telechelic linear polymer (**Figure 3.1 B**).

Results and Discussion

The investigation into the synthesis of star polymers from a core-first approach using O-ATRP launched with the examination of the effect of different reaction concentrations on efficient and well-controlled star polymer synthesis. This investigation was motivated by the desire to avoid undesirable star-star coupling events, mitigate potential issues stemming from viscosity caused by high MW polymers, and to determine optimized conditions for the synthesis of well-defined star polymers using O-ATRP.

Initial polymerization conditions employed a 1:2 volumetric ratio of MMA:DMAc using multifunctional initiators possessing 2, 3, 4, 6, and 8 alkyl bromide initiating functionalities, targeting a degree of polymerization of 50 monomer units for each arm. Under these conditions, the results for all stars indicated a well-controlled system at monomer conversions above 50%. However, closer analysis of the polymerization revealed less control at lower monomer conversions. For all stars, this relatively less-controlled regime is characterized by high *Đ*, and low initiator efficiencies (*I**) (see Experimental Section for full details). For the synthesis of complex

globular and compact polymeric architectures, a difference in actual and measured dispersity caused by changes in elution behavior from GPC has been observed and theoretically predicted.[38,39] A high I^* is indicative of agreement between theoretically calculated number average molecular weight ($M_{n(theo.)}$) and measured number average molecular weight ($M_{n(actual.)}$). The lesser degree of control found in these initial experiments can perhaps be attributed to inefficient activation caused by low PC concentrations, resulting in insufficient amounts of $^2PC^{\bullet+}$ and subsequently poor deactivation.

In the case of the linear polymer synthesized from the difunctional initiator, polymerization after 8 hours reached 78% conversion with an M_n of 9.2 kDa, $Đ$ of 1.30 and $I^* = 89\%$. Synthesis of a 3-arm star under these conditions gave 66% conversion, $M_n = 14.2$ kDa, $Đ$ of 1.13 and $I^* = 74\%$. The synthesis of the 4-arm star polymer yielded a product with $Đ = 1.45$, $M_n = 11.1$ kDa, and $I^* = 115\%$ at 60% conversion while the 6-arm star gave $Đ = 1.33$, $M_n = 19.5$ kDa, and $I^* = 91\%$ at 56% conversion. The 8-arm star was synthesized to a polymer with $Đ = 1.47$, $M_n = 25.4$ kDa, $I^* = 108\%$ at 65% conversion. Importantly in this case, there was no deleterious increase in reaction solution viscosity, shown by an observed uniform stirring rate during the course of polymerization times.

Observing that for all stars control over polymerization was decreased at low monomer conversions using dilute conditions, further studies using a 1:1 volumetric ratio of MMA:DMAc at the onset of polymerization was performed. To prevent undesirable effects from increased viscosity at high polymer MWs, an additional 1.0 mL of DMAc was added at the 3rd hour of polymerization. These experiments resulted in increased control over the polymerization at all stages of monomer conversion. After 8 hours of polymerization under these conditions, the use of the difunctional initiator was polymerized to a linear polymer with M_n of 13.6 kDa, $Đ$ of 1.29, and

I* = 83% at 84% conversion (**Table 3.1, entry 1**). A *Đ* of 1.18, M_n of 11.6 kDa and *I** = 89% at

65% conversion was realized for the 3-arm star (**Table 3.1, entry 2**). An analysis of the 4-arm, 6-

arm, and 8-arm star showed 70% conversion *Đ* = 1.30, M_n = 15.1, *I** = 97% and 50% conversion,

Đ = 1.22, M_n = 17.1 kDa, *I** = 95% and 60% conversion, *Đ* = 1.33, M_n = 25.4 kDa, and *I** = 101%

respectively (**Table 3.1, entries 3, 4, 5**). The results for 1:1 MMA:DMAc and 1:2 MMA:DMAc

concentrations, as well as corresponding GPC traces for 1:1 MMA:DMAc conditions can be

exemplified for the 3-arm and 8-arm stars in **Figure 3.2**.

Table 3.1: Results of O-ATRP of MMA after 8 hours using multifunctional initiators with 2, 3, 4, 6, and 8 number initiating sites and an initial 1:1 MMA:DMAc ratio, by volume.[a]

Entry	# arms	[MMA]:[RBr$_n$] :[PC]	Conv. (%)[b]	$M_{n\,(actual)}$ (kDa)[c]	$M_{n\,(theo.)}$ (kDa)[d]	*Đ* (M_w/M_n)[c]	*I** (%)[e]
1	2	[1000]:[10]:[1]	84	13.6	8.8	1.29	83
2	3	[1500]:[10]:[1]	65	11.6	10.3	1.18	89
3	4	[2000]:[10]:[1]	70	15.1	14.7	1.30	97
4	6	[3000]:[10]:[1]	50	17.1	16.2	1.22	95
5	8	[4000]:[10]:[1]	60	25.4	25.7	1.33	101

[a]Polymerization conditions are using 1:1 MMA:DMAc by volume with a total reaction volume of 2 mL, with addition of 1 mL of DMAc after 3 hours of polymerization. Each polymer arm is targeting a degree of polymerization of 50 at 100% monomer conversion. The polymerization is irradiated by white LEDs. [b]Determined by ^{1}H NMR spectroscopy. [c]Measured using GPC. [d]Calculated by $(Conv \times [Mon]/[Init.] \times Mw_{Mon})/1000$. [e]Calculated by $(Theo. M_n/Calc. M_n) \times 100$.
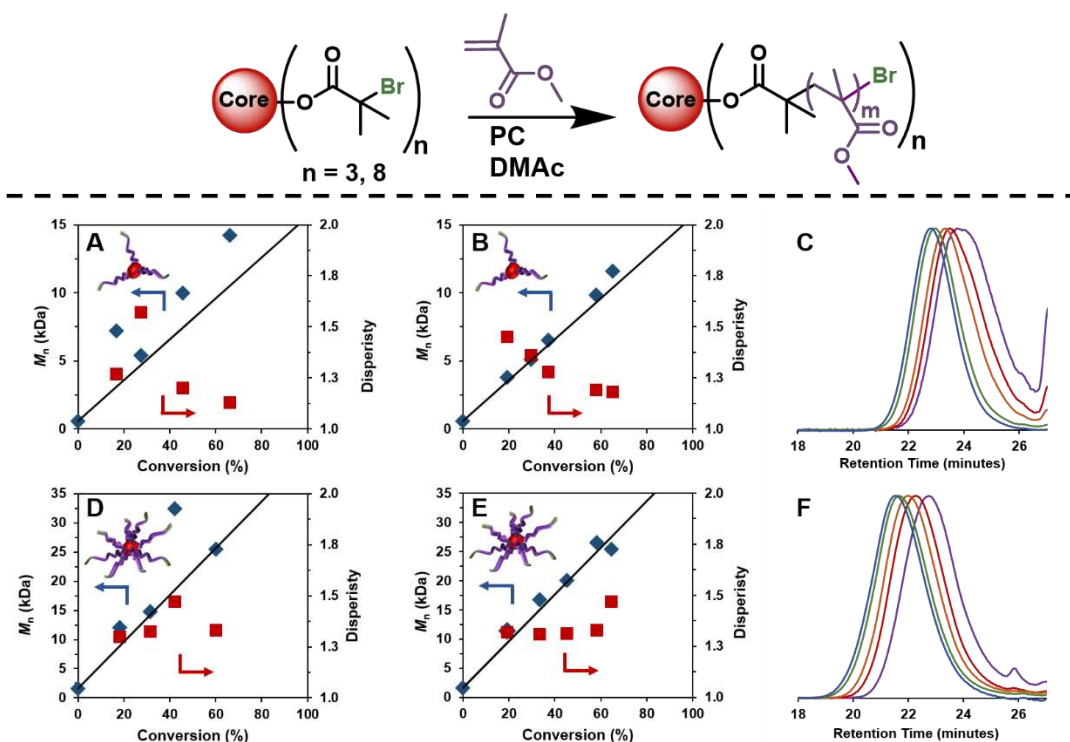
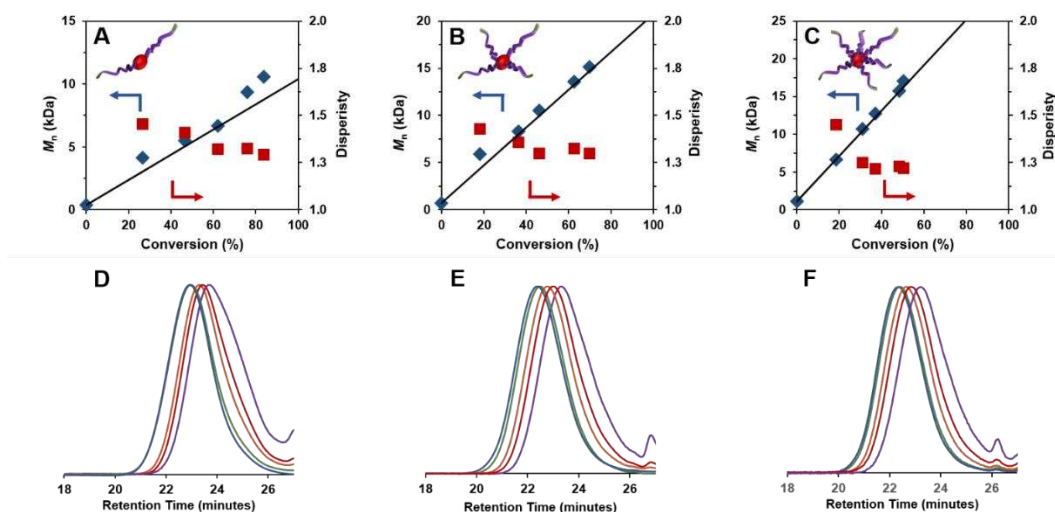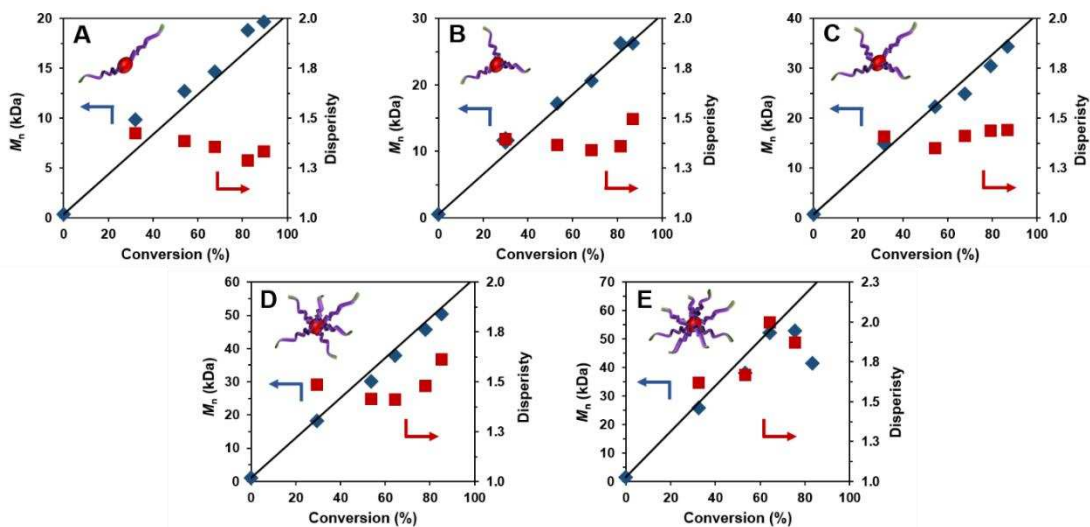**Figure 3.2:** Top: A schematic representation of the synthesis of star polymers. Bottom: Plots of number average molecular weight (blue diamonds), dispersity (red squares), and theoretical M_n (black line) versus monomer conversion for the O-ATRP of MMA using (a) 1:2 MMA:DMAc by volume and (b) 1:1 MMA:DMAc by volume with (c) corresponding GPC traces for 1:1 MMA:DMAc by volume for a 3-arm star polymer. The results for an 8-arm star polymer are shown for (d) 1:2 MMA:DMAc by volume and (e) 1:1 MMA:DMAc by volume with (f) corresponding GPC traces for 1:1 MMA:DMAc by volume.

In general, for all the stars using 1:1 MMA:DMAc by volume reaction conditions, dispersity typically decreased over time (**Figures 3.2 and 3.3**), with the exception of the 8-arm star, where Đ remained nearly constant until 58% conversion and rose to 1.47 at 65% conversion (**Figure 3.2 E**). Significantly, no detectable star-star coupling events were observed in all cases as evidenced by monomodal and symmetrical GPC traces coupled with high I*s. However, it was observed that Đ tended to increase with an increasing number of arms. Without any GPC evidence of star-star coupling, this increasing can be attributed to a higher number of other radical termination events, causing loss of chain-end functionality and increased molecular weight

53

distributions. In a comparison of both reaction concentration conditions tested, all experiments after ~50% conversion showed similar results (See Experimental Section for full description of results). In an analysis of the effect of relative photocatalyst concentrations to both moles of initiator and moles of bromide initiating sites, a universal ratio of [10]:[1] of moles of multifunctional initiator to moles of **1** was found effective in synthesizing star polymers with a high degree of control over polymerization for all initiators used in this study (**Table 3.5**).

Figure 3.3: Plots of number average molecular weight (blue diamonds), dispersity (red squares), and theoretical M_n (black line) versus monomer conversion for the O-ATRP of MMA using 1:1 MMA:DMAc by volume for (a) linear polymer, (b) 4-arm, and (c) 6-arm star polymers with corresponding GPC traces for the (d) the linear polymer, and (e) 4-arm, and (f) 6-arm star polymers.

Additional studies of star polymer synthesis using O-ATRP was performed using 1:1 of MMA:DMAc. This system was further extended to include the synthesis of higher MW star polymers targeting a degree of polymerization of 100 monomer units for each arm. In the case of the telechelic polymer and stars with 3, 4, and 6 arms the synthesis was well-controlled (**Figure 3.4 A, B, C, D**), resulting in Đ = 1.33, 1.50, 1.44, and 1.61 as well as I^* = to 93%, 102%, 103%, and 104%, respectively (**Table 3.2**). However, when using the octo-functional initiator (**Figure**

3.4 E) loss of control was observed after 53% conversion, upon which dispersity rose from 1.67 to 2.00, the growth of molecular weight ceased to be linear, and I^* rose to 165%. With conversions ranging from 84% to 90%, no star-star coupling events were observed in the GPC traces or molecular weight results (See Experimental Section for full GPC traces). However, in the case of the 3-arm and 6-arm star polymers, dispersity began to rise after 80% conversion, perhaps as a consequence of increased radical termination events.

Table 3.2: Results of O-ATRP of MMA after 8 hours using multifunctional initiators with 2, 3, 4, 6, and 8 number of initiating sites and targeting a degree of polymerization of 100.[a]

Entry	# arms	[MMA]:[RBr$_n$]:[PC]	Conv. (%)[b]	$M_{n \text{ (actual)}}$ (kDa)[b]	$M_{n \text{ (theo.)}}$ (kDa)[b]	$Đ$ (M_w/M_n)[b]	I^* (%)[b]
1	2	[2000]:[10]:[1]	90	19.6	18.3	1.33	93
2	3	[3000]:[10]:[1]	87	26.3	26.7	1.50	102
3	4	[4000]:[10]:[1]	87	34.3	35.5	1.44	103
4	6	[6000]:[10]:[1]	85	50.3	52.3	1.61	104
5	8	[8000]:[10]:[1]	84	41.5	68.4	1.90	165

[a]Polymerizations using 1:1 MMA:DMAc by volume with a total reaction volume of 2 mL, with addition of 1 mL of DMAc after 3 hours of polymerization. The polymerization is irradiated by white LEDs. [b]See footnote for Table 3.1 for details.

Figure 3.4: Plots of number average molecular weight (blue diamond), dispersity (red square), and theoretical M_n (black line) versus monomer conversion for the O-ATRP of MMA targeting a degree of polymerization of 100 for each polymer arm using 1:1 MMA:DMAc by volume for (a) linear polymer, and (b) 3-arm, (c) 4-arm, (d) 6-arm, and (e) 8-arm star polymers.

To confirm chain-end group fidelity of the synthesized star polymers, diblock star polymer synthesis was performed through a chain-extension experiment. Chain-extension was achieved through star polymer macroinitiator synthesis under the optimized polymerization conditions, targeting conversions between 35% and 45% to ensure chain-end group fidelity, followed by macroinitiator isolation and subsequent reintroduction to polymerization conditions of the star polymer as the multifunctional initiator species (**Figure 3.5 A**). For all stars, chain-extension using benzyl methacrylate was successful, as evidenced by baseline resolved shifts in GPC traces (**Figure 3.5 B**). Similar to the synthesis of star homopolymers, Đ was observed to increase with a corresponding increase in number of arms. In total, the ability to efficiently synthesize diblock star polymers provides a platform for targeted macromolecular engineering using O-ATRP.
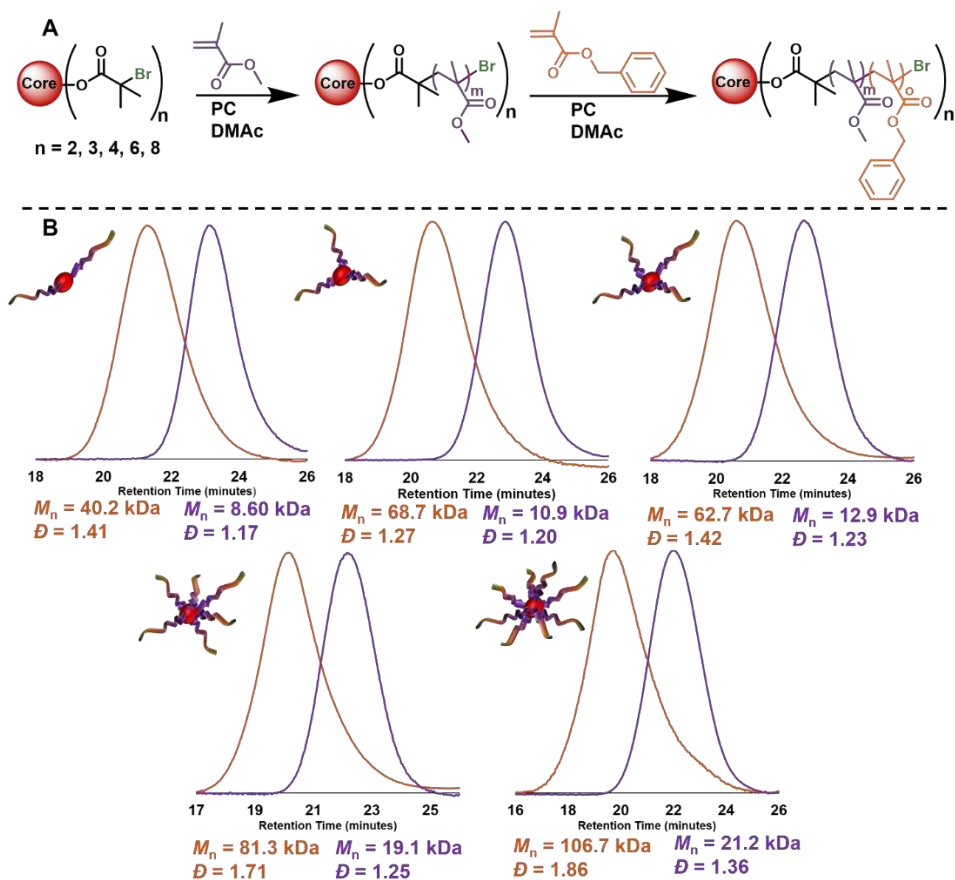
Figure 3.5: (a) Reaction scheme for chain-extension of telechelic linear polymer and 3, 4, 6, and 8 arm PMMA star polymers extended with benzyl methacrylate to produce diblock star polymers and (b) corresponding GPC traces with the star polymer macroinitiator (purple) and diblock star polymer (orange).

Conclusions

Star polymers possessing 3, 4, 6, and 8 arms as well as a linear telechelic polymer were successfully synthesized using O-ATRP and a core-first approach. These reactions produced well-defined products using uniform stoichiometric conditions, reliant on maintaining a relatively concentrated reaction solution at the onset of polymerization. Significantly, star-star coupling events were not observed at monomer conversions as high as 87%. The synthesis was further expanded to include high MW star polymers with a high degree of polymerization of each arm. The success of this polymerization methodology for the synthesis of star polymers was further

highlighted through the chain-extension of star polymers, providing an efficient and well-controlled method for the synthesis of higher order architectures using O-ATRP.

Experimental Section

Materials and Methods:

Chemicals:

Methyl methacrylate (MMA) was purchased from VWR and benzyl methacrylate (BzMA) was purchased from Sigma Aldrich. The monomers were dried over calcium hydride, distilled, and stored under inert atmosphere at -10 ºC. ACS-grade *N,N*-Dimethylacetamide (DMAc) with a sure-seal was purchased from Sigma Aldrich, stored under inert atmosphere, and used as received. Ethylene bis(2-bromoisobutyrate) and pentaerythritol tetrakis(2-bromoisobutyrate) multifunctional initiators were purchased from Sigma Aldrich and used as received. All other reagents for catalyst and multifunctional initiator synthesis were purchased from Sigma Aldrich or VWR and used as received. 1,1,1-Tris(2-bromoisobutyryloxymethyl)ethane, dipentaerythritol hexakis(2-bromoisobutyrate), and tripentaerythritol octakis(2-bromoisobutyrate) were synthesized according to modified literature procedures.[40,41] PC 3,7-Di(4-biphenyl) 1-Naphthalene-10-Phenoxazine (**1**) was synthesized according to literature procedure.[34]

Characterization:

Nuclear magnetic resonance (NMR) spectra were recorded on a Bruker Avance-III 300 MHz spectrometer or a Varian Inova 400 MHz spectrometer. Chemical shifts were referenced using internal solvent resonance, 7.26 ppm for $CDCl_3$ and 7.16 ppm for C_6D_6. Deuterated chloroform was purchased from Cambridge Isotope Laboratories.

Analysis of polymer molecular weight and dispersity was performed using gel permeation chromatography (GPC) coupled with multi-angle light scattering (MALS), using an Agilent HPLC fitted with one guard column and three PLgel 5 µm MIXED-C gel permeation columns in series. The detectors used were a Wyatt Technology TrEX differential refractometer and a Wyatt Technology miniDAWN TREOS light scattering detector, which allows the direct measurement of absolute M_w and does not require any correction factor for accurate MW measurement. The solvent used was THF with a flow rate of 1.0 mL/minute.

Visible-light photoreactor:

All polymerizations were carried out using the same photoreactor system as previously reported.[35] All materials to build the light source were purchased from Creative Lighting Solutions.

Figure 3.6: LED beaker photoreactors shown off (left) and on (right).

General star polymer synthesis using core-first approach:
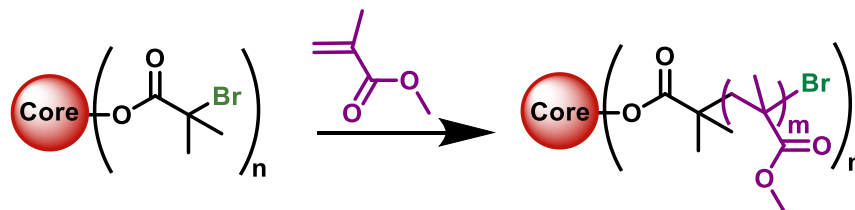
Figure 3.7: Reaction scheme for synthesis of poly(methyl methacrylate) star polymers using cores with n number of initiating sites, where n is 2, 3, 4, 6, or 8.

Using the difunctional initiator as an example for a typical polymerization using the core-first approach, the stoichiometry was determined as follows for a targeted degree of polymerization of 50 for each arm: [MMA]:[RBr$_n$]:[PC] is [1000]:[10]:[1], where RBr$_n$ is the molar amount of multifunctional initiator used. To set up polymerization, a 20 mL scintillation vial with a polypropylene lined cap was charged with a small stir bar and 33.8 mg (9.39 x 10^{-2} mmol) of multifunctional ATRP initiator, then brought into a glovebox with nitrogen atmosphere. Then 5.74 mg (9.39 µmol) PC from a stock solution was added, followed by 1.00 mL (9.39 mmol) of methyl methacrylate (MMA). At that time, the vial was capped and placed in a photoreactor and irradiated by white LEDs (**Figure 3.6**). Once the reactions exhibited increased viscosity an additional 1 mL of DMAc was added, typically in the 3rd hour. Aliquots were taken for kinetic analysis by quenching approximately 75 µL of reaction mixture into 0.7 mL of deuterated chloroform containing 250 ppm of butylated hydroxytoluene as radical inhibitor. For each aliquot collected, 0.5 mL of the quenched aliquot was used for ^{1}H NMR analysis. Conversion was determined through relative integration of the methyl ester monomer peak at 3.46 ppm to the methyl ester polymer peak at 3.32 ppm. The remaining 0.2 mL of quenched aliquot was dried under ambient conditions for a minimum of 24 hours, then fully dissolved in THF, filtered through a syringe

filter, and analyzed by GPC for molecular weight and dispersity analysis. Full details of stoichiometric amounts for each star type can be seen below (**Table 3.3**).

Table 3.3: Stoichiometry used for O-ATRP of methyl methacrylate targeting a degree of polymerization of 50 for each arm for telechelic polymer and stars containing 3, 4, 6, and 8 arms.

# arms	[MMA]:[RBr$_n$]:[PC]	MMA (mL)	RBr$_n$ (mg)	PC (mg)
2	[1000]:[10]:[1]	1	33.8	5.74
3	[1500]:[10]:[1]	1	36.4	3.84
4	[2000]:[10]:[1]	1	34.4	2.88
6	[3000]:[10]:[1]	1	35.9	1.90
8	[6000]:[10]:[1]	1	36.7	1.44

Macroinitiator Synthesis:
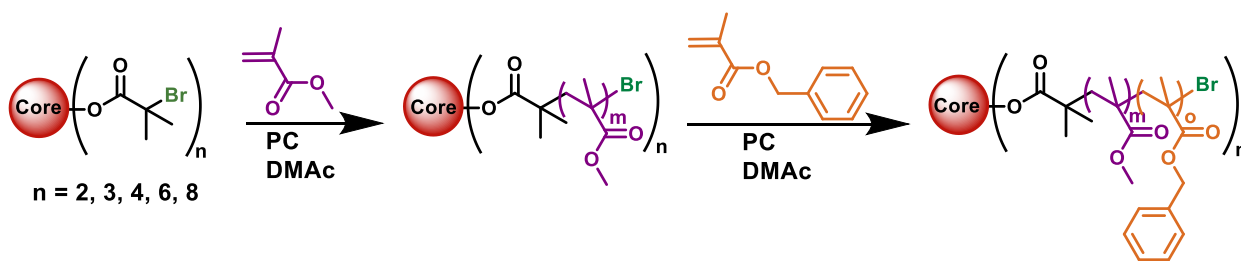
Figure 3.8: Reaction scheme for synthesis of multifunctional macroinitiator containing *n* number of arms, followed by chain extension using benzyl methacrylate (BzMA).

Star polymer macroinitiator synthesis was carried out by setting up a standard polymerization experiment with initial stoichiometry targeting a degree of polymerization of 50 for each arm. Each macroinitiator synthesis used 1 molar equivalent of **1** for 10 molar equivalents of initiator. Polymerization was stopped at 1.5 hours, targeting conversions between 35% and 45%. An aliquot was taken for ¹H NMR analysis to determine monomer conversion. The resulting macroinitiator was purified by precipitation into cold methanol, followed by isolation via gravity

filtration through a fine filter frit. The resulting white powder was dried overnight under vacuum

at 50 ℃. See **Table 3.4** for full results of polymerization and stoichiometric details.

Table 3.4: Overview of results of PMMA star polymer macroinitiator synthesis using O-ATRP.[a]

# arms	[MMA]:[RBr$_n$]:[PC]	Conv. (%)[b]	M_n (kDa)[c]	Đ (M_w/M_n)[c]	Yield (%)[d]
2	[1000]:[10]:[1]	37	8.6	1.17	26
3	[1500]:[10]:[1]	38	10.9	1.27	41
4	[2000]:[10]:[1]	43	12.9	1.42	59
6	[3000]:[10]:[1]	43	19.1	1.25	64
8	[6000]:[10]:[1]	42	21.2	1.36	56

[a]Experimental conditions are using 1:1 of MMA:DMAc, using a constant 1 mL of MMA for each reaction. Irradated by white LEDs. [b]Determined by ^{1}H NMR. [c]Determined by GPC. [d]Determined by mass recovered after polymer purification.
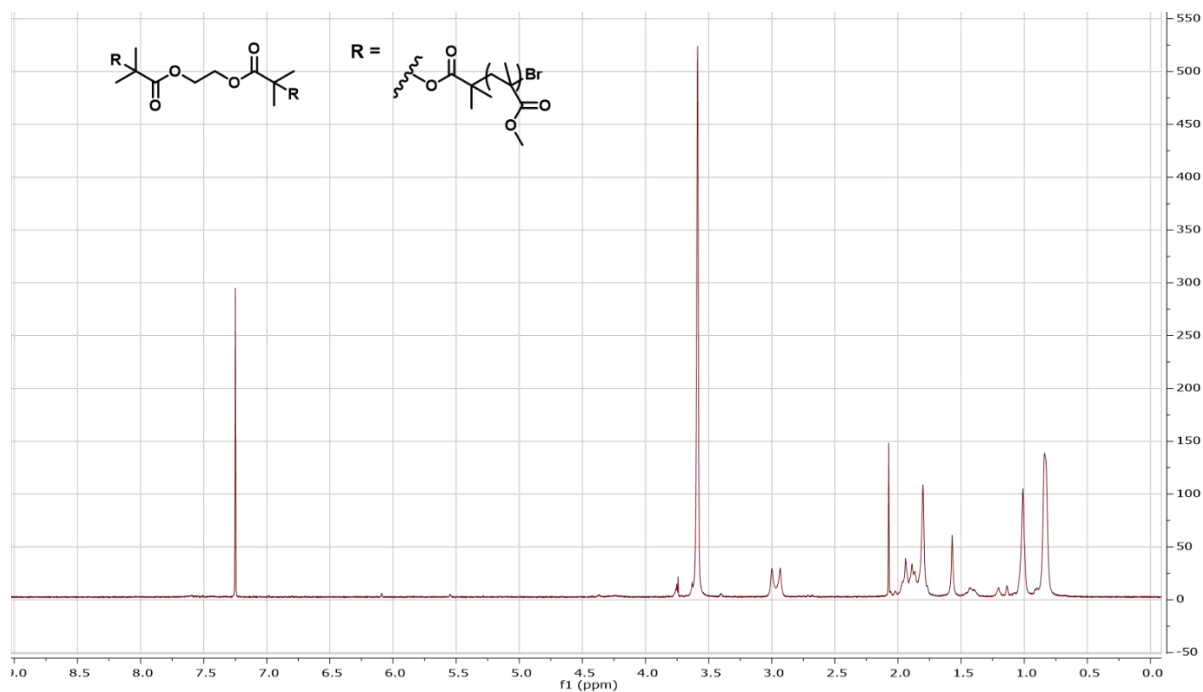
Figure 3.9: ^{1}H NMR spectra of 2-arm telechelic polymer macroinitiator.
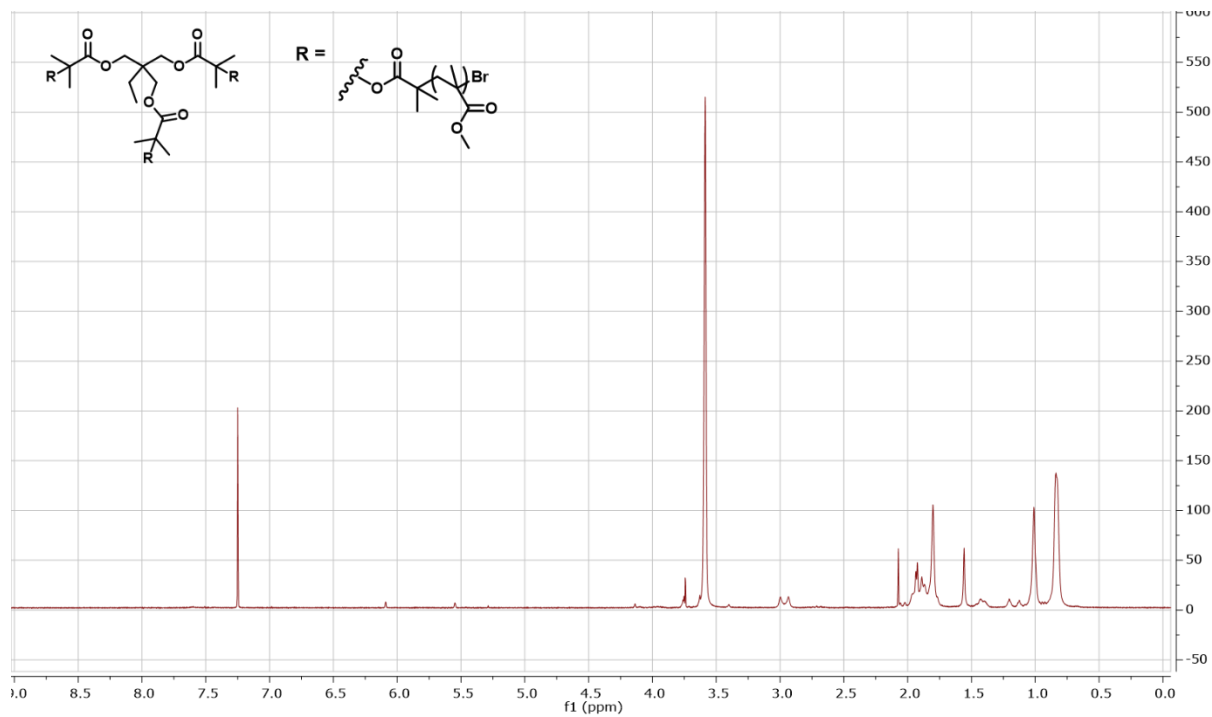
Figure 3.10: ^{1}H NMR spectra of 3-arm star polymer macroinitiator.
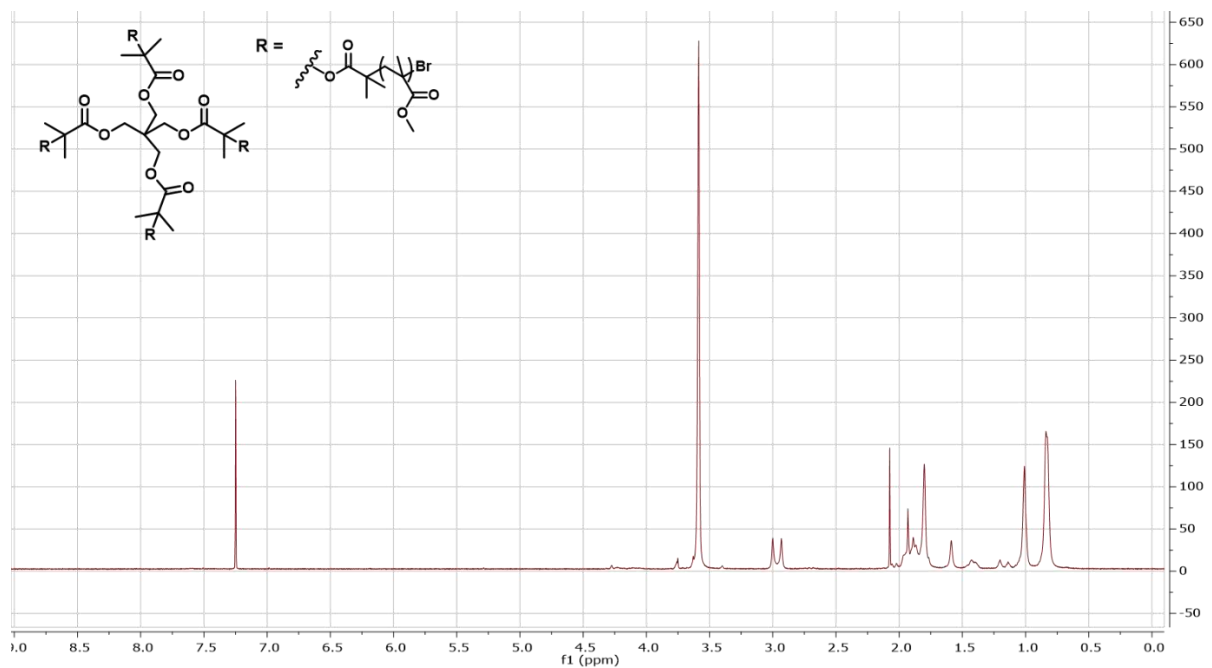
Figure 3.11: ^{1}H NMR spectra of 4-arm star polymer macroinitiator.
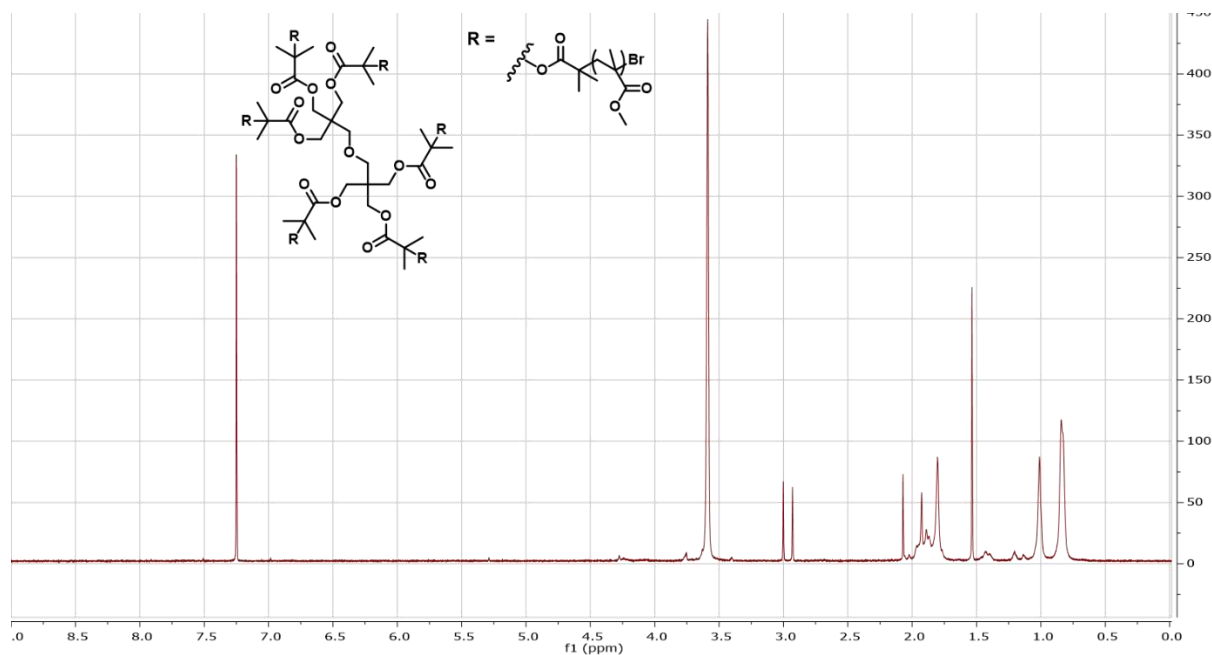
Figure 3.12: ^{1}H NMR spectra of 6-arm star polymer macroinitiator.
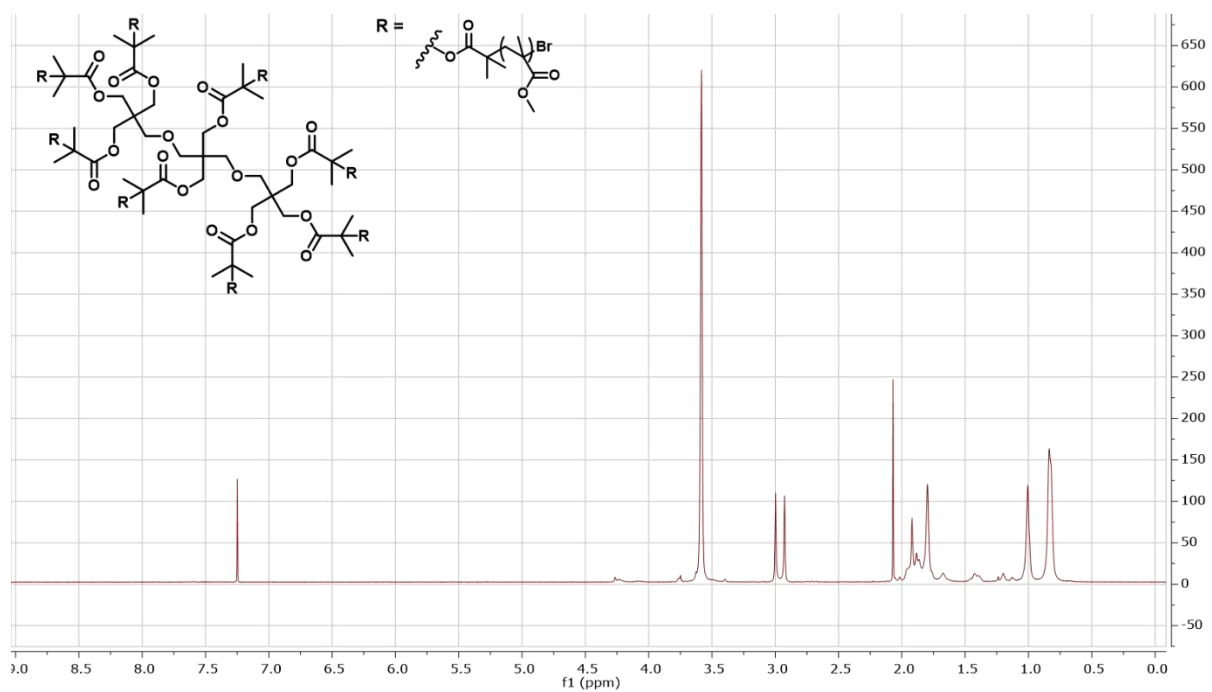
Figure 3.13: ^{1}H NMR spectra of 8-arm star polymer macroinitiator.

General Procedure for Chain-Extension:

50 mg of purified macroinitiator was loaded into a 20 mL scintillation vial with a small stir bar, then brought into a nitrogen atmosphere glovebox. Then, DMAc was added to the vial, the vial was capped and allowed to stir until all macroinitiator was dissolved, or approximately 1 hour. At that time, a stock solution containing PC **1** was added, followed by benzyl methacrylate (BzMA), targeting an additional 100 monomer units for each star polymer arm. All reactions used a total reaction volume of 2 mL, combined from BzMA and DMAc, and a ratio of [10]:[1] of [RBr$_n$]:[**1**]. After all components were loaded into the vial, the vial was capped and irradiated by white LEDs for 8 hours. Then, the reactions were brought out of the glovebox, quenched with methanol, isolated via gravity filtration through a fine filter frit, and dried at 50 ℃ for 48 hours. The polymer was then weighed and analyzed via ^{1}H NMR and GPC. See **Table 3.5** for full results and stoichiometric details.

Table 3.5: Results of PMMA block copolymer star polymer synthesis using O-ATRP.[a]

# arms	[BzMA]:[RBr$_n$]: [PC]	BzMA (mL)	DMAc (mL)	Yield (%)[b]	$M_{n\,theo}$ (kDa)[c]	M_n (kDa)[d]	Đ (M_w/ M_n)[d]	I^* (%)[e]
2	[2000]:[10]:[1]	0.20	1.80	72	31.3	40.2	1.41	128
3	[3000]:[10]:[1]	0.23	1.77	50	31.8	68.7	1.27	46
4	[4000]:[10]:[1]	0.26	1.74	83	69.2	62.7	1.42	111
6	[6000]:[10]:[1]	0.27	1.73	91	113.9	81.3	1.71	140
8	[8000]:[10]:[1]	0.32	1.68	94	151.9	107	1.86	143

[a]Experimental conditions are using 50 mg of macroinitiator (RBr$_n$) and a constant total reaction volume of 2 mL. Irradiated by white LEDs. [b]Determined gravimetrically. [c]Calculated by $(Conv \times [Mon]/[Init.] \times Mw_{Mon})/1000$. [d]Determined by GPC. [e]Calculated by $(Theo. M_n/Calc. M_n) \times 100$.
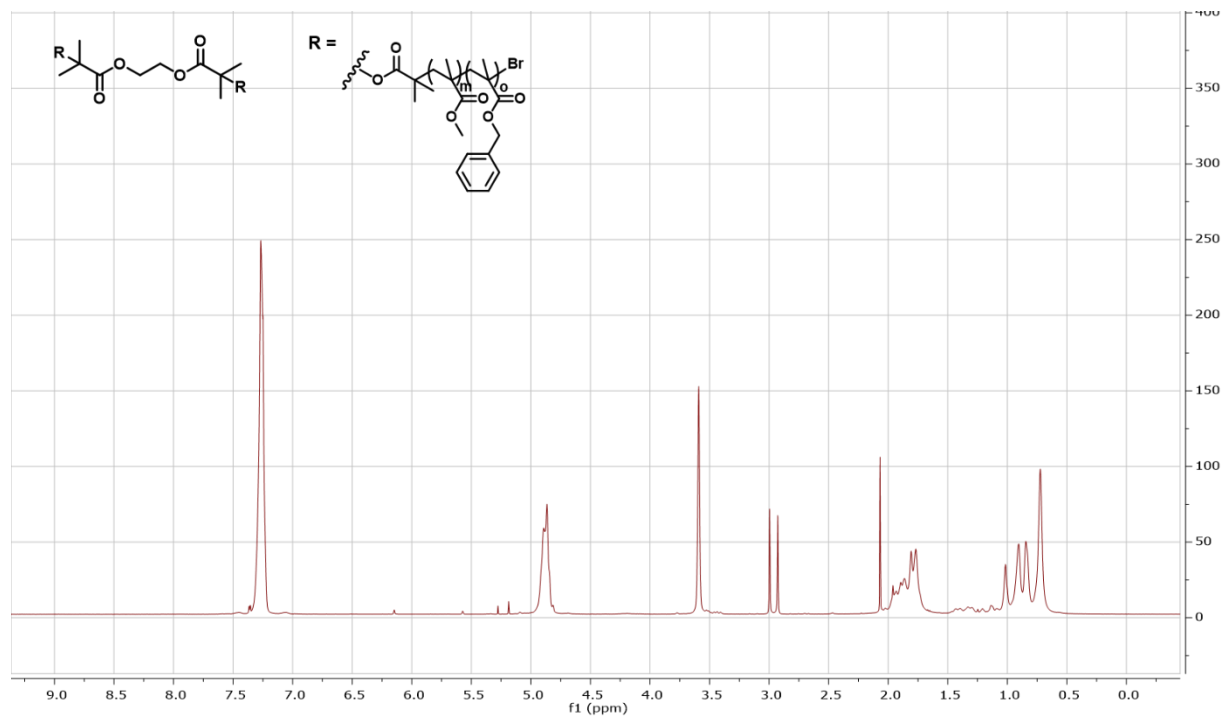
Figure 3.14: ^{1}H NMR spectra of telechelic 2-arm (MMA-BzMA) diblock polymer.
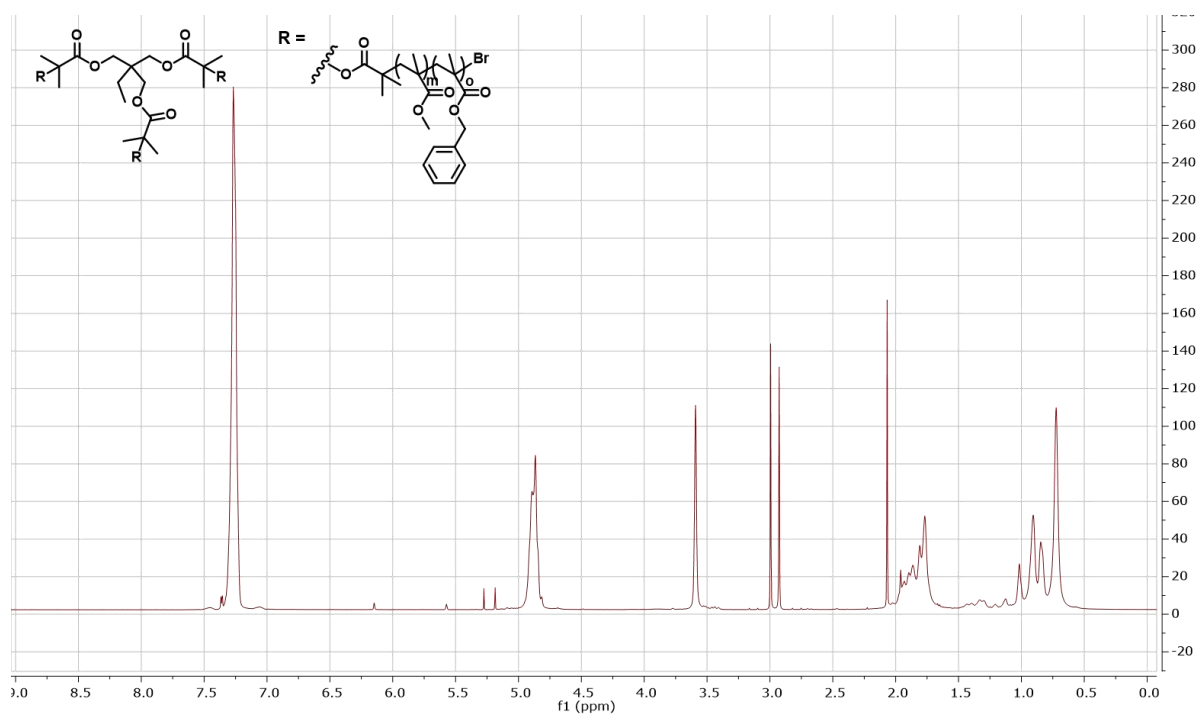
Figure 3.15: ^{1}H NMR spectra of 3-arm (MMA-BzMA) diblock star polymer.
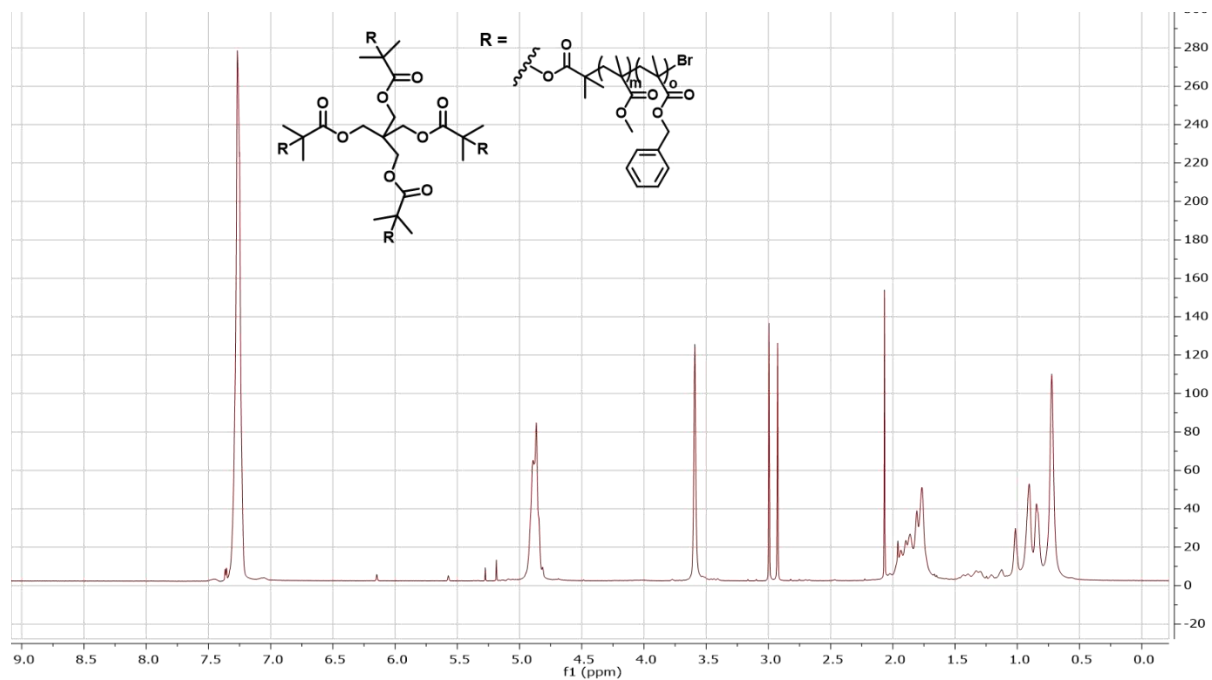
Figure 3.16: ^{1}H NMR spectra of 4-arm (MMA-BzMA) diblock star polymer.
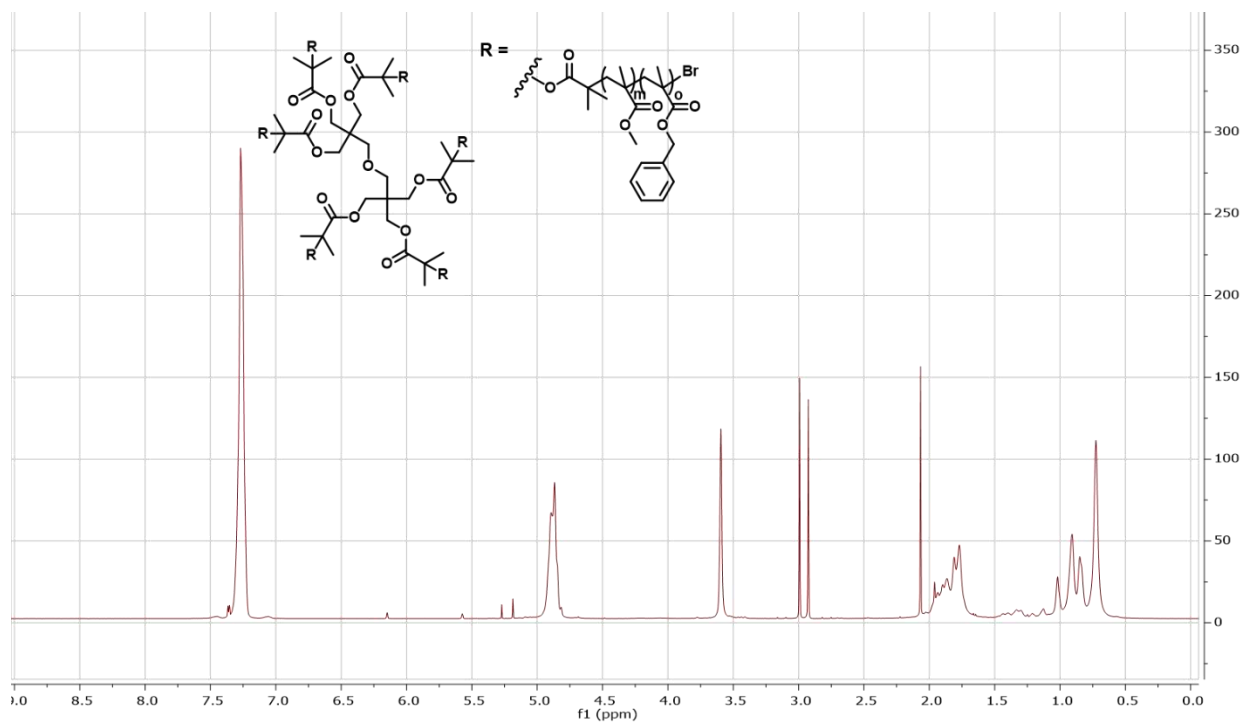
Figure 3.17: ^{1}H NMR spectra of 6-arm (MMA-BzMA) diblock star polymer.
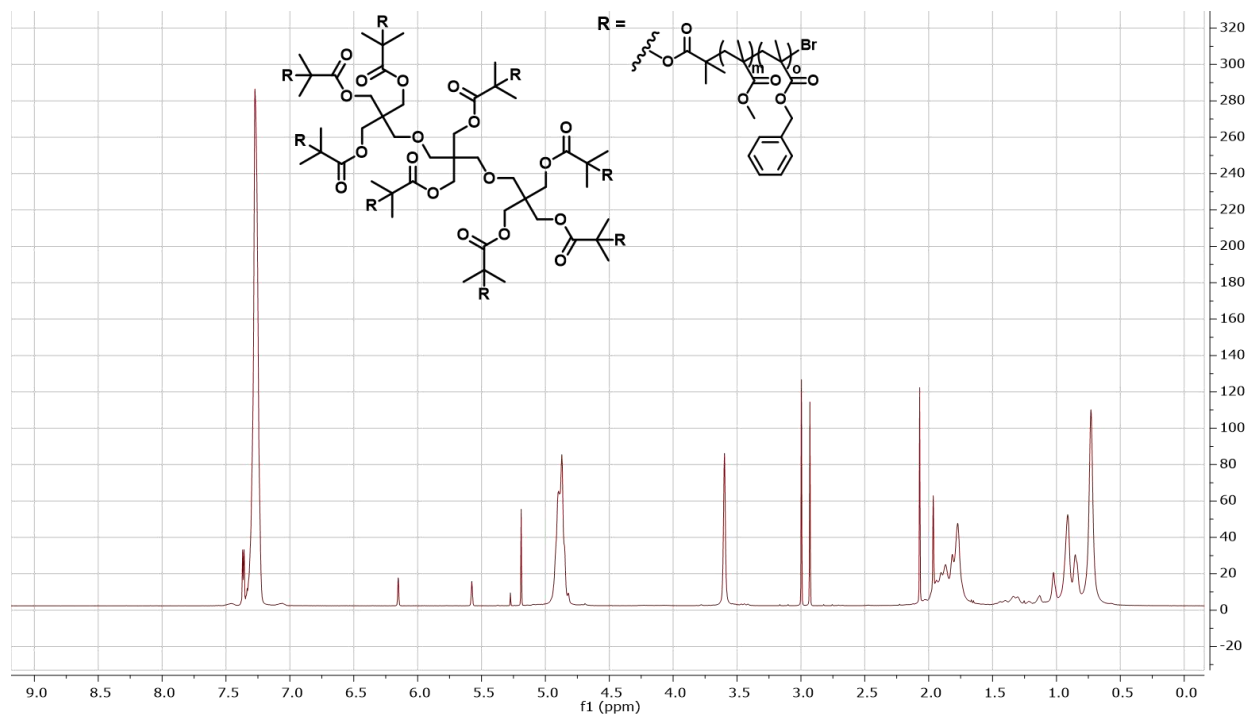
Figure 3.18: ^{1}H NMR spectra of 8-arm (MMA-BzMA) diblock star polymer.

Additional Results of Polymerization
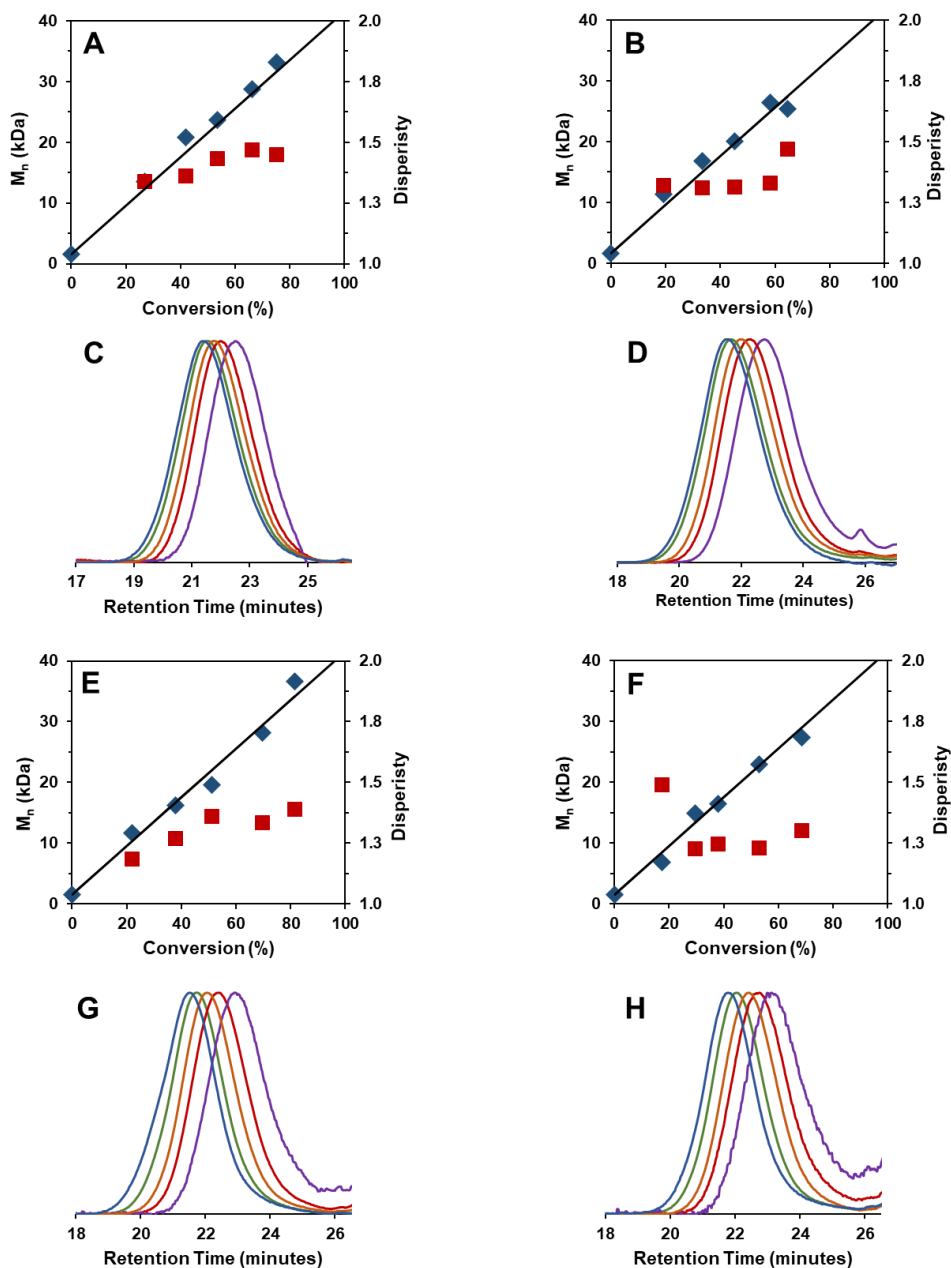
Effect of reaction concentrations:
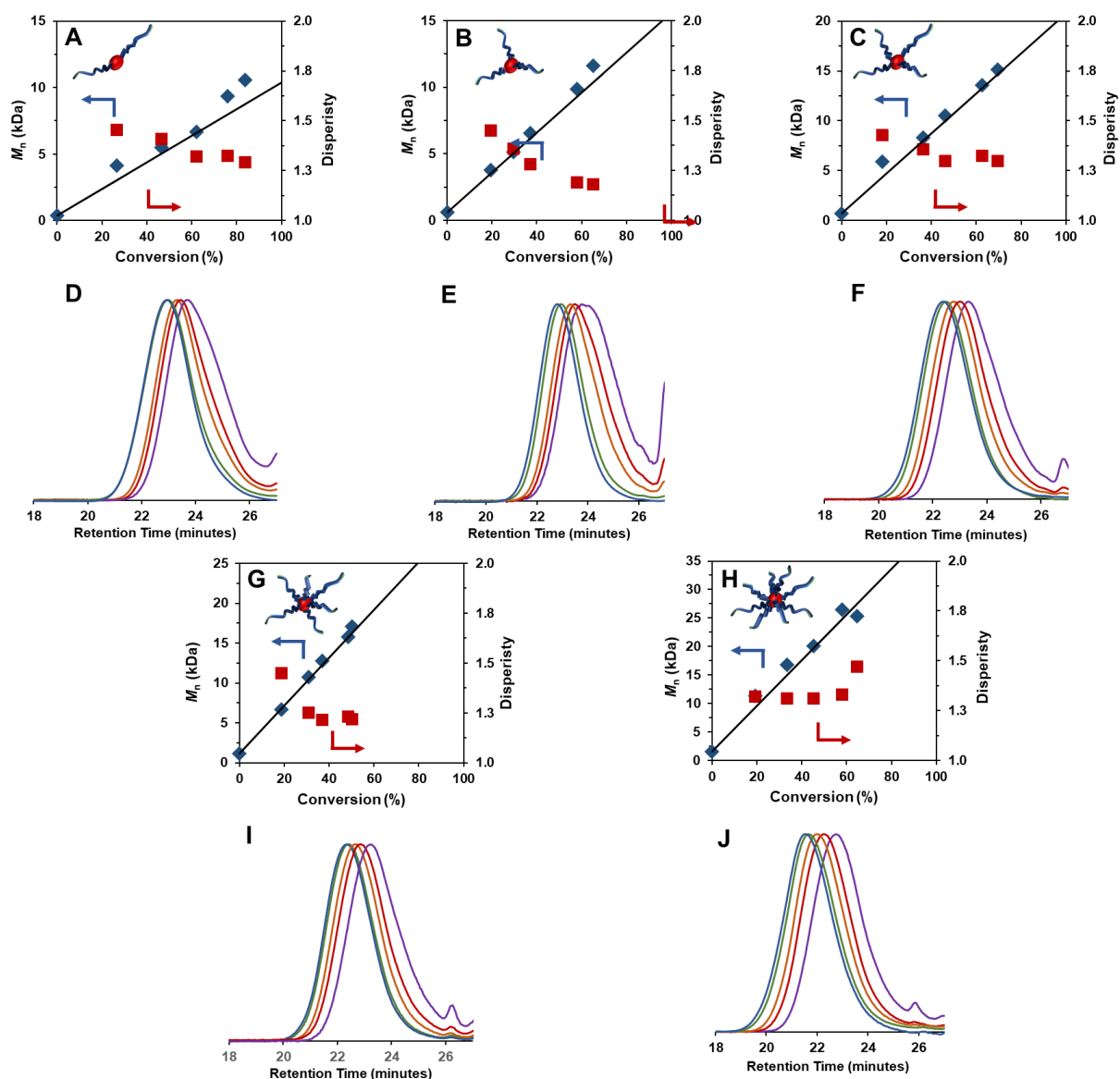
Figure 3.19: Plots of M_n (blue diamonds), dispersity (red squares) and theoretical M_n (black line) versus conversion for (a) linear polymer and (b) 3-arm, (c) 4-arm, (g) 6-arm, and (h) 8-arm star polymers with corresponding GPC traces shown. Conditions for polymerization are targeting 50 repeat units of MMA, [10]:[1] of [RBr$_n$]:[**1**], and 1 equivalents of DMAc to MMA by volume, using 1.0 mL of MMA. An additional 1.0 mL of DMAc was added at 3 hours. Polymerizations are irradiated by white LEDs.
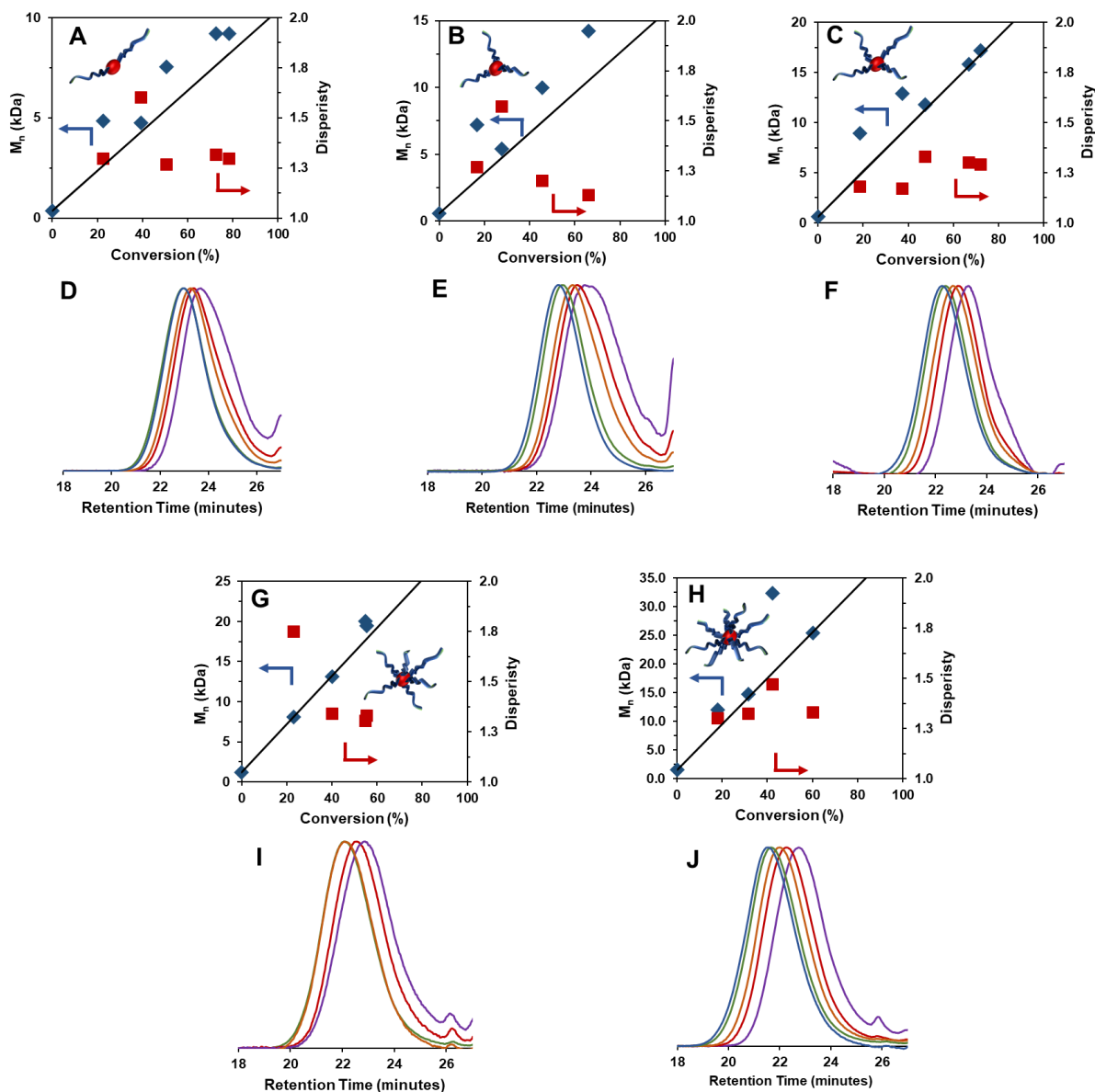
Figure 3.20: Plots of M_n (blue diamonds), dispersity (red squares) and theoretical M_n (black line) versus conversion for (a) linear polymer and (b) 3-arm, (c) 4-arm, (g) 6-arm, and (h) 8-arm star polymers with corresponding GPC traces shown. Conditions for polymerization are targeting 50 repeat units of MMA, [10]:[1] of [RBr$_n$]:[**1**], and 2 equivalents of DMAc to MMA by volume, using 0.67 mL of MMA. An additional 1.0 mL of DMAc was added at 3 hours. Polymerizations are irradiated by white LEDs.

PC loading studies:

2-arm star:
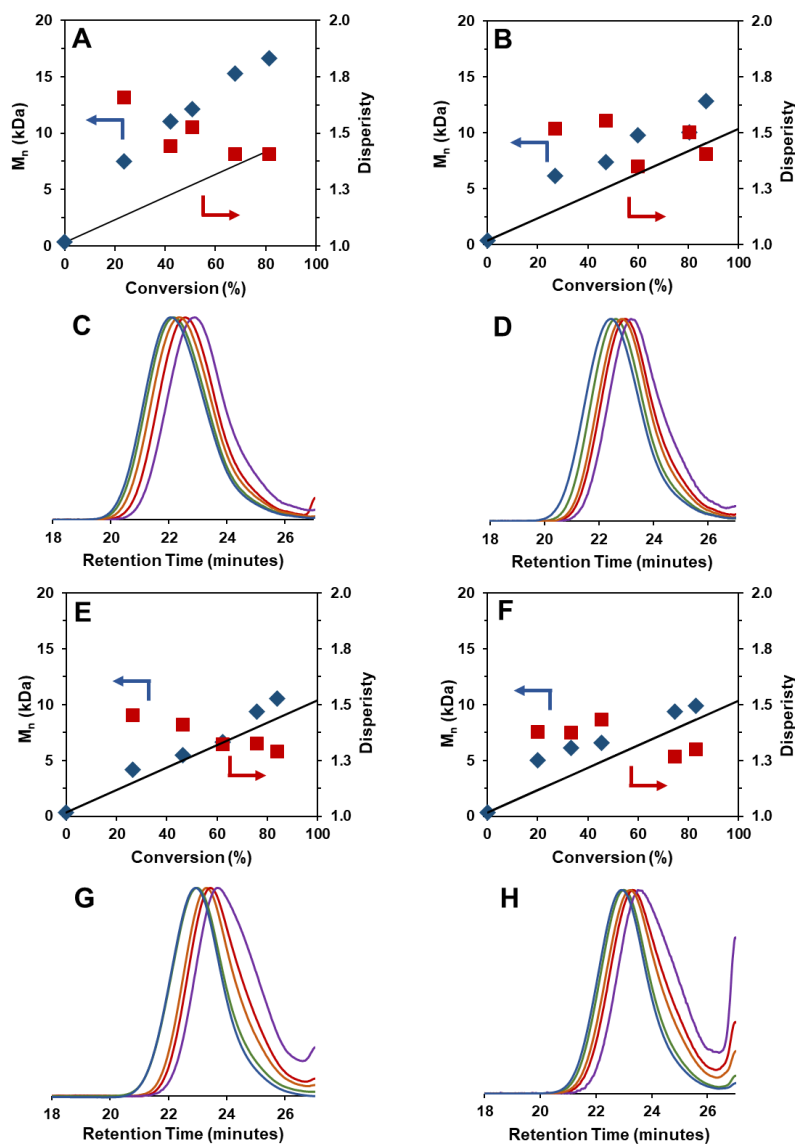
Figure 3.21: Plots of M_n (blue diamonds), dispersity (red squares) and theoretical M_n (black line) versus conversion for 2-arm linear polymer, using [1000]:[10] of [MMA]:[RBr$_2$] and (a) [10]:[0.1], (b) [10]:[0.2], (c) [10]:[1], and (d) [10]:[2] of [RBr$_2$]:[**1**] with corresponding GPC traces using 1:1 of MMA:DMAc by volume and 1.0 mL of MMA. An additional 1.0 mL of DMAc was added at 3 hours. Polymerizations are irradiated by white LEDs.

3-arm star:
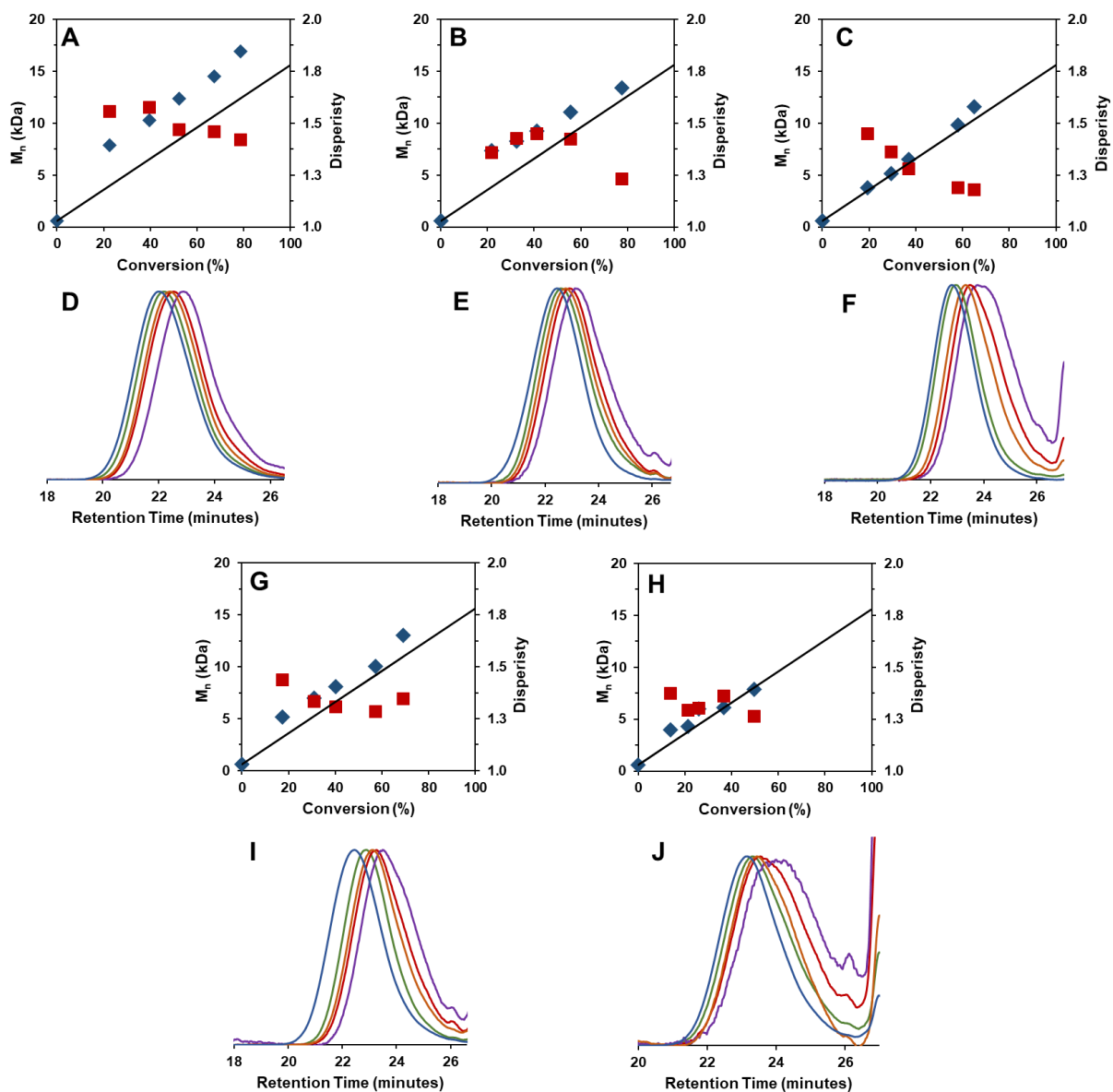
Figure 3.22: Plots of M_n (blue diamonds), dispersity (red squares) and theoretical M_n (black line) versus conversion for 3-arm star polymer using [1500]:[10] of [MMA]:[RBr$_3$] and (a) [10]:[0.15], (b) [10]:[0.3], (c) [10]:[1], (g) [10]:[1.5], and (h) [10]:[3] of [RBr$_3$]:[**1**] with corresponding GPC traces 1:1 of MMA:DMAc by volume and 1.0 mL of MMA. An additional 1.0 mL of DMAc was added at 3 hours. Polymerizations are irradiated by white LEDs.

4-arm star:
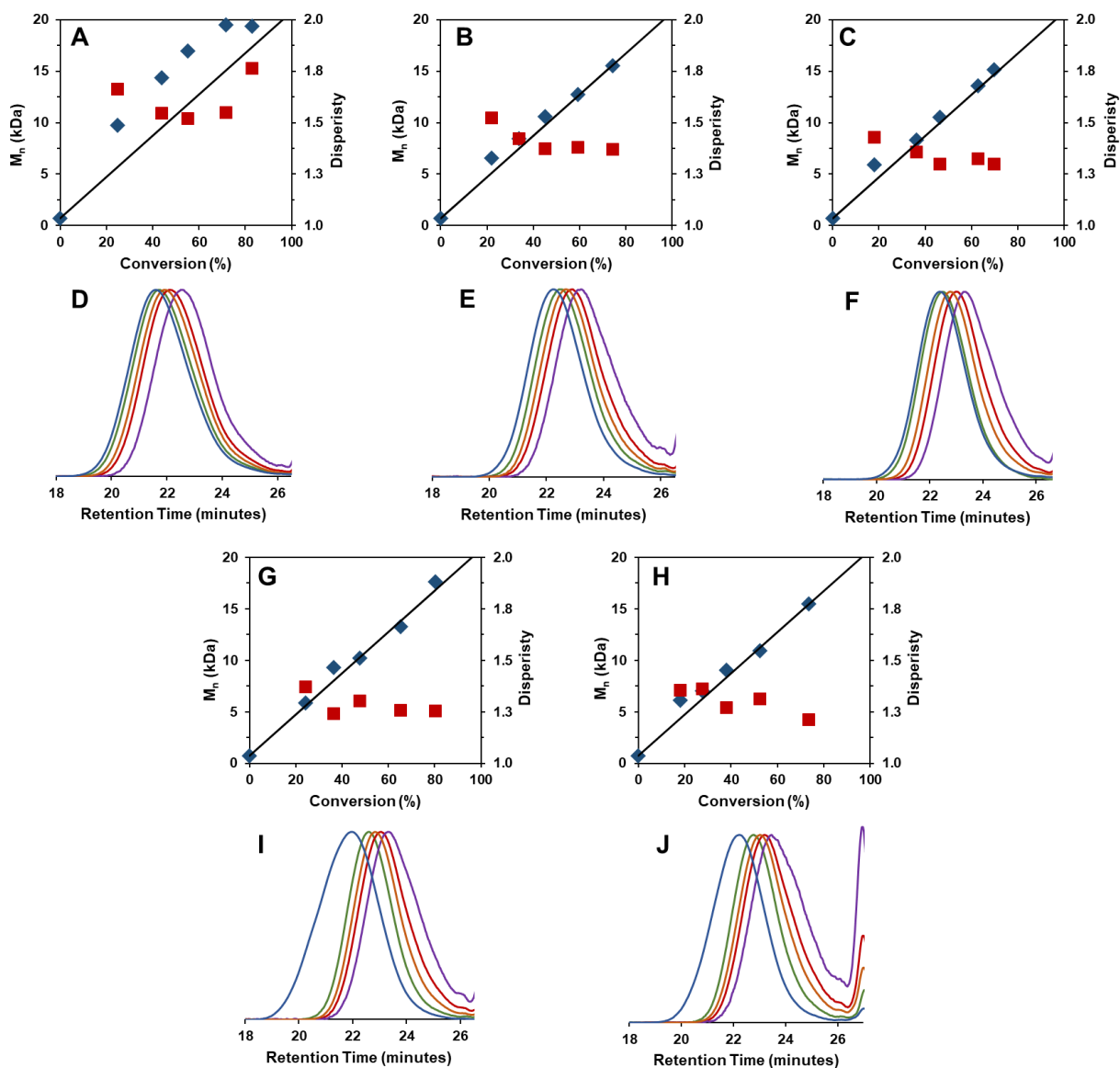
Figure 3.23: Plots of M_n (blue diamonds), dispersity (red squares) and theoretical M_n (black line) versus conversion for 4-arm star polymer, using [2000]:[10] of [MMA]:[RBr$_4$] and (a) [10]:[0.15], (b) [10]:[0.3], (c) [10]:[1], (g) [10]:[1.5], and (h) [10]:[3] of [RBr$_4$]:[**1**] with corresponding GPC traces 1:1 of MMA:DMAc by volume and 1.0 mL of MMA. An additional 1.0 mL of DMAc was added at 3 hours. Polymerizations are irradiated by white LEDs.

6-arm star:
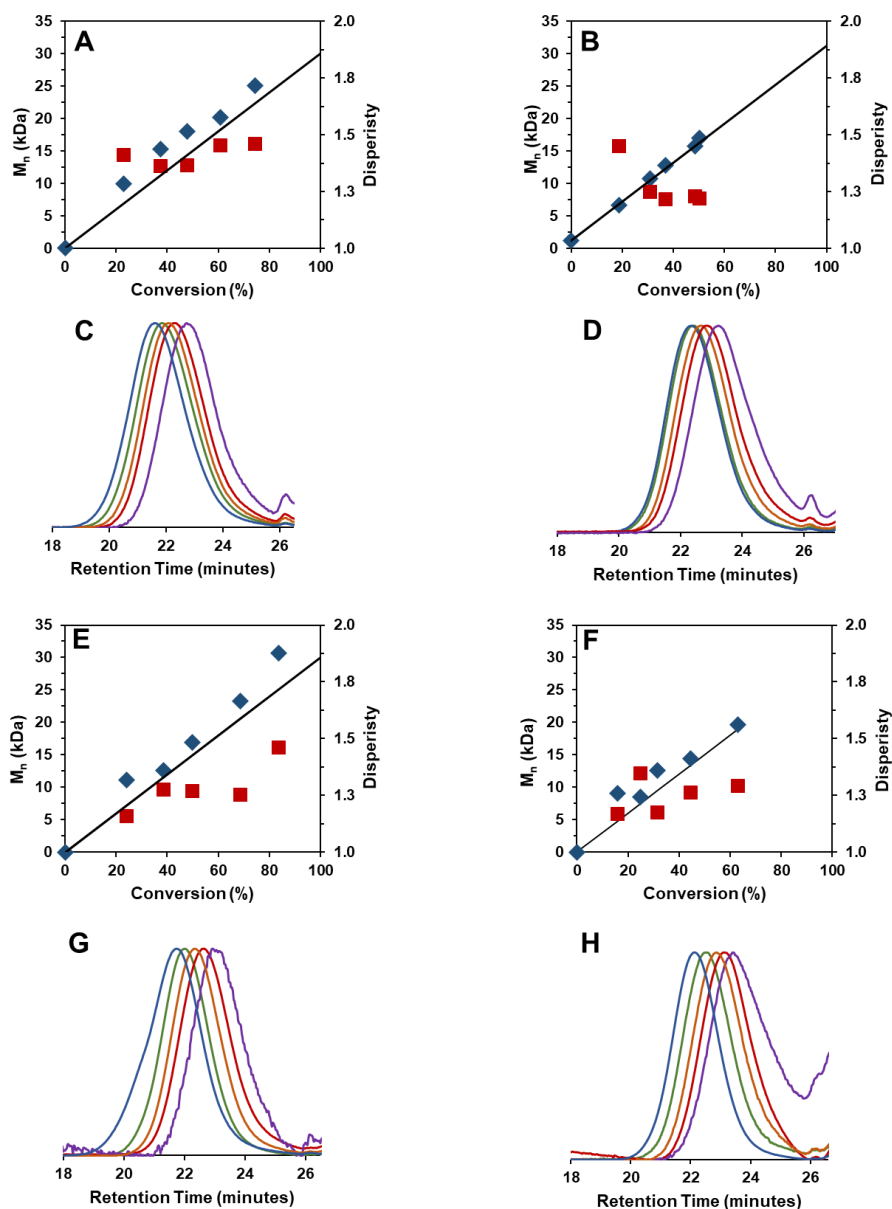
Figure 3.24: Plots of M_n (blue diamonds), dispersity (red squares) and theoretical M_n (black line) versus conversion for 6-arm star polymer, using [3000]:[10] of [MMA]:[RBr₆] and (a) [10]:[0.6], (b) [10]:[1], (c) [10]:[3], and (d) [10]:[6] of [RBr₆]:[**1**] with corresponding GPC traces using 1:1 of MMA:DMAc by volume and 1.0 mL of MMA. An additional 1.0 mL of DMAc was added at 3 hours. Polymerizations are irradiated by white LEDs.

8-arm star:

Figure 3.25: Plots of M_n (blue diamonds), dispersity (red squares) and theoretical M_n (black line) versus conversion for 8-arm star polymer using [4000]:[10] of [MMA]:[RBr$_8$] and (a) [10]:[0.8], (b) [10]:[1], (c) [10]:[4], and (d) [10]:[8] of [RBr$_8$]:[**1**] with corresponding GPC traces using 1:1 of MMA:DMAc by volume and 1.0 mL of MMA. An additional 1.0 mL of DMAc was added at 3 hours. Polymerizations are irradiated by white LEDs.

Photocatalyst Loading Experiments Summary Table

Table 3.6: Overview of results of PMMA star polymer synthesis after 8 hours using O-ATRP.[a]

# arms	[MMA]:[RBr$_n$]:[PC]	Conv. (%)[b]	$M_{n\,(actual)}$ (kDa)[b]	$Đ$ (M_w/M_n)[b]	I^* (%)[b]
2	[1000]:[10]:[2]	83	9.8	1.30	88
	[1000]:[10]:[1]	84	8.8	1.29	83
	[1000]:[10]:[0.2]	87	12.8	1.40	71
	[1000]:[10]:[0.1]	81	16.7	1.41	51
3	[1500]:[10]:[3]	50	7.9	1.26	103
	[1500]:[10]:[1.5]	69	13.0	1.35	84
	[1500]:[10]:[1]	65	11.6	1.18	89
	[1500]:[10]:[0.3]	78	13.4	1.23	91
	[1500]:[10]:[0.15]	79	16.9	1.42	73
4	[2000]:[10]:[4]	74	15.5	1.21	100
	[2000]:[10]:[2]	80	17.6	1.25	95
	[2000]:[10]:[1]	70	15.1	1.30	97
	[2000]:[10]:[0.4]	74	15.5	1.37	100
	[2000]:[10]:[0.2]	83	19.4	1.76	90
6	[3000]:[10]:[6]	63	19.7	1.29	96
	[3000]:[10]:[3]	84	30.7	1.46	82
	[3000]:[10]:[1]	50	17.1	1.22	95
	[3000]:[10]:[0.6]	74	25.1	1.46	89
8	[4000]:[10]:[8]	69	27.3	1.30	106
	[4000]:[10]:[4]	82	36.6	1.39	93
	[4000]:[10]:[1]	60	25.4	1.33	101
	[4000]:[10]:[0.8]	75	33.1	1.45	96

[a]All experiments employ a targeted degree of polymerization of 50 for each arm, using 1 equivalent of DMAc to MMA by volume, with 2 mL of reaction volume total. [b]See footnote for Table 3.3 for full details.

References

1.   Matyjaszewski, K.; Tsarevsky, N.V. *J. Am. Chem. Soc.* **2014,** *136,* 6513-6533.

2.   Liu, J.; Duong, J.; Whittaker, M. R.; Davis, T. P.; Boyer, C. *Macromol. Rapid Commun.* **2012,** *33,* 760-766.

3.   Pearson, D. S.; Helfand, E. *Macromolecules* **1984,** *17,* 888-895.

4.   Hietala, S.; Mononen, P.; Strandman, S.; Jarvi, P.; Torkkeli, M.; Jankova, K.; Hvilsted, S.; Tenhu, H. *Polymer* **2007,** *48,* 4087-4096.

5.   Ren, J. M.; McKenzie, T. G.; Fu, Q.; Wong, E H. H.; Xu, J.; An, Z.; Shanmugam, S.; Davis, T. P.; Boyer, C.; Qiao, G. G. *Chem. Rev.* **2016,** *116,* 6743-6836.

6.   Ohno, K.; Wong, B.; Haddleton, D. M. *J. Polym. Sci., Part A: Polym. Chem.* **2001,** *39,* 2206-2214.

7.   Gao, H.; Matyjaszewski, K. *Macromolecules* **2006**, *39,* 3154-3160.

8.   Gao, H.; Matyjaszewski, K. *Prog. Poly. Sci.* **2009,** *34,* 317-350.

9.   Gao, H.; Matyjaszewski, K. *J. Am. Chem. Soc.* **2007,** *129,* 11828-11834.

10.   Xia, J.; Zhang, X.; Matyjaszewski, K. *Macromolecules* **1999,** *32,* 4482-4484.

11.   Iha, R. K.; Wooley, K. L.; Nystrom, A. M.; Burke, D. J.; Kade, M. J.; Hawker, C. J. *Chem. Rev.* **2009,** *109***,** 5620-5686.

12.   Khanna, K.; Varshney, S.; Kakkar, A.; *Macromolecules* **2010,** *43,* 5688-5698.

13.   Braunecker, W. A.; Matyjaszewski, K. *Prog. Polym. Sci.* **2007,** *32,* 93-146.

14.   Pan, X.; Tasdelen, M. A.; Laun, J.; Junkers, T.; Yagci, Y.; Matyjaszewski, K. *Prog. Polym. Sci.* **2016,** *62,* 73-125**.**

15 .   Patten, T. E.; Xia, J.; Abernathy, T.; Matyjaszewski, K. *Science* **1996,** *272,* 866-868.

16. Matyjaszewski, K.; Xia, J. *Chem. Rev.* **2001,** *101,* 2921-2990.

17. Matyjaszewski, K. *ACS Symposium Series* **2015,** *1187,* 1-17.

18. Matyjaszewski, K.; Tsarevsky, N. V.; *Nature Chemistry* **2009,** *1,* 276-288.

19. Gao, H.; Min, K.; Matyjaszewski, K. *Macromol. Chem. Phys.* **2007,** *208,* 1370-1378.

20. Taton, D.; Ganou, Y.; Matmour, R.; Angot, S.; Hou, S.; Francis, R.; Lepoittevin, B.; Moinard, D.; Babin, J. *Polym. Int.* **2006,** *55,* 1138-1145.

21. Ding, H.; Park, S.; Zhong, M.; Pan, S.; Pietrasik, J.; Bettinger, C. J.; Matyjaszewski, K. *Macromolecule,* **2016,** *49,* 6752-6760.

22. Gao, H.; Matyjaszewski, K. *Macromolecules* **2006,** *39,* 4960-4965.

23. Ueda, J.; Matsuyama, M.; Kamigaito, M.; Sawamoto, M. *Macromolecules* **1998,** *31,* 557-562.

24. Matyjaszewski, K.; Qin, S.; Boyce, J. R.; Shirvanyants, D.; Sheiko, S. S. *Macromolecules* **2003,** *36,* 1843-1849.

25. Mei, L.; Nazeem, M.; Jahed, K. M.; Matyjaszewski, K. *Macromolecules* **2004,** *37,* 2434-2441.

26. Boyer, C.; Derveax, A.; Zetterlund, P. B.; Wittaker, M. R. *Polym. Chem.* **2012,** *3,* 117-123.

27. Angot, S.; Murthy, K. S.; Taton, D.; Gnanou, Y. *Macromolecules* **1998,** *31,* 7218-7225.

28. Wenn, B.; Martens, A. C.; Chuang, Y. -M.; Gruber, J.; Junkers, T. *Polym. Chem.* **2016,** *7,* 2720.

29. Theriot, J. C.; McCarthy, B. G.; Lim, C. -H.; Miyake, G. M. *Macromol. Rapid Commun.* **2017,** *38,* 1700040.

30. Miyake, G. M.; Theriot, J. C. *Macromolecules* **2014,** *47,* 8255-8261.

31.   Theriot, J. C.; Lim, C. -H.; Yang, H.; Ryan, M. D.; Musgrave, C. B.; Miyake, G. M. *Science* **2016,** *352,* 1082

32.   Pearson, R. M.; Lim, C. -H.; McCarthy, B. G.; Musgrave, C. B.; Miyake, G. M. *J. Am. Chem. Soc.* **2016,** *138,* 11399-11407.

33.   Lim, C. -H.; Ryan, M. D.; McCarthy, B. G.; Theriot, J. C.; Sartor, S. M.; Damrauer, N. H.; Musgrave, C. B.; Miyake, G. M. *J. Am. Chem. Soc.* **2017,** *139,* 348-355.

34.   Ryan, M. D.; Theriot, J. C.; Lim, C. -H.; Yang, H.; Lockwood, A.; Garrison, N. G.; Lincoln, S. R.; Musgrave, C. B.; Miyake, G. M. *J. Polym. Sci. Part A: Polym. Chem.* **2017,** *55,* 3017-3027.

35.   Ryan, M. D.; Pearson, R. M.; French, T. A.; Miyake, G. M. *Macromolecules* **2017,** *50,* 4616-4622.

36.   Ramsey, B. L.; Pearson, R. M.; Beck, L. R.; Miyake, G. M. *Macromolecules* **2017,** *50,* 2668-2674.

37.   Du, Y.; Pearson, R. M.; Lim, C. -H.; Sartor, S. M.; Ryan, M. D.; Damrauer, N. H.; Miyake, G. M. *Chem. Eur. J.* **2017,** *23,* 10962-10968.

38.   Radke, W. *Macromol. Theory Simul.* **2001,** *10,* 343-348.

39.   Pomposo, J. A.; Perez-Baena, I.; Buranga, L.; Alegria, A.; Moreno, A. J.; Comenero, J. *Macromolecules* **2011,** *44,* 8644-8649.

40.   Saikia, B. J.; Dolui, S. K. *Polym. Sci. Part A: Polym. Chem.* **2016,** *54,* 1842-1851.

41.   Chu, C. -C.; Wang, Y. -W.; Yeh, C. -F.; Wang, L. *Macromolecules* **2008,** *41,* 5632-5640.

CHAPTER 4

Dimethyl-dihydroacridines as Photocatalysts in the Organocatalyzed Atom transfer

Radical Polymerization of Acrylate Monomers

Overview

Development of photocatalysts (PCs) with diverse properties has been essential in advancement of organocatalyzed atom transfer radical polymerization (O-ATRP). In this work, dimethyl-dihydroacridines are presented as a new family of organic PCs, for the first time enabling controlled polymerization of challenging acrylate monomers via O-ATRP. Structure-property relationships for seven PCs are established, demonstrating tunable photochemical and electrochemical properties and accessing a strongly oxidizing $^2PC^{\bullet+}$ intermediate for efficient deactivation. In O-ATRP, a combination of PC choice, implementation of continuous-flow reactors, and promotion of deactivation through addition of LiBr are critical to producing well-defined acrylate polymers with dispersities as low as 1.12. The utility of this approach is established through demonstration of the oxygen tolerance of the system and application to diverse acrylate monomers, including the synthesis of well-defined di- and triblock copolymers.

Introduction

The ability of photoredox catalysis to manipulate electron or energy transfer reactivity has revolutionized small molecule and macromolecular chemistry, presenting opportunities to develop new chemical transformations under mild and energy efficient reaction conditions.[1] Recently, photoredox catalysis has been applied in controlled radical polymerization (CRP) approaches for light-regulated synthesis of well-defined polymers, most commonly in atom transfer radical

polymerization (ATRP) and reversible addition-fragmentation transfer (RAFT).[2] ATRP, the most widely studied CRP methodology, is used to access polymers with controlled properties, higher-order architectures, and consequently diverse applications.[3] Traditionally, ATRP is operated through activation of a Cu(I) catalyst by heat to promote an inner-sphere electron transfer to generate a propagating radical species. However, in recent advances, new light-driven ATRP processes have been reported using photocatalysts (PCs) derived from copper, ruthenium, or iridium.[4]

Organocatalyzed atom transfer radical polymerization (O-ATRP) is a metal-free variant of photoredox-catalyzed ATRP which eliminates the concern of trace metal contamination in the polymer product and is advantageous in electronic and biomedical applications, while also enabling opportunities for "greener" reaction design in polymer synthesis.[5] Induced by light, O-ATRP relies on a strongly reducing organic PC to mediate an oxidative quenching catalytic cycle (**Figure 4.1 A**). O-ATRP processes following a reductive quenching pathway have also been reported but rely on the presence of stoichiometric quantities of sacrificial electron donors, which can also induce undesirable side reactions.[6] The proposed O-ATRP mechanism proceeds through four central steps.[7] Photoexcitation of a ground-state PC generates $^1PC^*$, which can undergo intersystem crossing to produce a long-lived $^3PC^*$. Either $^1PC^*$ or $^3PC^*$ then directly reduces an alkyl halide initiator through outer-sphere electron transfer to produce a propagating radical species, as well as the ion-pair $^2PC^{\bullet+}X^-$. Deactivation of the propagating chain-end occurs through reinstallation of the halide, generating the PC and a dormant polymer. Central to success in O-ATRP, as determined by control over polymer molecular weight (MW) and dispersity (*Đ)* close to 1.0, is the presence of a dynamic equilibrium between the activation and deactivation steps, where the rate of deactivation (with rate constant k_d) must be higher than the rates of propagation (k_p) and

activation (k_a), limiting radical concentrations and undesirable termination events via radical quenching.
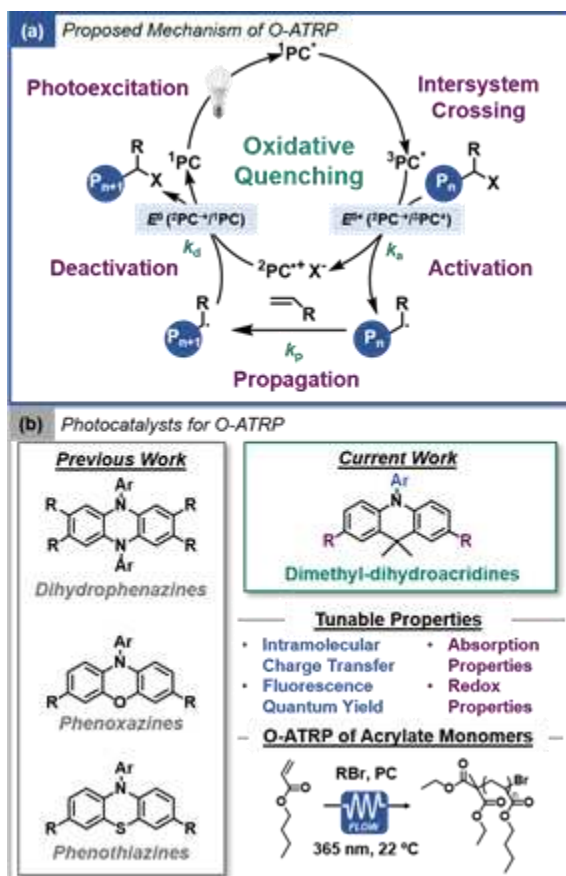
Figure 4.1. (a) Proposed mechanism of O-ATRP. (b) Previously reported PCs developed for O-ATRP (left) with the new dimethyl-dihydroacridine PC family investigated in this work (right).

To date, advances in O-ATRP have been enabled through development of strongly reducing organic PCs, which are capable of directly reducing an activated alkyl bromide ATRP initiator or dormant polymer chain-end (~-0.8 V vs. SCE).[8] In 2014, perylene and *N*-phenyl phenothiazine were reported as strongly-reducing PCs for the polymerization of methacrylate monomers via O-ATRP.[9] Since then, other organic PCs derived from *N,N*-diaryl dihydrophenazine[10] and *N*-aryl phenoxazine[11] families, among others[12], have been developed (**Figure 4.1 B**). *N*-aryl phenothiazine PCs have been applied in diverse contexts[13] and have also

been used for mechanistic analysis[14]. Recently, PC structure-property relationships have been studied using *N,N*-diaryl dihydrophenazine and *N*-aryl phenoxazine PCs.[15] Empirically, these studies have determined key PC design principles for effective catalytic performance in O-ATRP, among which are the ability of the PC to exhibit intramolecular charge transfer (CT) excited states, redox reversibility, and sufficient thermodynamic driving forces (redox potentials) to mediate the oxidative quenching O-ATRP cycle.[16] *N,N*-diaryl dihydrophenazine and *N*-aryl phenoxazine PCs have also been studied in diverse polymerization-related contexts, including the effects of light intensity and solvent, adaptation of O-ATRP to continuous-flow reactors, synthesis of star polymers, and demonstration of oxygen tolerance.[17a-e] In addition, these organic PCs were also applied in small molecule reactions, including trifluoromethylation, C-N and C-S cross couplings via dual catalytic approach with Ni(II) salts, and the reduction of carbon dioxide to methane using sunlight for solar fuel generation.[21f-g]

Despite advances in PC design, O-ATRP has largely been limited to polymerization of methacrylate monomers, but the controlled polymerization of other monomers is highly desired.[18] Poly(acrylates) possess disparate thermal and mechanical properties, enabling widespread industrial and academic use, including drug delivery, superabsorbent materials, coatings, adhesives and additive manufacturing.[19] As such, we sought to leverage current understanding of organic PC design to target the O-ATRP of acrylate monomers. The CRP of acrylates is inherently challenging due to high k_p, with values ranging from 15,000 to 24,000 L mol^{-1}s^{-1},[20] an order of magnitude larger than methacrylates. Furthermore, acrylate chain-end groups containing bromides are more difficult to reduce compared to the corresponding methacrylates, emphasizing the need for efficient PCs for activation.[21]

Photoinduced copper-catalyzed ATRP processes have been reported for successful CRP of acrylate monomers.[22] Additionally, a photoredox-catalyzed ATRP approach of acrylates was also performed using a precious metal-based *fac*-Ir(ppy)$_3$ PC following an oxidative quenching catalytic cycle, accessing control over MW growth to produce polymers with moderate *Đ*.[23] To access this polymerization with an organic PC, we hypothesized that a PC candidate must possess both a sufficiently oxidizing ^{2}PC$^{•+}$ with a correspondingly high $E_{1/2}$ (^{2}PC$^{•+}$/^{1}PC) potential to promote fast deactivation (high k_d) to compensate for high k_p, but also maintain a strongly reducing ^{3}PC* with sufficiently negative E^0(^{2}PC$^{•+}$/^{3}PC*) value for efficient alkyl bromide activation.

Using density functional theory (DFT) calculations to guide organic PC design, herein dimethyl-dihydroacridines are reported as a new class of organic PCs adept at controlled polymerizations of acrylate monomers via O-ATRP. Due to structural similarity to previously employed PCs in O-ATRP and tunable donor-acceptor motifs, we sought to investigate this class of molecules for use in photoredox-catalyzed processes, accessing tailored photo- and electrochemical properties. In this approach, well-defined acrylate polymers with controlled molecular weights and low dispersities (*Đ* ≤ 1.20) were synthesized using a 365 nm LED in a continuous-flow reactor in conjuction with LiBr salt additives, which are hypothesized to promote efficient deactivation.

Results and Discussion

1. Photocatalyst Development

Dimethyl-dihydroacridines have previously been applied in the development of organic LEDs as thermally activated delayed fluorescence emitters. Tunable absorption profiles, small S$_1$ and T$_1$ energy gaps (ΔE_{ST} < 0.4 eV), as well as CT characteristics were reported,[24] making this a promising structural motif for application in photoredox catalysis. Initial DFT calculations for 9,9-

dimethyl-10-(naphthalen-1-yl)-9,10-dihydroacridine (**1a**) predicted an E^0_{ox} (^{2}PC$^{\bullet+}$/^{1}PC) value of

0.72 V vs. SCE. Corroborating DFT prediction, **1a** was experimentally determined to have an $E_{p/2}$

value of 0.82 V vs. SCE (**Figure 4.2 A**). Although **1a** displayed a non-reversible cyclic

voltammogram, this relatively high $E_{p/2}$ value encouraged further exploration of dimethyl-

dihydroacridines as potential PC candidates, as current successful strongly-reducing PCs in O-

ATRP only have $E_{1/2}$ up to ~ 0.7 V vs. SCE.[16]

Notably, installation of biphenyl groups at the 2 and 7 positions of **1a** imparted redox

reversibility, a key requirement for catalyst turnover (**Figure 4.2 A**). Furthermore, relative to **1a**,

increasing the conjugation of the dimethyl-dihydroacridine molecules also red-shifted the

absorption profile by ~80 nm, presenting the possible use of milder irradiation conditions (Figure

2b). These results motivated us to synthesize a library of core-substituted derivatives and evaluate

their catalytic potential within the previously established design framework for O-ATRP PCs,

including absorption properties, excited-state characteristics, and redox properties.[7,15a] Seven

dimethyl-dihydroacridine PCs with diverse electron-poor (cyanophenyl), electron-rich

(methoxyphenyl), and highly conjugated (biphenyl or naphthalene) groups on both core and *N*-

aryl positions were synthesized (**Figure 4.2 C**). UV-vis spectroscopy was used to probe the ability

to tune the frontier orbitals with various substitutions, and as such tune the absorption profiles of

the PC (**Figure 4.2 B** and **Figures 4.49-4.55** in Experimental Section).

Installation of electron-donating or -withdrawing groups onto the core-substituent was

found to strongly influence $\lambda_{max,abs}$. For example, installation of 4-cyanophenyl groups (PC **3**, 382

nm) red-shifted $\lambda_{max,abs}$ by 42 nm compared to 4-methoxyphenyl groups (PC **2,** 340 nm) (**Figure

4.2 B**). In a comparison of *N*-aryl modifications with biphenyl core substituents, decreasing *N*-aryl

conjugation from a 1-naphthyl group (PCs **1** and **4**) to a phenyl group (PC **5**) led to a decrease in
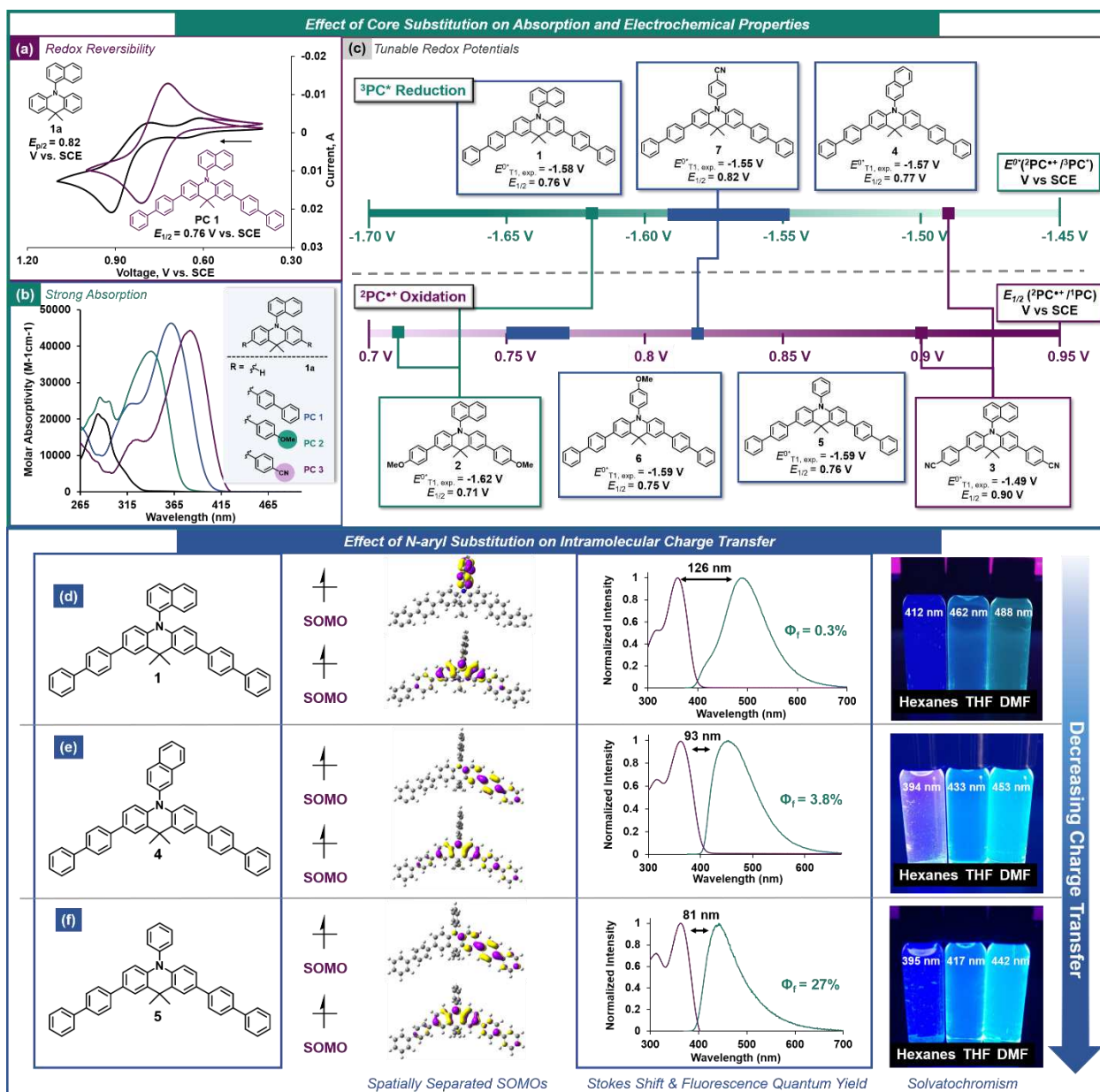
Figure 4.2. (a) Cyclic voltammogram of PC 1a and PC 1. (b) UV-vis spectrum of PCs 1a, 1, 2, and 3. (c) Electrochemical series of experimentally-measured excited state redox potentials $E^{0*}_{T1, exp.} = E^0(^2PC^{\bullet+}/^3PC^*)$ and oxidation potentials $E_{1/2}$ ($^2PC^{\bullet+}/^1PC$) of PCs investigated in this study. High- and low-lying SOMO for PCs with electronically neutral N-aryl groups, overlays of the absorption profiles (purple) and emission profiles (teal) with the experimentally determined Stokes shifts for each PC, and photographs of the PCs dissolved in solvents with increasing polarity with $\lambda_{max,emission}$ for each solvent for PC 1 (d), 4 (e), and 5 (f). All CV, UV-vis, and emission data collected in N,N-dimethylformamide. See SI for full experimental and computational details.

86

molar absorptivity (ε), (difference of ~18,000 $M^{-1}cm^{-1}$) but similar $\lambda_{max,abs}$ at 361 nm and 360 nm, respectively (**Table 4.1, entries 1 and 4**). Despite increasing pi-system conjugation through core-substitution, most PCs did not absorb beyond 400 nm. As an exception, the presence of 4-cyanophenyl groups at either core or *N*-aryl positions resulted in greater red-shifting of $\lambda_{max,abs}$, yielding some visible-light absorption. Notably, all the core-modified dimethyl-dihydroacridine PC candidates showed strong light absorption compared to non-core-modified **1a**, with ε ranging from 31,500 $M^{-1}cm^{-1}$ to 50,140 $M^{-1}cm^{-1}$. This high degree of efficiency in photoexcitation is also corroborated through computationally predicted oscillator strengths (*f* values ranging from 1.211 to 1.749) indicating high π- π^* transition probabilities (**Table 4.5** in Experimental Section).

To study the nature of PC*, which governs alkyl bromide activation, a combination of DFT calculations and experimental studies were used to evaluate the ability of these PCs to access CT excited states, which have been empirically shown beneficial for good O-ATRP performance in structurally similar *N,N*-diaryl dihydrophenazine and *N*-aryl phenoxazine PCs.[25,15a] In these systems, electron density is transferred from the electron rich core to either the *N*-aryl or core-substituent, generating a shift in charge density within the molecule in its excited state, which is dictated by the electron accepting ability of the aryl "acceptor" as well as the environment surrounding the "donor" tricyclic core. The connection between PC CT and superior O-ATRP performance were investigated but with dissimilar conclusions. For *N*-aryl phenoxazines, increasing CT character has been shown to augment triplet yields, positing that higher concentrations of ^{3}PC* promotes fast activation.[26] Conversely, studies with *N,N*-diaryl dihydrophenazine PCs suggests that CT lowers *PC reduction potentials, slowing down activation, reducing radical concentrations, and minimizing termination.[15c]

Table 4.1. Summary of photophysical and electrochemical measurements for PCs **1-7**.

PC	$\lambda_{max,abs}$ (nm)[a]	ε (M^{-1}cm^{-1})	$\lambda_{max,S1em.}$ (nm)[b]	Φ_f (%)	$E_{S1,exp.}$ (eV)[c]	$E_{T1,calc.}$ (eV)[d]	$E_{T1,77K}$ (eV)[c,e]	$E_{1/2}$ (^{2}PC$^{•+}$/^{1}PC) (V vs. SCE)[f]	$E^{0*}_{S1,exp.}$ (^{2}PC$^{•+}$/^{1}PC*) (V vs. SCE)[g]	$E^{0*}_{T1,exp.77K}$ (^{2}PC$^{•+}$/^{3}PC*) (V vs. SCE)[e,g]	$E^{0*}_{T1,calc.}$ (^{2}PC$^{•+}$/^{3}PC*) (V vs. SCE)[d]
1	361	46,300	487	0.3	2.55	2.41	2.34	0.76	-1.79	-1.58	-1.86
2	340	38,600	509	0.1	2.44	2.36	2.33	0.71	-1.73	-1.62	-1.94
3	382	44,300	458	83	2.71	2.43	2.39	0.90	-1.81	-1.49	-1.69
4	360	49,800	453	3.8	2.74	2.30	2.34	0.77	-1.98	-1.57	-1.77
5	361	31,500	443	27	2.80	2.29	2.35	0.76	-2.04	-1.59	-1.75
6	363	43,100	444	70	2.79	2.28	2.34	0.75	-2.04	-1.59	-1.78
7	355	50,100	535	8.2	2.32	2.39	2.37	0.82	-1.50	-1.55	-1.78

[a]Absorption wavelength measured using ultraviolet-visible spectroscopy in DMF. [b]Emission wavelength measured using steady-state fluorescence spectroscopy in DMF. [c]Energies were calculated using the maximum wavelength of emission. [d]DFT calculations performed at uM06/6-311+Gdp/uM06/6-31+Gdp level of theory with CPCM-described solvation in aqueous solvent. [e]Spectral emission measured at 77 K after 1 ms gate-delay. [f]All measurements were performed in a 3-compartment electrochemical cell with an Ag/AgNO$_3$ reference electrode in MeCN (0.01 M) and 0.1 M NBu$_4$PF$_6$ electrolyte solution with DMF analyte solution. Platinum was used at the working and counter electrodes. [g]Excited-state redox potentials were calculated using energies estimated from the maximum wavelength of singlet or triplet emission and the experimentally measured $E_{1/2}$; $E^{0*}_{S1,exp.} = E_{1/2} - E_{S1,exp.}$ and $E^{0*}_{T1, exp. 77K} = E_{1/2} - E_{T1,7}$
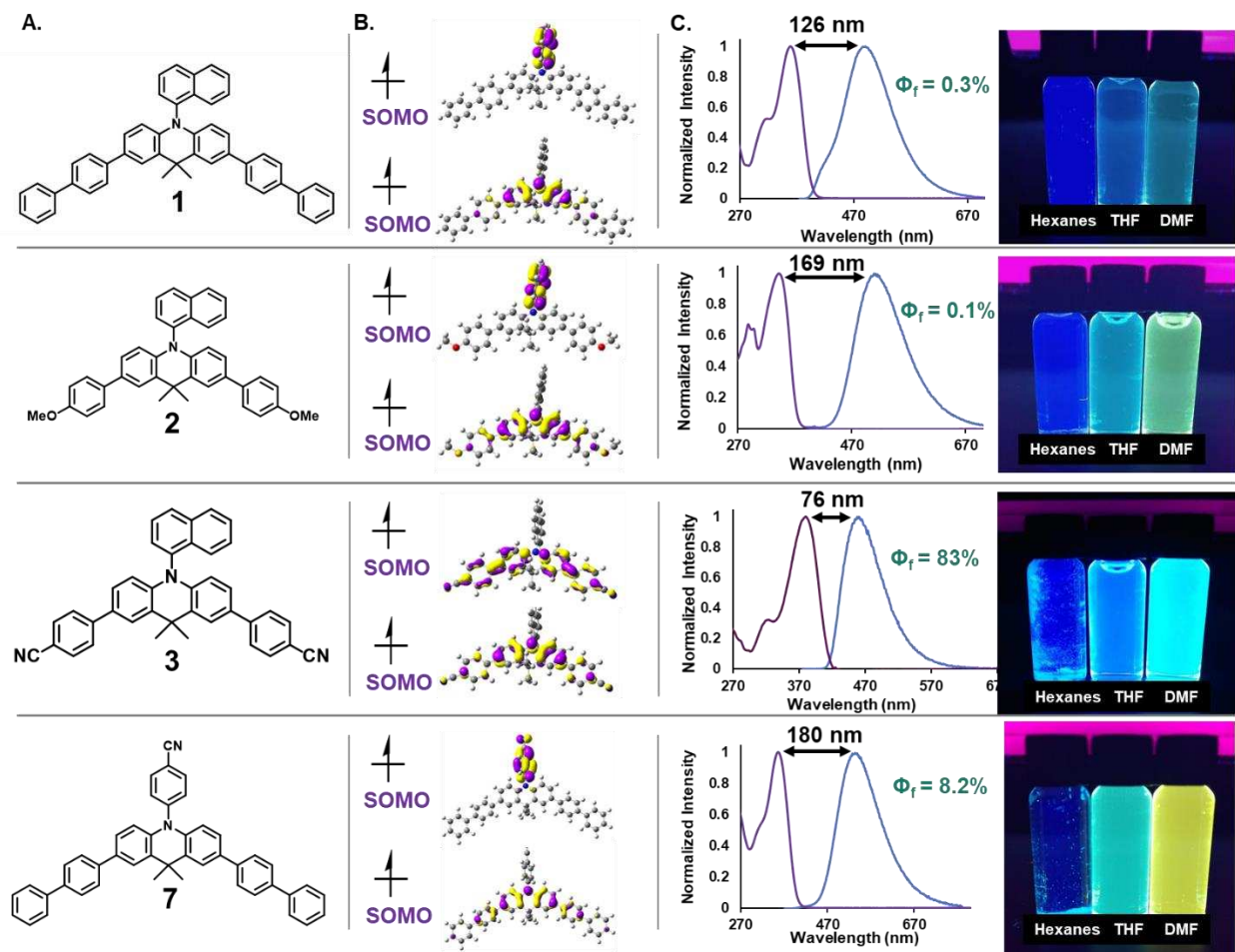
Figure 4.3. Higher-lying SOMOs (top) and low-lying SOMO (bottom) for PCs 1, 2, 3, and 7 (b). Overlays of the absorption profiles (purple) and emission profiles (blue) with the experimentally determined Stokes Shifts for each PC (c). Photographs of the PCs dissolved in solvents with increasing polarity (d). All CV, absorption, and emission experiments were performed in DMF.

Computationally, CT characteristics can be predicted through the presence of charge-separated singly occupied molecular orbitals (SOMOs) for ^{3}PC*. Of the PCs evaluated in this study, PCs **1**, **2,** and **7,** which possess either electron withdrawing groups or an extended π system as the *N*-aryl moiety, were predicted to have localization of the higher-lying SOMO onto the *N*-aryl substituent. PCs **4, 5,** and **6** all showed a higher-lying SOMO localization onto one core substituent, while PC **3** showed a higher-lying SOMO distributed across both core substituents (**Figure 4.3**).

Experimentally, CT character can be observed through a large Stokes shift and visualized through solvatochromism, where the polar ^{1}PC* is progressively stabilized by increasing solvent polarity, resulting in lower-energy emission and a corresponding red-shift in $\lambda_{max,em}$. Evaluation of CT from ^{1}PC* can estimate the CT character of ^{3}PC*, as CT singlet and triplet excited states are expected to be energetically degenerate, with low ΔE_{ST}.[24] A high fluorescence quantum yield (Φ_f) can indicate a lack of CT, as CT states have been shown to minimize fluorescence and increase triplet yields.[26] Consistent with previous observations in *N,N*-diaryl dihydrophenazine and *N*-aryl phenoxazine studies, for dimethyl-dihydroacridines subtle *N*-aryl substitution differences were found to be significant in influencing the nature of experimentally-observed CT character. Of these candidates, PCs **1** (**Figure 4.2 D**), **2**, and **7** displayed the largest degree of CT through the largest measured Stokes shifts (ranging from 126 to 180 nm) paired with low Φ_f (0.1% to 8.7%), and the most dramatic solvatochromism spanning blue to yellow wavelengths of emission (**Figure 4.2 D and 4.3**). By the same analysis, PCs **4** and **5** (**Figure 4.2 E and F**) displayed a moderate degree of CT, while PCs **3** and **6** displayed the least amount of CT character (**Figure 4.3**). Notably, Φ_f values ranging from 0.1% (PC **2**) to 83% (PC **3**) can be obtained by modulating core-substitution.

Evaluation of excited-state redox potentials of these PCs was performed by DFT calculations to predict $E^{0*}_{T1,calc.}$ (^{2}PC$^{\bullet+}$/^{3}PC*) values (**Table 4.1**). Experimentally, $E^{0*}_{S1,exp.}$ (^{2}PC$^{\bullet+}$/^{1}PC*) was determined by a modified Rehm-Weller equation: $E^{0*}_{S1,exp.} = E_{1/2} - E_{S1,exp.}$, where $E_{S1,exp.}$ was measured from the maximum wavelength of steady-state emission at room temperature. Experimental triplet energies ($E_{T1,exp.}$) were measured from PC phosphorescence at 77 K with a 1 ms gate-delay using time-resolved spectroscopy. $E_{S1,exp.}$ was also evaluated at 77 K with no gate delay, finding significant shifts in emission profiles. Interestingly, the PCs with the highest Stokes shifts, PCs **2** and **7** presented the lowest ΔE_{ST} values at 77 K (0.39 and 0.34 eV)

(**Table 4.6** in Experimental Section). Furthermore, computational E_{T1} predictions corresponded well with experimental values, with differences less than 0.07 eV.

Like absorption, the electronics of core-substitution strongly influenced $E^{0*}_{T1,exp.}$, where the PC with the lowest energy absorption (PC **3**) also possessed the lowest $E^{0*}_{T1,exp.}$ (-1.49 V vs. SCE). Correspondingly, PC **2,** with a relatively high energy absorption, was predicted to have the most reducing $E^{0*}_{T1,exp.}$ of -1.62 V vs SCE. Despite diverse absorption and CT properties, systematic study of various withdrawing, donating, and neutral *N*-aryl groups showed minimal influence on reduction potential, with $E^{0*}_{T1,exp.}$ ranging from -1.59 to -1.55 V vs. SCE.

The stability of the deactivating species $^2PC^{\bullet+}$ was measured by CV to determine $E_{1/2}$ ($^2PC^{\bullet+}/^1PC$), finding similar influence of the electronics of the core subsituent as was observed for both measured absorption characteristics and $E^{0*}_{T1,exp.}$ values. The presence of donating groups (PC **2**) resulted in stabilization of $^2PC^{\bullet+}$ ($E_{1/2}$ = 0.71 V vs SCE). Withdrawing groups (PC **3**) destabilized $^2PC^{\bullet+}$ and accessed a strongly oxidizing $^2PC^{\bullet+}$ ($E_{1/2}$ = 0.90 V vs. SCE). As in evaluation of $E^{0*}_{T1,exp.}$, the nature of the *N*-aryl group has minimal influence on $E_{1/2}$, with a range of 0.75 to 0.82 V vs. SCE. Computationally, the oxidizing ability of $^2PC^{\bullet+}$ (E^0_{ox}) was predicted by DFT, with values systematically ~0.25 V lower than the experimentally measured $E_{1/2}$, justifying the difference in magnitude between $E^{0*}_{T1,exp.}$ and $E^{0*}_{T1,calc.}$. In sum, the characterization of these dimethyl-dihydroacridine PC candidates shows that photophysical and electrochemical properties can be tuned in an analagous fashion to other established organic PCs with similar donor-acceptor motifs, while accessing more strongly oxidizing $^2PC^{\bullet+}$ characteristics and offering opportunities for previously unaccessable reactivity.

1. Application of Dimethyl-dihydroacridines to O-ATRP of Acrylate Monomers

To test the ability of these dimethyl-dihydroacridine PC candidates to catalyze O-ATRP of challenging acrylate monomers, initial polymerizations were conducted using *n*-butyl acrylate (BA) monomer, Diethyl 2-bromo-2-methylmalonate (DBMM) initiator, in *N,N*-dimethylacetamide (DMAc) solvent under 365 nm LED irradiation in batch reactor conditions. For comparison to dimethyl-dihydroacridine PCs, other well-studied organic PCs with diverse redox properties, including 3,7-di(4-biphenyl) 1-naphthalene-10-phenoxazine (**PhenO**), 5,10-di-(2-naphthyl)-5-10-dihydrophenazine (**PhenN**), and 1,2,3,5-tetrakis(carbazol-9-yl)-4,6-dicyanobenzene (**4Cz-IPN)** were applied in the O-ATRP of BA under the same reaction conditions. **PhenO** and **PhenN** both possess strongly reducing $E^{0*}_{T1,calc}$ (-1.70 and -2.12 V vs. SCE) and somewhat stabilized $E_{1/2}$ (0.65 and 0.21 V vs. SCE) while **4Cz-IPN** is a moderate reductant and strong oxidant (-1.06 and 1.50 V vs. SCE, respectively).[17f,7] In all cases these polymerizations were uncontrolled. For **4Cz-IPN**, M_n decreased over the course of polymerization from 170 kDa to 63 kDa, with $Đ > 2.0$ (**Figure 4.4 A**). **PhenN** and **PhenO** showed some characteristics of an O-ATRP process, but suffered from non-linear growth of MW and high $Đ$ (**Figure 4.4 B and C**).
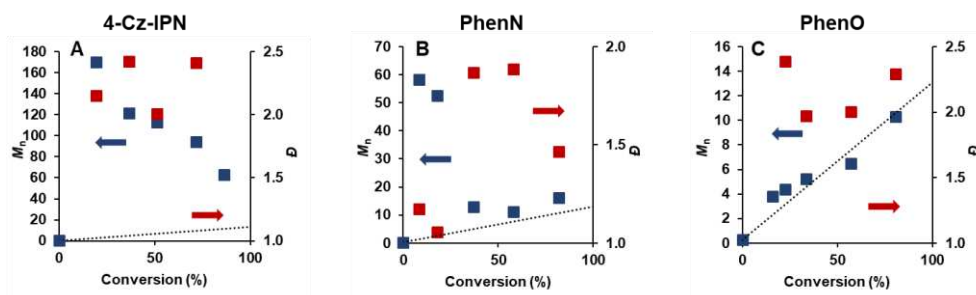
Figure 4.4: Plots of M_n vs. conversion (blue) and $Đ$ vs. conversion (red) for O-ATRP of BA plotted against the theoretical M_n (dashed line) using **4-Cz-IPN** (a), **PhenN** (b), and **PhenO** (c). Conditions are [1000]:[10]:[1] of [BA]:[DBMM]:[PC] with 1.0 eq. by volume of DMAc irradiated by 365 nm LEDs in batch conditions.

Initial application of PCs **1-7** to O-ATRP of BA supported that CT was required for good O-ATRP performance, similar to what was observed in *N,N*-diaryl dihydrophenazines.[28] For the PCs with the least amount of CT character (PCs **3** and **6**), the polymerization was uncontrolled, with MWs decreasing with increasing monomer conversion and $Đ > 2.0$. Excitingly, control over polymer MW growth, an indication of efficient deactivation processes, was realized for PCs **1**, **2**, **4**, **5**, and **7,** with all $I*$ values near 100% (**Table 4.2, entries 1-7**), where $I* = (M_{n,GPC}/M_{n, theo.})$ x 100. PC **2** provided the best results with $I* = 96\%$ at 77% conversion (**Figure 4.6 A**) but produced a polymer with high $Đ$ at 1.53. For PCs **1, 2, 4, 5, and 7**, bimodal gel permeation chromatography (GPC) traces revealed an accompanying high MW p(BA) species present in low quantities. Control experiments with BA in DMAc under 365 nm irradiation revealed significant monomer autopolymerization (63% conversion at 2.5 hours) (**Table 4.8** in Experimental Section) and thus likely contributed to the formation of this undesired high MW species.

As the best performing PC in these conditions (PC **2**) possessed the highest $E^{0*}_{T1,exp.}$ but also the lowest $E_{1/2}$, we hypothesized that promoting efficient activation could outcompete autopolymerization side-reactivity, leading to lower $Đ$ while maintaining control over MW growth. Notably, acrylate alkyl halide chain-end groups are more difficult to reduce compared to methacrylates, which can be observed by CV measurements of representative alkyl bromide initiators with methacrylate and acrylate functionalities. An acrylate analogue, methyl 2-bromopropionate, was found to undergo one-electron reduction at $E_{p/2} = -0.96$ V vs SCE, while a methacrylate model, methyl α-bromoisobutyrate, was reduced at $E_{p/2} = -0.80$ V vs. SCE, or a difference of 0.16 V (**Figure 4.5**), highlighting the need for high $E^{0*}_{T1,exp.}$ for efficient activation of acrylate-derived chain-end groups.
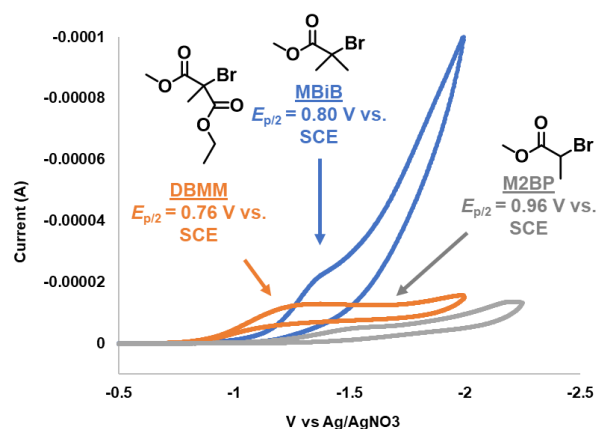
Figure 4.5: Cyclic voltammograms for Diethyl 2-bromo-2-methyl malonate (orange), methyl α-bromoisobutyate (blue) and methyl 2-bromopropionate (grey).

Table 4.2: Summary of results of O-ATRP of BA performed in batch and flow using PCs 1-7.[a]

Entry	PC	Reactor	Conv. (%)[b]	$M_{n,calc}$ (kDa)[c]	Đ (M_w/M_n)[c]	I^* (%)[d]
1	1	Batch	65	9.3	1.64	92
2	2	Batch	77	10.6	1.53	96
3	3	Batch	42	31.4	4.93	35
4	4	Batch	68	9.6	1.62	93
5	5	Batch	59	8.7	1.70	90
6	6	Batch	72	25.8	3.52	37
7	7	Batch	76	10.9	1.89	92
8	1	Flow	67	8.9	1.59	100
9	2	Flow	81	11.0	1.35	97
10	3	Flow	71	13.1	4.57	72
11	4	Flow	81	11.1	1.48	96
12	5	Flow	79	10.2	1.48	102
13	6	Flow	82	11.4	3.58	94
14	7	Flow	73	9.6	1.54	100

[a]Conditions are [1000]:[10]:[1] of [BA]:[DBMM]:[PC] with 1.0 eq. DMAc to BA by volume and irradiated by 365 nm LEDs. Batch reactions are conducted under ambient temperatures and flow reactions at 22 ºC. [b]Determined by ^{1}H NMR. [c]Measured using GPC. [d]Calculated by (Conv. x [Mon]/[RX] x $M_{w,Mon}$)/1000. [e]Initiator efficiency (I^*) calculated by (Theo. M_n/Calc. M_n) x 100.

One alternative to batch reactor systems are continuous flow reactors, which provide more uniform reaction irradiation and have been shown to improve photoinduced CRP systems through enhancing PC photoexcitation, thus promoting efficient alkyl bromide activation.[27] In this approach, a commercially available temperature-controlled Hepatochem PhotoRedOx box, an 18 W EvoluChem 365 nm LED, and a 2 mL PFA flow reactor was employed. Importantly, control experiments with BA in DMAc under these conditions did not produce any undesired autopolymerization (**Table 4.17** in Experimental Section). PCs **1-7** were then evaluated for the O-ATRP of BA in continuous flow, showing similar trends in performance as batch conditions, albeit with consistently lower *Đ* (**Table 4.2, entries 8-14**). PC **2** again proved superior, however with initial high *Đ* > 1.5 at conversions < 50% but lowered to 1.35 with *I** = 97% at 81% conversion.
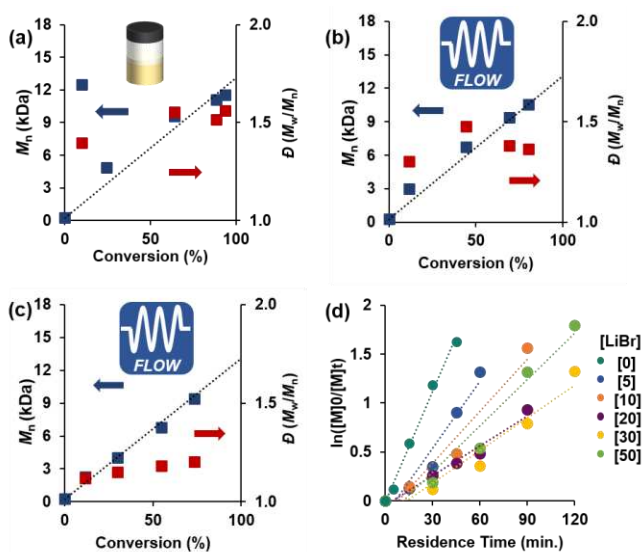
Figure 4.6: (a) Plots of M_n vs. conversion (blue) and *Đ* vs. conversion (red) for O-ATRP of BA plotted against the theoretical M_n (dashed line) using PC 2 conducted in batch reactor, (b) flow reactor, and (c) flow reactor with 30 eq. LiBr relative to PC. (d) First order kinetic plot of O-ATRP of BA with varying LiBr eq. relative to PC. Conditions are [1000]:[10]:[1]:[x] of [BA]:[DBMM]:[PC 2]:[LiBr] with 1.0 eq. by volume of DMAc for (a) and 1.5 eq. for (b) and (c), and irradiated by 365 nm LEDs.

Using PC **2,** further reaction optimization analyzing the effects of initiator, PC loading, and reaction concentration were conducted (see detailed results in Experimental Section). Increasing

the DMF:BA ratio (1:1 to 1.5:1 v/v) significantly improved polymerization results, with $Đ < 1.5$ at all monomer conversions (**Figure 4.6 B**). To further improve the system, the addition of various bromide salts was investigated, as this has been shown to promote deactivation in aqueous copper-catalyzed ATRP systems and in some photoredox-catalyzed ATRP systems.[28] Analysis of LiBr, NaBr, KBr, and tetrabutylammonium bromide salts showed some decrease in $Đ$, with LiBr providing the greatest effect ($Đ \leq 1.23$) (**Table 4.22** in Experimental Section). O-ATRP of BA using lithium salts with diverse anions (LiCl, LiI, LiPF$_6$) was also performed. A complete loss of MW control and $Đ > 2.0$ in all cases was observed (Table S20), illustrating the significance of the bromide anion in deactivation. Analysis of relative LiBr concentrations showed the conditions producing polymers with lowest $Đ$ (30 eq. LiBr relative to PC, or 83.3 mM) to also have the slowest overall reaction rate (**Figure 4.6 C and D**), which paired with lower $Đ$, suggests LiBr concentration plays a key role in deactivation.

Next, a combination of DFT calculations and experimental studies were employed to explore the role of the LiBr salt in this O-ATRP system, probing its potential influence on both activation and deactivation mechanistic steps. One possibility is a Lewis-acid driven activation by Li$^+$ of the alkyl bromide ester polymer chain-end, facilitating rapid activation. However, CV revealed no change in reduction $E_{p/2}$ (RX/RX$^{\bullet-}$) of methyl-2-bromopropionate upon addition of LiBr ($E_{p/2} = -0.92$ V vs. SCE) (**Figure 4.75** in Experimental Section). To evaluate potential effects of LiBr on PC photophysical behavior, PC **2** absorption and emission characterization was performed in the presence of LiBr, finding no changes in these properties (**Figure 4.68 and 4.69** in Experimental Section).

Formally, the deactivation step is a termolecular process requiring low concentrations of P$_n^{\bullet}$, ^{2}PC$^{\bullet+}$, and X$^-$ to collide, which is entropically unfavorable. Previous studies with

dihydrophenazines have shown that decreasing solvent polarity promotes ion-pairing of ^{2}PC$^{\bullet+}$X$^-$, with a subsequent decrease in polymerization rate and improvement in performance.[25] As such, we propose that efficient deactivation requires oxidation of P$_n^{\bullet}$ by a ^{2}PC$^{\bullet+}$X$^-$ ion-pair, which shifts a formal three-body collisional event to a more favorable pseudo-two-body event. In addition, we hypothesize a concerted mechanism for the oxidation of P$_n^{\bullet}$ by a ^{2}PC$^{\bullet+}$X$^-$ ion-pair, where the formation of P$_n$-X is tied to the nuclear coordinate of X$^-$ thus avoiding thermodynamically unfavorable carbocation P$_n^+$ intermediary species. Using DFT, the association of ^{2}PC$^{\bullet+}$ + X$^-$ → ^{2}PC$^{\bullet+}$X$^-$ using PC **2** was predicted to be slightly endergonic ($\Delta G^0_{complex}$ = 0.6 kcal/mol). As such, we postulate that the presence of excess bromide ions through LiBr addition increases the population of the proposed ^{2}PC$^{\bullet+}$X$^-$ deactivator species, promoting rapid deactivation of the propagating chain-end and explaining the observed decrease in polymerization rates and lower Đ.

To further elucidate the relative importance of PC choice and the optimized reaction conditions in successful O-ATRP of acrylates, polymerizations were also conducted using **4-CzIPN**, **PhenO**, and **PhenN** in continuous-flow with LiBr additives. For **4Cz-IPN**, no polymerization was observed in the presence of LiBr, while O-ATRP without LiBr yielded an uncontrolled polymerization with M_n > 40 kDa and Đ > 2.0. (**Table 4.24** in Experimental Section). The O-ATRP of BA using **PhenO** and **PhenN** was moderately improved under the optimized conditions, showing some control over molecular weight growth and with Đ < 1.5 at higher monomer conversions. However, both polymerizations displayed bimodal MW distributions by GPC, with I^* ranging from 31-109%.

Using these optimized conditions, MW control in the O-ATRP of BA catalyzed by PC **2** was demonstrated through adjustment of reaction stoichiometry, accessing MWs ranging from 2 to 26 kDa with Đ < 1.36 (**Table 4.2, entries 1-5**). However, targeting high MWs proved

challenging, with $I^* > 100\%$, perhaps from a confluence of increased termination events and viscosity changes within the reactor. The O-ATRP of other alkyl and glycol acrylate monomers was performed using PC **2** with excellent control over MW and Đ (**Table 4.2, entries 7-11**). O-ATRP of methyl methacrylate (MMA) was also accomplished, realizing low Đ but with slightly bimodal GPC traces (**Table 4.2, entry 12**). As expected due to lower k_p, the O-ATRP of MMA was significantly slower than BA requiring 600 minutes of residence time for 72% monomer conversion, as compared to ~100 minutes for acrylates.

Table 4.3: Summary of results of O-ATRP of acrylate monomers performed using PC 2.[a]
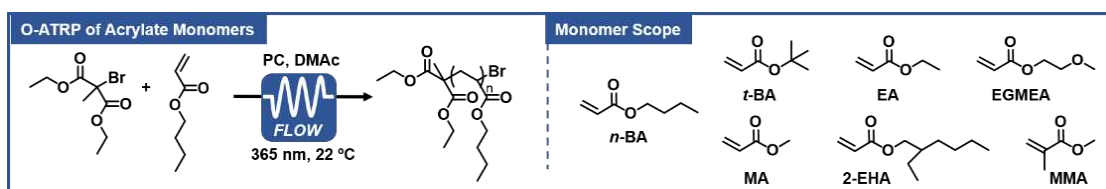
Entry	Monomer	[Monomer]:[DBMM]	Res. Time (min.)	Conv. (%)	$M_{n,calc,}$ (kDa)	$M_{w,calc,}$ (kDa)	Đ (M_w/M_n)	I^* (%)
1	n-BA	[1000]:[2.5]	90	89	26.4	45.7	1.35	173
2	n-BA	[1000]:[5]	120	88	15.2	22.8	1.32	150
3	n-BA	[1000]:[10]	120	73	9.4	9.7	1.20	103
4	n-BA	[1000]:[20]	180	80	7.3	5.4	1.19	74
5	n-BA	[1000]:[40]	180	67	5.4	2.4	1.18	44
6[b]	n-BA	[1000]:[10]	120	85	10.3	11.1	1.24	108
7	t-BA	[1000]:[10]	120	92	13.8	12.1	1.23	88
8	MA	[1000]:[10]	90	92	10.0	8.1	1.30	81
9	EA	[1000]:[10]	90	76	7.5	7.8	1.19	105
10	2-EHA	[1000]:[10]	90	90	16.3	16.8	1.53	104
11	EGMEA	[1000]:[10]	60	92	10.5	12.3	1.37	117
12	MMA	[1000]:[10]	600	72	8.8	7.4	1.17	85

[a]Conditions are [1000]:[x]:[1]:[30] of [monomer]:[DBMM]:[PC 2]:[LiBr] with 1.5 mL DMAc relative to 1 mL monomer performed in continuous-flow and irradiated by 18 W 365 nm LED at 22 ºC. [b]Reaction components sparged with air for 30 minutes before polymerization. See Experimental Section for full details.

In batch conditions, no monomer conversion was observed using PC **2** under ambient atmosphere (**Table 4.8** in Experimental Section). Recently, *N*-aryl phenoxazines were found to

perform a well-controlled O-ATRP under ambient conditions when no vial headspace was present.[17e] To further test the oxygen-tolerance of dimethyl-dihydroacridines, the O-ATRP of BA was performed in optimized flow conditions using reagents and solvents previously exposed to ambient air proceeded efficiently with no observed induction period, with $Đ ≤ 1.24$ and I^* close to 100% (**Table 4.3, entry 6**).

To demonstrate the temporal control characteristic of an O-ATRP process, pulsed irradiation polymerization experiments were performed in batch conditions, showing no monomer conversion during dark periods with no irradiation (**Figure 4.7**). Analysis of bromide chain-end group retention of p(BA) was performed through MALDI mass spectrometry, revealing the presence of H-terminated and bimolecular radical termination products (**Figure 4.168** in Experimental Section). Notably, no significant differences in chain-end groups between polymers synthesized with and without LiBr were observed (**Figure 4.169** in Experimental Section).
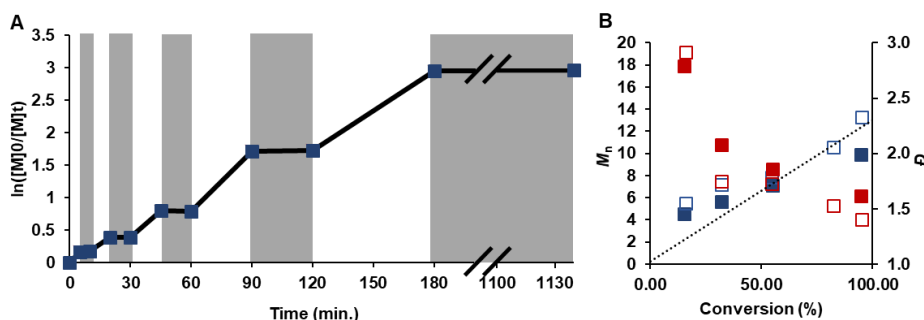
Figure 4.7: First order kinetic plot for the O-ATRP of BA with period on (white) and off periods (grey) (a). Plot of M_n (blue) and dispersity (red) versus conversion for on (filled squares) and off (open squares) periods (b). Conditions are [1000[:[10]:[1] of [BA]:[DBMM]:[PC 2] with 1.5 mL DMAc to 1 mL BA, irradiated by 365 nm LEDs in batch conditions at ambient temperature.

To validate the chain-end group fidelity of the system and demonstrate the ability of this system to produce complex polymeric materials, chain-extensions were performed in continous-flow of an isolated p(n-BA) macroinitiator ($M_n = 4.6$ kDa, $Đ = 1.26$) with ethyl acrylate (EA) to produce a block-copolymer p(n-BA)-b-p(EA) with $Đ = 1.16$ (12 kDa). This polymer was then

again reintroduced as a macroinitiator and further extended with *tert*-butyl acrylate to produce a well-defined triblock copolymer (M_n = 20 kDa, Đ = 1.44) (**Figure 4.8**). An ^{1}H NMR spectrum for the p(*n*-BA) macroinitiator with detailed assignments (**Figure 4.165** in Experimental Section) also shows the presence of α- and ω- chain-end groups.
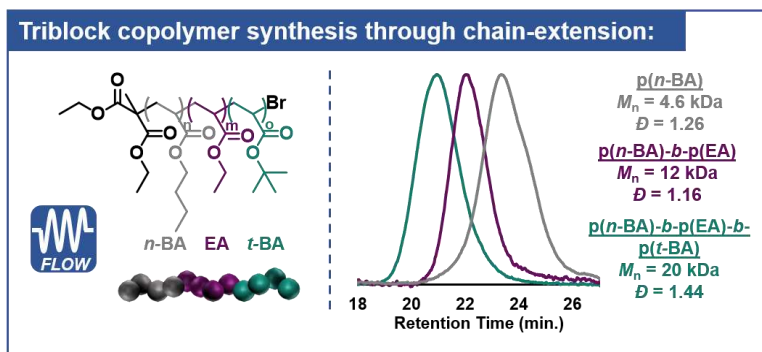
Figure 4.8: Results of sequential chain-extension experiments with corresponding GPC traces to produce a p(*n*-BA)-*b*-p(EA)-*b*-p(*t*-BA) triblock copolymer.

Conclusion

In summary, we have reported the first successful O-ATRP of acrylate monomers with controlled MW and low Đ, enabled by rational design and development of a new family of dimethyl-dihydroacridine photocatalysts. Relationships between PC properties and catalytic performance are discussed, finding an interplay of photophysical and electrochemical properties is necessary to achieve the desired reactivity, as is supported by the best performing PC having the highest $E^{0}*_{T1,exp.}$ but the lowest $E_{1/2}$. A combination of reactor choice and LiBr additives is found to be significant in achieving a well-controlled system, which are proposed to promote the respective activation and deactivation steps of the O-ATRP cycle. We envision that dimethyl-dihydroacridines, with distinct properties and new reactivity, will further enable the advancement of organic photoredox catalysis in both small molecule and macromolecular syntheses, aiding in the replacement of precious-metal catalysts for sustainable photoredox processes.

Experimental

Materials and Methods

Purchased Chemicals:

C-N Coupling: 9,9-Dimethyl-9,10-dihydroacridine was purchased from Ark Pharm. Bromobenzene, 2-bromonaphthalene, 1-bromonaphthalene, 4-bromobenzonitrile, and 4-bromoanisole were purchased from VWR. Bis(dibenzylideneacetone) palladium(0) and 1M tri-*tert*-butylphosphine in toluene were purchased from Sigma Aldrich. Dicyclohexylphosphino-2,6-diisopropoxybiphenyl (RuPhos) and chloro-(2-dicyclohexylphosphino-2,6-diisopropoxy-1,1-biphenyl_[2-(2-aminoethyl)phenyl]palladium(II)-methyl-t-butyl ether adduct (RuPhos precatalyst) were purchased from Sigma Aldrich. Sodium tert-butoxide was purchased from Sigma Aldrich. Dioxane was purified using an mBraun MB-SPS-800 solvent purification system and kept under nitrogen atmosphere. Anhydrous 99.8% toluene was purchased from Sigma Aldrich and kept under nitrogen atmosphere.

Bromination: *N*-bromosuccinimide was purchased from VWR. HPLC grade THF was purchased from VWR.

Suzuki Coupling: Tetrakis(triphenylphosphine) palladium(0) was purchased from Sigma Aldrich. Potassium carbonate was purchased from VWR. 4-biphenylboronic acid was purchased from TCI America. 4-cyanobenzeneboronic acid and 4-methoxyphenylboronic acid were purchased from Sigma Aldrich.

Polymerizations: All monomers and initiators were purchased from Sigma Aldrich. Anhydrous *N,N*-dimethylacetamide (DMAc), dimethylsulfoxide (DMSO), and anhydrous benzene were purchased from Sigma Aldrich. Tetrahydrofuran (THF) and *N,N*-dimethylformamide (DMF) were

purified using an mBraun MB-SPS-800 solvent purification system and kept under nitrogen atmosphere.

Chemical Preparation and Storage:

All reagents for catalyst synthesis were used as received. All monomers and initiators for polymerizations were dried with calcium hydride overnight, distilled under vacuum, and freeze-pump-thawed 3 times. All monomers and initiators were stored under inert atmosphere at -10 ℃ and in the dark.

Instrumentation for Photocatalyst and Precursors Characterization:

Structural analysis was performed by a Varian 400 MHz NMR Spectrometer. UV-visible spectroscopy was carried out using a Cary 5000 UV-Vis-NIR spectrophotometer from Agilent. Steady state photoluminescence spectroscopy and absolute fluorescence quantum yields measurements were performed using a FS5 Spectrofluorometer from Edinburgh Instruments. Time-resolved spectral emission measurements were performed on an LP980 spectrometer from Edinburgh Instruments equipped with a Nd:Yag laser operating at 355 nm and an intensified CCD camera for detection. Cyclic Voltammetry experiments were conducted using a Gamry Interface 1010B potentiostat. For full experimental details see each characterization section below.

Instrumentation for Polymer Characterization:

Monomer conversion was determined by a Varian 400 MHz NMR Spectrometer. Molecular weight analysis was performed using gel permeation chromatography (GPC) coupled with multi-angle light scattering (MALS) using an Agilent HPLC system fitted with one guard

column and 3 PL-gel mixed C columns running THF as eluent at 1.0 mL/minute. The detectors used for GPC were a Wyatt Technology TrEX differential refractometer (RI) and a Wyatt Technology miniDAWN Treos light scattering detector (MALS). A dn/dc value of 0.065 was used for all poly(butyl acrylate) analyses and 0.080 for poly(methyl methacrylate). dn/dc values for all other polymers was determined through analysis with a known sample concentration.

Batch Reactor Supplies:

Batch polymerizations were performed in a 100 mL beaker wrapped in aluminum foil with a 12-inch strip of 12 V 365 nm LEDs purchased from LED Lighting Hut (365nm UV LED Light Strip, 60 SMD5050 LEDs/M, 5M/reel, DC12V Input from ledlightinghut.com). Polymerizations using 380 nm and 455 nm light sources were performed with 12 V LED strips from Creative Lighting Solutions (CL-FRS5050WPDD-5M-12V-UV and CL-FRS5050WPDD-5M-12V-BL from creativelightings.com).

Flow Reactor Supplies:

Flow polymerizations were performed using a Hepatochem Photoredox Temperature Controlled reactor with a 2 mL flow attachment. The light source used was a 18W 365 nm EvoluChem bulb (part no. HCK1012-01-011 from Hepatochem). The flow tubing was 1/16 in O.D. and 0.003 in I.D. with PFA as the tubing material. The flow rate was controlled using a Pump 11 Elite Syringe Pump from Harvard Apparatus with a 50 mL stainless steel syringe with 1/16 tubing fitting. See detailed reactor set-up and design details in polymerization section.

<u>Computational Details</u>

All PCs developed in this work relied on DFT for predictions of important PC properties. All computations were performed by Dr. Chern Hooi-Lim. In this dissertation, the computational details are included as a means to clarify important assumptions and methods.

All calculations were performed using computational chemistry software package Gaussian 09 ver. D01.[29]

Reduction Potentials: Standard reduction potentials (E^0) were calculated following previously reported procedures.[30,31,32,33] A value of -100.5 kcal/mol was assumed for the reduction free energy of the standard hydrogen electrode (SHE). Thus, $E^0 = (-100.5 - \Delta G_{red})/23.06$ (V vs. SHE); for E^0 ($^2PC^{\bullet+}/^3PC*$), $\Delta G_{red} = G(^3PC*) - G(^2PC^{\bullet+})$ while for E^0 ($^2PC^{\bullet+}/^1PC$), $\Delta G_{red} = G(^1PC) - G(^2PC^{\bullet+})$. The Gibbs free energies of $^3PC*$, $^2PC^{\bullet+}$, and ^1PC were calculated at the unrestricted M06/6-311+G** level of theory in CPCM-H_2O solvent (single point energy) using geometries optimized at unrestricted M06/6-31+G** level of theory in CPCM-H_2O solvent. To reference to the Saturated Calomel Electrode (SCE), E^0 (vs. SHE) is converted to E^0 (vs. SCE) using E^0 (vs. SCE) = E^0 (vs. SHE) - 0.24 V. Triplet energies (in eV) of PCs were obtained by [G($^3PC*$) - G(^1PC), in kcal/mol]/23.06. Based on the comparison of our large experimental and computational data set, the choice of CPCM solvation model is justified as the computed reduction potential closely approximates the experimental values. For example, the computed ground state oxidation potentials between the $^2PC^{\bullet+}/^1PC$ redox couple is typically within ~0.2 to 0.3 V from the experimental values.

Excited State Calculation: Using optimized ground state geometries, single point time dependent density functional theory (TD-DFT) calculations were performed using the rCAM-B3LYP/6-31+G(d,p)/CPCM-DMA level of theory.[34] rCAM-B3LYP was chosen because it gave

better λ_{max} predictions that are closer to experimental values in comparison to rωB97xd level of theory. TD-DFT calculations (with our chosen CAM-B3LYP method) corroborate experimental observations that UV-vis absorption becomes increasingly red-shifted with higher molar absorptivity as the aryl conjugation at the core position is increased.

Summary of Photocatalyst Properties

Table 4.4: Summary of experimental photophysical and electrochemical data for PCs 1-7.

PC	$\lambda_{max,abs}$ (nm)[a]	ε ($M^{-1}cm^{-1}$)	$\lambda_{max,em}$ (nm)[b]	$E_{S1, exp}$ (eV)[c]	$E_{T1, 77K, exp}$ (eV)[c,d]	$E_{1/2}$ ($^2PC^{\bullet+}/^1PC$) (V vs. SCE)[e]	$E^{0*}_{S1,exp.}$ ($^2PC^{\bullet+}/^1PC*$) (V vs. SCE)[f]	$E^{0*}_{T1,exp. 77K}$ ($^2PC^{\bullet+}/^3PC*$) (V vs. SCE)[e,f]
1	361	46,270	487	2.55	2.34	0.76	-1.79	-1.58
2	340	38,560	509	2.44	2.33	0.71	-1.73	-1.62
3	382	44,340	458	2.71	2.39	0.90	-1.81	-1.49
4	360	49,780	453	2.74	2.34	0.77	-1.98	-1.57
5	361	31,500	443	2.80	2.35	0.76	-2.04	-1.59
6	363	43,120	444	2.79	2.34	0.75	-2.04	-1.59
7	355	50,140	535	2.32	2.37	0.82	-1.50	-1.55

[a]Absorption wavelength measured using ultraviolet-visible spectroscopy in DMF. [b]Emission wavelength measured using steady-state fluorescence spectroscopy in DMF. [c]Singlet and triplet energies were calculated using the maximum wavelength of emission. [d]Spectral emission measured at 77 K after 1 ms gate-delay. . [e]All measurements were performed in a 3-compartment electrochemical cell with an Ag/AgNO$_3$ reference electrode in MeCN (0.01 M) and 0.1 M NBu$_4$PF$_6$ electrolyte solution. DMF was used to solvate the PCs. Platinum was used at the working and counter electrodes. [f]Excited state redox potentials were calculated using the singlet energies estimated from the maximum wavelength of emission and the experimentally measured $E_{1/2.}$

Table 4.5: Summary of computationally-predicted photophysical and electrochemical data for PCs 1-7.

PC	$\lambda_{max,abs}$ (nm)	f	$E_{T1,\ calc}$ (eV)	E^0_{ox} ($^2PC^{\bullet+}/^1PC$) (V vs. SCE)	$E^{0*}_{T1,calc.}$ ($^2PC^{\bullet+}/^3PC^*$) (V vs. SCE)
1	326	1.689	2.41	0.55	-1.86
2	311	1.211	2.36	0.42	-1.94
3	343	1.446	2.43	0.74	-1.69
4	328	1.655	2.30	0.53	-1.77
5	329	1.748	2.29	0.54	-1.75
6	329	1.741	2.28	0.50	-1.78
7	324	1.749	2.39	0.61	-1.78

Photocatalyst Synthesis

General Synthetic Scheme:
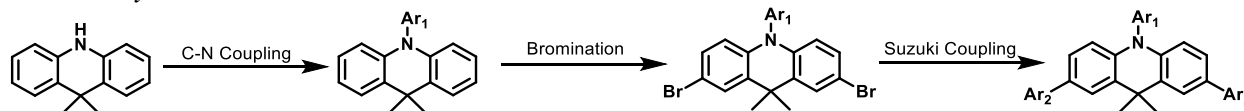
Figure 4.9: The general synthetic scheme for PCs 1-7 follows a previously developed synthetic strategy.[11a,15a]

Synthesis of 9,9-dimethyl-10-(naphthalen-1-yl)-9,10-dihydroacridine
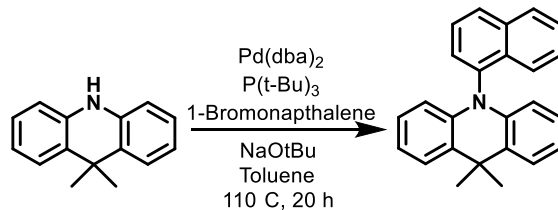
A storage tube was loaded with 5.0 g (23.9 mmol, 1 eq.) 9,10-Dihydro-9,9-dimethylacridine, 7.42 g 1-bromonaphthalene (36.0 mmol, 1.5 eq.), 137.5 mg of Bis(dibenzylideneacetone)palladium(0) (0.89 µmol, 1 mol%), 717 µL of 1M in toluene Tri-*tert*-butylphosphine (0.717 mmol, 3 mol %), 6.0 g sodium *tert*-butoxide (71.7 mmol), and 100 mL toluene under nitrogen atmosphere. The solution was heated to 110 ℃. After 20 hours, the brown-orange liquid was poured directly through a silica plug and rinsed with toluene. All blue fluorescent portions were collected and concentrated to 50 mL volume via rotary evaporation. The product was precipitated by slow addition of ~75 mL of ethyl acetate. The product, a white solid, was isolated by vacuum filtration and washed with ethyl acetate and methanol. The product was dried overnight under vacuum to yield 5.88 g (73.4% yield). ^{1}H NMR (400 MHz, Chloroform-*d*) δ 8.06 – 7.95 (m, 2H), 7.68 (ddd, *J* = 8.4, 4.1, 3.0 Hz, 2H), 7.57 – 7.46 (m, 4H), 7.36 (ddd, *J* = 8.3, 6.8, 1.2 Hz, 1H), 6.96 – 6.78 (m, 4H), 6.03 (dd, *J* = 8.1, 1.4 Hz, 2H), 1.85 (s, 3H), 1.75 (s, 3H). ^{13}C NMR (101 MHz, CDCl$_3$) δ 140.51, 137.71, 135.47, 131.84, 129.71, 129.04, 128.80, 128.67, 127.10, 126.93, 126.68, 126.54, 125.60, 123.78, 120.47, 114.20, 77.34, 77.02, 76.70, 36.03, 33.02, 31.89. HRMS (ESI) calculated for (M+H)+ for C$_{25}$H$_{21}$N, 336.17468; Found, 336.17468.
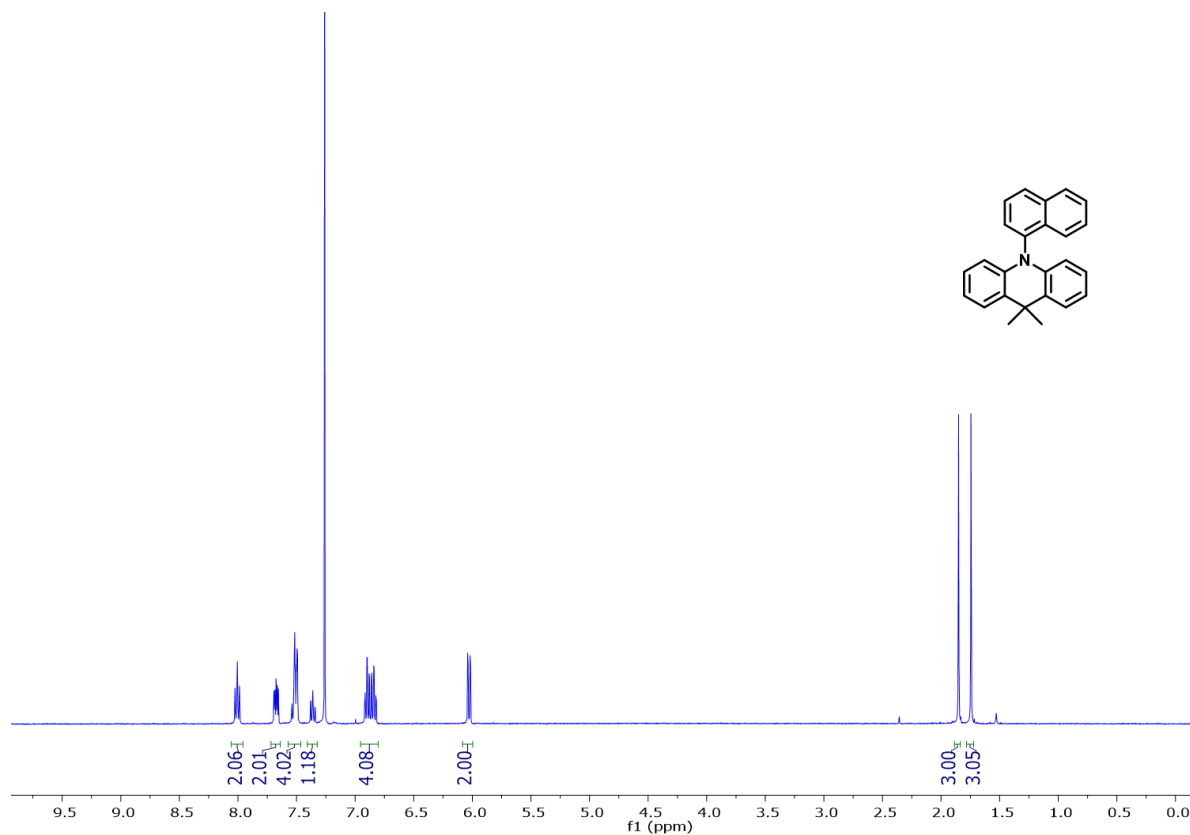
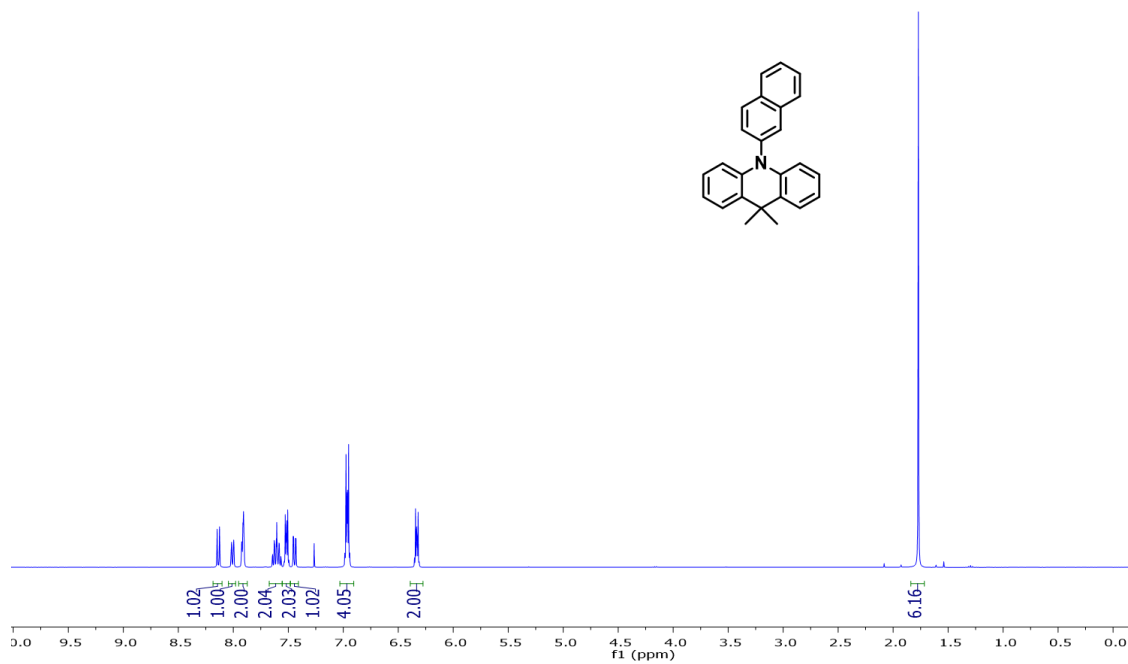**Figure 4.10:** ^{1}H NMR spectrum of 9,9-dimethyl-10-(naphthalen-1-yl)-9,10-dihydroacridine in CDCl$_3$.
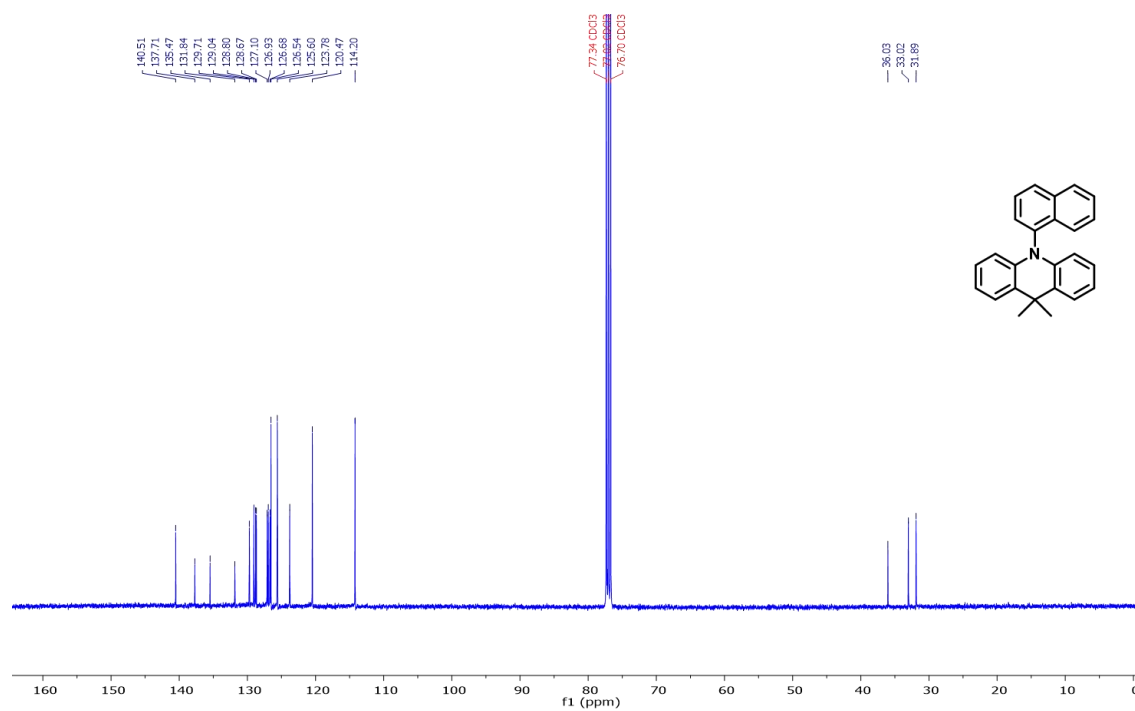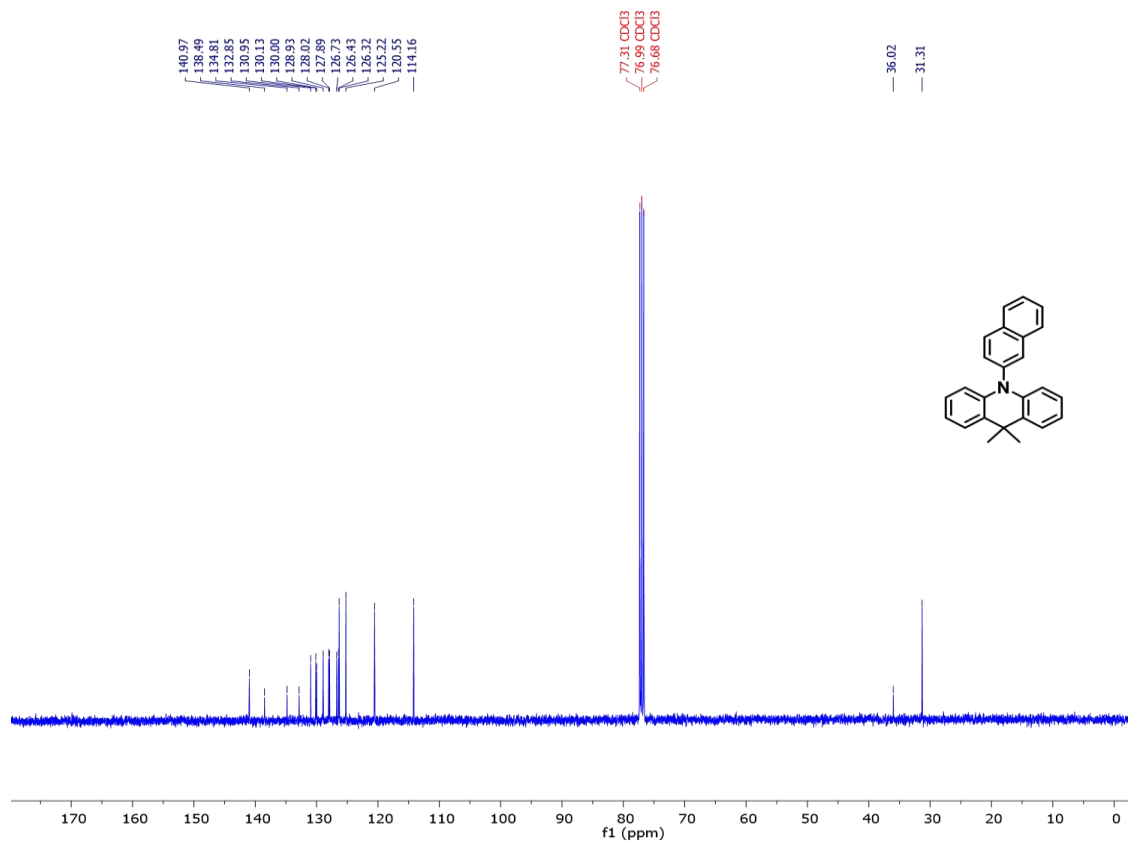

Figure 4.11: ^{13}C NMR spectrum of 9,9-dimethyl-10-(naphthalen-1-yl)-9,10-dihydroacridine in CDCl$_3$.

Synthesis of 2,7-dibromo-9,9-dimethyl-10-(naphthalen-1-yl)-9,10-dihydroacridine
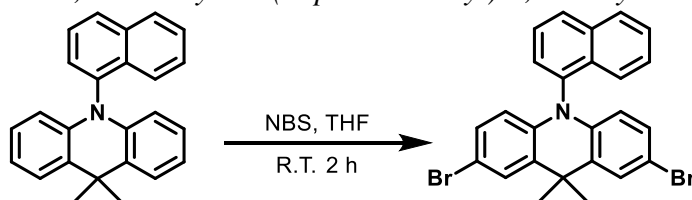
5.0 g of 9,10-dihydro-9,9-dimethyl-10-(1-napthalenyl)-acridine (14.9 mmol, 1.0 eq.) was dissolved in 200 mL THF under ambient atmosphere. 5.83 g of *N*-Bromosuccinimide (32.8 mmol, 2.2 eq.) was slowly added to make a light brown solution. The reaction then stirred for 2 hours. The solution was then concentrated via rotary evaporation, washed with water 3 times, and dried with magnesium sulfate. The product was recrystallized using DCM layered with methanol at -10 ºC overnight. The product was isolated by filtration and dried under vacuum to give a pale brown solid, which was used without further purification. Yield: 6.4 g, 87%. ^{1}H NMR (400 MHz, Chloroform-*d*) δ 8.08 – 7.97 (m, 2H), 7.67 (dd, *J* = 8.3, 7.2 Hz, 1H), 7.59 – 7.50 (m, 4H), 7.47 (dd, *J* = 7.2, 1.2 Hz, 1H), 7.44 – 7.36 (m, 1H), 6.93 (dd, *J* = 8.8, 2.3 Hz, 2H), 5.90 (d, *J* = 8.8 Hz, 2H), 1.82 (s, 3H), 1.69 (s, 3H). ^{13}C NMR (101 MHz, Chloroform-*d*) δ 139.32, 136.71, 135.50, 131.37, 131.18, 129.54, 129.35, 128.88, 128.72, 128.42, 127.44, 126.94, 126.91, 123.24, 116.04, 113.27, 36.35, 32.87, 31.30.
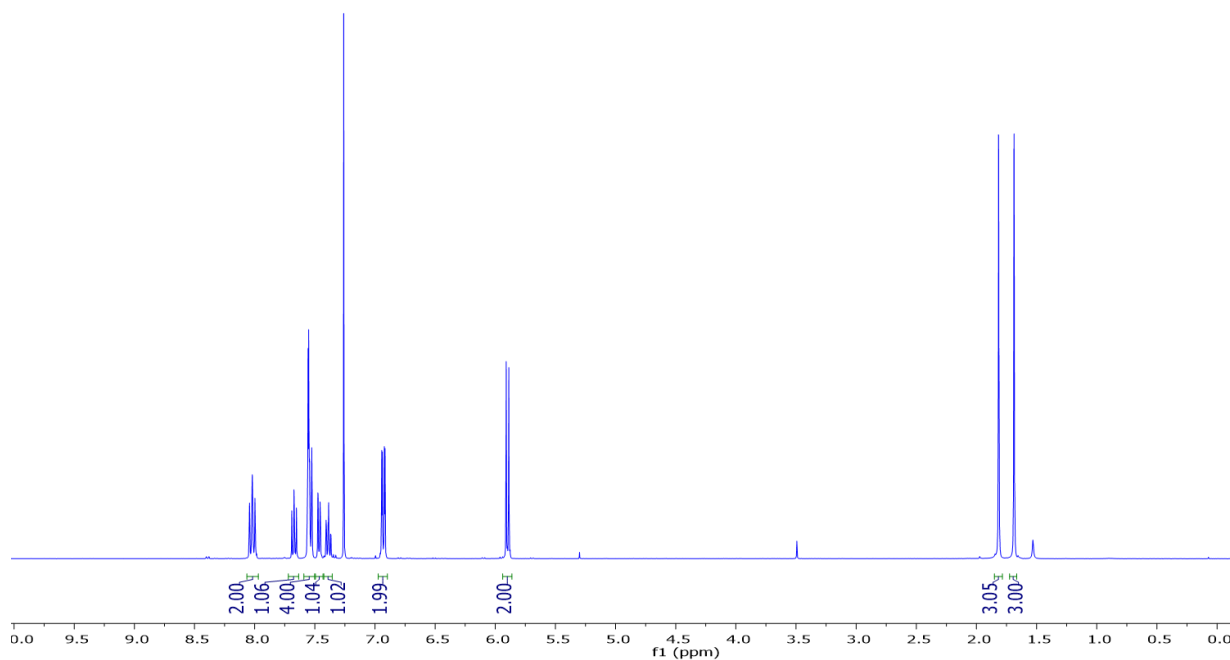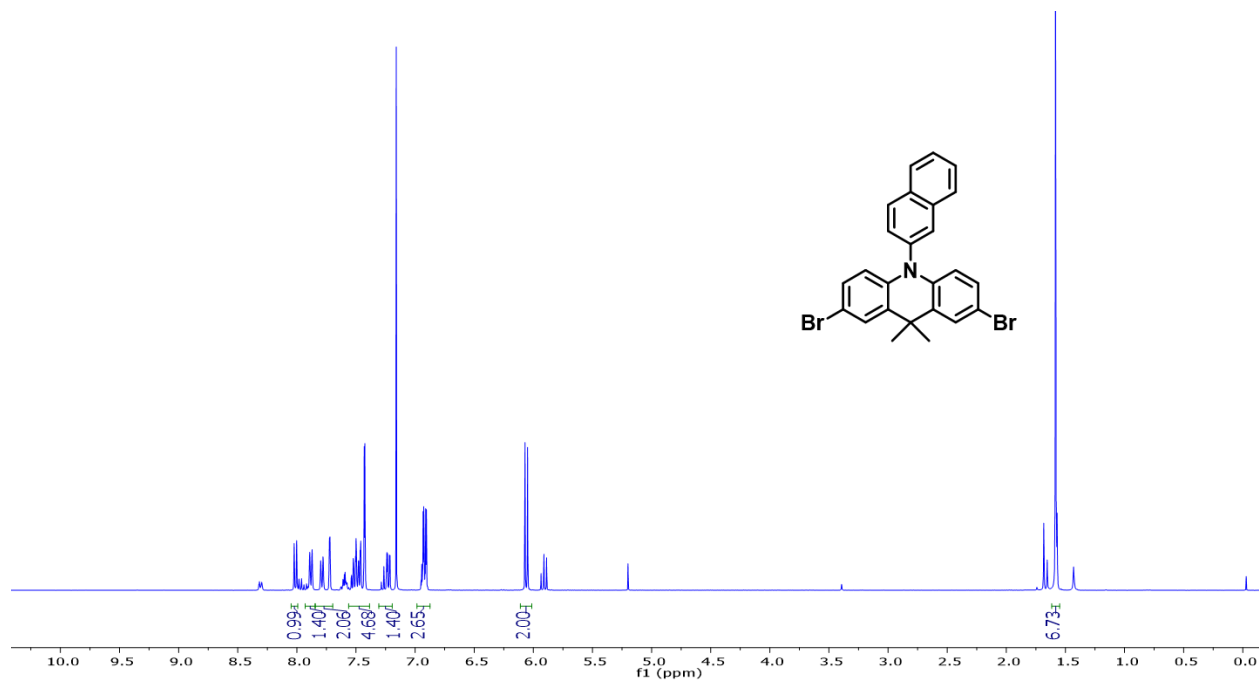
Figure 4.12: ^{1}H NMR spectrum of 2,7-dibromo-9,9-dimethyl-10-(naphthalen-1-yl)-9,10-dihydroacridine in CDCl$_3$.
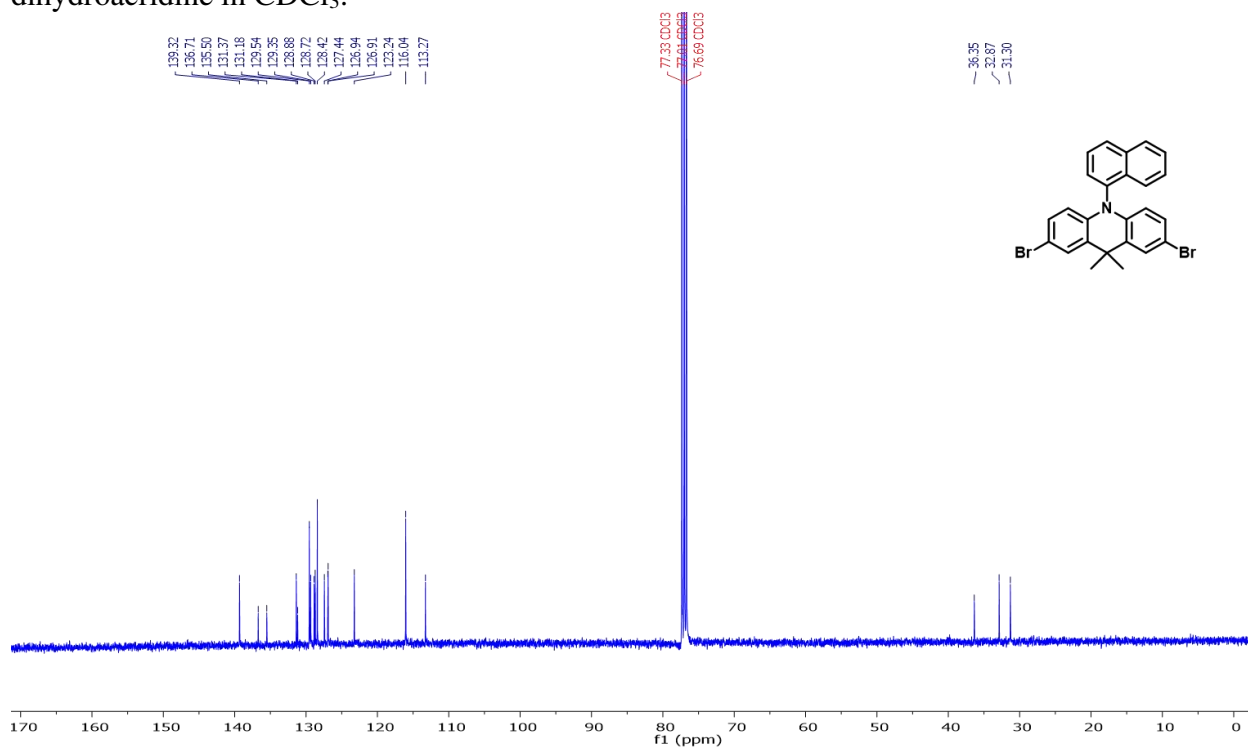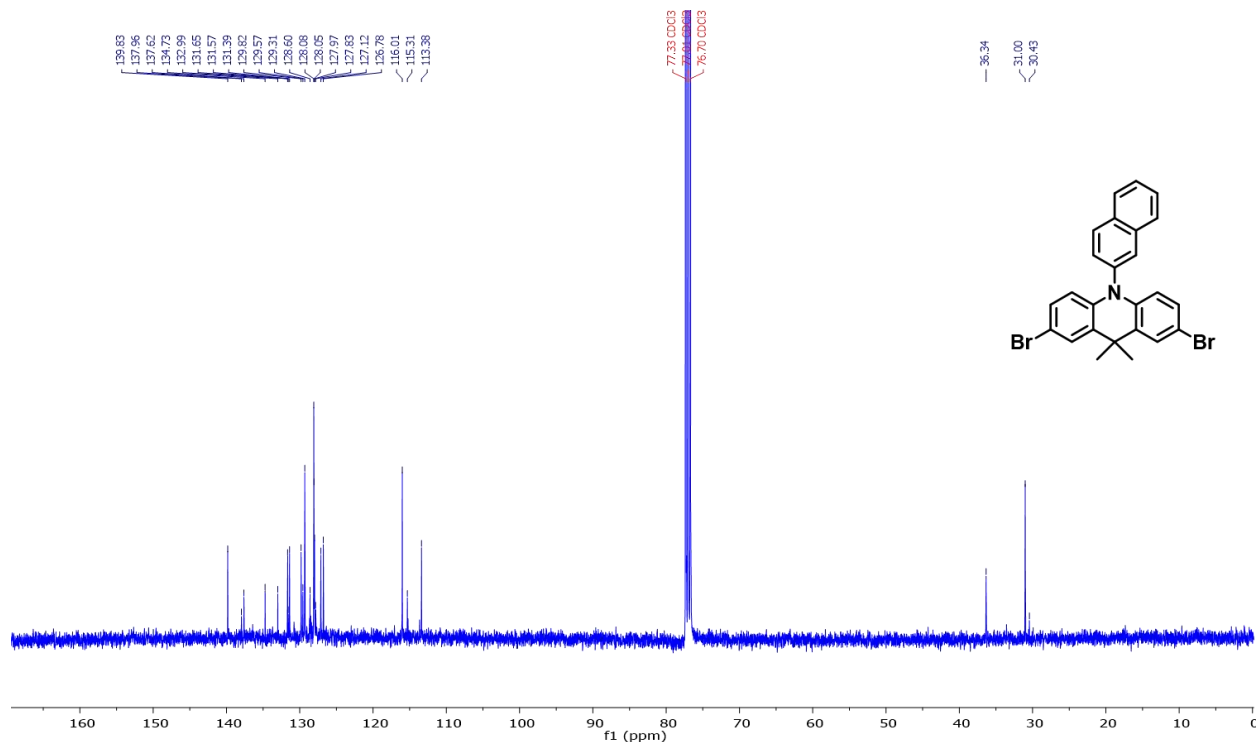

Figure 4.13: ^{13}C NMR spectrum of 2,7-dibromo-9,9-dimethyl-10-(naphthalen-1-yl)-9,10-dihydroacridine in CDCl$_3$.

Synthesis of 2,7-di([1,1'-biphenyl]-4-yl)-9,9-dimethyl-10-(naphthalen-1-yl)-9,10-dihydroacridine
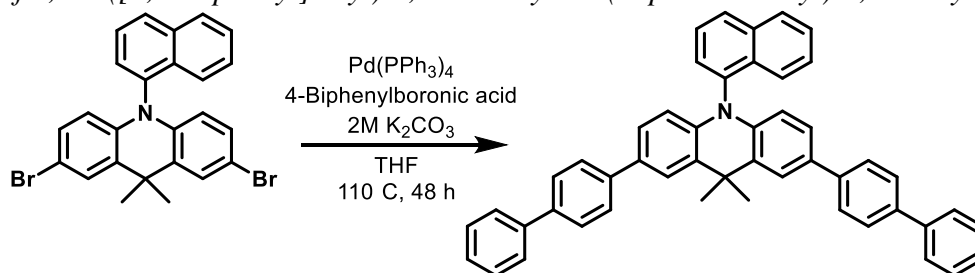
2.0 g 2,7-dibromo-9,10-dihydro-9,9-dimethyl-10-(1-napthalenyl)-acridine (4.1 mmol, 1 eq.) was loaded into a storage tube. 3.2 g 4-Biphenylboronic acid (16.2 mmol, 4 eq.) was added under ambient conditions. The flask was brought into a nitrogen-filled glovebox. Then, 0.468 g Tetrakis(triphenylphosphine)palladium(0) (0.41 mmol, 10 mol %) was added. 60 mL of THF was added to produce a yellow solution. The flask was taken out of the glovebox, where 45 mL of degassed 2M K_2CO_3 was added using a long needle and syringe. The biphasic solution was then sealed and heated to 110 °C for 48 hours. At that time, the solution was cooled to room temperature and concentrated on rotovap to produce a reddish-brown oil. The crude mixture was redissolved in DCM then passed through a silica plug. The yellow filtrate was collected and concentrated, then purified by column chromatography with hexanes: ethyl acetate ramping from 100:0 to 70:30. The product, a white solid, was then recrystallized with DCM/MeOH at -25 °C to give 1.61 g of a fluffy white solid with 62% yield. ^{1}H NMR (400 MHz, Chloroform-*d*) δ 8.12 – 8.01 (m, 2H), 7.82 (d, *J* = 2.1 Hz, 2H), 7.79 – 7.71 (m, 2H), 7.68 – 7.54 (m, 14H), 7.45 (dd, *J* = 8.4, 7.1 Hz, 5H), 7.38 – 7.30 (m, 2H), 7.16 (dd, *J* = 8.5, 2.1 Hz, 2H), 6.16 (d, *J* = 8.5 Hz, 2H), 2.01 (s, 3H), 1.91 (s, 3H). ^{13}C NMR (101 MHz, Chloroform-*d*) δ 140.84, 140.15, 139.85, 139.28, 137.48, 135.52, 132.98, 131.71, 130.09, 129.05, 128.96, 128.79, 127.44, 127.33, 127.18, 126.98, 126.84, 125.31, 124.62, 123.67, 114.80, 36.44, 33.50, 32.48. HRMS (ESI) calculated for (M+H)+ for $C_{49}H_{37}N$, 640,29988; Found, 640.29710.
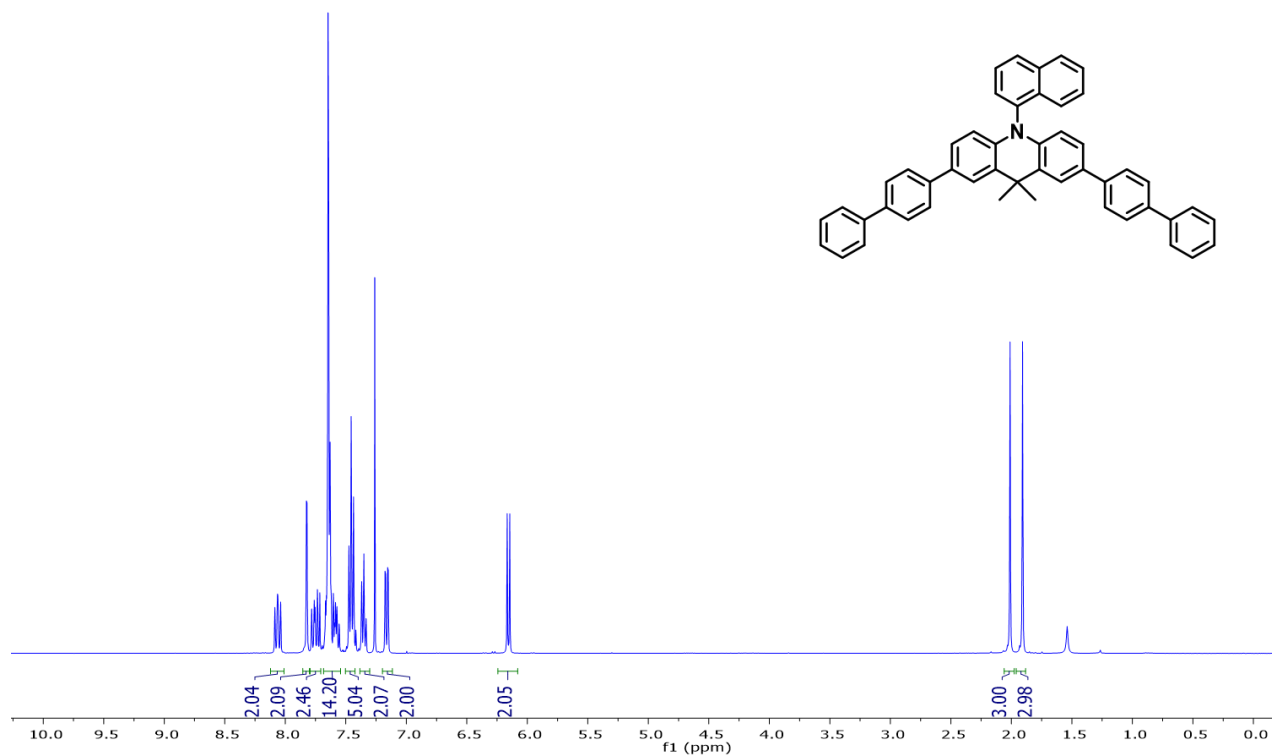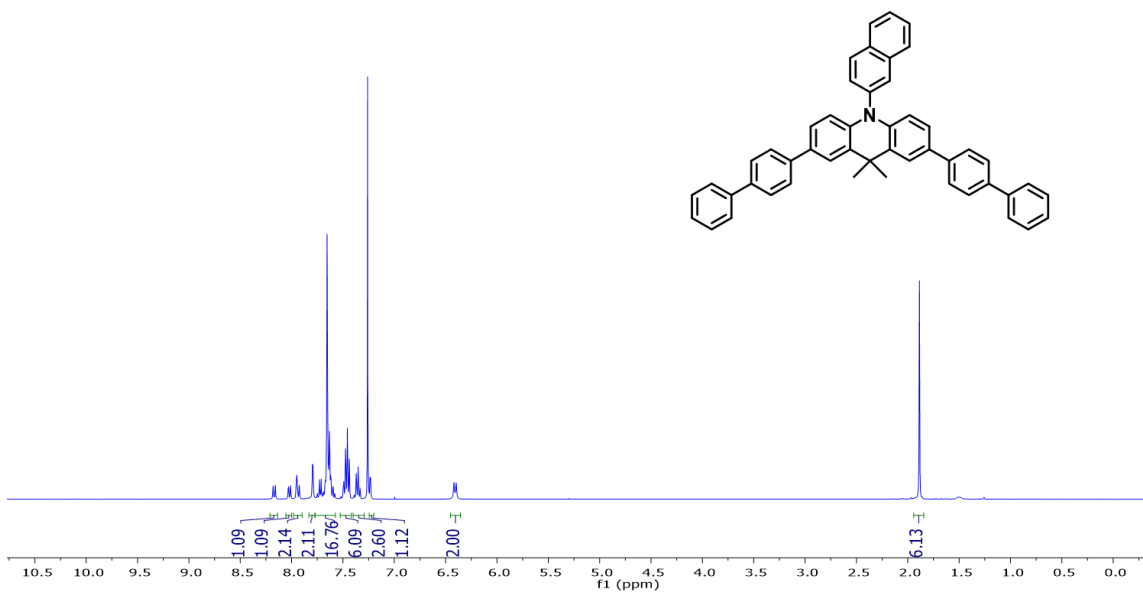
Figure 4.14: ¹H NMR spectrum of 2,7-di([1,1'-biphenyl]-4-yl)-9,9-dimethyl-10-(naphthalen-1-yl)-9,10-dihydroacridine in CDCl₃.
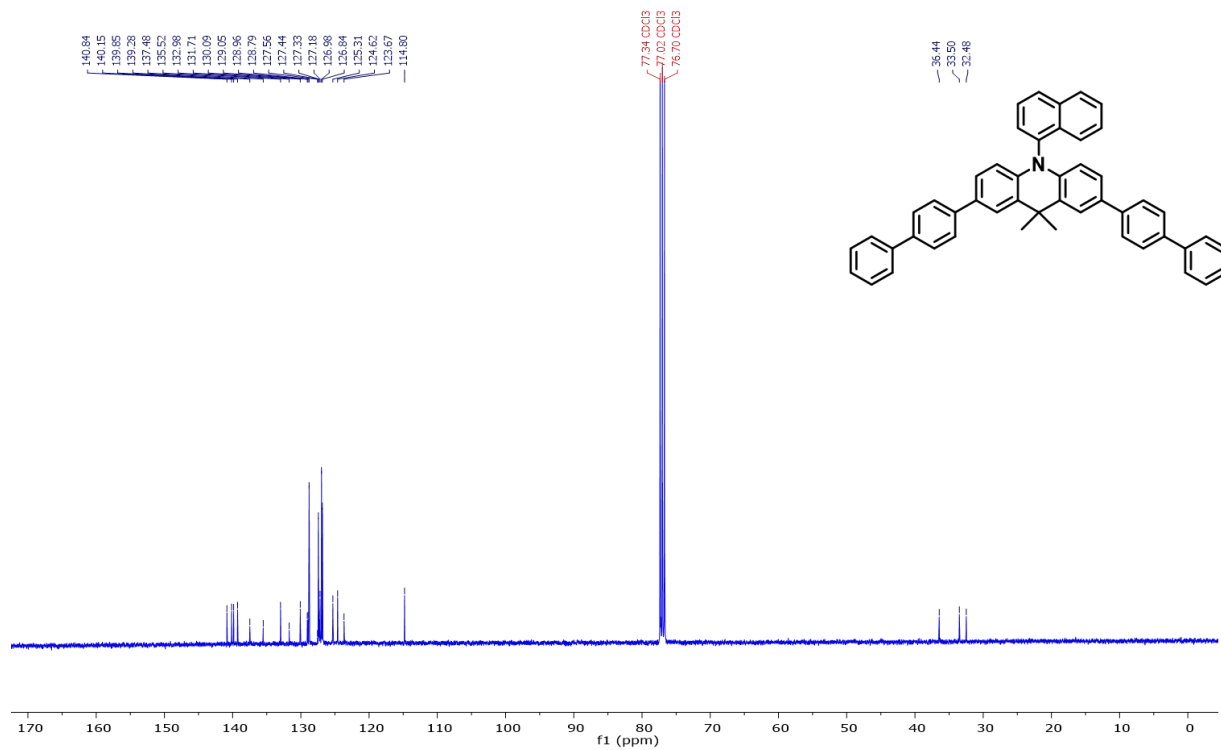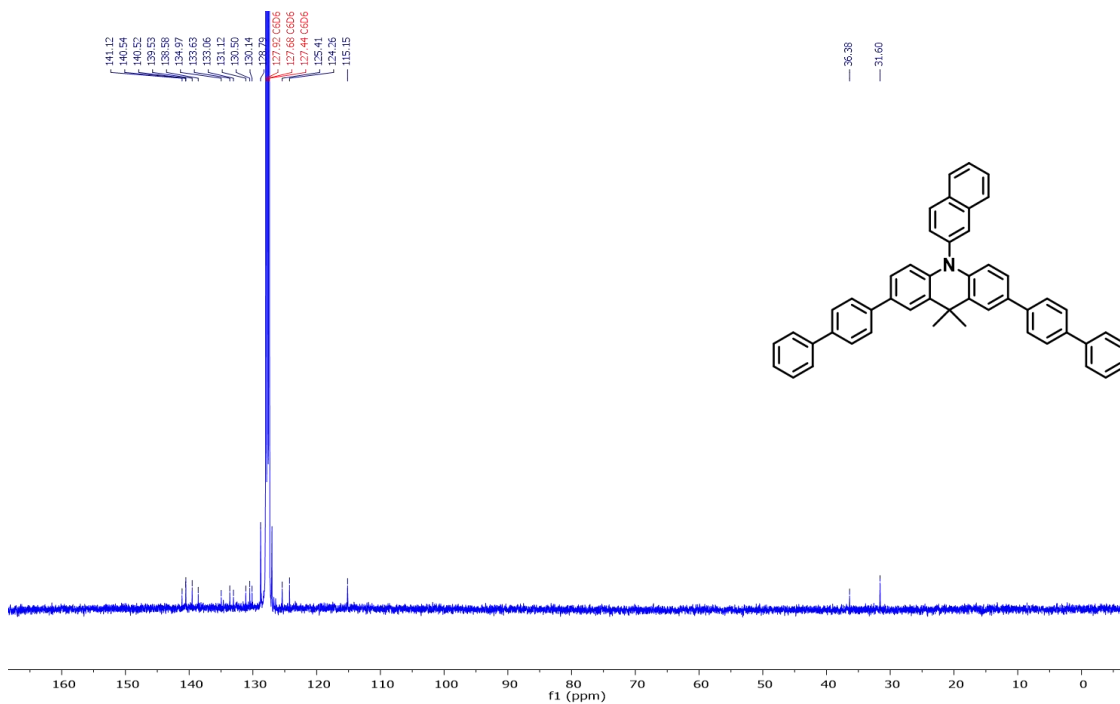

Figure 4.15: ¹³C NMR spectrum of 2,7-di([1,1'-biphenyl]-4-yl)-9,9-dimethyl-10-(naphthalen-1-yl)-9,10-dihydroacridine in CDCl₃.

Synthesis of 2,7-bis(4-methoxyphenyl)-9,9-dimethyl-10-(naphthalen-1-yl)-9,10-dihydroacridine
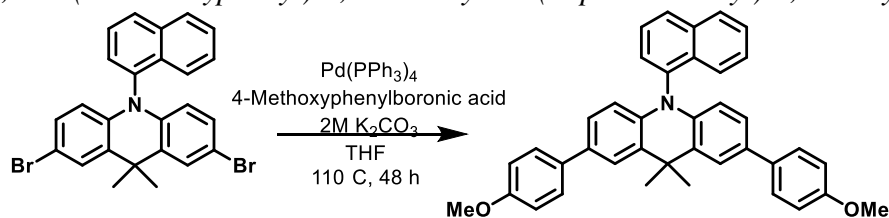
2.5 g 2,7-dibromo-9,10-dihydro-9,9-dimethyl-10-(1-napthalenyl)-acridine (5.1 mmol, 1 eq.) was loaded into a storage tube. 3.1 g 4-Methoxyphenylboronic acid (20.2 mmol, 4 eq.) was added under ambient conditions. The flask was brought into a nitrogen-filled glovebox. Then, 0.586 Tetrakis(triphenylphosphine)palladium(0) (0.51 mmol, 10 mol %) was added. 80 mL of THF was added to produce a yellow solution. The flask was taken out of the glovebox, where 56 mL of degassed 2M K_2CO_3 was added using a long needle and syringe. The biphasic solution was then sealed and heated to 110 ºC for 24 hours. At that time, the solution was cooled to room temperature and concentrated on rotovap to produce a reddish oil. The crude mixture was dissolved in 200 mL ethyl acetate and washed 3 times with water. The organic layer was dried with magnesium sulfate, filtered, and concentrated. The product was isolated by column chromatography using 80:20 hexane:ethyl acetate. TLC indicated decomposition of the product when using DCM on silica coated plates. Then, the product was recrystallized 3 times using ethyl acetate layered with methanol to yield a white solid. Yield: 1.76 g, 63.3% yield. ^{1}H NMR (400 MHz, Benzene-d_6) δ 7.97 – 7.90 (m, 1H), 7.86 (d, J = 2.1 Hz, 2H), 7.72 (dd, J = 8.2, 3.8 Hz, 2H), 7.54 – 7.45 (m, 4H), 7.40 – 7.28 (m, 2H), 7.25 – 7.19 (m, 1H), 7.11 (td, J = 7.6, 6.8, 1.3 Hz, 1H), 7.02 (dd, J = 8.5, 2.1 Hz, 2H), 6.92 – 6.84 (m, 4H), 6.30 (d, J = 8.5 Hz, 2H), 3.36 (s, 6H), 1.91 (s, 3H), 1.81 (s, 3H). HRMS (ESI) calculated for M+ for $C_{39}H_{33}NO_2$, 547.25058; Found, 547.25074.
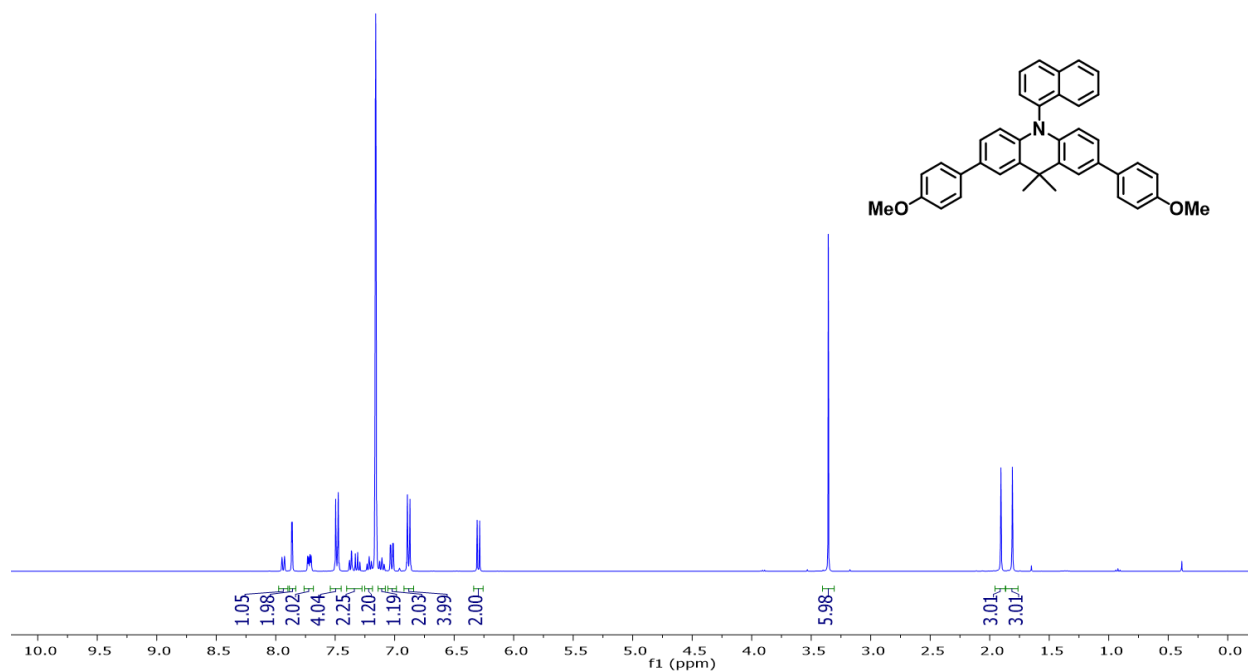
Figure 4.16: ^{1}H NMR spectrum of 2,7-bis(4-methoxyphenyl)-9,9-dimethyl-10-(naphthalen-1-yl)-9,10-dihydroacridine in C_6D_6.
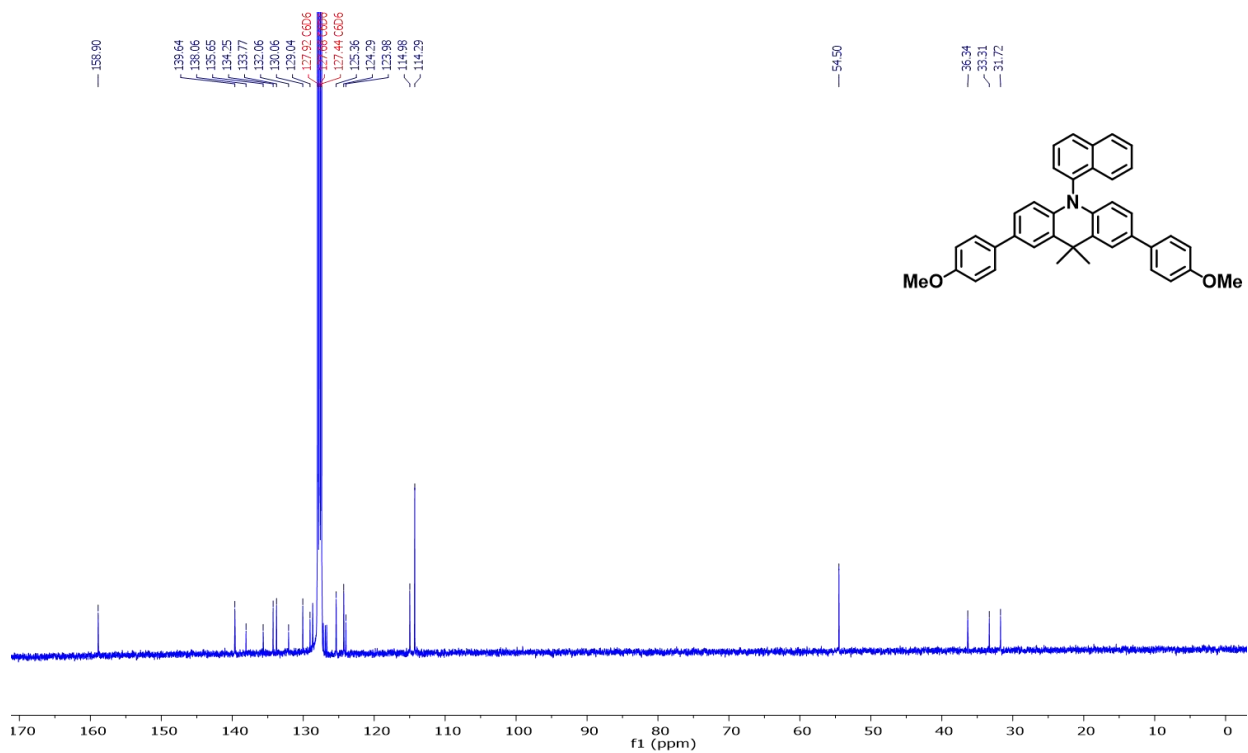
Figure 4.17: ^{13}C NMR spectrum of 2,7-bis(4-methoxyphenyl)-9,9-dimethyl-10-(naphthalen-1-yl)-9,10-dihydroacridine in C_6D_6.

114

Synthesis of 4,4'-(9,9-dimethyl-10-(naphthalen-1-yl)-9,10-dihydroacridine-2,7-diyl)dibenzonitrile
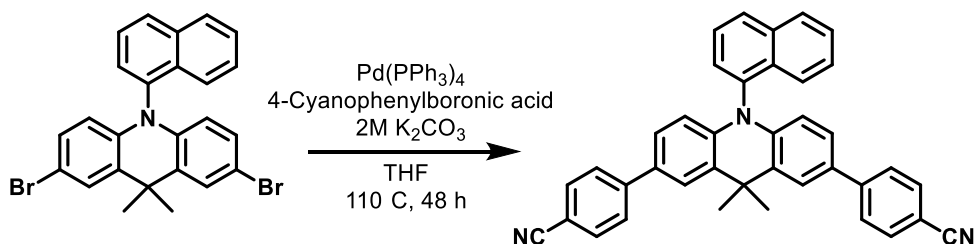
0.3 g of 2,7-dibromo-9,10-dihydro-9,9-dimethyl-10-(1-napthalenyl)-acridine (0.61 mmol, 1 eq.) and 0.36 g of 4-Cyanophenylboronic acid (2.4 mmol, 4 eq.) was loaded into a storage tube under ambient atmosphere. The storage tube was taken into a nitrogen-filled glovebox, then loaded with 0.105 g Tetrakis(triphenylphosphine)palladium(0) (0.09 mmol, 15 mol %). The solids were dissolved in 50 mL THF. The storage tube was sealed and brought out of the glovebox, where 8.0 mL of degassed 2M K_2CO_3 was added using a long needle and syringe to produce a biphasic yellow and colorless solution. The solution was heated to 110 °C for 46 hours, then brought to room temperature. The solution turned reddish-brown upon exposure to air. The solution was concentrated and extracted into DCM, then passed through a silica plug and rinsed with DCM. The yellow filtrate was collected and concentrated to give a pale-yellow solid. Pure product was obtained by recrystallizing with ethyl acetate layered with methanol at -25 °C to give a yield of 0.287 g, 87%. ^{1}H NMR (400 MHz, Chloroform-*d*) δ 8.15 – 8.05 (m, 2H), 7.82 – 7.55 (m, 14H), 7.45 (ddd, *J* = 8.3, 6.9, 1.2 Hz, 1H), 7.15 (dd, *J* = 8.6, 2.2 Hz, 2H), 6.19 (d, *J* = 8.6 Hz, 2H), 2.00 (s, 3H), 1.88 (s, 3H). ^{13}C NMR (101 MHz, C_6D_6) δ 144.75, 140.56, 137.14, 135.62, 132.27, 132.01, 131.50, 130.19, 129.19, 127.92, 127.68, 127.44, 126.49, 125.87, 124.51, 123.38, 118.70, 115.29, 110.40, 36.22, 33.35, 31.36. HRMS (ESI) calculated for M+ for $C_{39}H_{27}N_3$, 536.21267; Found, 536.16531.
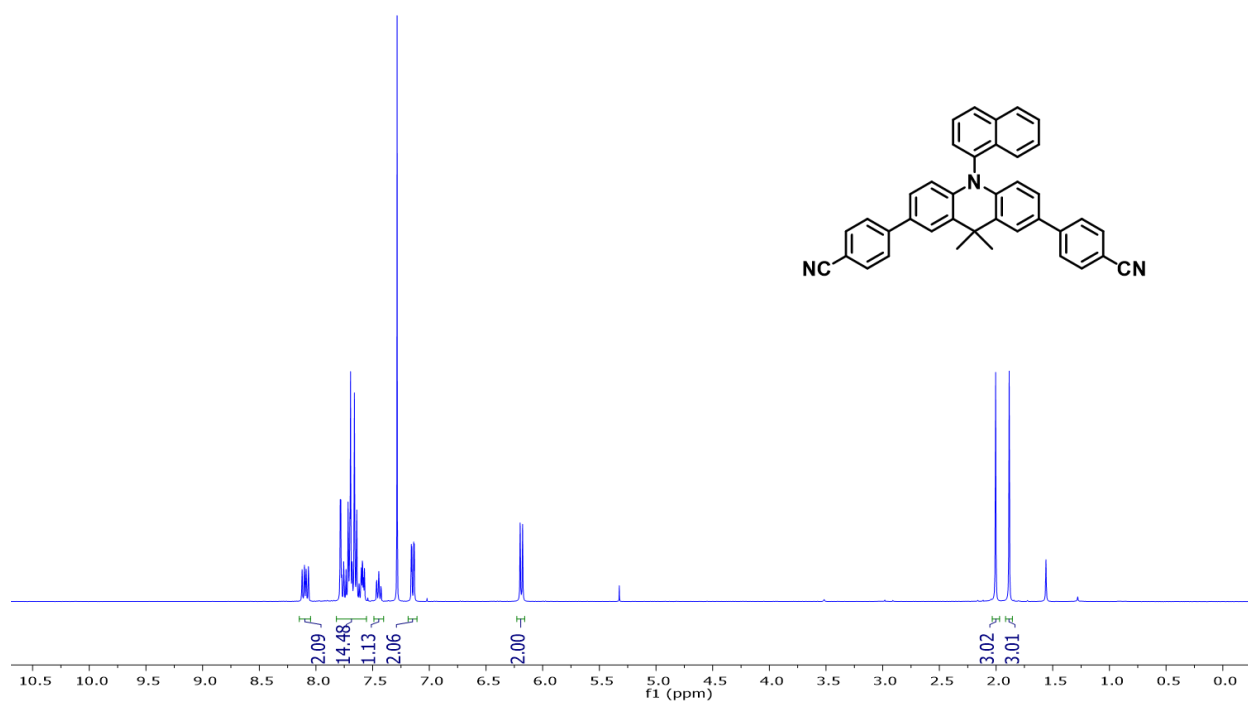
Figure 4.18: ^{1}H NMR spectrum of 4,4'-(9,9-dimethyl-10-(naphthalen-1-yl)-9,10-dihydroacridine-2,7-diyl)dibenzonitrile in CDCl$_3$.
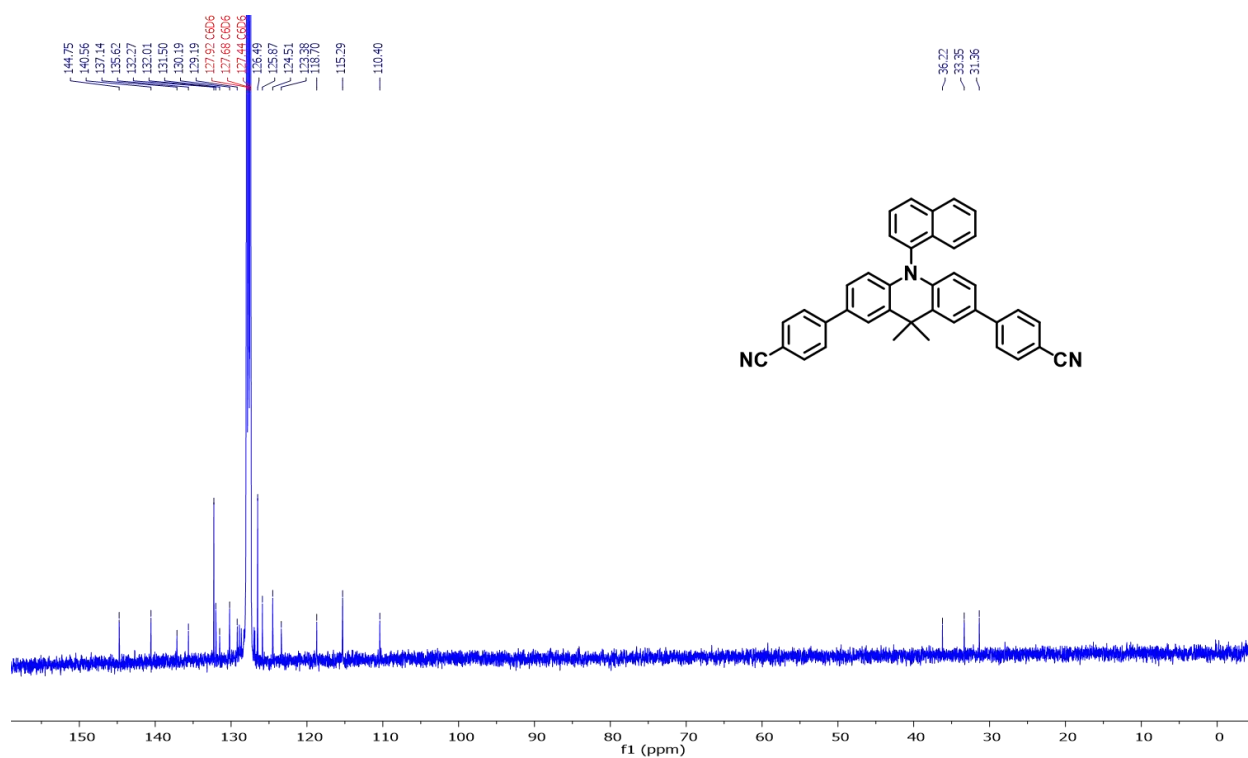
Figure 4.19: ^{13}C NMR spectrum of 4,4'-(9,9-dimethyl-10-(naphthalen-1-yl)-9,10-dihydroacridine-2,7-diyl)dibenzonitrile in C$_6$D$_6$.

Synthesis of 9,9-dimethyl-10-(naphthalen-2-yl)-9,10-dihydroacridine
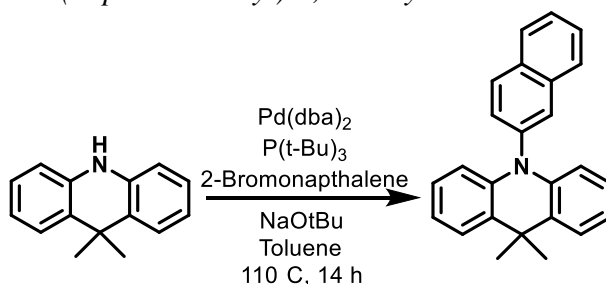
A storage tube was loaded with 1.0 g (4.8 mmol, 1 eq.) 9,10-Dihydro-9,9-dimethylacridine, 1.48 g 2-bromonaphthalene (7.1 mmol, 1.5 eq.), 27.5 mg of Bis(dibenzylideneacetone)palladium(0) (0.48 µmol, 1 mol%), 134 µL of 1M in toluene Tri-*tert*-butylphosphine (0.134 mmol, 3 mol %), 1.4 g sodium *tert*-butoxide (14.4 mmol, 3 eq.), and 50 mL toluene under nitrogen atmosphere. The solution was heated to 110 °C. After 14 hours, the reddish-purple liquid with a white precipitate was passed directly through a silica plug and rinsed with toluene. All blue fluorescent portions were collected and concentrated via rotary evaporation. The product was recrystallized 3 times with DCM/methanol at -25 °C. The product was collected via vacuum filtration, washed with methanol, and dried overnight under vacuum to yield 1.16 g (72.6% yield). ^{1}H NMR (400 MHz, Chloroform-*d*) δ 8.14 (d, *J* = 8.6 Hz, 1H), 8.04 – 7.98 (m, 1H), 7.91 (dt, *J* = 4.7, 1.8 Hz, 2H), 7.60 (dqd, *J* = 8.3, 6.9, 1.5 Hz, 2H), 7.55 – 7.48 (m, 2H), 7.44 (dd, *J* = 8.6, 2.0 Hz, 1H), 7.03 – 6.90 (m, 4H), 6.39 – 6.27 (m, 2H), 1.77 (s, 6H). ^{13}C NMR (101 MHz, Chloroform-*d*) δ 140.97, 138.49, 134.81, 132.85, 130.95, 130.13, 130.00, 128.93, 128.02, 127.89, 126.73, 126.43, 126.32, 125.22, 120.55, 114.16, 36.02, 31.31. HRMS (ESI) calculated for M+ for $C_{25}H_{21}N$, 336.17468; Found, 336.1755.

Figure 4.20: ¹H NMR spectrum of 9,9-dimethyl-10-(naphthalen-2-yl)-9,10-dihydroacridine in CDCl₃.

Figure 4.21: ¹³C NMR spectrum of 9,9-dimethyl-10-(naphthalen-2-yl)-9,10-dihydroacridine in CDCl₃.

Synthesis of 2,7-dibromo-9,9-dimethyl-10-(naphthalen-2-yl)-9,10-dihydroacridine
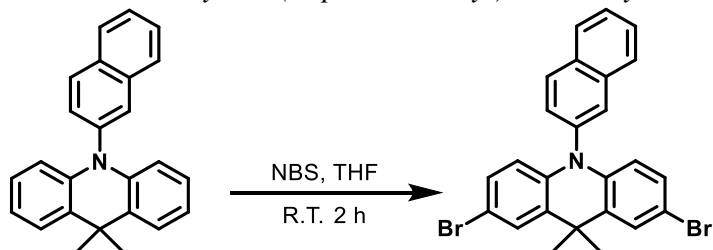
0.75 g of 9,10-dihydro-9,9-dimethyl-10-(2-napthalenyl)-acridine (2.2 mmol, 1.0 eq.) was dissolved in 20 mL THF under ambient atmosphere. 0.90 g of *N*-Bromosuccinimide (5.0 mmol, 2.25 eq.) was slowly added to make a light brown solution. The reaction then stirred at room temperature for 2 hours. The solution was then concentrated via rotary evaporation, washed with water 3 times, and dried with magnesium sulfate. The product was recrystallized using DCM layered with methanol at -25 ºC overnight. The product was isolated by filtration and dried under vacuum to give a pale brown crystalline solid. ^{1}H NMR revealed a mix of products, which was carried over to the next step without further purification. Yield: 0.95 g, 86%. ^{1}H NMR (400 MHz, Chloroform-*d*) δ 8.01 (d, *J* = 8.6 Hz, 1H), 7.93 – 7.84 (m, 1H), 7.84 – 7.70 (m, 2H), 7.56 – 7.39 (m, 5H), 7.31 – 7.19 (m, 1H), 6.92 (ddd, *J* = 8.8, 4.4, 2.3 Hz, 3H), 6.06 (d, *J* = 8.8 Hz, 2H), 1.58 (s, 7H). ^{13}C NMR (101 MHz, CDCl$_3$) δ 139.83, 137.96, 137.62, 134.73, 132.99, 131.65, 131.57, 131.39, 129.82, 129.57, 129.31, 128.60, 128.08, 128.05, 127.97, 127.83, 127.12, 126.78, 116.01, 115.31, 113.38, 77.33, 77.01, 76.70, 36.34, 31.00, 30.43.

Figure 4.22: ^1H NMR spectrum 2,7-dibromo-9,9-dimethyl-10-(naphthalen-2-yl)-9,10-dihydroacridinein C_6D_6.

Figure 4.23: ^{13}C NMR spectrum 2,7-dibromo-9,9-dimethyl-10-(naphthalen-2-yl)-9,10-dihydroacridinein $CDCl_3$.

Synthesis of 2,7-di([1,1'-biphenyl]-4-yl)-9,9-dimethyl-10-(naphthalen-2-yl)-9,10-dihydroacridine
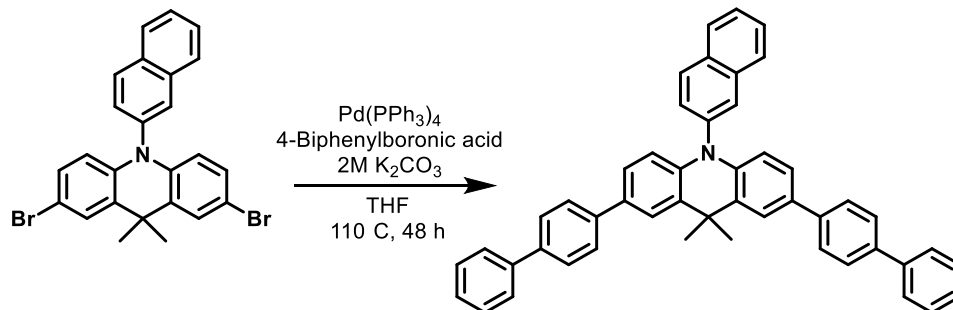
0.8 g of 2,7-dibromo-9,10-dihydro-9,9-dimethyl-10-(2-napthalenyl)-acridine (1.6 mmol, 1 eq.) and 1.28 g of 4-Biphenylboronic acid (6.5 mmol, 4 eq.) was loaded into a storage tube under ambient atmosphere. The storage tube was taken into a nitrogen-filled glovebox, then loaded with 0.281 g Tetrakis(triphenylphosphine)palladium(0) (0.243 mmol, 15 mol %). The solids were dissolved in 50 mL THF. The storage tube was sealed and brought out of the glovebox, where 18 mL of degassed 2M K_2CO_3 (22 eq.) was added using a long needle and syringe to produce a biphasic yellow and colorless solution. The solution was heated to 110 ℃ for 48 hours, then brought to room temperature. The solution turned reddish-brown upon exposure to air. The solution was concentrated and extracted into DCM, then dried using magnesium sulfate, filtered, and concentrated. The crude mixture was redissolved in DCM then passed through a silica plug. The yellow filtrate was collected and concentrated, then recrystallized with DCM/MeOH at -25 ℃ to give a white crystalline solid with a yield of 59.4%. ^{1}H NMR (400 MHz, Chloroform-*d*) δ 8.17 (d, *J* = 8.6 Hz, 1H), 8.06 – 8.00 (m, 1H), 7.98 – 7.90 (m, 2H), 7.79 (d, *J* = 2.1 Hz, 2H), 7.77 – 7.57 (m, 17H), 7.46 (td, *J* = 8.2, 6.4 Hz, 6H), 7.40 – 7.29 (m, 3H), 7.23 (d, *J* = 2.1 Hz, 1H), 6.41 (d, *J* = 8.5 Hz, 2H), 1.89 (s, 6H). ^{13}C NMR (101 MHz, C_6D_6) δ 141.12, 140.54, 140.52, 139.53, 138.58, 134.97, 133.63, 133.06, 131.12, 130.50, 130.14, 128.79, 127.92, 127.68, 127.44, 125.41, 124.26, 115.15, 36.38, 31.60. HRMS (ESI) calculated for (M+H)+ for $C_{49}H_{37}N$, 640,29988; Found, 640.2991.

Figure 4.24: ^{1}H NMR spectrum of 2,7-di([1,1'-biphenyl]-4-yl)-9,9-dimethyl-10-(naphthalen-2-yl)-9,10-dihydroacridine in CDCl$_3$.

Figure 4.25: ^{1}H NMR spectrum of 2,7-di([1,1'-biphenyl]-4-yl)-9,9-dimethyl-10-(naphthalen-2-yl)-9,10-dihydroacridine in C$_6$D$_6$.

Synthesis of 9,9-dimethyl-10-phenyl-9,10-dihydroacridine
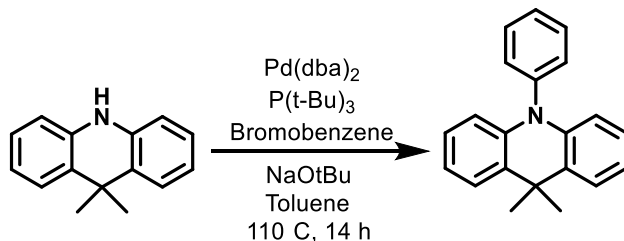
A storage tube was loaded with 1.0 g (4.8 mmol, 1 eq.) 9,10-Dihydro-9,9-dimethylacridine, 1.48 g bromobenzene (7.2 mmol, 1.5 eq.), 27.5 mg of Bis(dibenzylideneacetone)palladium(0) (0.48 µmol, 1 mol%), 143 µL of 1M in toluene Tri-*tert*-butylphosphine (0.134 mmol, 3 mol %), 1.4 g sodium *tert*-butoxide (14.4 mmol, 3 eq.), and 27 mL toluene under nitrogen atmosphere. The solution was heated to 110 ℃. After 14 hours, the reddish liquid with a white precipitate was passed directly through a silica plug and rinsed with toluene. All blue fluorescent portions were collected and concentrated via rotary evaporation. The product was recrystallized with ethyl acetate/methanol at -25 ℃ for 4 hours. The product was collected via vacuum filtration, washed with methanol, and dried overnight under vacuum to yield 1.0 g (73.5% yield) of a white crystalline solid. ^{1}H NMR (400 MHz, Chloroform-*d*) δ 7.67 – 7.59 (m, 2H), 7.54 – 7.47 (m, 1H), 7.46 (dd, *J* = 7.5, 1.8 Hz, 2H), 7.37 – 7.30 (m, 2H), 7.01 – 6.87 (m, 4H), 6.26 (dd, *J* = 7.9, 1.5 Hz, 2H), 1.70 (s, 6H). ^{13}C NMR (101 MHz, Chloroform-*d*) δ 141.20, 140.93, 131.32, 130.83, 129.95, 128.19, 126.32, 125.17, 120.48, 114.01, 35.98, 31.24. HRMS (ESI) calculated for (M+H)+ for $C_{21}H_{19}N$, 285.15175; Found, 285.1514.
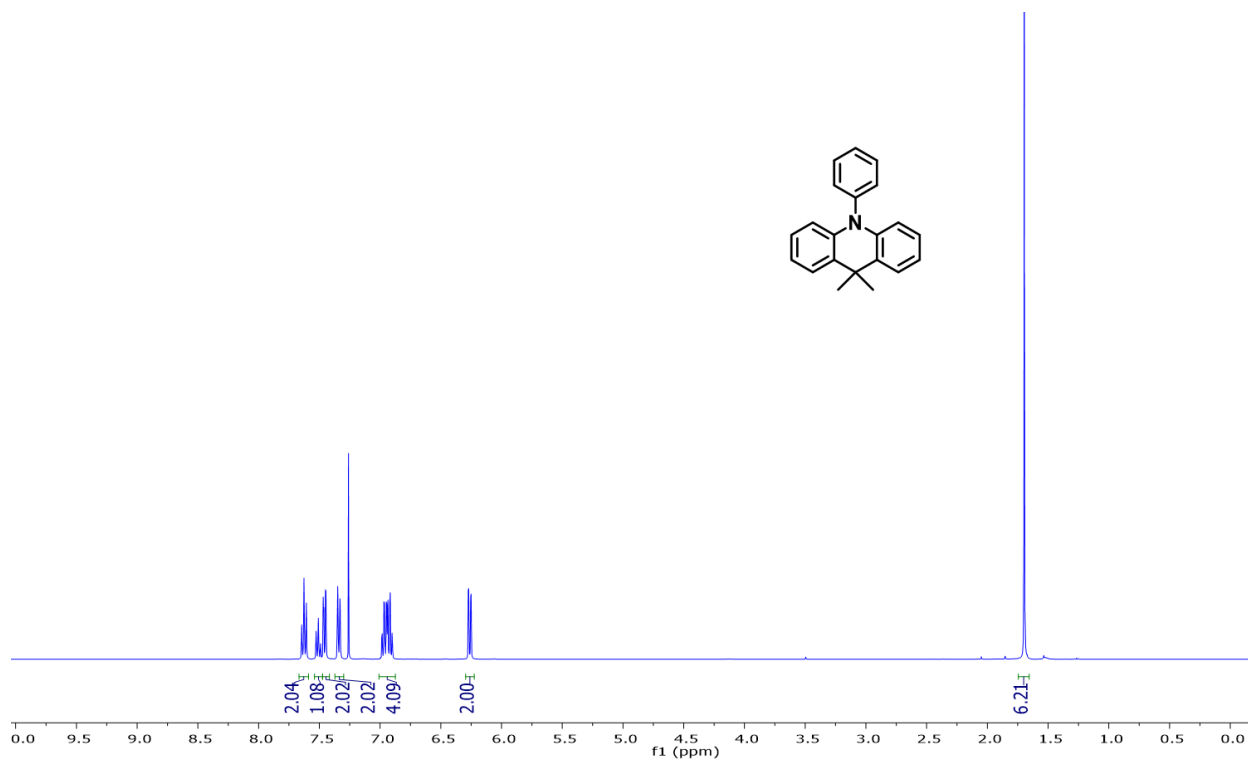
Figure 4.26: ^{1}H NMR spectrum of 9,9-dimethyl-10-phenyl-9,10-dihydroacridine in CDCl$_3$.
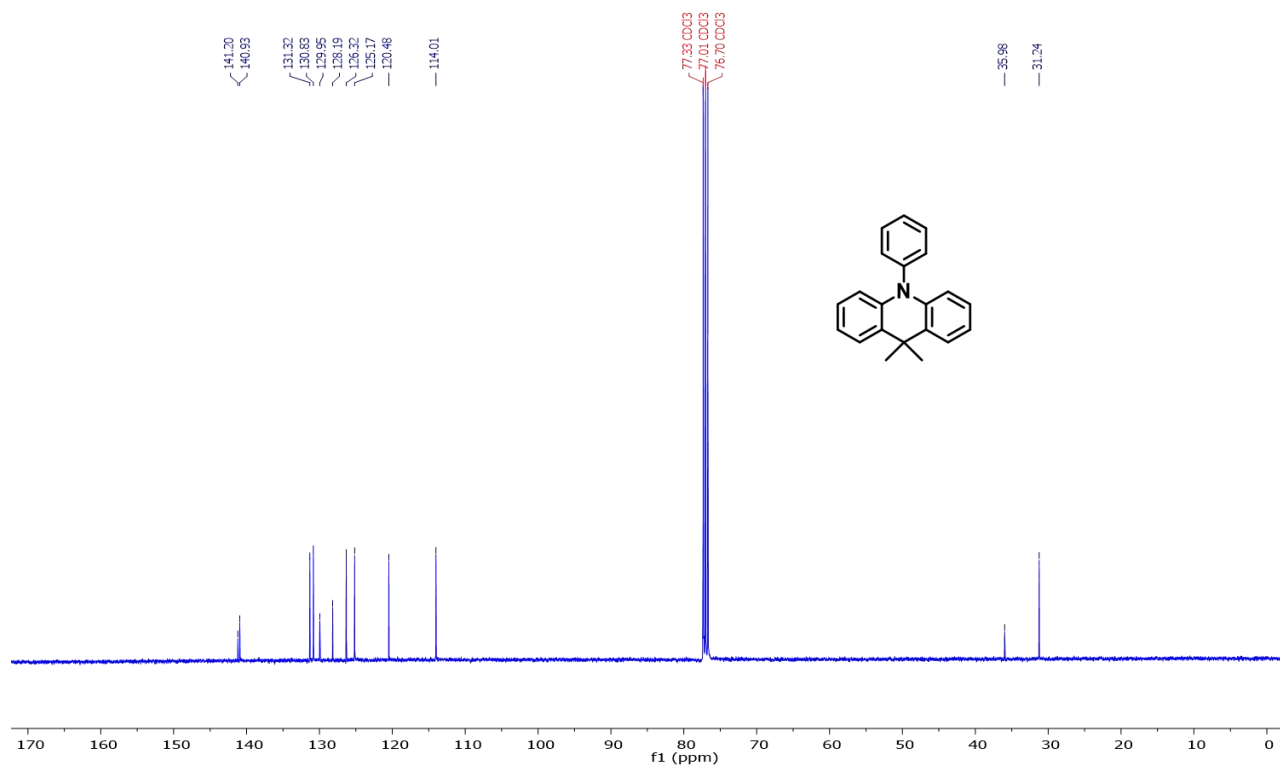
Figure 4.27: ^{13}C NMR spectrum of 9,9-dimethyl-10-phenyl-9,10-dihydroacridine in CDCl$_3$.

Synthesis of 2,7-dibromo-9,9-dimethyl-10-phenyl-9,10-dihydroacridine
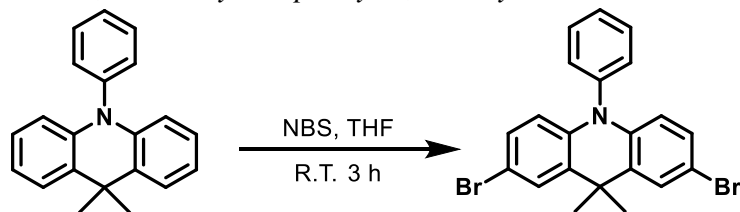
0.75 g of 9,10-dihydro-9,9-dimethyl-10-(phenyl)-acridine (2.2 mmol, 1.0 eq.) was dissolved in 50 mL THF under ambient atmosphere. 1.16 g of *N*-Bromosuccinimide (5.0 mmol, 2.5 eq.) was slowly added to make a light brown solution. The reaction then stirred at room temperature for 3 hours. The solution was then concentrated via rotary evaporation, washed with water 3 times, and dried with magnesium sulfate. The product was recrystallized using DCM layered with methanol at -25 ℃ overnight. The product was isolated by filtration and dried under vacuum to give a white solid. ^{1}H NMR analysis revealed a mix of brominated substitutions, which was carried over to the next step without further purification. Yield: 0.78 g, 67%. ^{1}H NMR (400 MHz, Chloroform-*d*) δ 7.71 – 7.63 (m, 1H), 7.59 – 7.48 (m, 1H), 7.48 – 7.37 (m, 2H), 7.22 – 7.17 (m, 1H), 7.12 – 7.04 (m, 1H), 6.96 (ddd, *J* = 8.9, 7.9, 2.3 Hz, 2H), 6.02 (dd, *J* = 8.8, 3.0 Hz, 2H), 1.54 (d, *J* = 4.5 Hz, 6H). ^{13}C NMR (101 MHz, CDCl$_3$) δ 140.39, 139.76, 139.45, 139.42, 134.52, 132.70, 131.73, 131.60, 131.12, 130.81, 129.39, 129.29, 128.72, 128.19, 128.02, 122.71, 115.85, 115.70, 113.64, 113.29, 77.33, 77.01, 76.70, 36.28, 30.93.
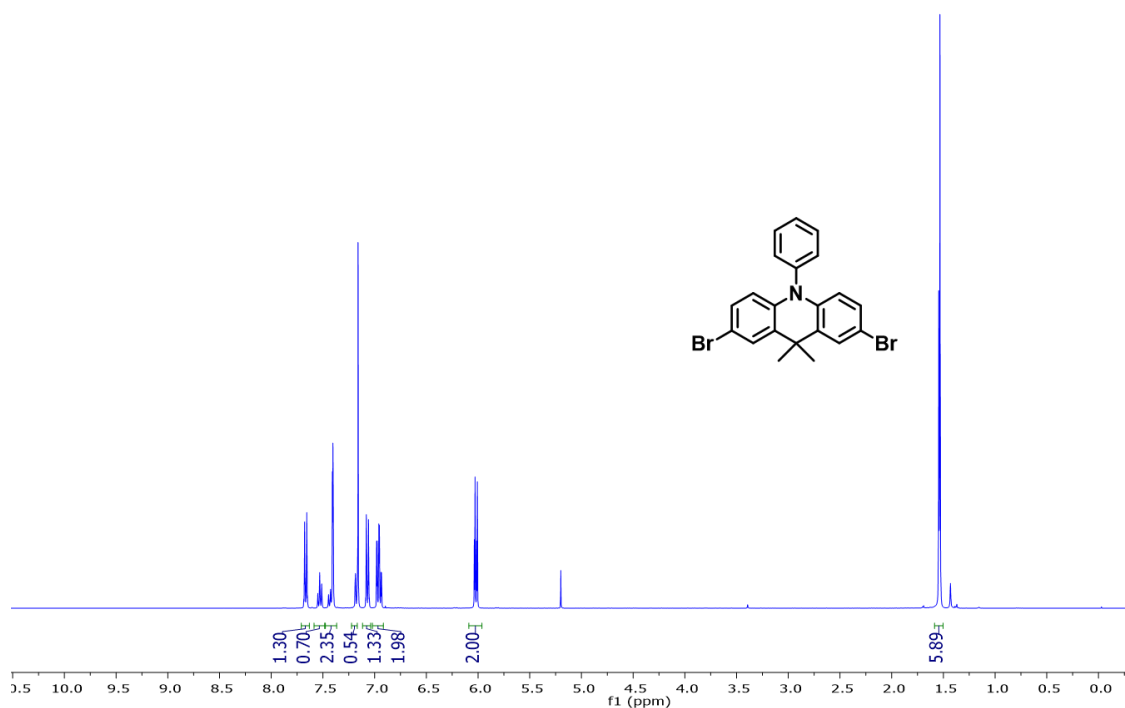
Figure 4.28: ^{1}H NMR spectrum of 2,7-dibromo-9,9-dimethyl-10-phenyl-9,10-dihydroacridine in CDCl$_3$.
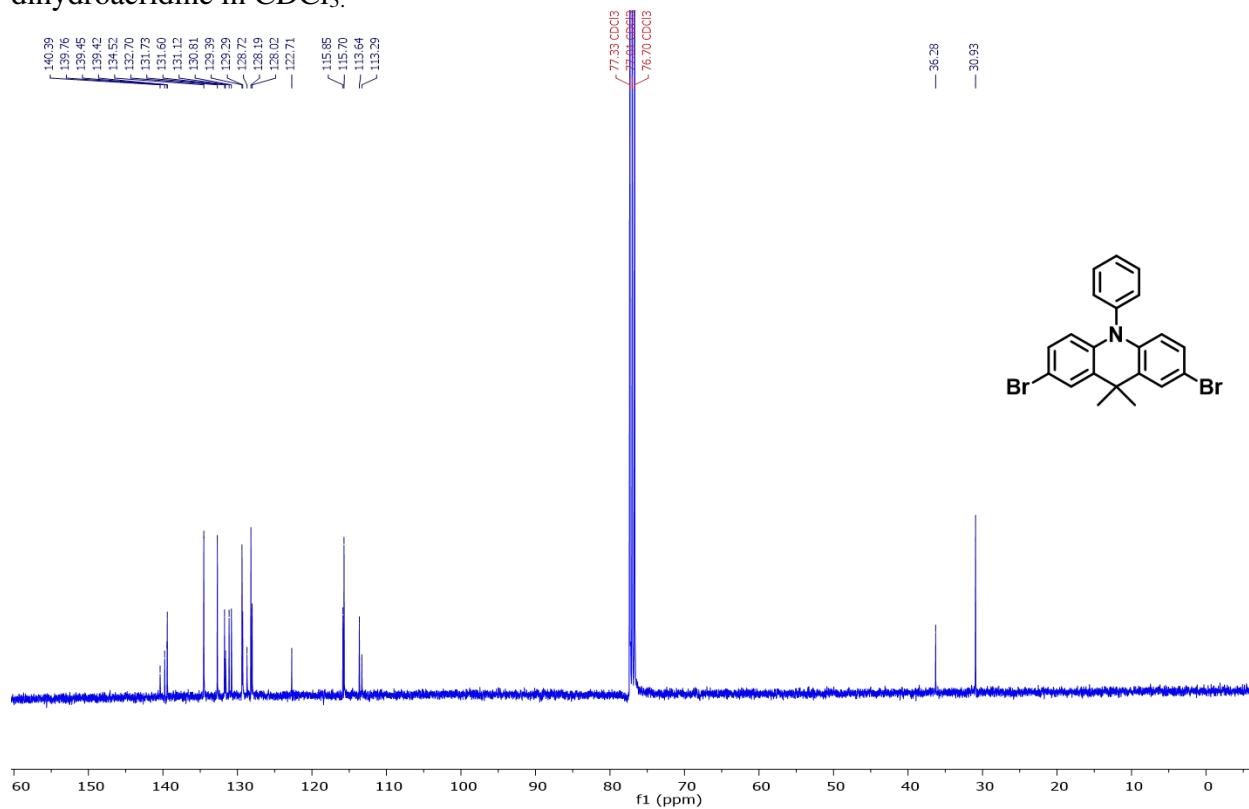
Figure 4.29: ^{13}C NMR spectrum of 2,7-dibromo-9,9-dimethyl-10-phenyl-9,10-dihydroacridine in CDCl$_3$.

Synthesis of 2,7-di([1,1'-biphenyl]-4-yl)-9,9-dimethyl-10-phenyl-9,10-dihydroacridine
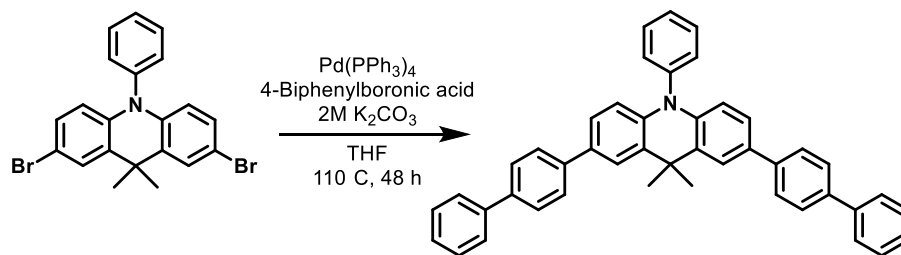
0.5 g of 2,7-dibromo-9,10-dihydro-9,9-dimethyl-10-(phenyl)-acridine (1.1 mmol, 1 eq.) and 0.89 g of 4-Biphenylboronic acid (4.5 mmol, 4 eq.) was loaded into a storage tube under ambient atmosphere. The storage tube was taken into a nitrogen-filled glovebox, then loaded with 0.194 g Tetrakis(triphenylphosphine)palladium(0) (0.168 mmol, 15 mol %). The solids were dissolved in 20 mL THF. The storage tube was sealed and brought out of the glovebox, where 12 mL of degassed 2M K_2CO_3 (22 eq.) was added using a long needle and syringe to produce a biphasic yellow and colorless solution. The solution was heated to 110 °C for 48 hours, then brought to room temperature. The solution turned reddish-brown upon exposure to air. The solution was concentrated and extracted into DCM, then dried using magnesium sulfate, filtered, and concentrated. The crude mixture was redissolved in DCM then passed through a silica plug. The yellow filtrate was collected and concentrated, then purified by column chromatography with hexanes: ethyl acetate ramping from 100:0 to 70:30. The product, a white solid, was then recrystallized with Ethyl acetate/MeOH at -25 °C to give 0.665 g of a white crystalline solid with a yield of 62%. ^{1}H NMR (400 MHz, Benzene-d_6) δ 7.94 (d, J = 2.1 Hz, 2H), 7.74 – 7.54 (m, 19H), 7.40 – 7.25 (m, 10H), 6.68 (d, J = 8.5 Hz, 2H), 1.83 (s, 6H). ^{13}C NMR (101 MHz, CDCl$_3$) δ 141.01, 140.86, 140.21, 139.33, 133.12, 133.03, 131.52, 131.16, 131.00, 130.36, 130.27, 129.52, 128.89, 128.83, 128.80, 128.46, 127.69, 127.59, 127.56, 127.49, 127.47, 127.38, 127.19, 127.08, 127.05, 126.99, 126.90, 126.89, 125.09, 124.23, 114.61, 77.34, 77.02, 76.70, 36.38, 31.85. HRMS (ESI) calculated for (M+H)+ for C$_{45}$H$_{35}$N, 589.27694; Found, 589.2764.
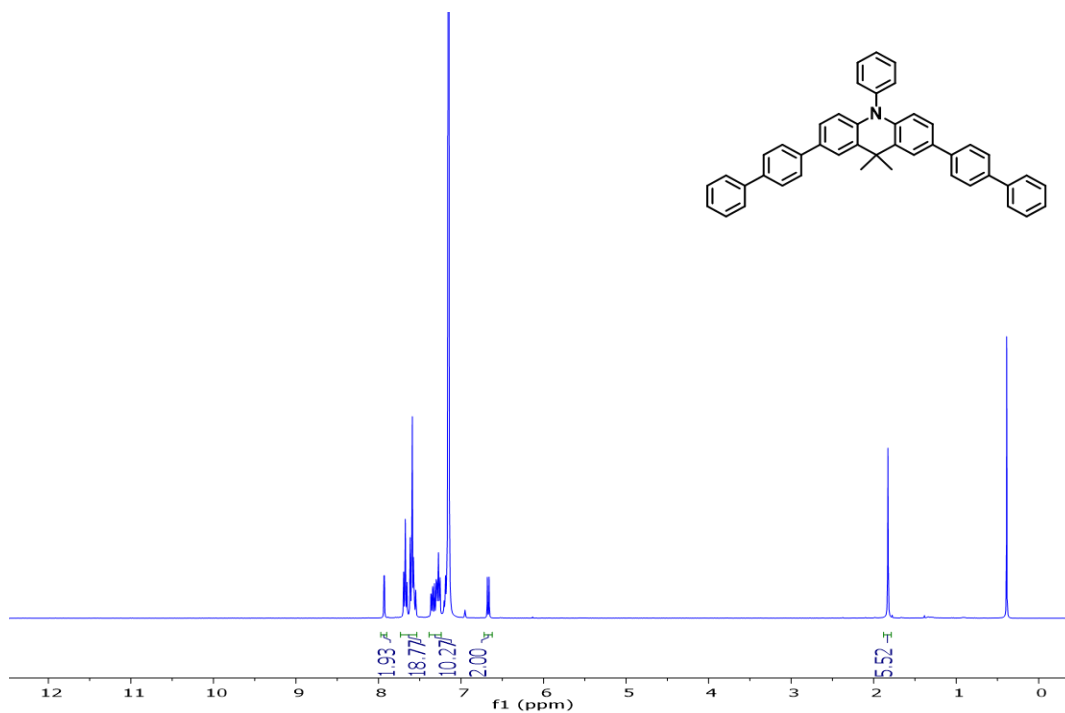
Figure 4.30: ^{1}H NMR spectrum of 2,7-di([1,1'-biphenyl]-4-yl)-9,9-dimethyl-10-phenyl-9,10-dihydroacridine in C$_6$D$_6$.
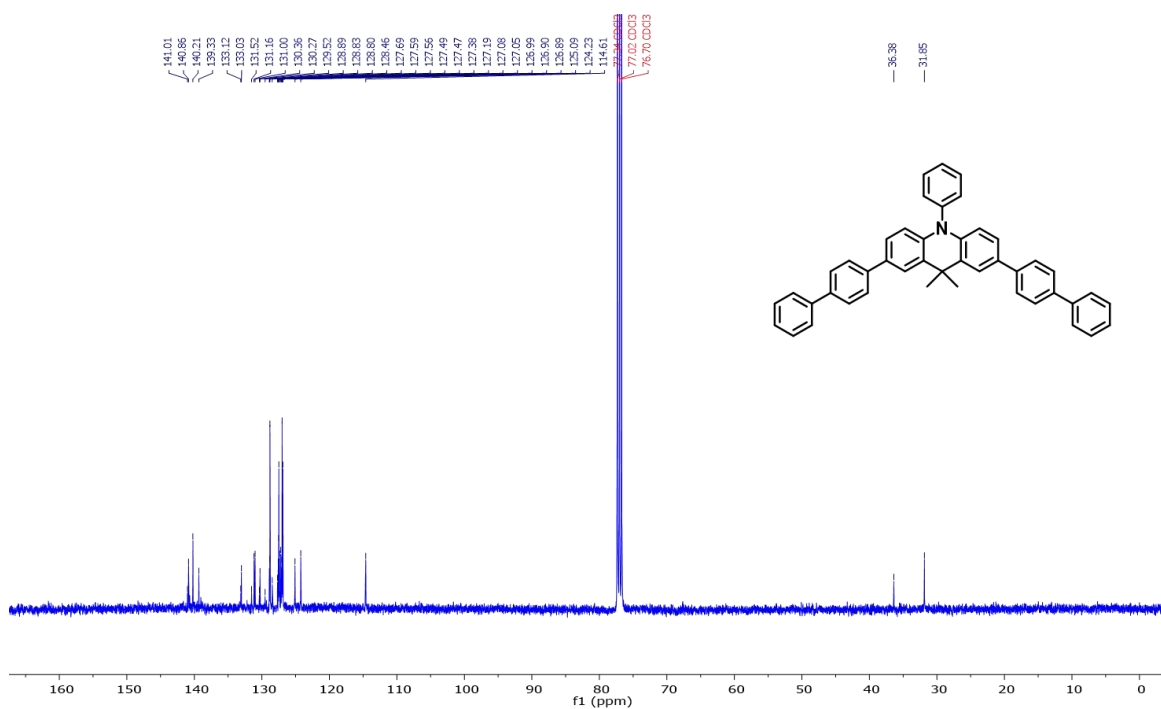
Figure 4.31: ^{13}C NMR spectrum of 2,7-di([1,1'-biphenyl]-4-yl)-9,9-dimethyl-10-phenyl-9,10-dihydroacridine in CDCl$_3$.

Synthesis of 10-(4-methoxyphenyl)-9,9-dimethyl-9,10-dihydroacridine
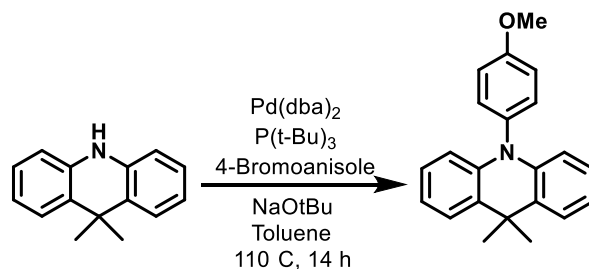
A storage tube was loaded with 1.0 g (4.8 mmol, 1 eq.) 9,10-Dihydro-9,9-dimethylacridine, 0.9 mL 4-Bromoanisole (7.2 mmol, 1.5 eq.), 27.5 mg of Bis(dibenzylideneacetone)palladium(0) (0.48 µmol, 1 mol%), 143 µL of 1M in toluene Tri-*tert*-butylphosphine (0.134 mmol, 3 mol %), 1.4 g sodium *tert*-butoxide (14.4 mmol, 3 eq.), and 27 mL toluene under nitrogen atmosphere. The solution was heated to 110 ºC. After 14 hours, the brown liquid with a white precipitate was passed directly through a silica plug and rinsed with toluene. All fluorescent blue portions were collected and concentrated via rotary evaporation. The product was recrystallized with DCM/methanol at - 25 ºC for 2 hours. The product was collected via vacuum filtration, washed with methanol, and dried overnight under vacuum to yield 1.25 g (82.8% yield) of white crystalline needles. ^{1}H NMR (400 MHz, Benzene-d_6) δ 7.45 – 7.36 (m, 2H), 7.02 – 6.88 (m, 6H), 6.82 – 6.73 (m, 2H), 6.56 – 6.44 (m, 2H), 3.29 (s, 3H), 1.65 (s, 6H). ^{13}C NMR (101 MHz, C$_6$D6) δ 159.16, 141.52, 133.83, 132.15, 129.97, 126.43, 125.22, 120.62, 115.89, 114.28, 54.61, 35.89, 31.09. HRMS (ESI) calculated for (M+H)+ for C$_{22}$H$_{21}$NO, 316.16959; Found, 316.16916.
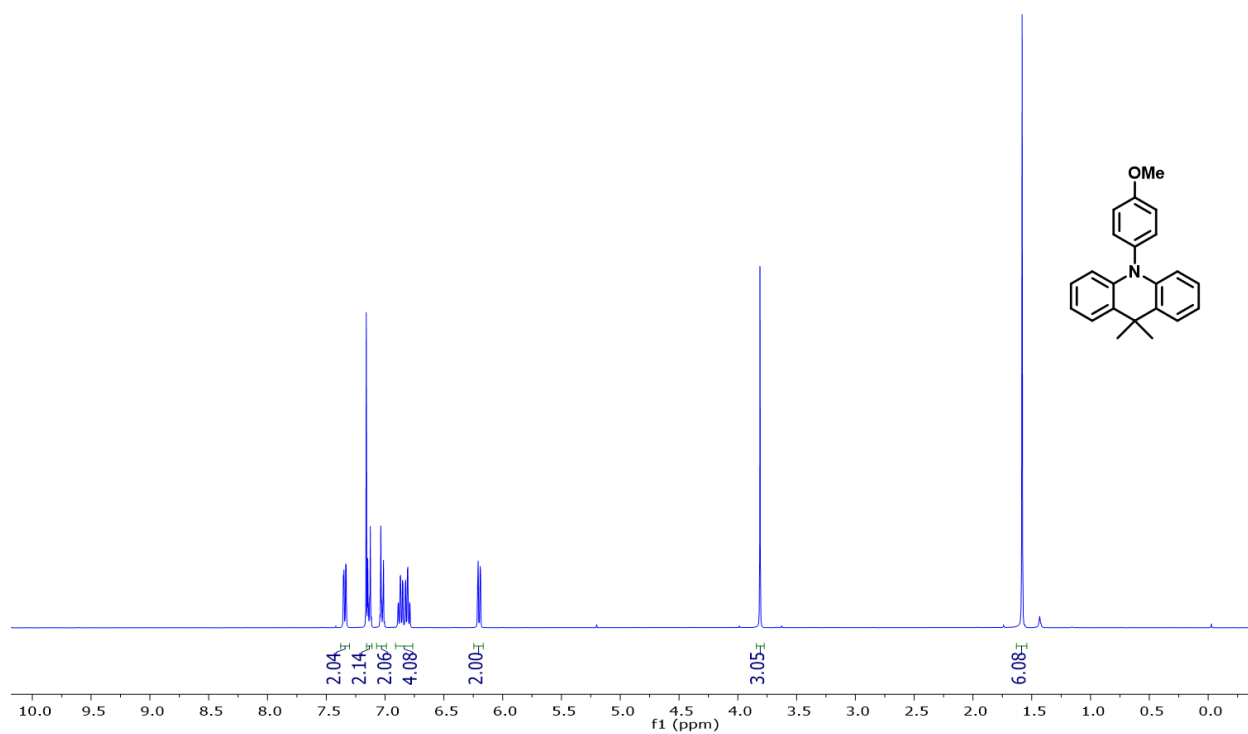
Figure 4.32: ¹H NMR spectrum of 10-(4-methoxyphenyl)-9,9-dimethyl-9,10-dihydroacridine in C_6D_6.
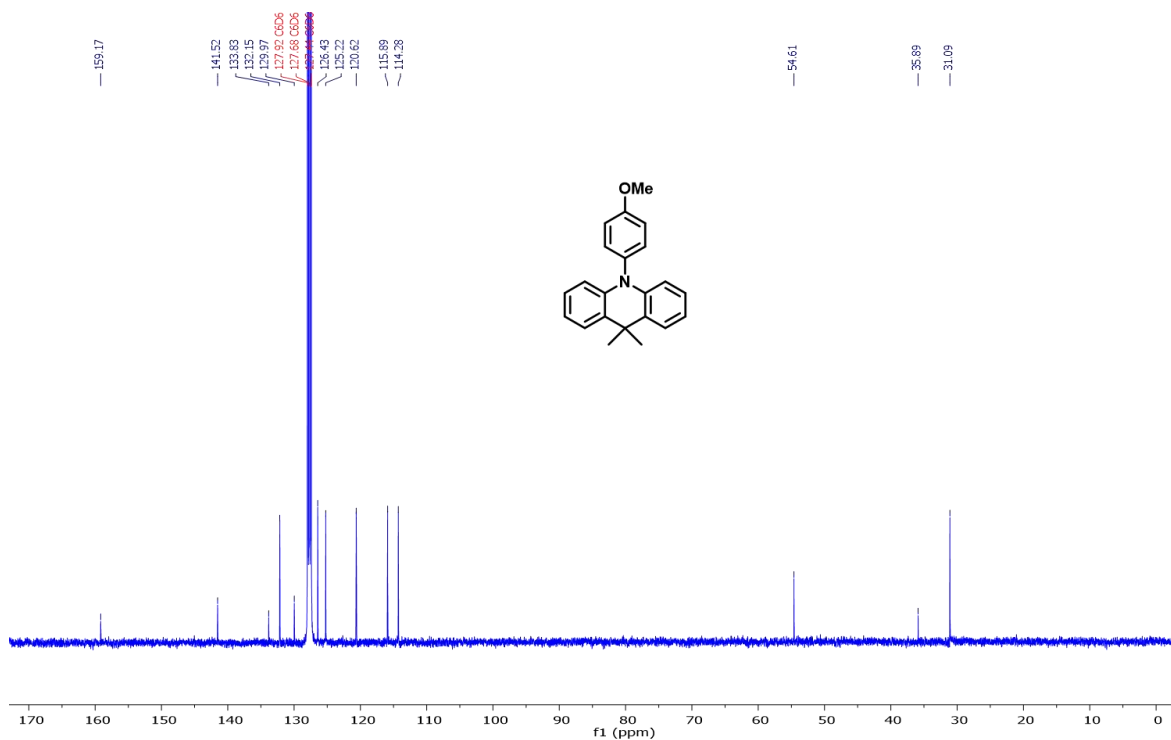
Figure 4.33: ¹³C NMR spectrum of 10-(4-methoxyphenyl)-9,9-dimethyl-9,10-dihydroacridine in C_6D_6.

Synthesis of 2,7-dibromo-10-(4-methoxyphenyl)-9,9-dimethyl-9,10-dihydroacridine
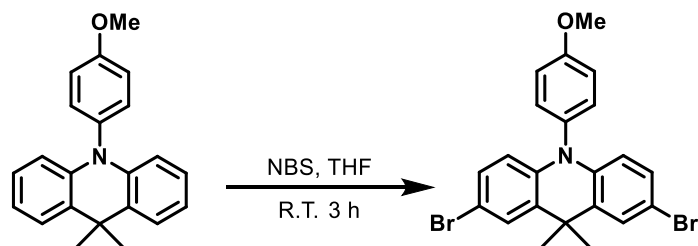
1.0 g of 9,10-dihydro-9,9-dimethyl-10-(4-Methoxyphenyl)-acridine (3.2 mmol, 1.0 eq.) was dissolved in 50 mL THF under ambient atmosphere. 1.41 g of *N*-Bromosuccinimide (7.9 mmol, 2.5 eq.) was slowly added to make a light brown solution. The reaction then stirred at room temperature for 3 hours. The solution was then concentrated via rotary evaporation, washed with water 3 times, and dried with magnesium sulfate. The product was recrystallized using DCM layered with methanol at -25 ℃ overnight. The product was isolated by filtration and dried under vacuum to give a brownish-white solid, which was used without further purification. Yield: 1.16 g, 77.6%. ^{1}H NMR (400 MHz, Chloroform-*d*) δ 7.49 (d, *J* = 2.3 Hz, 2H), 7.21 – 7.09 (m, 4H), 7.05 (dd, *J* = 8.8, 2.3 Hz, 2H), 6.17 (d, *J* = 8.7 Hz, 2H), 3.91 (s, 3H), 1.63 (s, 6H). ^{13}C NMR (101 MHz, Chloroform-*d*) δ 159.46, 140.08, 132.78, 131.71, 131.60, 129.27, 127.97, 116.22, 115.86, 113.17, 55.56, 36.26, 30.93.
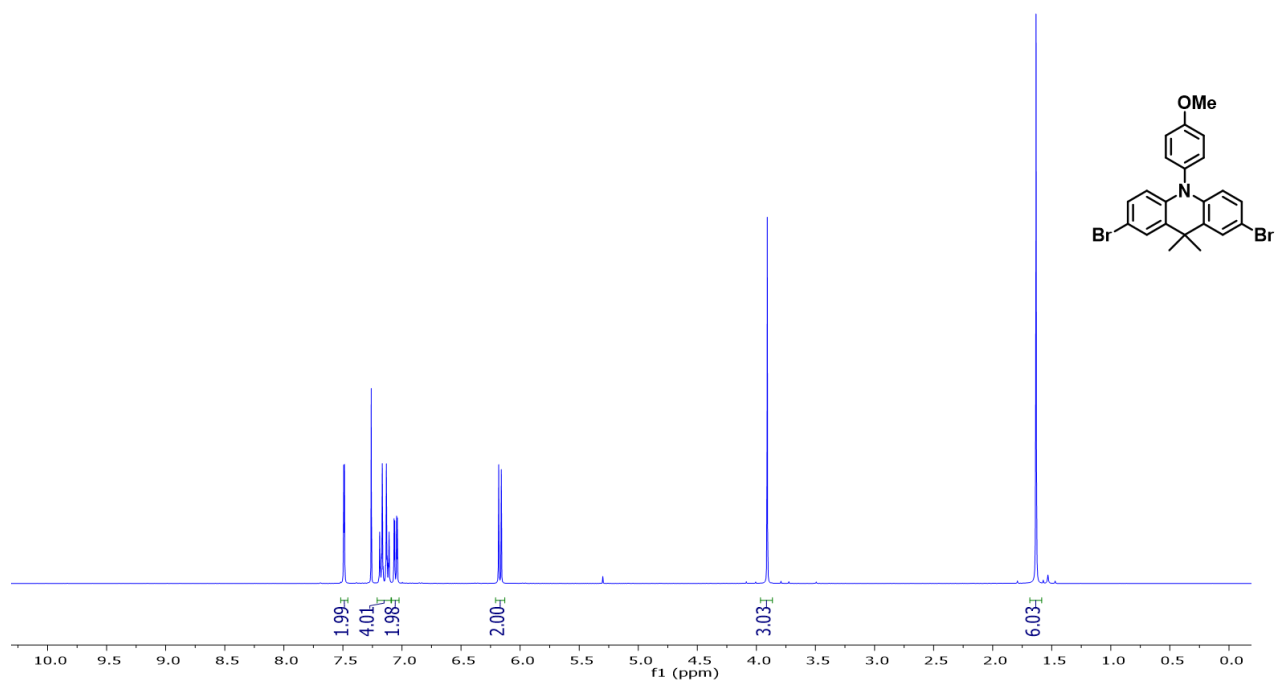
Figure 4.34: ^{1}H NMR spectrum of 2,7-dibromo-10-(4-methoxyphenyl)-9,9-dimethyl-9,10-dihydroacridine in CDCl$_3$.
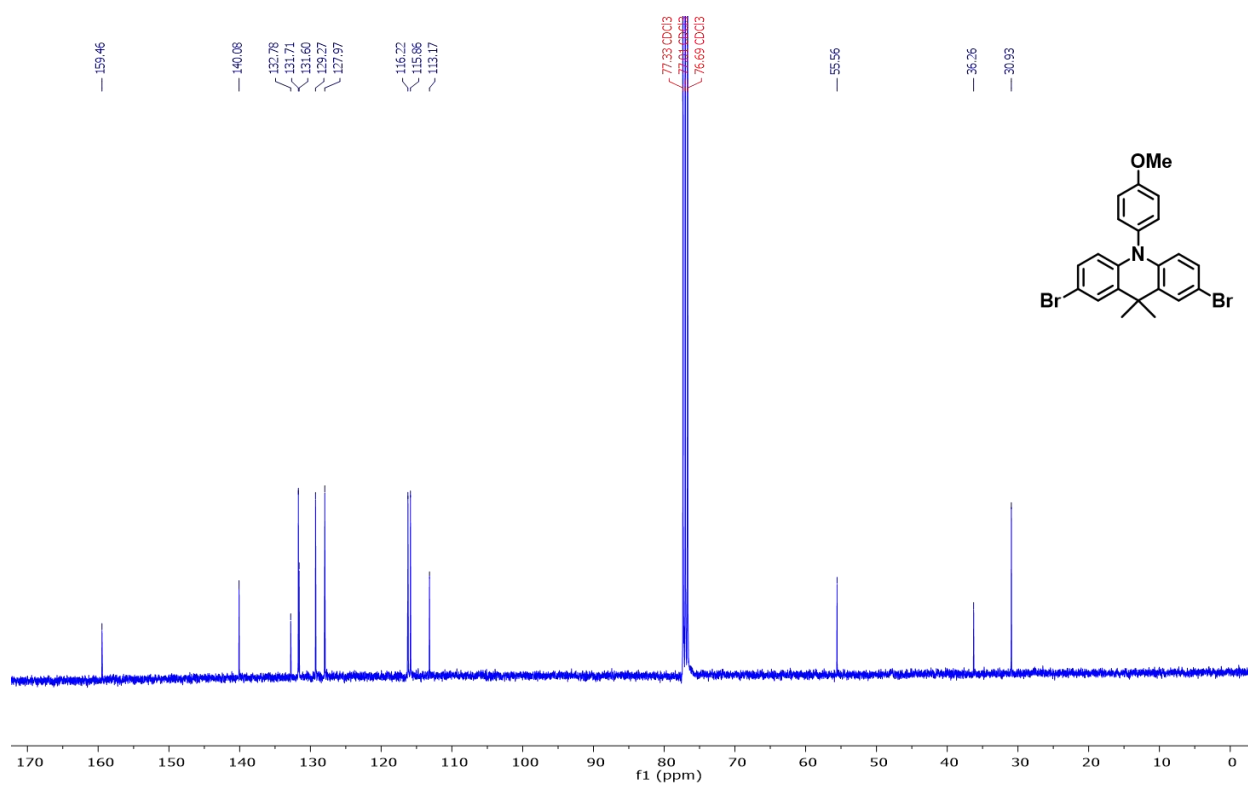
Figure 4.35: ^{13}C NMR spectrum of 2,7-dibromo-10-(4-methoxyphenyl)-9,9-dimethyl-9,10-dihydroacridine in CDCl$_3$.

Synthesis of 2,7-di([1,1'-biphenyl]-4-yl)-10-(4-methoxyphenyl)-9,9-dimethyl-9,10-dihydroacridine
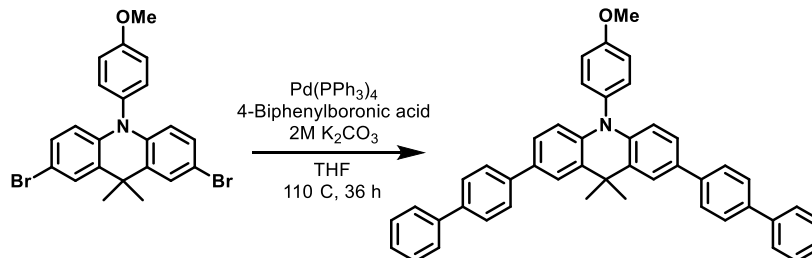
0.5 g of 2,7-dibromo-9,10-dihydro-9,9-dimethyl-10-(4-Methoxyphenyl)-acridine (1.1 mmol, 1 eq.) and 0.89 g of 4-Biphenylboronic acid (4.5 mmol, 4 eq.) was loaded into a storage tube under ambient atmosphere. The storage tube was taken into a nitrogen-filled glovebox, then loaded with 0.184 g Tetrakis(triphenylphosphine)palladium(0) (0.159 mmol, 15 mol %). The solids were dissolved in 40 mL THF. The storage tube was sealed and brought out of the glovebox, where 12 mL of degassed 2M K_2CO_3 (22 eq.) was added using a long needle and syringe to produce a biphasic yellow and colorless solution. The solution was heated to 110 °C for 36 hours, then brought to room temperature. The solution turned reddish-brown upon exposure to air. The solution was concentrated and extracted into DCM, then dried using magnesium sulfate, filtered, and concentrated. The crude mixture was redissolved in DCM then passed through a silica plug. The filtrate was concentrated, then dissolved in toluene and passed through an additional silica plug to remove residual palladium. The filtrate was collected and concentrated, then purified by column chromatography with hexanes: ethyl acetate ramping from 100:0 to 80:20. The product, a white solid, was then recrystallized with Ethyl acetate/MeOH at -25 °C to give 0.385 g of a white solid with a yield of 58.6%. ^{1}H NMR (400 MHz, Benzene-d_6) δ 7.91 (d, J = 2.1 Hz, 2H), 7.73 – 7.65 (m, 4H), 7.64 – 7.50 (m, 11H), 7.40 – 7.33 (m, 3H), 7.27 (td, J = 7.7, 2.4 Hz, 5H), 6.91 – 6.84 (m, 2H), 6.64 (d, J = 8.5 Hz, 2H), 3.34 (s, 3H), 1.81 (s, 6H). ^{13}C NMR (101 MHz, CDCl$_3$) δ 159.32, 140.86, 140.68, 140.53, 140.24, 139.58, 139.30, 132.93, 132.02, 130.27, 128.83, 128.79, 127.56, 127.46, 127.38, 127.18, 127.05, 126.99, 126.88, 125.08, 124.21, 116.12, 114.61, 77.33, 77.01,

76.70, 55.59, 36.34, 31.86. HRMS (ESI) calculated for (M+H)+ for C$_{46}$H$_{37}$NO, 619.28751; Found, 619.2877.
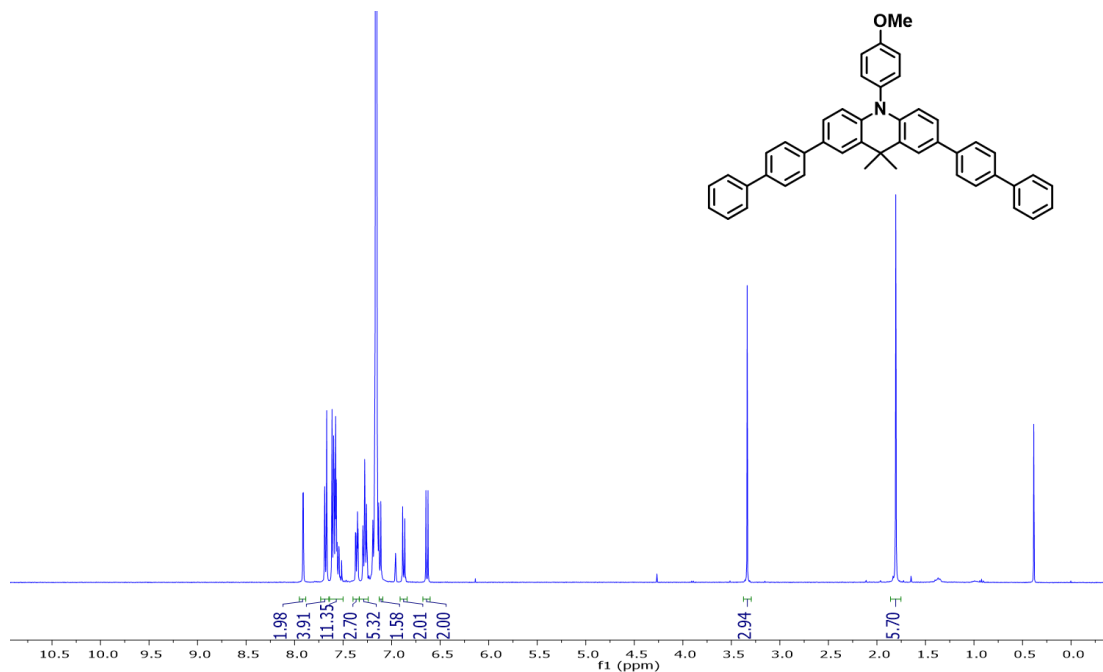
Figure 4.36: ^{1}H NMR spectrum of 2,7-di([1,1'-biphenyl]-4-yl)-10-(4-methoxyphenyl)-9,9-dimethyl-9,10-dihydroacridine in C$_6$D$_6$.
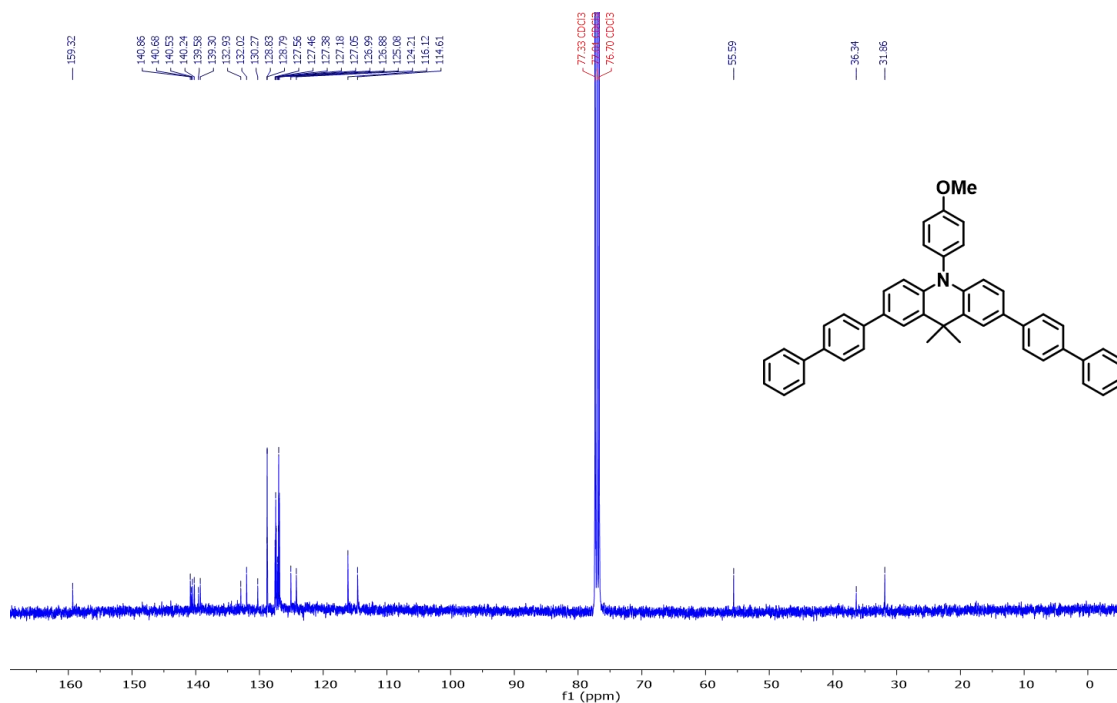
Figure 4.37: ^{13}C NMR spectrum of 2,7-di([1,1'-biphenyl]-4-yl)-10-(4-methoxyphenyl)-9,9-dimethyl-9,10-dihydroacridine in C$_6$D$_6$.

Synthesis of 4-(9,9-dimethylacridin-10(9H)-yl)benzonitrile
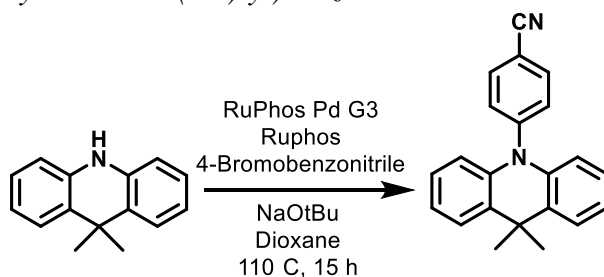
A storage tube was loaded with 2.0 g (9.6 mmol, 1 eq.) 9,10-Dihydro-9,9-dimethylacridine, 3.5 g 4-Bromobenzonitrile (19.1 mmol, 2.0 eq.), 0.118 g RuPhos ligand (0.28 mmol, 0.03 eq.), and 1.8 g sodium *tert*-butoxide (19.1 mmol, 2 eq.) under ambient atmosphere, then brought into a nitrogen-filled glovebox. Then, 0.244 g RuPhos Pd G3 precatalyst (0.28 mmol, 0.03 eq.) and 15 mL of degassed dioxane was added. The solution was sealed and brought outside of the glovebox, then heated to 110 ℃ for 15 hours. The solution was cooled to room temperature, then transferred to a flask and concentrated. The brown solid was dissolved in toluene then passed through a silica plug. The filtrate was concentrated, then recrystallized with DCM/MeOH at -25 ℃ overnight. The product was collected via vacuum filtration, washed with methanol, and dried overnight under vacuum to yield 1.7 g (57.3% yield) of pale-yellow solid. ^{1}H NMR (400 MHz, Chloroform-*d*) δ 8.21 – 8.12 (m, 2H), 7.79 – 7.70 (m, 4H), 7.32 – 7.19 (m, 4H), 6.59 – 6.51 (m, 2H), 1.93 (s, 6H). ^{13}C NMR (101 MHz, Chloroform-*d*) δ 146.12, 140.17, 134.76, 131.53, 131.06, 126.48, 125.45, 121.69, 118.39, 114.81, 111.38, 36.21, 30.85. HRMS (ESI) calculated for (M+H)+ for $C_{22}H_{18}N_2$, 311.15428; Found, 311.15351.
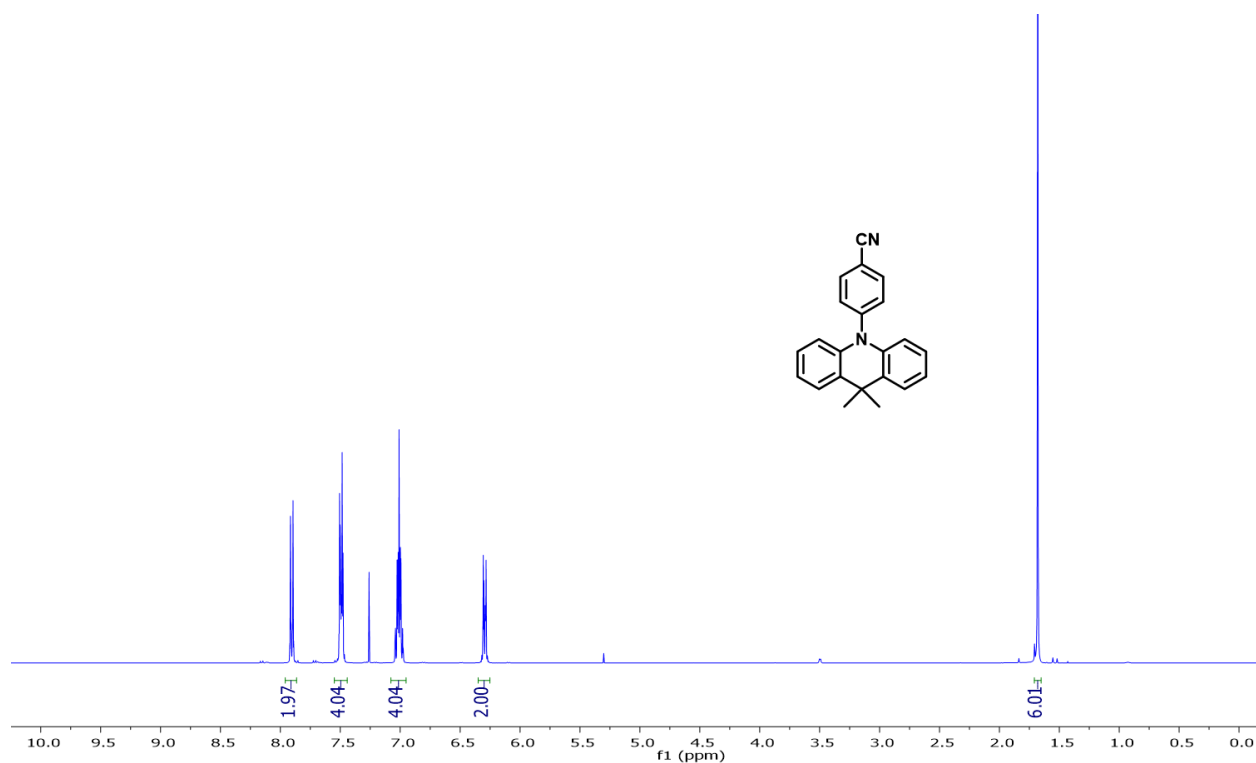
Figure 4.38: ^{1}H NMR spectrum of 4-(9,9-dimethylacridin-10(9H)-yl)benzonitrile in CDCl$_3$.
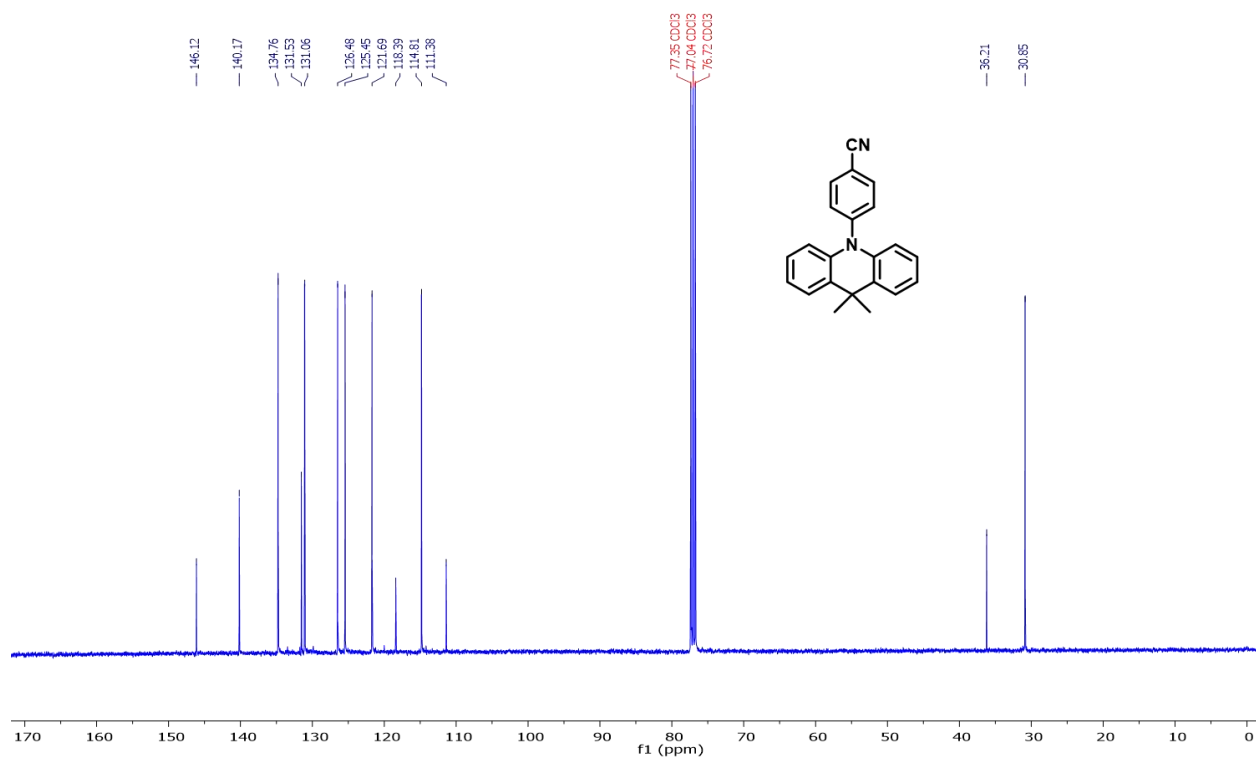
Figure 4.39: ^{13}C NMR spectrum of 4-(9,9-dimethylacridin-10(9H)-yl)benzonitrile in CDCl$_3$.

Synthesis of 4-(2,7-dibromo-9,9-dimethylacridin-10(9H)-yl)benzonitrile
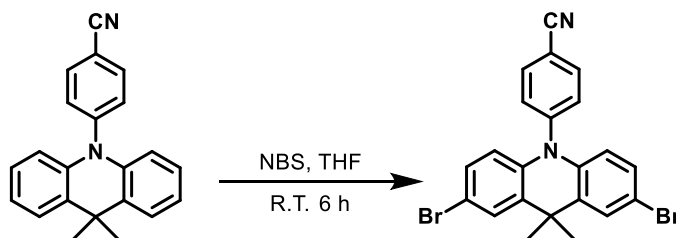
1.0 g of 9,10-dihydro-9,9-dimethyl-10-(4-cyanophenyl)-acridine (3.2 mmol, 1.0 eq.) was dissolved in 20 mL THF under ambient atmosphere. 1.26 g of *N*-Bromosuccinimide (7.1 mmol, 2.2 eq.) was slowly added to make a colorless solution. The reaction then stirred at room temperature for 6 hours. The solution was then concentrated via rotary evaporation, washed with water 3 times, and dried with magnesium sulfate. The product was recrystallized using DCM layered with methanol at -25 ℃ overnight. The product was isolated by filtration and dried under vacuum to give a pale yellow crystalline solid, which was used without further purification. Yield: 1.0g, 66%. ^{1}H NMR (400 MHz, Chloroform-*d*) δ 7.91 – 7.82 (m, 2H), 7.46 (d, *J* = 2.3 Hz, 2H), 7.41 – 7.35 (m, 2H), 7.02 (dd, *J* = 8.8, 2.3 Hz, 2H), 6.01 (d, *J* = 8.8 Hz, 2H), 1.57 (s, 6H). ^{13}C NMR (101 MHz, Chloroform-*d*) δ 145.00, 138.97, 135.07, 132.42, 131.65, 129.50, 128.41, 117.97, 115.93, 114.34, 112.59, 36.40, 30.78.
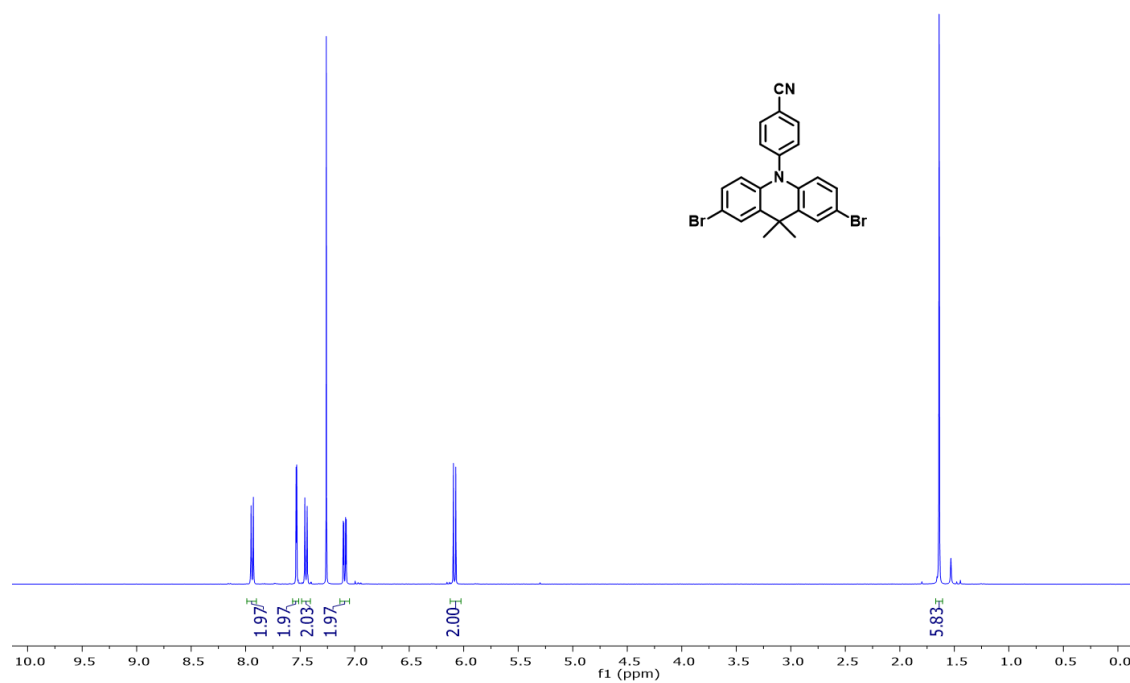
Figure 4.40: ¹H NMR spectrum of 4-(2,7-dibromo-9,9-dimethylacridin-10(9H)-yl)benzonitrile in CDCl₃.
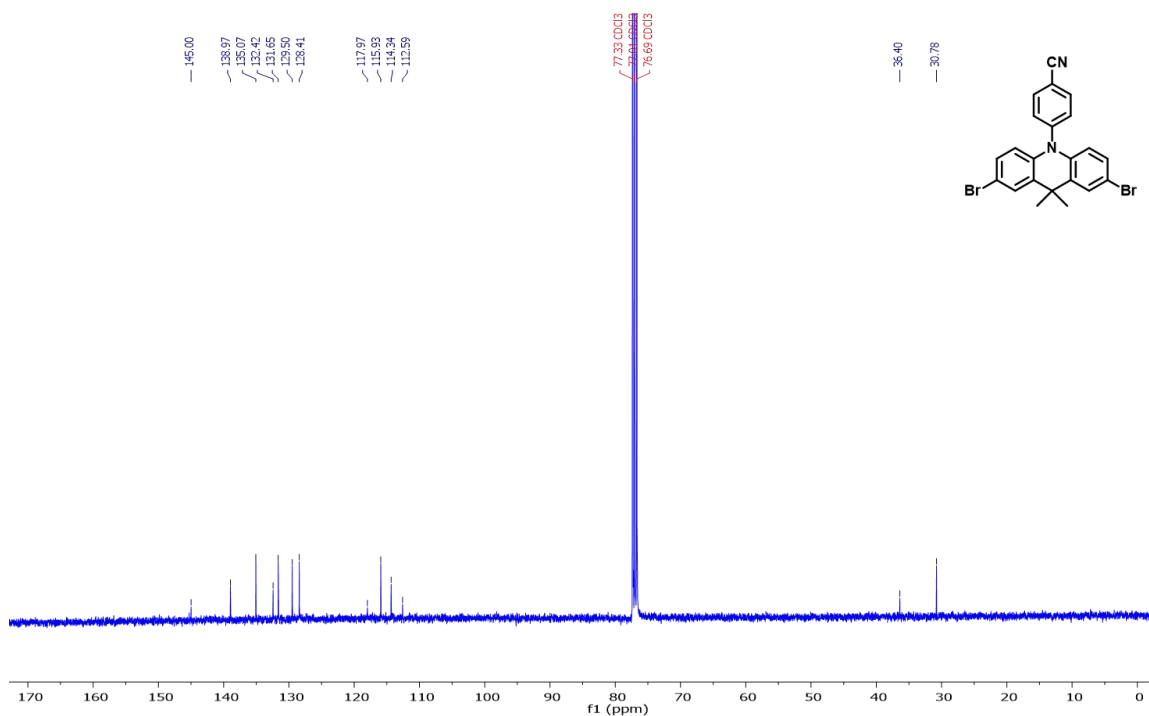
Figure 4.41: ¹³C NMR spectrum of 4-(2,7-dibromo-9,9-dimethylacridin-10(9H)-yl)benzonitrile in CDCl₃.

Synthesis of 4-(2,7-di([1,1'-biphenyl]-4-yl)-9,9-dimethylacridin-10(9H)-yl)benzonitrile
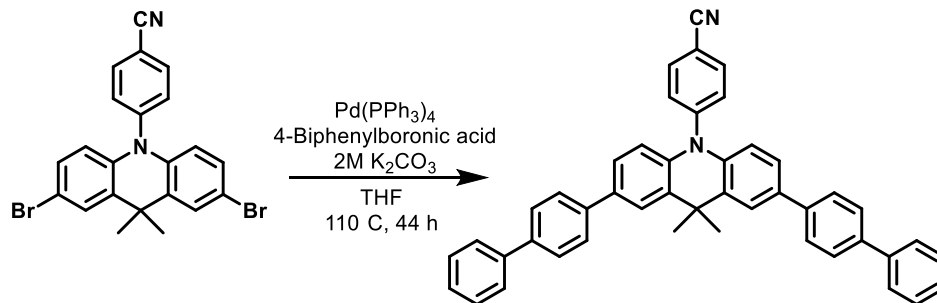
0.8 g of 2,7-dibromo-9,10-dihydro-9,9-dimethyl-10-(4-cyanophenyl)-acridine (1.7 mmol, 1 eq.) and 1.4 g of 4-Biphenylboronic acid (6.8 mmol, 4 eq.) was loaded into a storage tube under ambient atmosphere. The storage tube was taken into a nitrogen-filled glovebox, then loaded with 0.296 g Tetrakis(triphenylphosphine)palladium(0) (0.257 mmol, 15 mol %). The solids were dissolved in 50 mL degassed THF. The storage tube was sealed and brought out of the glovebox, where 19 mL of degassed 2M K_2CO_3 (22 eq.) was added using a long needle and syringe to produce a biphasic yellow and colorless solution. The solution was heated to 110 ºC for 44 hours, then brought to room temperature. The solution turned red upon exposure to air. The solution was concentrated and extracted into DCM. A yellow emulsion formed, which was filtered and washed with methanol to produce the crude product as a pale-yellow powder. The solid was dissolved in DCM and washed with water 3 times, then dried with magnesium sulfate and concentrated. The product was recrystallized with DCM/MeOH at room temperature 2 times to give 0.88 g at 84% yield. ^{1}H NMR (400 MHz, Benzene-d_6) δ 7.87 (d, J = 2.1 Hz, 2H), 7.72 – 7.55 (m, 12H), 7.38 – 7.24 (m, 6H), 7.24 – 7.18 (m, 2H), 7.11 – 7.03 (m, 2H), 6.84 – 6.75 (m, 2H), 6.23 (d, J = 8.5 Hz, 2H), 1.73 (s, 6H). ^{13}C NMR (101 MHz, CDCl$_3$) δ 145.01, 141.04, 140.22, 139.99, 139.64, 134.51, 134.47, 131.34, 131.25, 128.92, 128.00, 127.76, 127.52, 127.18, 127.10, 125.39, 124.46, 118.01, 115.07, 112.21, 36.42, 31.27. HRMS (ESI) calculated for (M+H)+ for $C_{46}H_{34}N_2$, 614.2722; Found, 614.2736.
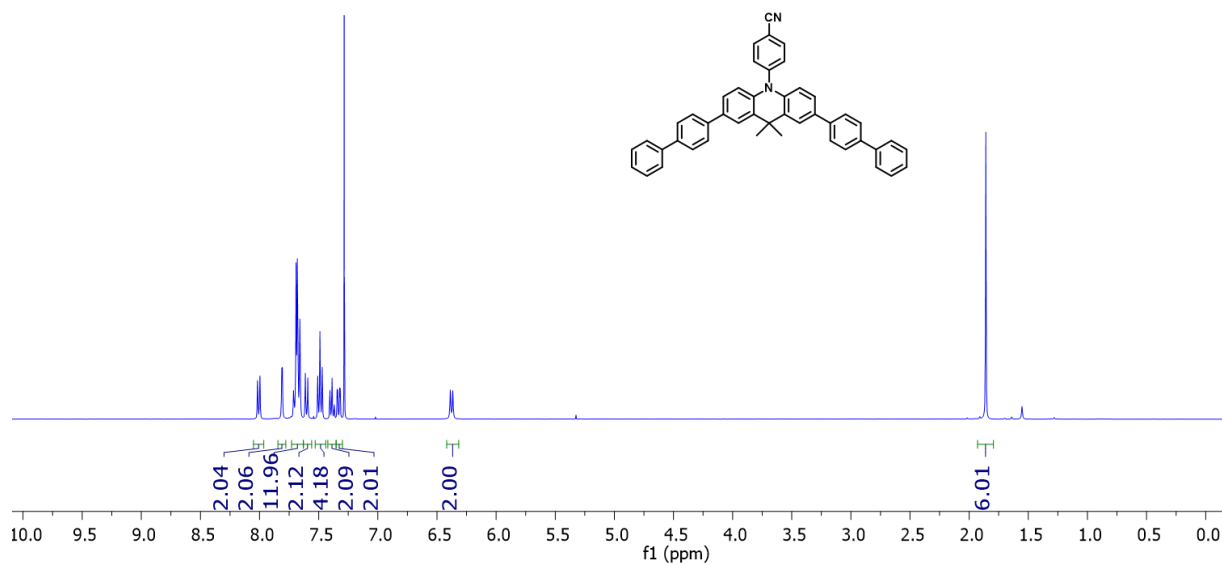
Figure 4.42: ^{1}H NMR spectrum of 4-(2,7-di([1,1'-biphenyl]-4-yl)-9,9-dimethylacridin-10(9H)-yl)benzonitrile in CDCl$_3$.
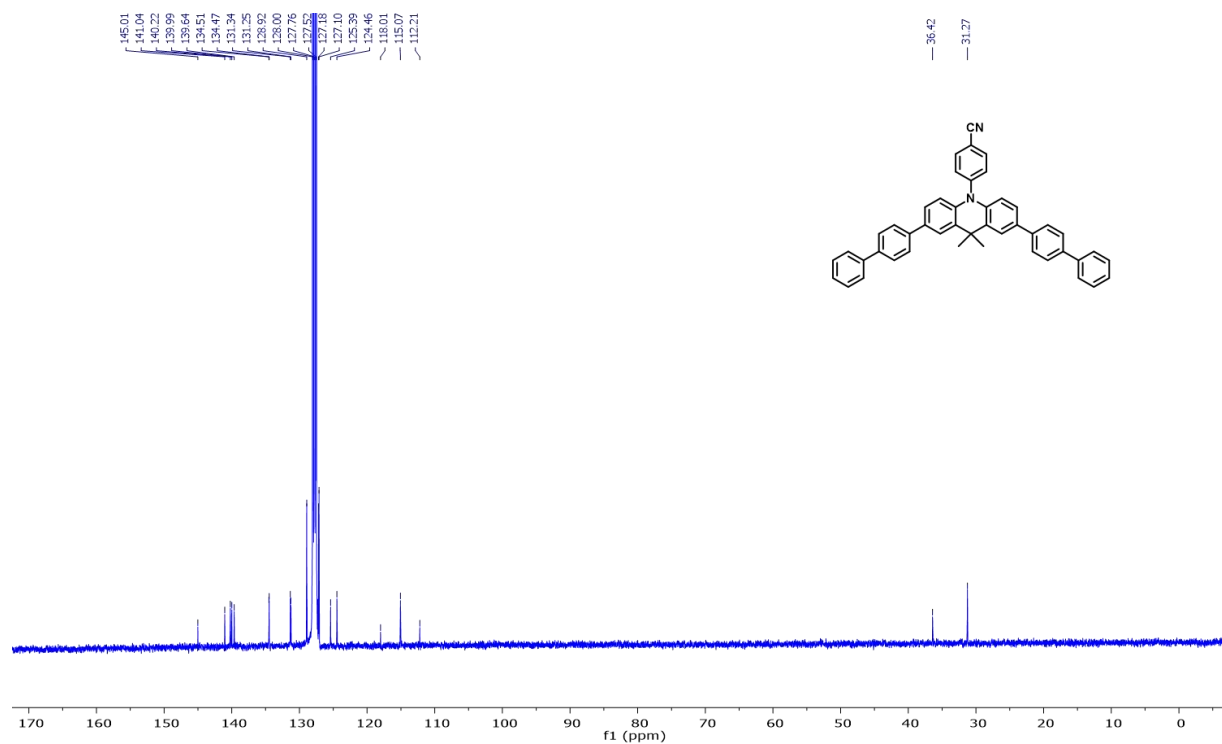
Figure 4.43: ^{13}C NMR spectrum of 4-(2,7-di([1,1'-biphenyl]-4-yl)-9,9-dimethylacridin-10(9H)-yl)benzonitrile in C$_6$D$_6$.

Photophysical and Electrochemical Characterization

UV-visible Spectroscopy:
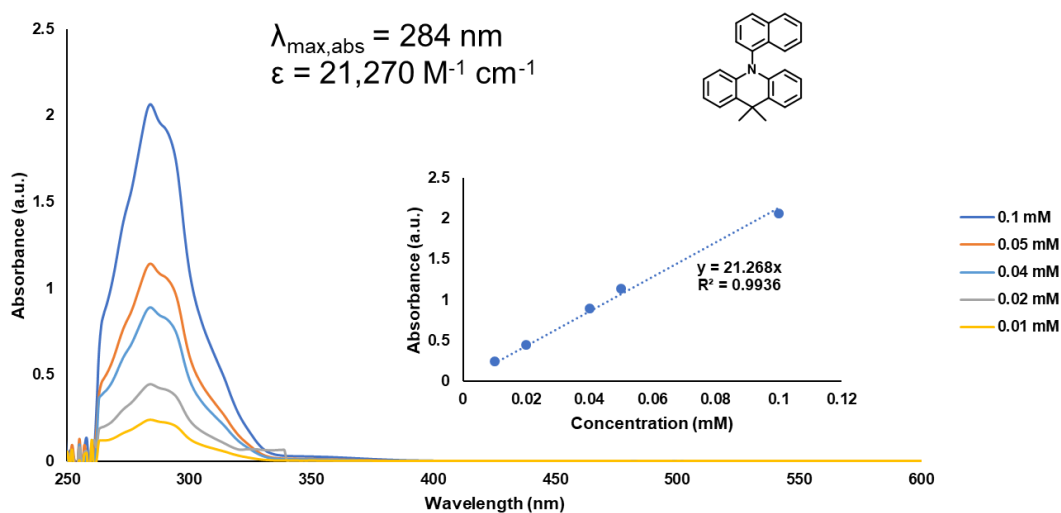
Figure 4.44: UV-vis spectrum of Acrid-1N (parent compound for **PCs 1, 2,** and **3**) at different concentrations in DMF with a path length of 1 cm. Graph in the lower left demonstrates the Beer-Lambert law relationship at the maximum wavelength of absorbance.
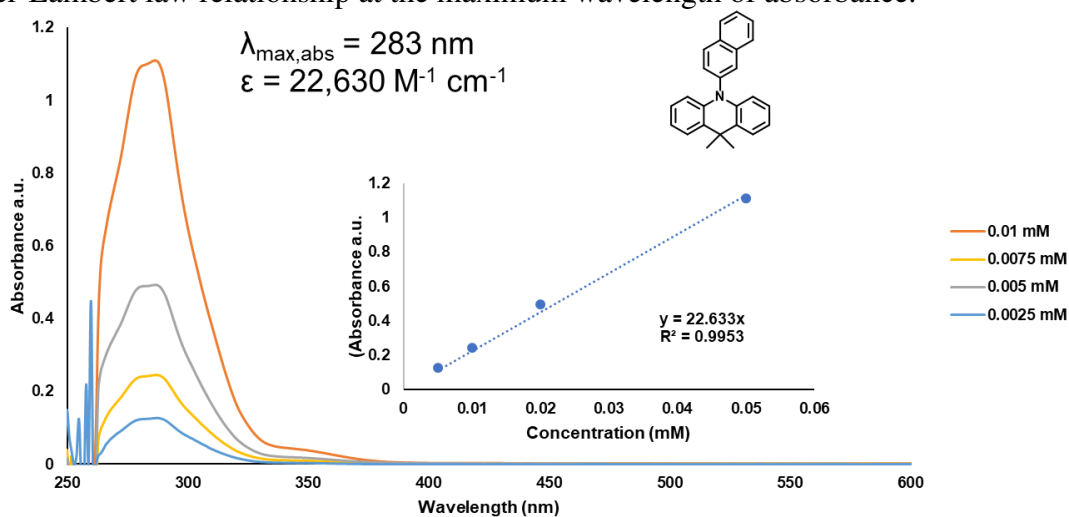
Figure 4.45: UV-vis spectrum of Acrid-2N (parent compound for **PC 4**) at different concentrations in DMF with a path length of 1 cm. Graph in the lower left demonstrates the Beer-Lambert law relationship at the maximum wavelength of absorbance.
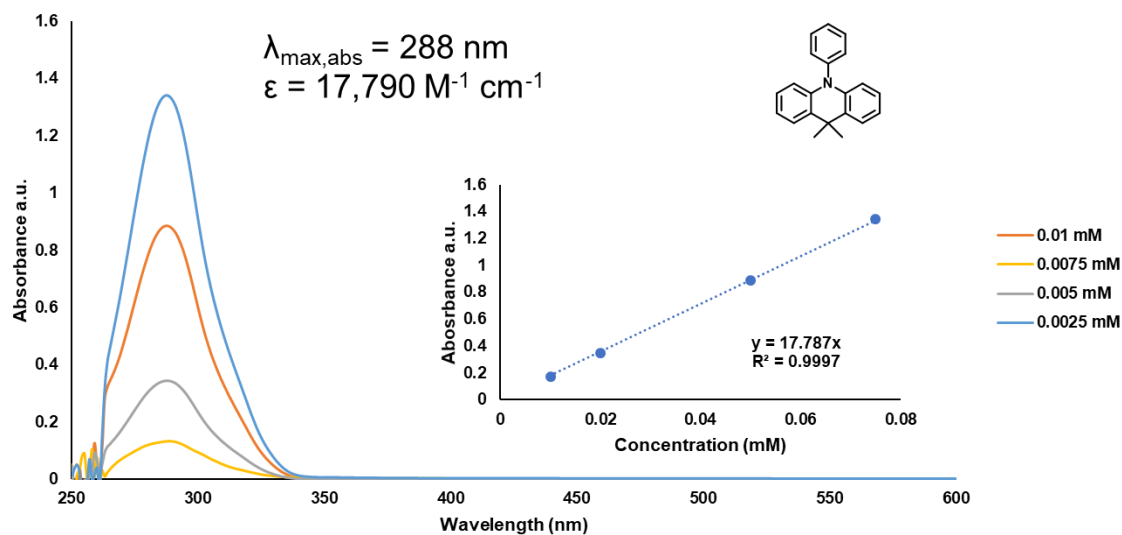
Figure 4.46: UV-vis spectrum of Acrid-Ph (parent compound for **PC 5**) at different concentrations in DMF with a path length of 1 cm. Graph in the lower left demonstrates the Beer-Lambert law relationship at the maximum wavelength of absorbance.
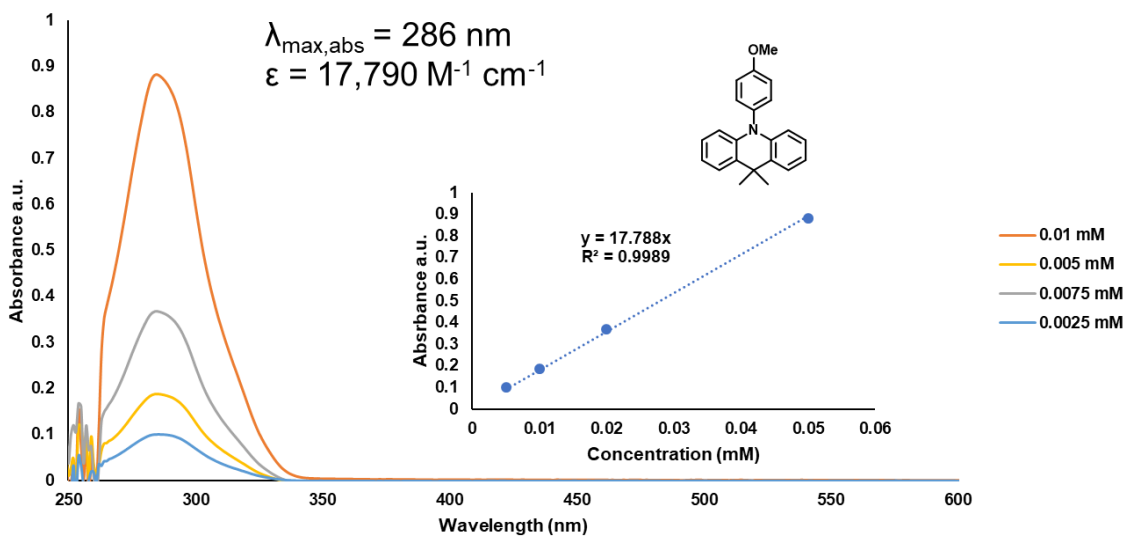
Figure 4.47: UV-vis spectrum of Acrid-OMe (parent compound for **PC 6**) at different concentrations in DMF with a path length of 1 cm. Graph in the lower left demonstrates the Beer-Lambert law relationship at the maximum wavelength of absorbance.
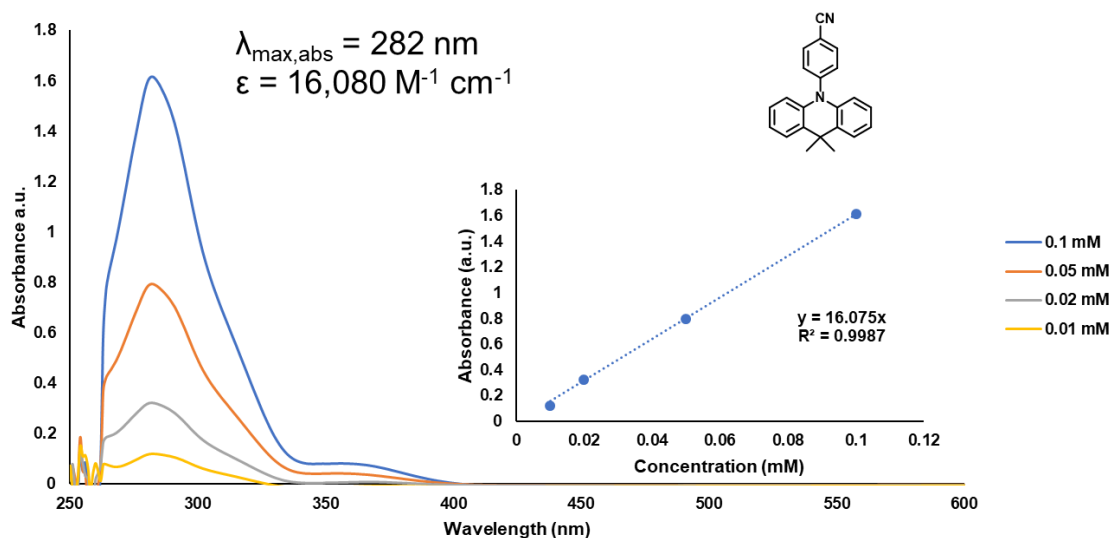
Figure 4.48: UV-vis spectrum of Acrid-CN (parent compound for **PC 7**) at different concentrations in DMF with a path length of 1 cm. Graph in the lower left demonstrates the Beer-Lambert law relationship at the maximum wavelength of absorbance.
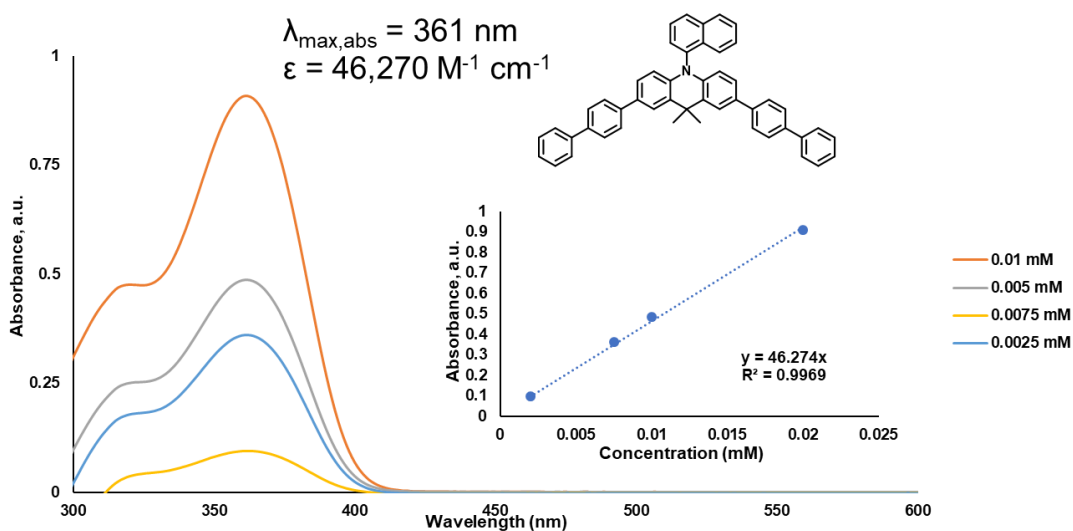
Figure 4.49: UV-vis spectrum of **PC 1** at different concentrations in DMF with a path length of 1 cm. Graph in the lower left demonstrates the Beer-Lambert law relationship at the maximum wavelength of absorbance.
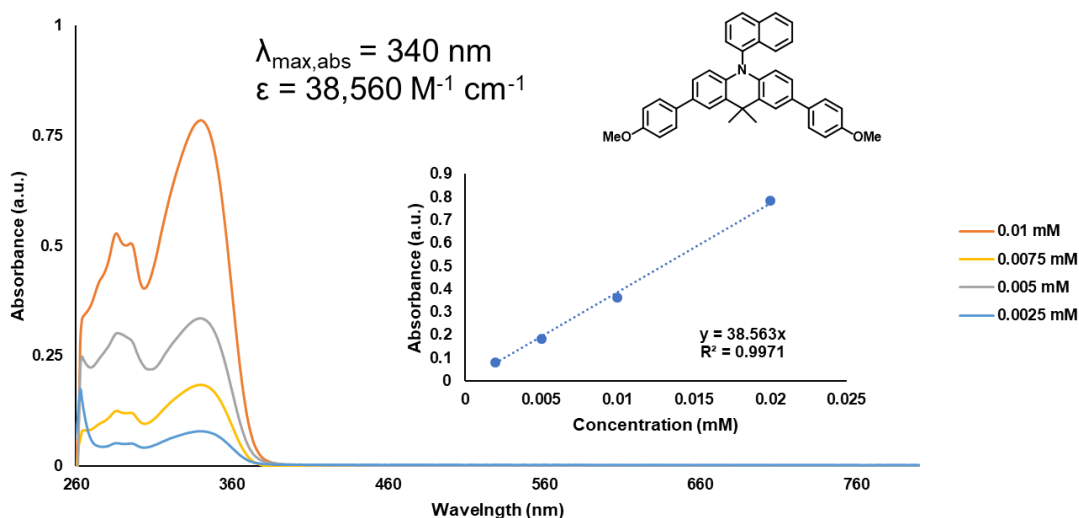
Figure 4.50: UV-vis spectrum of **PC 2** at different concentrations in DMF with a path length of 1 cm. Graph in the lower left demonstrates the Beer-Lambert law relationship at the maximum wavelength of absorbance.
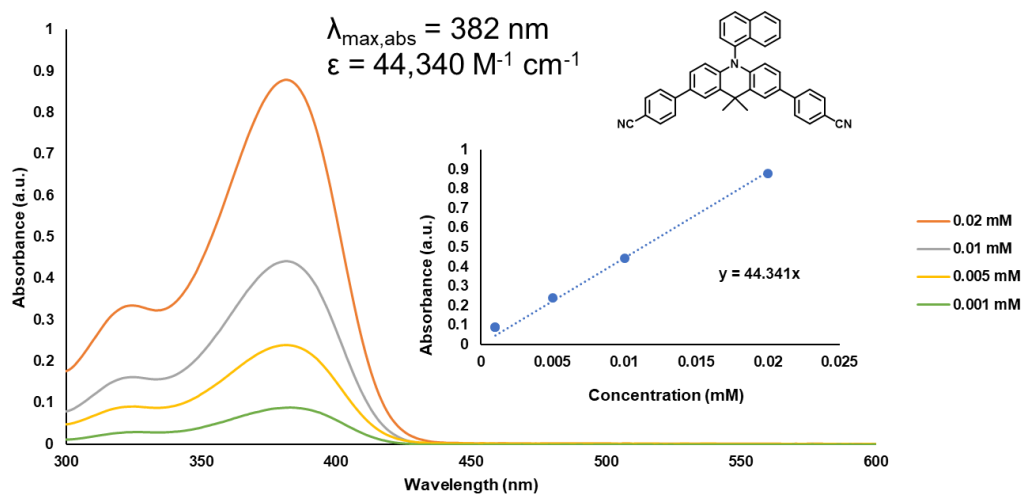
Figure 4.51: UV-vis spectrum of **PC 3** at different concentrations in DMF with a path length of 1 cm. Graph in the lower left demonstrates the Beer-Lambert law relationship at the maximum wavelength of absorbance.
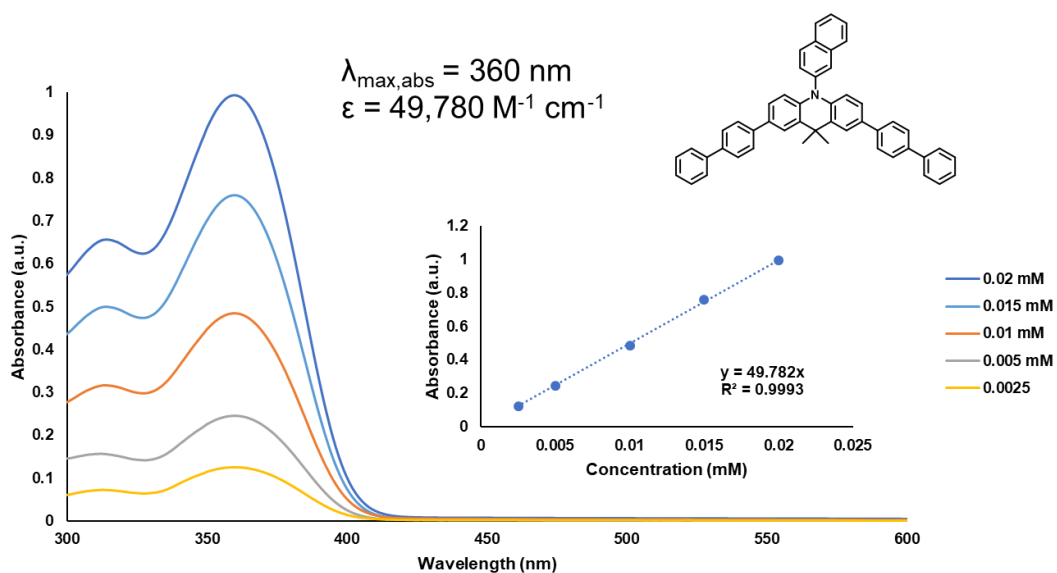
Figure 4.52: UV-vis spectrum of **PC 4** at different concentrations in DMF with a path length of 1 cm. Graph in the lower left demonstrates the Beer-Lambert law relationship at the maximum wavelength of absorbance.
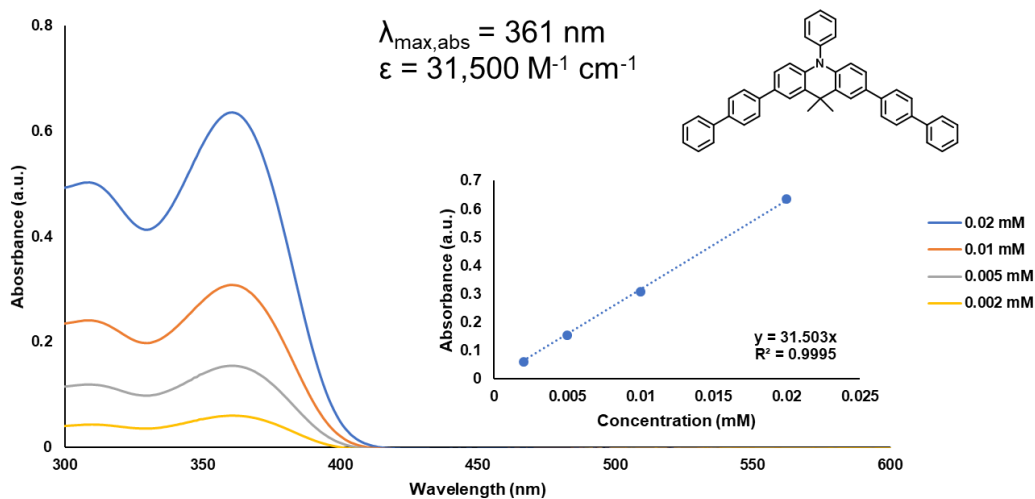
Figure 4.53: UV-vis spectrum of **PC 5** at different concentrations in DMF with a path length of 1 cm. Graph in the lower left demonstrates the Beer-Lambert law relationship at the maximum wavelength of absorbance.
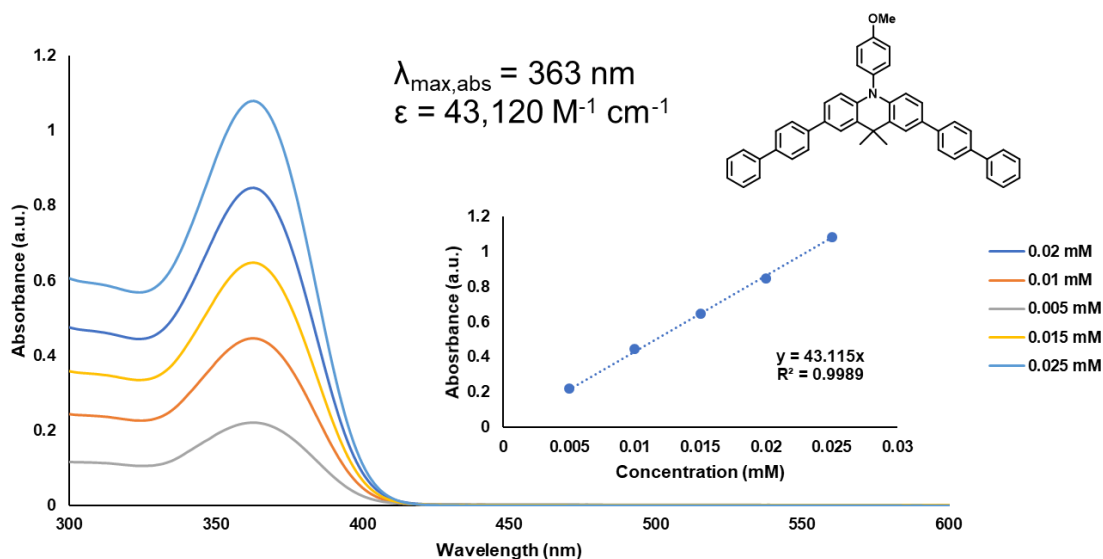
Figure 4.54: UV-vis spectrum of **PC 6** at different concentrations in DMF with a path length of 1 cm. Graph in the lower left demonstrates the Beer-Lambert law relationship at the maximum wavelength of absorbance.
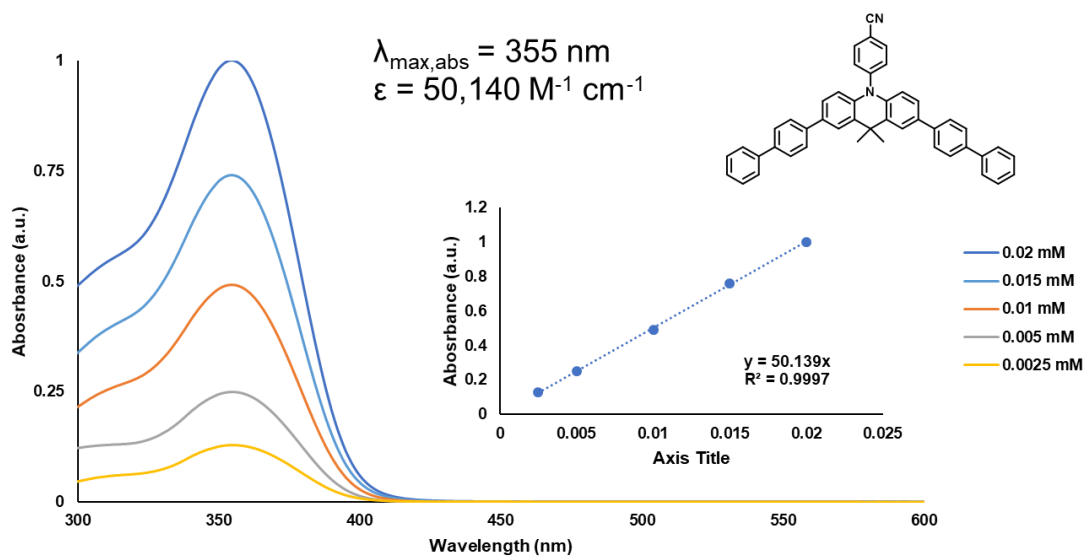
Figure 4.55: UV-vis spectrum of **PC 7** at different concentrations in DMF with a path length of 1 cm. Graph in the lower left demonstrates the Beer-Lambert law relationship at the maximum wavelength of absorbance.

Fluorescence Spectroscopy:

Emission data was measured using an FS5 spectrofluorometer from Edinburg Instruments. All samples were prepared at 0.1 mM concentrations inside a nitrogen-filled glovebox. Measurements were taken in a 1 cm quartz cuvette, sealed with electrical tape. All precursor molecules were excited at 280 nm. All PCs were excited at 365 nm. Each measurement used a step size of 1 nm, a dwell time of 0.1 s, with 3 averaged scans.
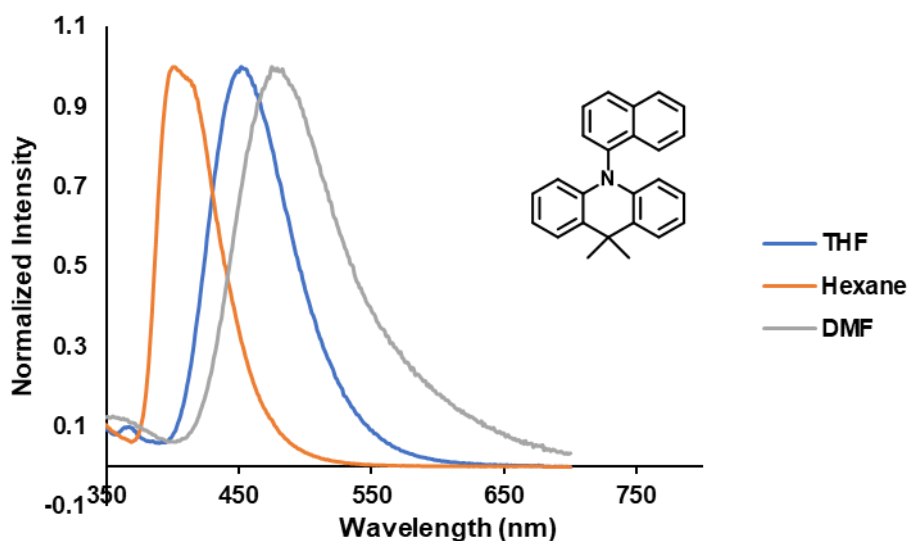
Figure 4.56: Normalized emission for Acrid-1N (precursor for **PCs 1, 2,** and **3**) measured in Hexane (orange), THF (blue) and DMF (grey).
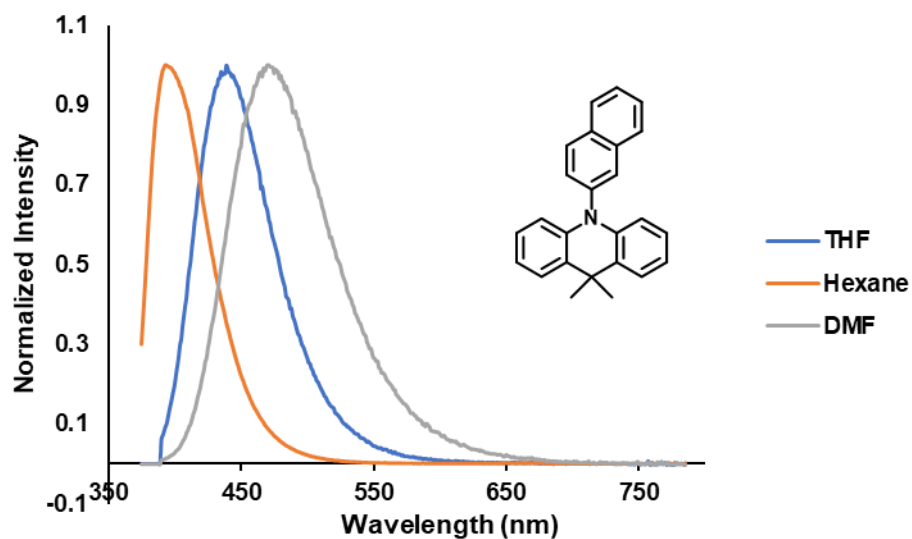
Figure 4.57: Normalized emission for Acrid-2N (precursor for **PC 4**) measured in Hexane (orange), THF (blue) and DMF (grey).
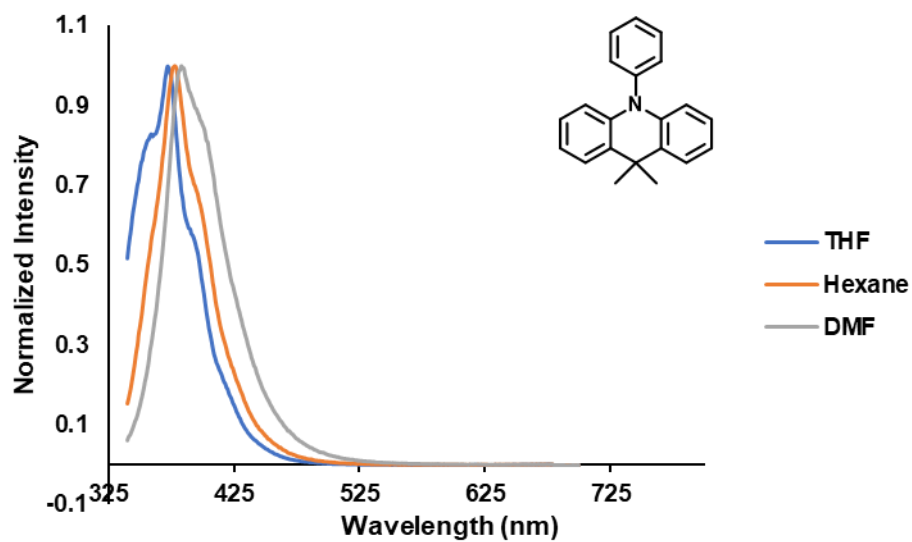
Figure 4.58: Normalized emission for Acrid-2N (precursor for **PC 5**) measured in Hexane (orange), THF (blue) and DMF (grey).
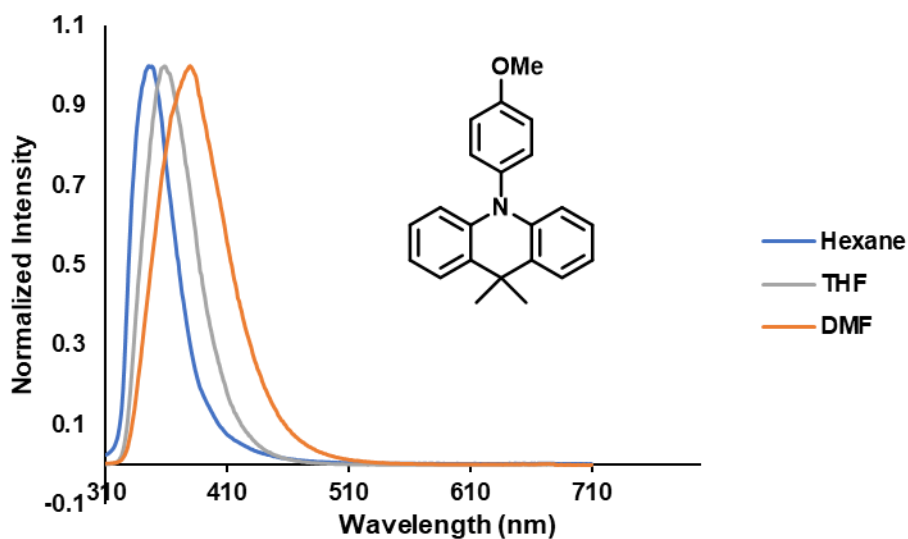
Figure 4.59: Normalized emission for Acrid-2N (precursor for **PC 6**) measured in Hexane (orange), THF (blue) and DMF (grey).
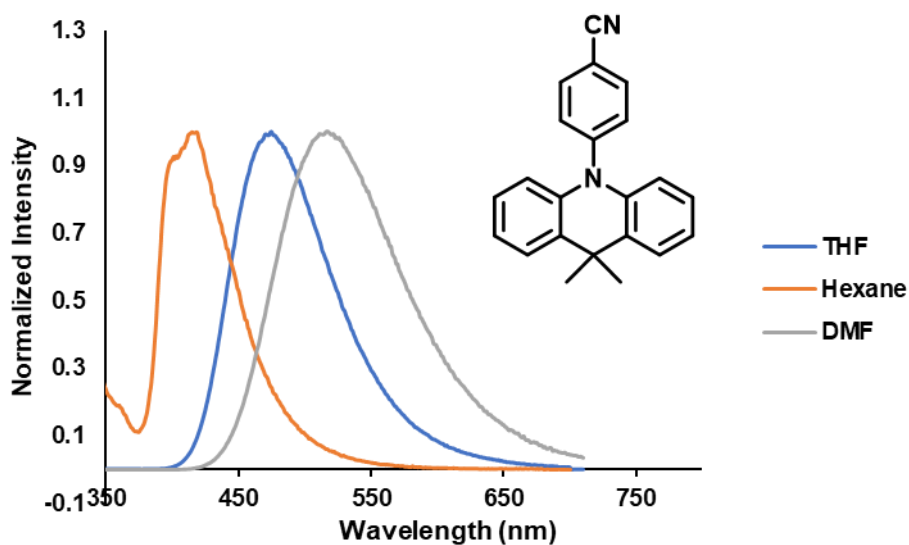
Figure 4.60: Normalized emission for Acrid-2N (precursor for **PC 7**) measured in Hexane (orange), THF (blue) and DMF (grey).
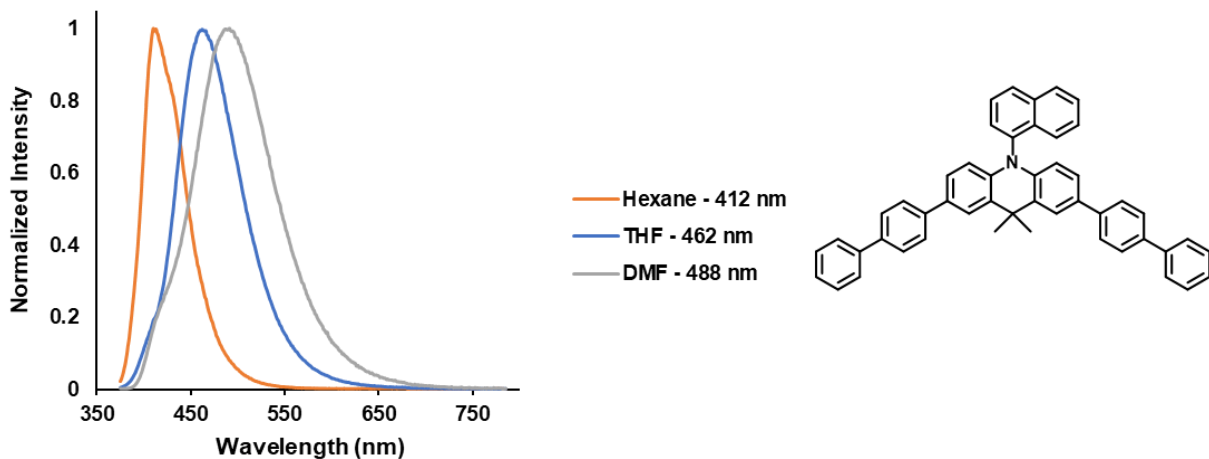
Figure 4.61: Normalized emission for **PC 1** measured in Hexane (orange), THF (blue) and DMF (grey).
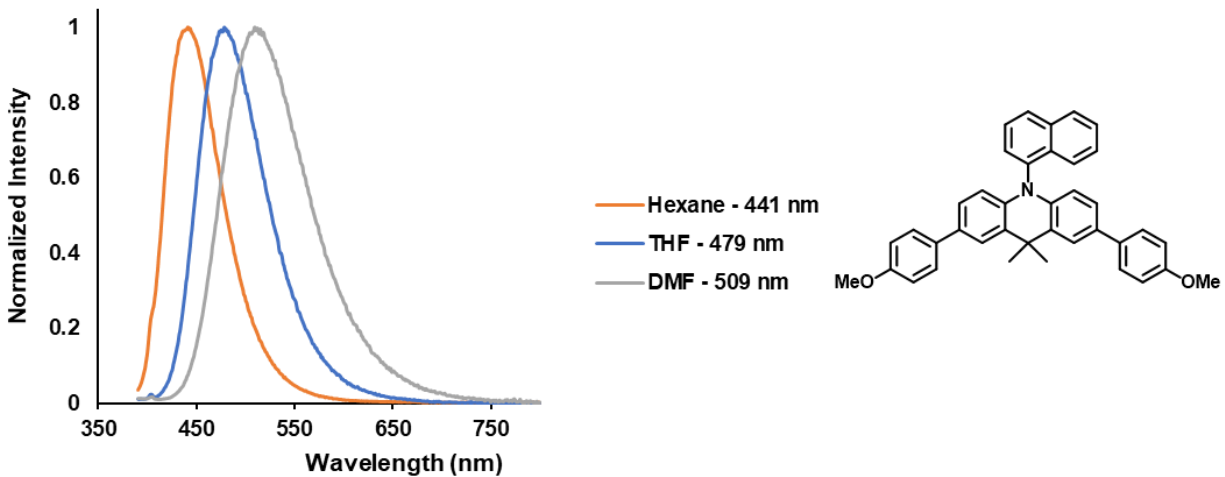
Figure 4.62: Normalized emission for **PC 2** measured in Hexane (orange), THF (blue) and DMF (grey).
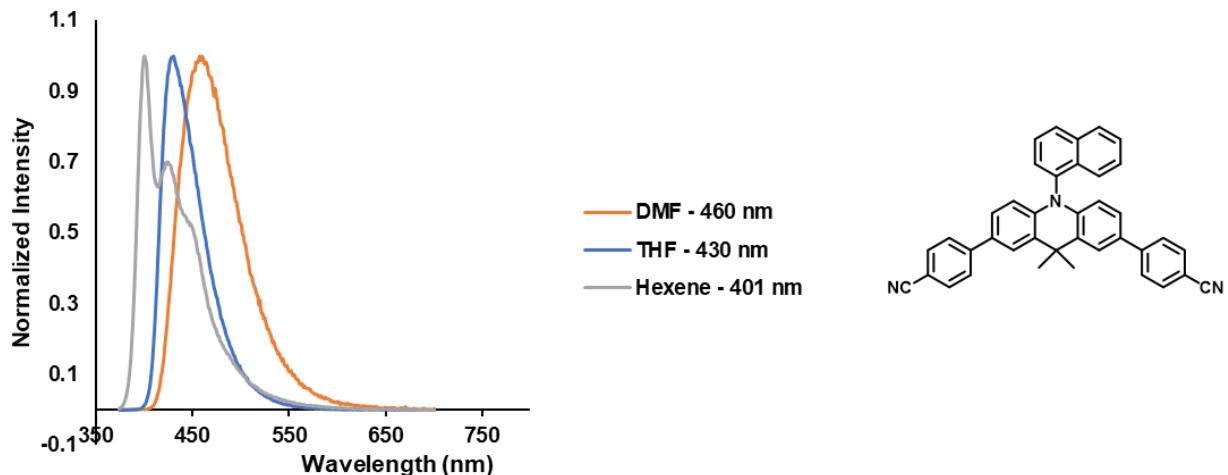
Figure 4.63: Normalized emission for **PC 3** measured in Hexane (orange), THF (blue) and DMF (grey).
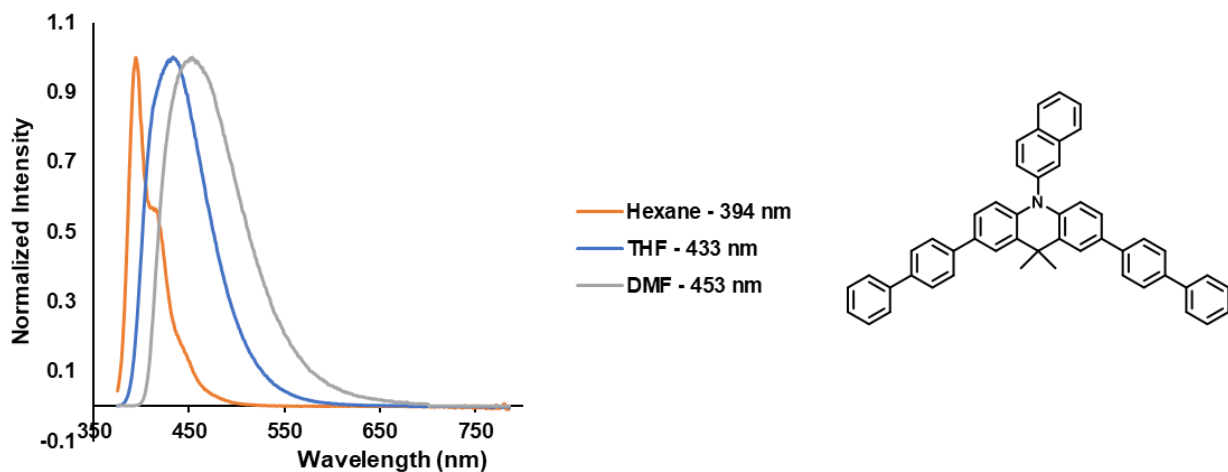
Figure 4.64: Normalized emission for **PC 4** measured in Hexane (orange), THF (blue) and DMF (grey).
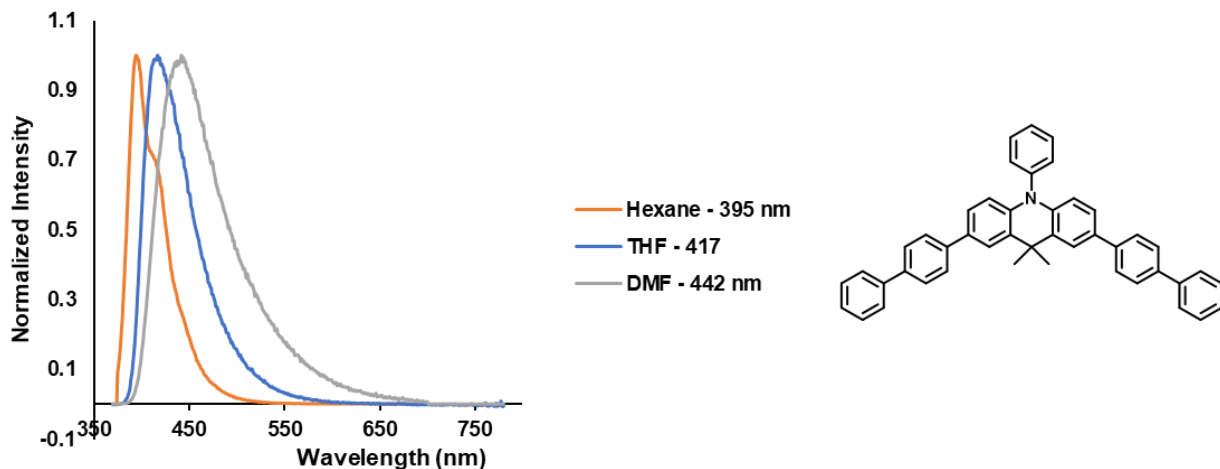
Figure 4.65: Normalized emission for **PC 5** measured in Hexane (orange), THF (blue) and DMF (grey).
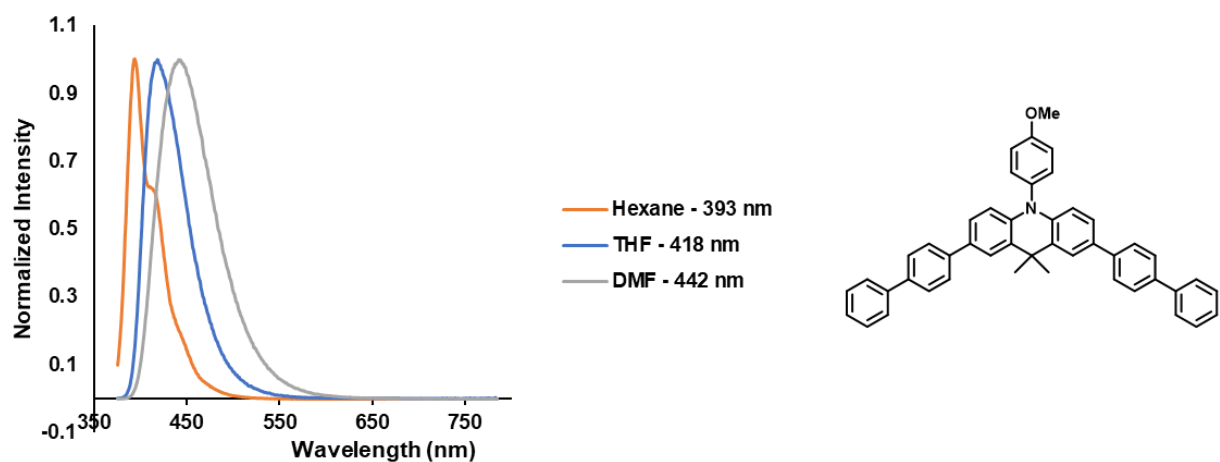
Figure 4.66: Normalized emission for **PC 6** measured in Hexane (orange), THF (blue) and DMF (grey).
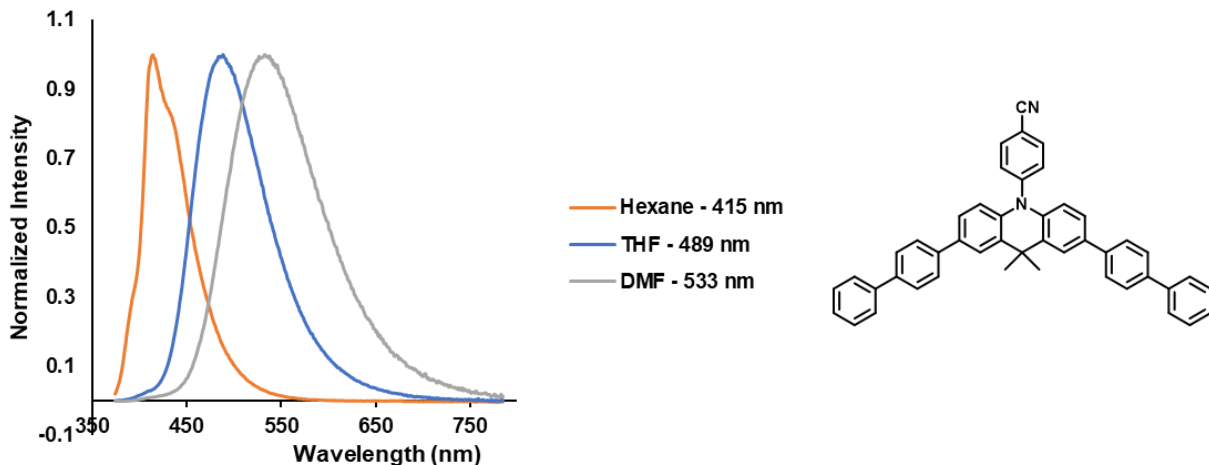
Figure 4.67: Normalized emission for **PC 7** measured in Hexane (orange), THF (blue) and DMF (grey).

Absolute Fluorescence Quantum Yields:

Absolute fluorescence quantum yields (AFQY) of PCs 1-7 were measured using an FS5 Spectrofluorometer from Edinburg Instruments with an SC-30 Integrating Sphere accessory using a direct excitation measurement method. Measurement was made over the photocatalyst samples (S) and reference solvents (R) scattering (R_s and S_s) and emission (R_e and S_e). The equation for the calculation of AFQY using the direct excitation method is as follows:

$$AFQY = \frac{S_e - R_e}{R_s - S_s} \; x \; 100$$

Scattering and emission spectral regions were measured separately. An O.D. filter for the scattering region with a correction of 9.67 x for R_s and S_s (in the case of excitation at 365 nm) after measurement. The transmission of the O.D. filter was measured at O.D. 0.103 using a Cary 5000 with diffuse reflectance accessory. All samples were prepared inside a nitrogen-filled glovebox at concentrations of 0.1 mM in degassed spectrochemical grade DMAc. Quartz cuvettes with white

Teflon caps and a path length of 1 cm were used. The AFQY value was calculated using the Fluoracle software using the equation described above.

To represent reaction conditions, AFQY values were measured at 365 nm. PCs 3,4,5, and 6 showed some emission at 365 nm and so all PCs were also measured at 325 nm, with PC 2 measured with excitation at 305 nm due to strong absorption at 325 nm.

Table 4.6: Results of measurement of fluorescence quantum yields of PCs 1-7 with excitation at 365 nm and 325 nm.

PC	$\Phi_{f, 365 nm}$	$\Phi_{f, 325 nm}$
1	0.1	0.3
2	0.7	0.1[a]
3	94	83
4	5.7	3.8
5	38	27
6	98	70
7	6.4	8.2

[a]Due to strong PC absorption at 325 nm, 305 nm was used for excitation wavelength.

Time Resolved Emission Measurements:

Time-resolved spectral emission measurements were performed on an LP980 spectrometer from Edinburgh Instruments equipped with a Continuum Minilight flashlamp pumped Q-switched Nd:Yag laser operating at 355 nm with a pulse-width of 2 ns and an intensified CCD camera for detection.

154

General Procedure: 0.5 mL of a 50 uM solution of PC dissolved in DMF was loaded into an NMR tube under inert atmosphere. The tube was frozen under liquid nitrogen, then placed into the sample chamber for analysis before thawing. Time-resolved emission was measured at time = 0 (no gate delay) with a 100 ns integration time and also with a delay of 1 ms with 30 ms integration time. Room temperature measurements were performed with time = 0, or no gate delay. To confirm that the 1 ms delayed emission at 77 K can be attributed to phosphorescence, room temperature measurements were also performed under the same conditions and no emission was detected for any PC. To evaluate influences of solvent polarity on time-resolved measurements, the above procedures were repeated in 2-MeTHF and Toluene for **PC 2**. In the case of measurements at 77 K with no gate delay, some scattering signals at 355 nm and 710 nm from the laser was observed.

Table 4.7: Summary of results of time-resolved emission for PCs 1-7 at room temperature and 77 K compared to computationally predicted triplet energies.

PC	$\lambda_{max,em,\,RT}$ (nm)[a]	$\lambda_{max,em,\,77\,K}$ (nm)[b]	$\lambda_{max,em,77\,K,\,1\,ms}$ (nm)[c]	$E_{S1,\,exp}$ (eV)[d]	$E_{S1,\,exp,\,77\,K}$ (eV)[d]	$E_{T1,\,exp,\,77\,K}$ (eV)[d]	$\Delta E_{ST,\,77\,K}$ (eV)[e]	$E_{T1,\,Calc}$ (eV)[f]	$E^{0*}_{S1,exp.}$ ($^2PC^{•+}/^1PC^*$) (V vs. SCE)[g]	$E^{0*}_{S1,exp,\,77\,K.}$ ($^2PC^{•+}/^1PC^*$) (V vs. SCE)[g]
1	494	428	530	2.55	2.90	2.34	0.56	2.41	-1.79	-2.14
2	505	455	531	2.44	2.72	2.33	0.39	2.36	-1.73	-2.01
2[h]	482	456	538	2.57	2.72	2.30	0.42	2.36	-1.86	-2.01
2[i]	459	435	532	2.70	2.85	2.33	0.52	2.36	-1.99	-2.14
3	459	435	518	2.71	2.85	2.39	0.46	2.43	-1.81	-1.95
4	471	423	530	2.74	2.93	2.34	0.59	2.30	-1.98	-2.16
5	442	421	527	2.80	2.95	2.35	0.60	2.29	-2.04	-2.19
6	446	419	530	2.79	2.96	2.34	0.62	2.28	-2.04	-2.21
7	529	458	524	2.32	2.71	2.37	0.34	2.39	-1.50	-1.89

[a]Room temperature emission measured with no delay. [b]Emission measured at 77 K with no delay. [c]Emission measured at 77 K after 1 ms delay. [d]Energies were calculated from the maximum wavelength of emission. [e]Calculated from $\Delta E_{ST} = E_{S1,\,exp.} - E_{T1,\,exp.}$ [f] DFT calculations performed at uM06/6-311+Gdp/uM06/6-31+Gdp level of theory with CPCM-described solvation in aqueous solvent. [g] Excited-state redox potentials were calculated using the energies estimated from the maximum wavelength of emission and the experimentally measured $E_{1/2}$; $E^{0*}_{S1,\,exp.} = E_{1/2} - E_{S1,exp.}$ [h]Measurements performed in 2-methyl tetrahydrofuran. [i]Measurements performed in toluene. All other measurements were performed in DMF.
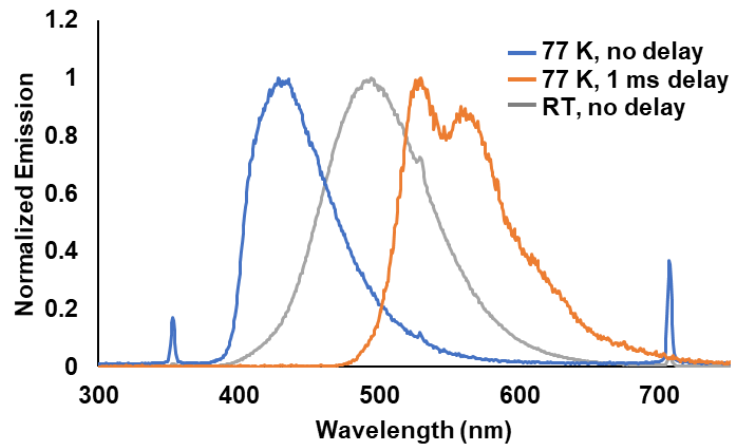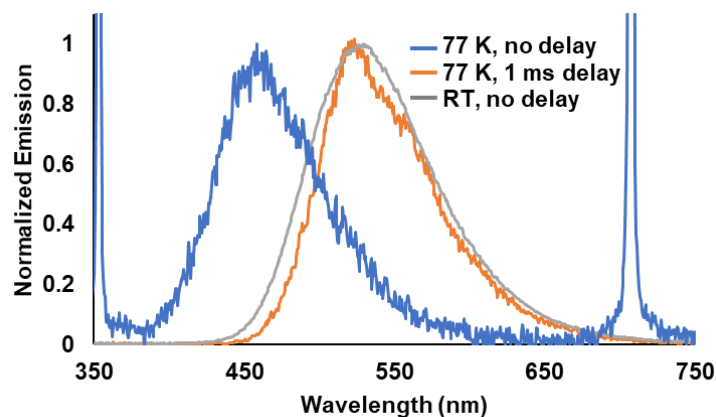
Figure 4.68: Normalized emission for **PC 1** measured at 77 K with no gate delay (blue), a 1 ms gate delay (orange) and at room temperature with no gate delay (grey) in DMF.
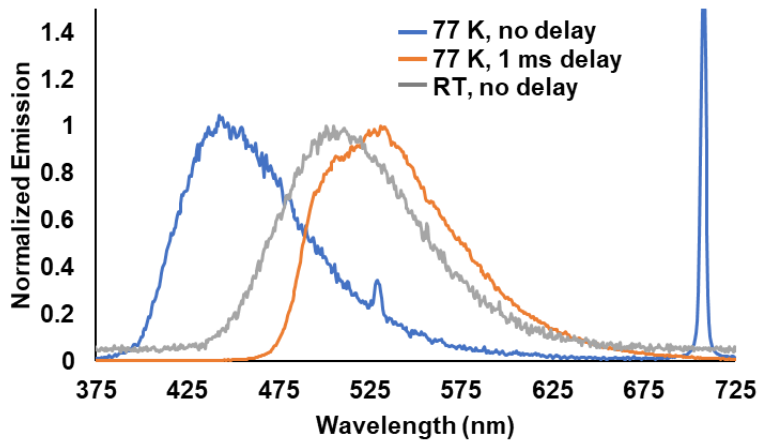
Figure 4.69: Normalized emission for **PC 2** measured at 77 K with no gate delay (blue), a 1 ms gate delay (orange) and at room temperature with no gate delay (grey) in DMF.
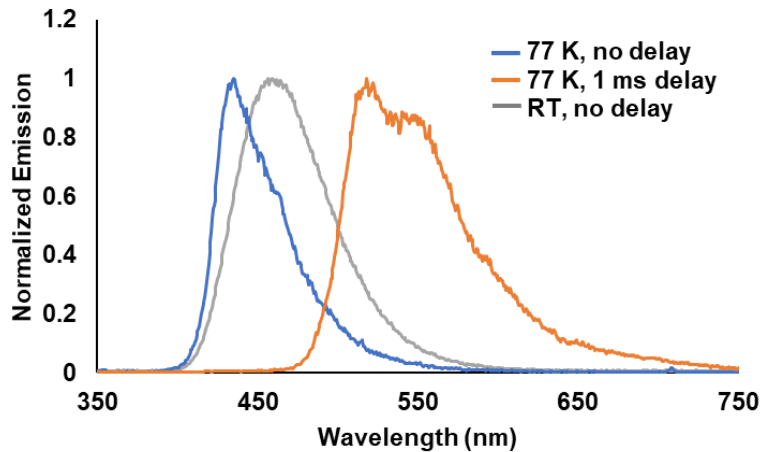
Figure 4.70: Normalized emission for **PC 3** measured at 77 K with no gate delay (blue), a 1 ms gate delay (orange) and at room temperature with no gate delay (grey) in DMF.
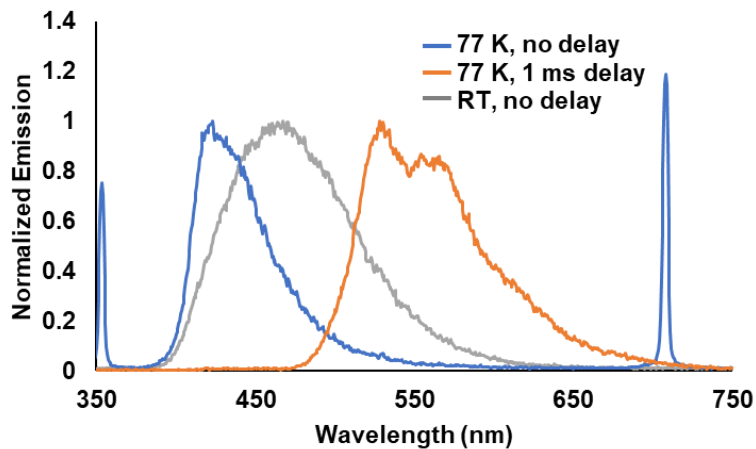
Figure 4.71: Normalized emission for **PC 4** measured at 77 K with no gate delay (blue), a 1 ms gate delay (orange) and at room temperature with no gate delay (grey) in DMF.
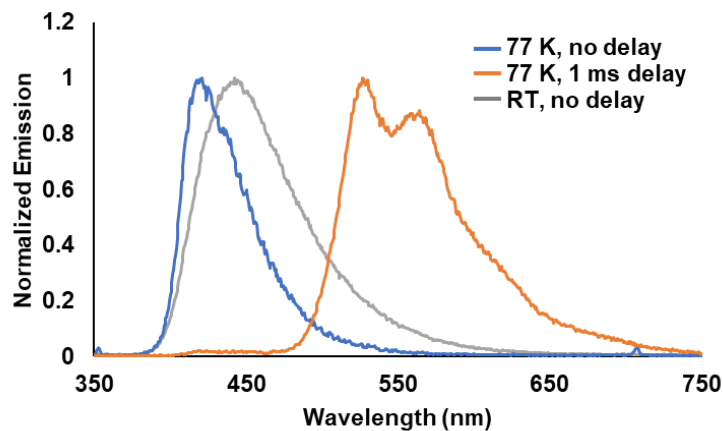
Figure 4.72: Normalized emission for PC 5 measured at 77 K with no gate delay (blue), a 1 ms gate delay (orange) and at room temperature with no gate delay (grey) in DMF.
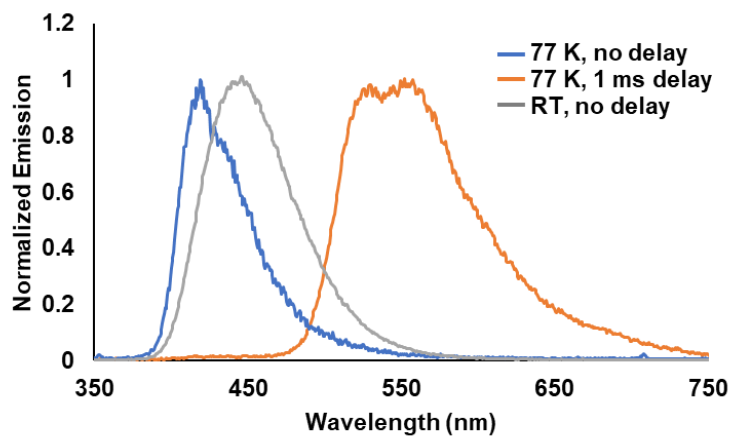
Figure 4.73: Normalized emission for PC 6 measured at 77 K with no gate delay (blue), a 1 ms gate delay (orange) and at room temperature with no gate delay (grey) in DMF.

Figure 4.74: Normalized emission for **PC 7** measured at 77 K with no gate delay (blue), a 1 ms gate delay (orange) and at room temperature with no gate delay (grey) in DMF.

Cyclic Voltammetry:

General Procedure for ATRP Initiators: Cyclic voltammetry of ATRP initiators was performed in a 3-compartment electrochemical cell with $Ag/AgNO_3$ (0.01 M) in acetonitrile as the reference electrode, $TBAPF_6$ in DMF (0.1 M) as the electrolyte solution, and platinum for the working and counter electrodes. All solutions were prepared on the benchtop, then sparged with nitrogen for 15 minutes before analysis. 1 mM solutions of analyte were used. Scans were performed at 100 mV/s with 2 cycles each. $E_{p/2}$ values were determined from the average of the onset of reduction and peak potential on the first cycle.
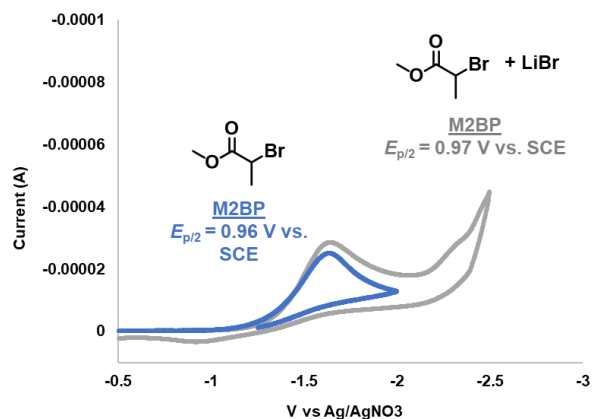
Figure 4.75: Cyclic voltammograms for methyl 2-bromopropionate (blue) and methyl 2-bromopropionate with 3 mM LiBr additive (grey).

General Procedure for PCs: Cyclic voltammetry of PCs 1-7 and their precursor compounds were performed in a 3-compartment electrochemical cell with Ag/AgNO$_3$ (0.01 M) in acetonitrile as the reference electrode, TBAPF$_6$ in DMF (0.1 M) as the electrolyte solution, and platinum for the working and counter electrodes. All solutions were prepared on the benchtop, then sparged with nitrogen for 15 minutes before analysis. For the non-reversible PC precursors, scans were conducted at 20 mV/s and 100 mV/s. Analysis of PCs 1-7 was conducted at 20 mV/s, 50 mV/s, 80 mV/s, and 100 mV/s with 5 cycles each.
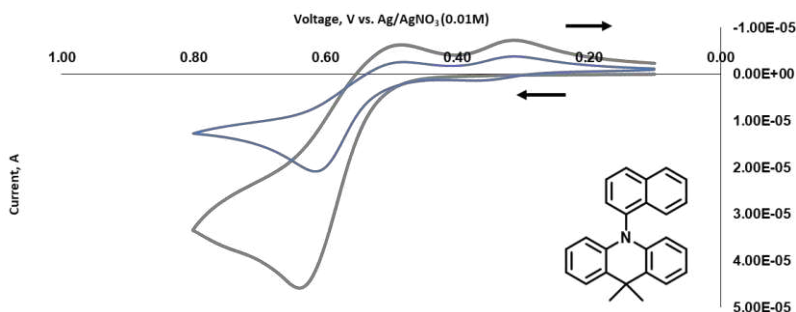
Figure 4.76: Cyclic voltammogram of Acrid-1N (precursor for **PCs 1, 2, and 3**) at 20 mV/s (blue) and 100 mV/s (grey).
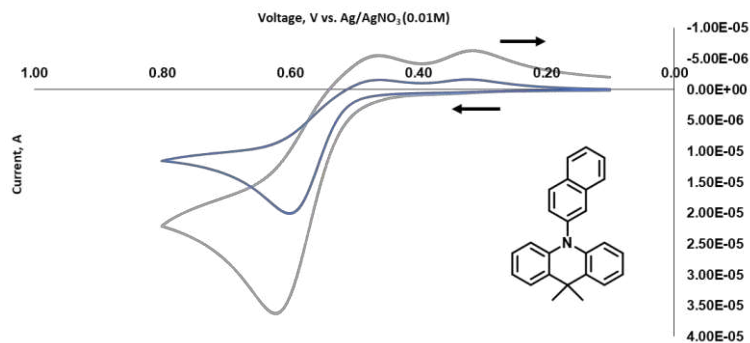
Figure 4.77: Cyclic voltammogram of Acrid-2N (precursor for **PC 4**) at 20 mV/s (blue) and 100 mV/s (grey).
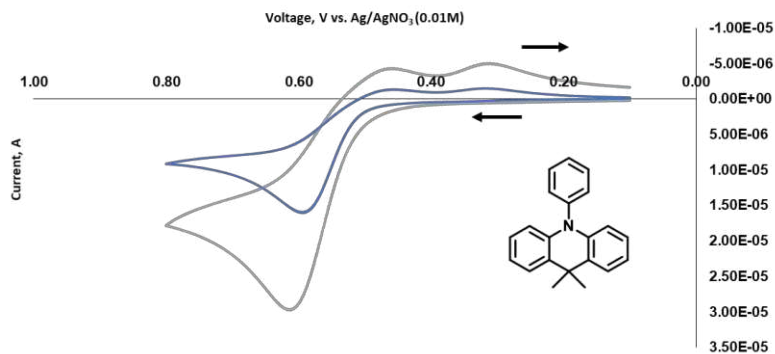
Figure 4.78: Cyclic voltammogram of Acrid-Ph (precursor for **PC 5**) at 20 mV/s (blue) and 100 mV/s (grey).
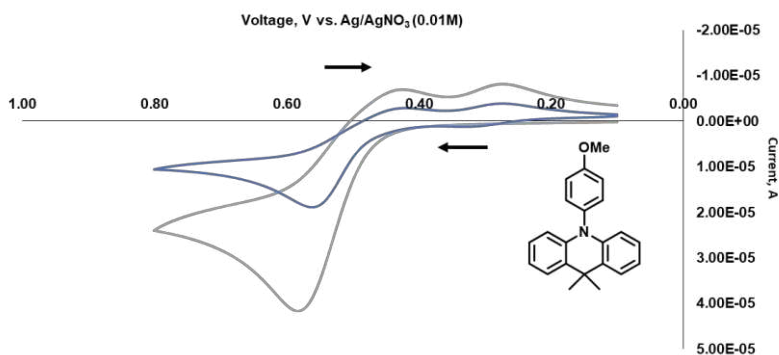
Figure 4.79: Cyclic voltammogram of Acrid-OMe (precursor for **PC 6**) at 20 mV/s (blue) and 100 mV/s (grey).
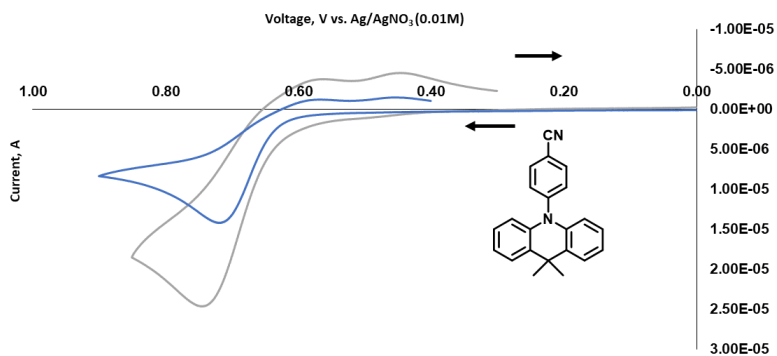
Figure 4.80: Cyclic voltammogram of Acrid-CN (precursor for **PC 7**) at 20 mV/s (blue) and 100 mV/s (grey).
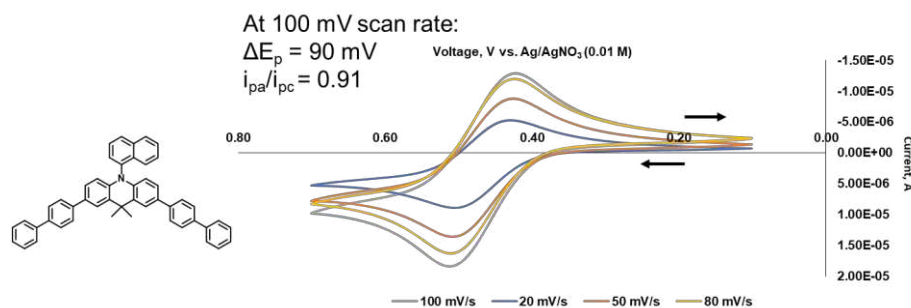
Figure 4.81: Cyclic voltammogram of **PC 1** at 20 mV/s (blue), 50 mV/s (orange), 80 mV/s (yellow) and 100 mV/s (grey).
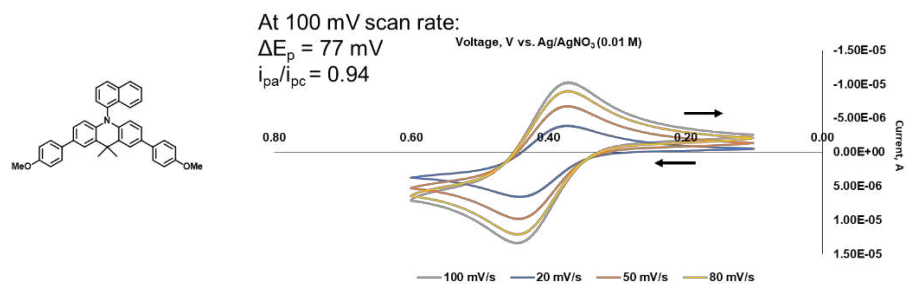
Figure 4.82: Cyclic voltammogram of **PC 2** at 20 mV/s (blue), 50 mV/s (orange), 80 mV/s (yellow) and 100 mV/s (grey).
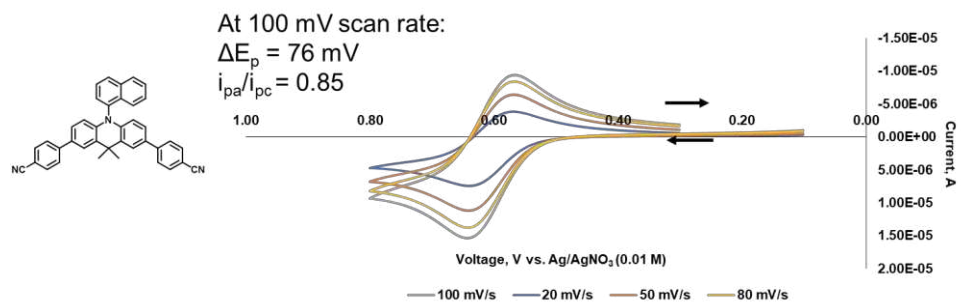
Figure 4.83: Cyclic voltammogram of **PC 3** at 20 mV/s (blue), 50 mV/s (orange), 80 mV/s (yellow) and 100 mV/s (grey).
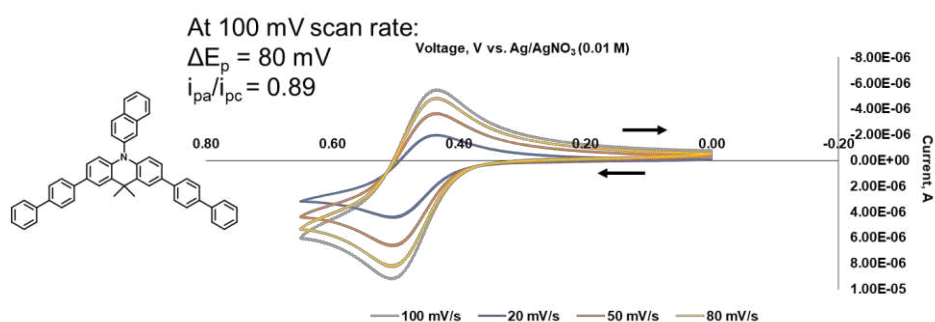
Figure 4.84: Cyclic voltammogram of **PC 4** at 20 mV/s (blue), 50 mV/s (orange), 80 mV/s (yellow) and 100 mV/s (grey).
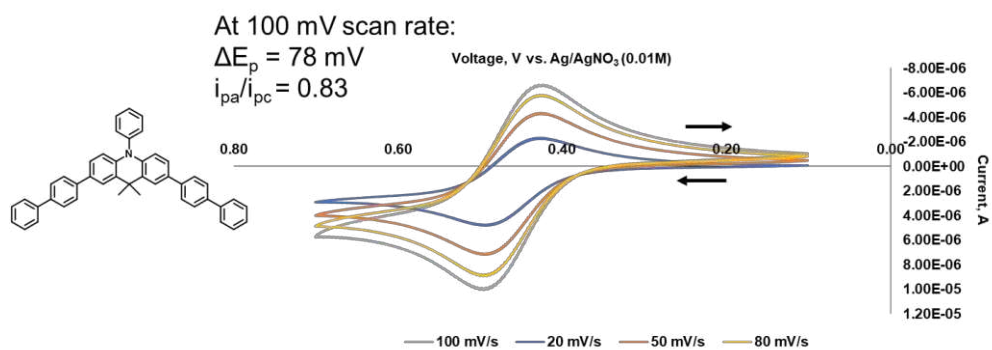
Figure 4.85: Cyclic voltammogram of **PC 5** at 20 mV/s (blue), 50 mV/s (orange), 80 mV/s (yellow) and 100 mV/s (grey).
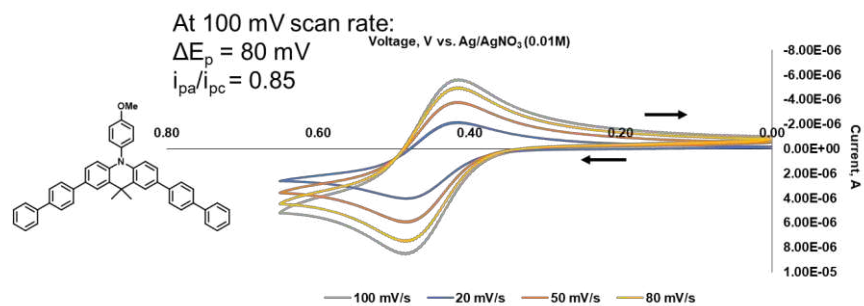
Figure 4.86: Cyclic voltammogram of **PC 6** at 20 mV/s (blue), 50 mV/s (orange), 80 mV/s (yellow) and 100 mV/s (grey).
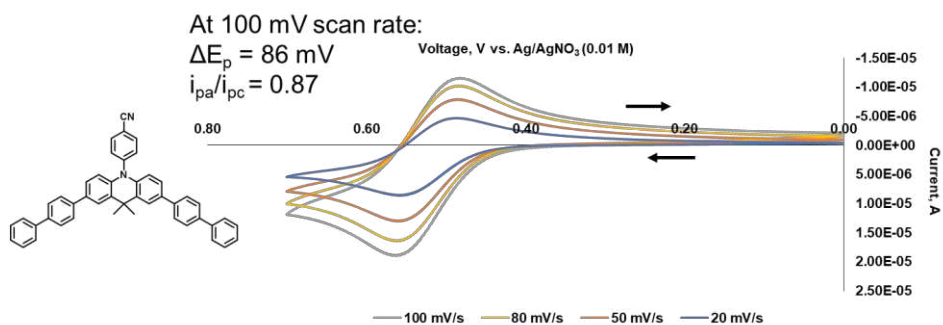
Figure 4.87: Cyclic voltammogram of **PC 7** at 20 mV/s (blue), 50 mV/s (orange), 80 mV/s (yellow) and 100 mV/s (grey).

Singly Occupied Molecular Orbital Calculations:

*Performed by Dr. Chern Hooi-Lim
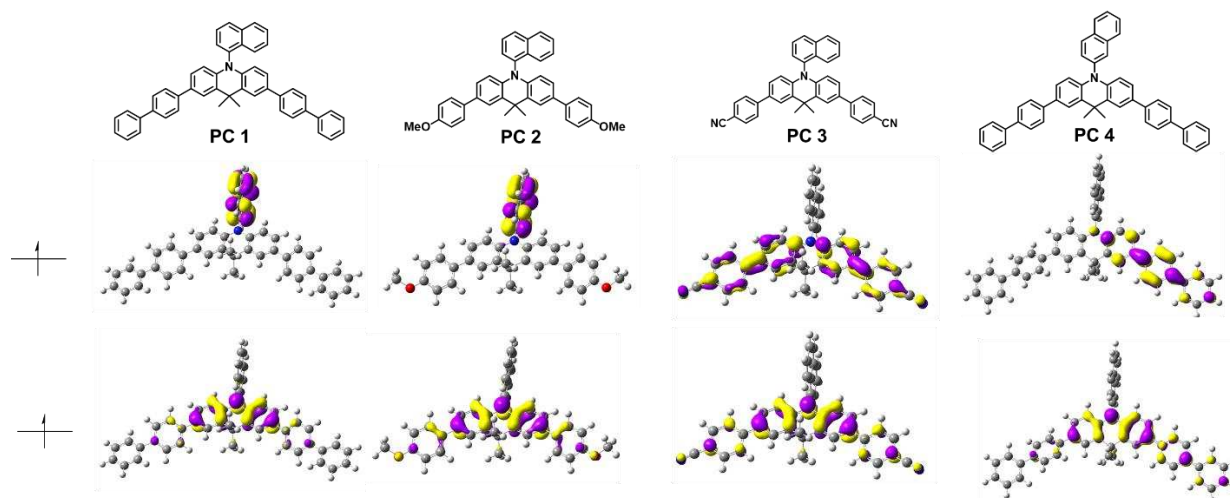
Figure 4.88: Computed singly occupied molecular orbitals (SOMOs) for PCs 1, 2, 3, and 4 (from left to right); the lower lying SOMO (bottom) and higher lying SOMO (top) for each PC in the triplet excited state are shown.
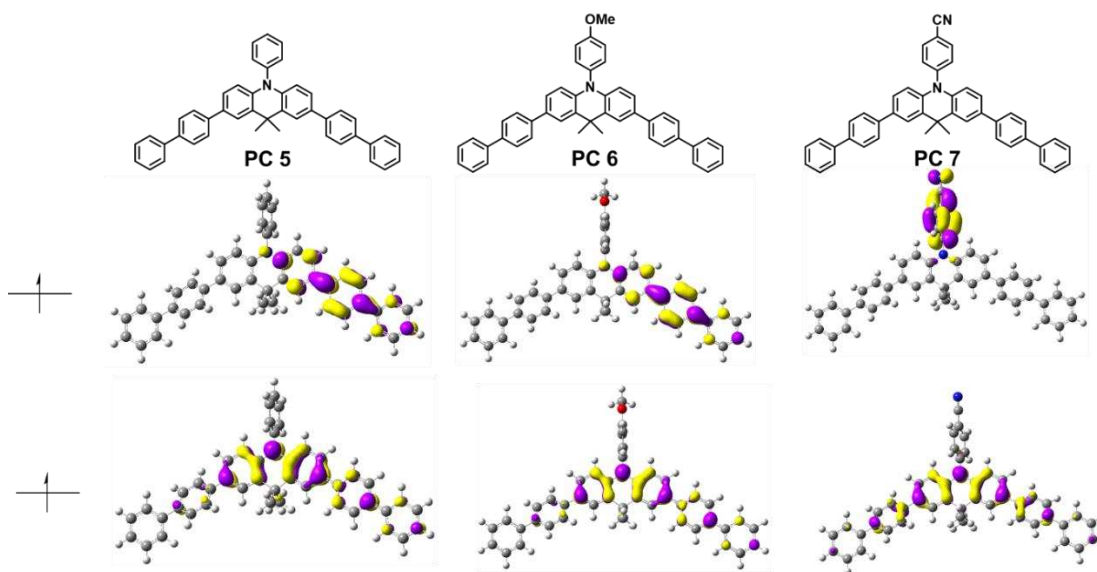
Figure 4.89: Computed singly occupied molecular orbitals (SOMOs) for PCs 5, 6, and 7 (from left to right); the lower lying SOMO (bottom) and higher lying SOMO (top) for each PC in the triplet excited state are shown.

Characterization of PC 2 in Presence of LiBr:
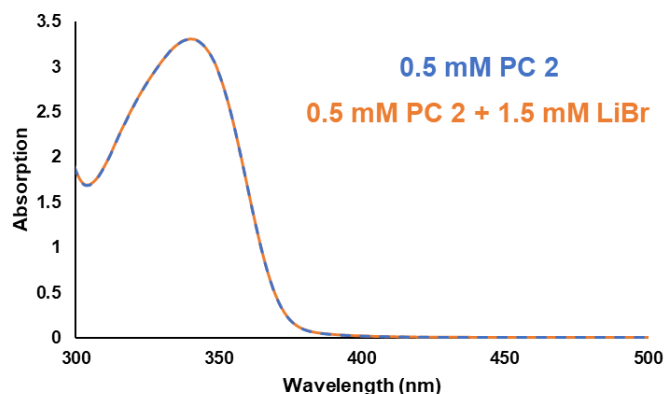
Figure 4.90: Absorption spectra of a 0.5 mM solution of PC 2 in DMF (blue) compared to absorption of a 0.5 mM solution of PC 2 and 1.5 mM solution of LiBr in DMF.
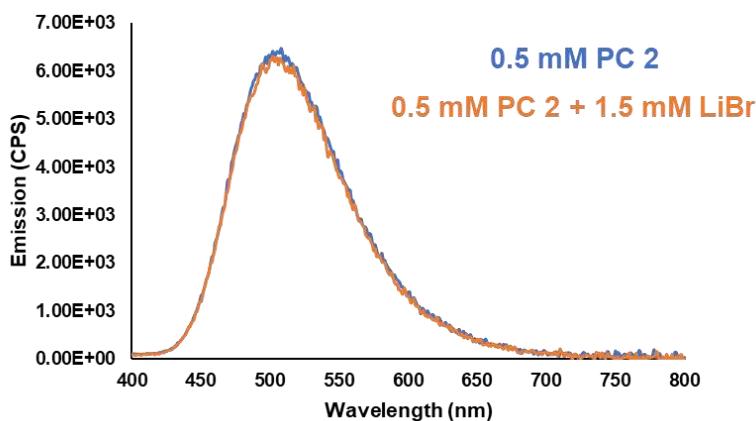
Figure 4.91: Emission spectra of a 0.5 mM solution of PC 2 in DMF (blue) compared to emission of a 0.5 mM solution of PC 2 and 1.5-mM solution of LiBr in DMF.

Polymerization Results in Batch
Batch Photoreactor Design:

Batch polymerizations were performed in a 100 mL beaker wrapped in aluminum foil with

a 12-inch strip of 12 V 365 nm LEDs purchased from LED Lighting Hut. Polymerizations using

380 nm and 455 nm light sources were performed with 12 V LED strips from Creative Lighting Solutions.
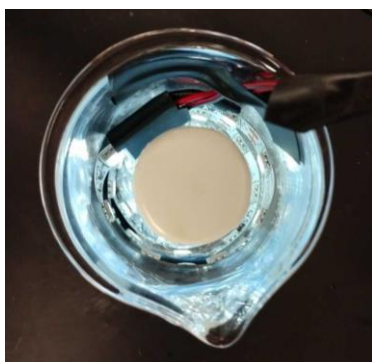
Figure 4.92: Batch photoreactor used for O-ATRP using dimethyl-dihydroacridines.

General Polymerization Procedure in Batch:

In a typical polymerization procedure, a scintillation vial with a small stir bar was loaded with 3.82 mg of PC 2 (6.97 µmol, 1 eq) and brought into a nitrogen-filled glovebox. Under red-light irradiation, 1 mL of *N,N*-dimethylacetamide (DMAc) was added to dissolve the PC, followed by 1 mL of butyl acrylate (6.97 mmol, 1000 eq.) and 13.3 µL of Diethyl 2-bromo-2-methylmalonate (DBMM) (0.70 µmol, 10 eq). The vial was then closed and placed into the photoreactor. Aliquots were taken by withdrawing 0.1 mL of reaction solution and quenching by injecting into a sealed vial with 0.8 mL of $CDCl_3$ containing 250 ppm BHT with air headspace. The sample was then taken out of the glovebox, where ^{1}H NMR analysis was performed. The sample was then dried under ambient conditions, dissolved in THF and molecular weight analysis was performed by GPC.

Polymerization Optimization in Batch Conditions:

Control polymerizations:

Table 4.8: Results of control experiments of O-ATRP of butyl acrylate using **PC 2** in batch reactor.[a]

Entry	[BA]:[DBMM]:[PC 2]	Time (min.)	Conv. (%)	$M_{n, calc.}$ (kDa)	$Đ$ (M_w/M_n)
1	[1000]:[0]:[1]	150	86	169	2.01
2	[1000]:[0]:[1][b]	120	0	--	--
3	[1000]:[10]:[0]	150	71	218	1.81
4	[1000]:[0]:[0]	60	30	327	1.63
5	[1000]:[0]:[0][c]	60	0	--	--
6	[1000]:[0]:[0][d]	60	0	--	--
7	[1000]:[10]:[1][e]	120	0	--	--

[a]Conditions are 1:1.5 of BA:DMAc by volume, irradiated by 365 nm LEDs, and performed at ambient temperatures. [b]Performed in the presence of air. [c]380 nm LEDs. [d]455 nm LEDs. [e]Conducted in the dark.
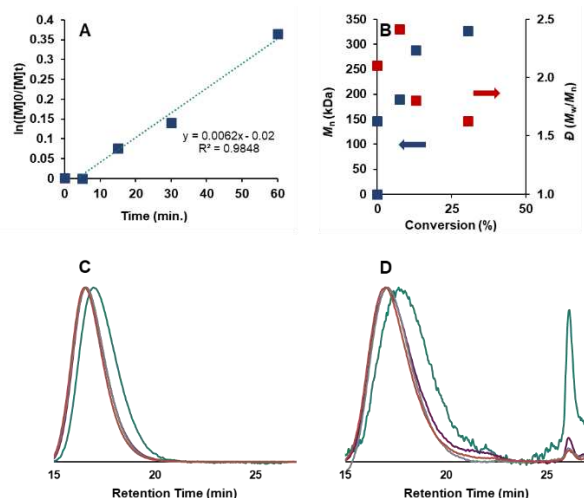
Figure 4.93: First order kinetic plot (a) and plot of M_n (blue) and dispersity (red) versus conversion (b) for reaction of BA and DMAc under 365 nm irradiation in batch reactor with corresponding SEC-MALS (c) and dRI (d) GPC traces.
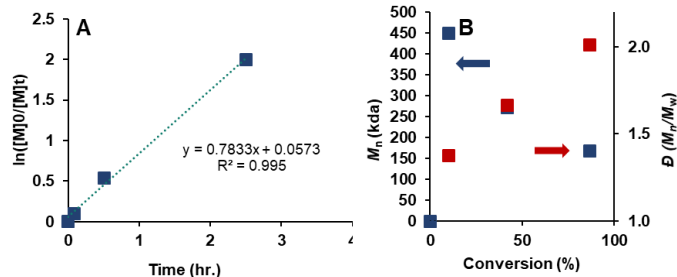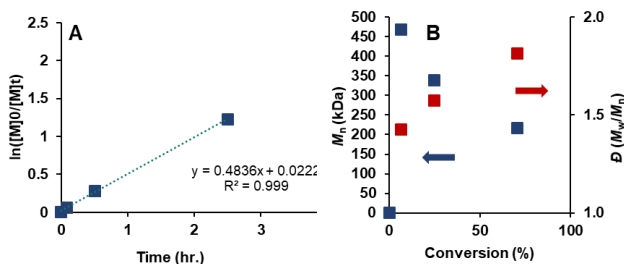
Figure 4.94: First order kinetic plot (a) and plot of M_n (blue) and dispersity (red) versus conversion (b) for reaction of BA and **PC 2** in DMAc under 355 nm irradiation in a batch reactor.

Figure 4.95: First order kinetic plot (a) and plot of M_n (blue) and dispersity (red) versus conversion (b) for reaction of BA and DBMM in DMAc under 365 nm irradiation in a batch reactor.

Light Source Optimizations:

Table 4.9: Results of light source optimizations using **PC 2** conducted in batch reactor.[a]

Entry	Light Source (nm)	Time (min.)	Conv. (%)	$M_{n, calc.}$ (kDa)	$Đ$ (M_w/M_n)	I^* (%)
1	365	77	10.6	10.2	1.53	96
2	380	120	73	21.4	9.6	45
3	455	120	86	31.2	3.79	37

[a]Conditions are [1000]:[10]:[1] of [BA]:[DBMM]:[PC 2] with 1 mL of BA to 1 mL of DMAc in 100 mL batch reactor beaker and performed at ambient temperatures.
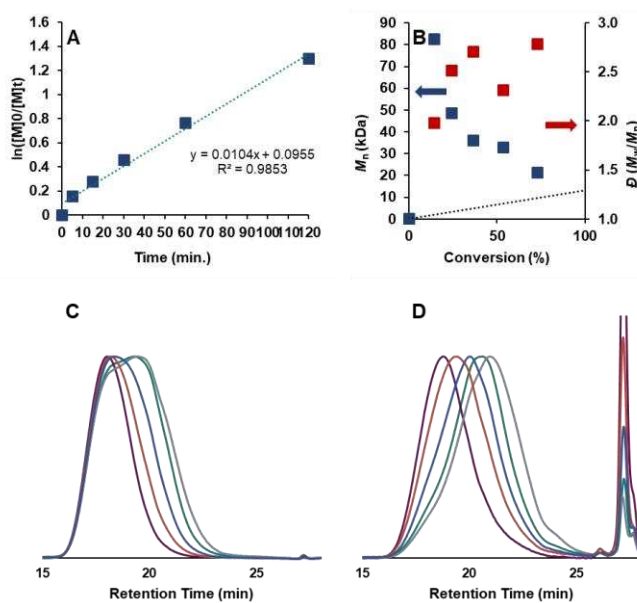
Figure 4.96: First order kinetic plot (a) and plot of M_n (blue) and dispersity (red) versus conversion (b) plotted against the theoretical M_n for O-ATRP of BA using **PC 2** under 380 nm irradiation in batch reactor with corresponding SEC-MALS (c) and dRI (d) GPC traces.
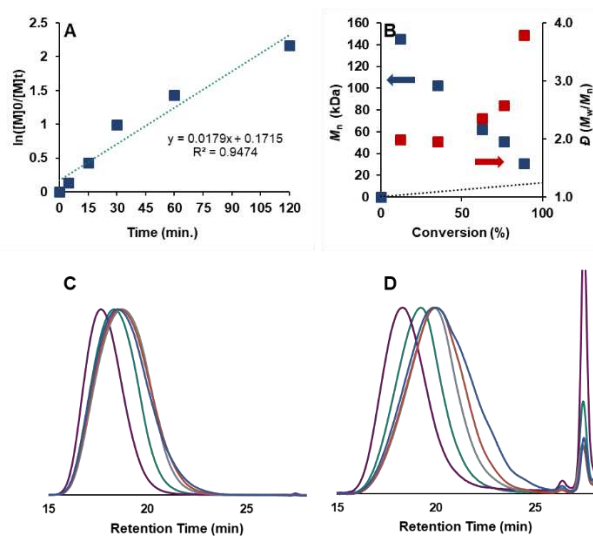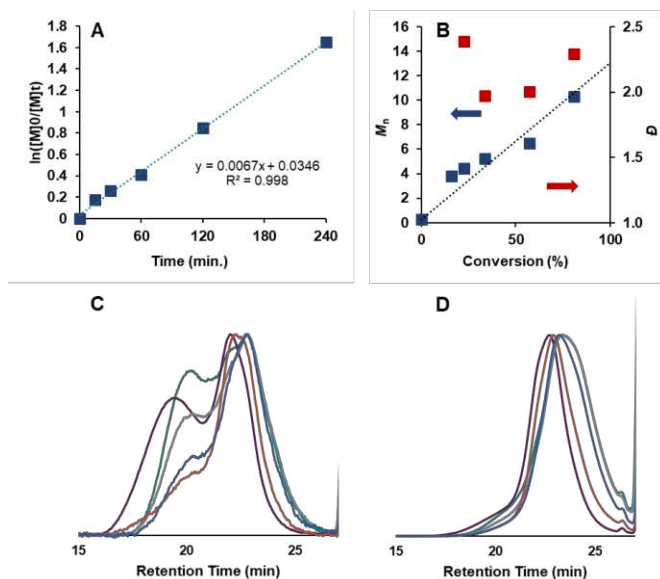

Figure 4.97: First order kinetic plot (a) and plot of M_n (blue) and dispersity (red) versus conversion (b) plotted against the theoretical M_n for O-ATRP of BA using **PC 2** under 455 nm irradiation in batch reactor with corresponding SEC-MALS (c) and dRI (d) GPC traces.

171

Common Organic Photocatalysts Screen:

Table 4.10: Results of O-ATRP of butyl acrylate using well-studied organic PCs.[a]

Entry	PC	Time (min.)	Conv. (%)[b]	$M_{n, calc.}$ (kDa)[c]	$M_{n, theo.}$ (kDa)[d]	Đ (M_w/M_n)[c]	I^* (%)[e]
1	PhenO	240	81	10.3	10.6	2.29	103
2	PhenN	240	82	16.2	10.7	1.47	66
3	4-CzIPN	120	86	63.1	11.3	3.15	18

[a]Conditions are [1000]:[10]:[1] of [BA]:[DBMM]:[PC] with 1 eq of DMAc to BA by volume. Reactions were irradiated by 365 nm LEDs in batch conditions at ambient temperatures. [b]Determined by ^{1}H NMR. [c]Measured using GPC. [d]Calculated by $(Conv \times [Mon]/[Init.] \times Mw_{Mon})/1000$. [e]Initiator efficiency (I^*) calculated by $(Theo. M_n/Calc. M_n) \times 100$.

Figure 4.98: First order kinetic plot (a) and plot of M_n (blue) and dispersity (red) versus conversion (b) plotted against the theoretical M_n for O-ATRP of BA using **PhenO** under 365 nm irradiation in batch reactor with corresponding SEC-MALS (c) and dRI (d) GPC traces. Conditions are [1000[:[10]:[1] of [BA]:[DBMM]:[PC] with 1 mL DMAc to 1 mL BA.
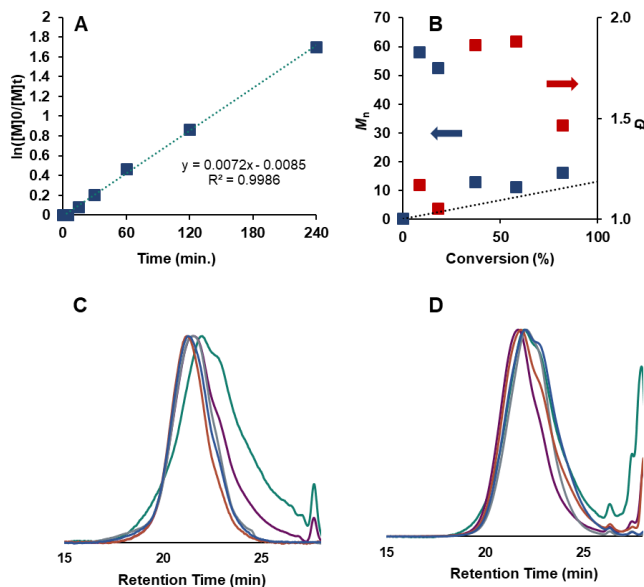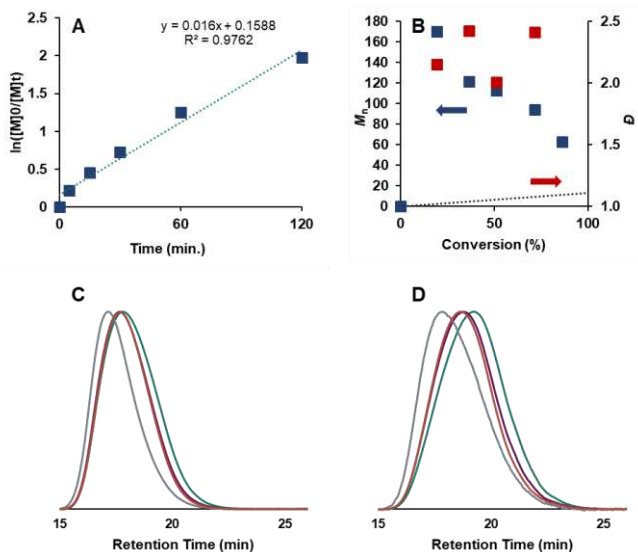
Figure 4.99: First order kinetic plot (a) and plot of M_n (blue) and dispersity (red) versus conversion (b) plotted against the theoretical M_n for O-ATRP of BA using **PhenN** under 365 nm irradiation in batch reactor with corresponding SEC-MALS (c) and dRI (d) GPC traces. Conditions are [1000[:[10]:[1] of [BA]:[DBMM]:[PC] with 1 mL DMAc to 1 mL BA.
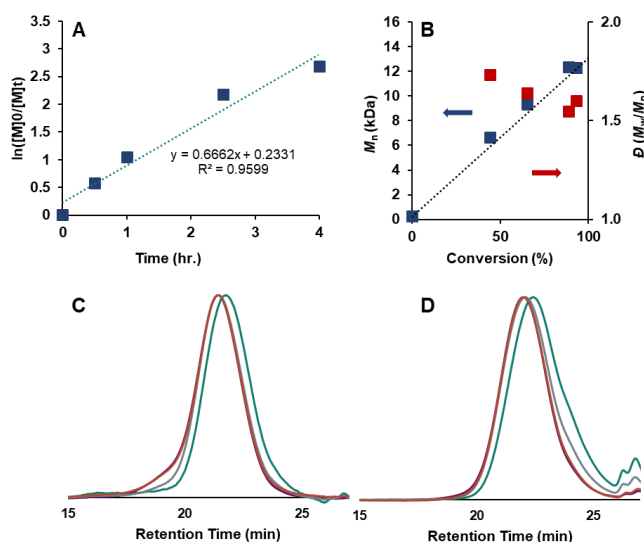

Figure 4.100: First order kinetic plot (a) and plot of M_n (blue) and dispersity (red) versus conversion (b) plotted against the theoretical M_n for O-ATRP of BA using **4-CzIPN** under 365 nm irradiation in batch reactor with corresponding SEC-MALS (c) and dRI (d) GPC traces. Conditions are [1000[:[10]:[1] of [BA]:[DBMM]:[PC] with 1 mL DMAc to 1 mL BA.

173

Dimethyl-dihydroacridine Photocatalyst Screen:

Table 4.11: Results of O-ATRP of butyl acrylate using **PCs 1-7** after 60 minutes irradiation.[a]

Entry	PC	Conv. (%)[b]	$M_{n, calc.}$ (kDa)[c]	$M_{n, theo.}$ (kDa)[d]	Đ (M_w/M_n)[c]	$I*$ (%)[e]
1	1	65	9.3	8.6	1.64	92
2	2	77	10.6	10.2	1.53	96
3	3	42	31.4	11.0	4.93	35
4	4	68	9.6	8.9	1.62	93
5	5	59	8.7	7.8	1.70	90
6	6	72	25.8	9.5	3.52	37
7	7	76	10.9	10.1	1.89	92

[a]Conditions are [1000]:[10]:[1] of [BA]:[DBMM]:[PC] with 1 eq of DMAc to BA by volume. Reactions were irradiated by 365 nm LEDs in batch conditions at ambient temperatures. [b]Determined by ^{1}H NMR. [c]Measured using GPC. [d]Calculated by $(Conv \times [Mon]/[Init.] \times Mw_{Mon})/1000$. [e]Initiator efficiency ($I*$) calculated by $(Theo. M_n/Calc. M_n) \times 100$.

Figure 4.101: First order kinetic plot (a) and plot of M_n (blue) and dispersity (red) versus conversion (b) plotted against the theoretical M_n for O-ATRP of BA using **PC 1** under 365 nm irradiation in batch reactor with corresponding SEC-MALS (c) and dRI (d) GPC traces. Conditions are [1000[:[10]:[1] of [BA]:[DBMM]:[PC] with 1 mL DMAc to 1 mL BA.
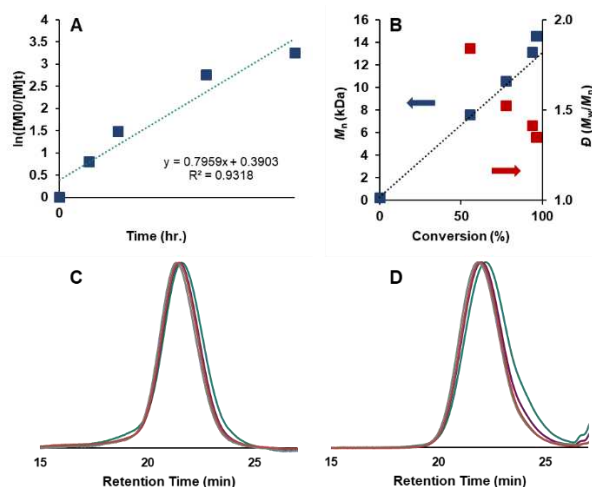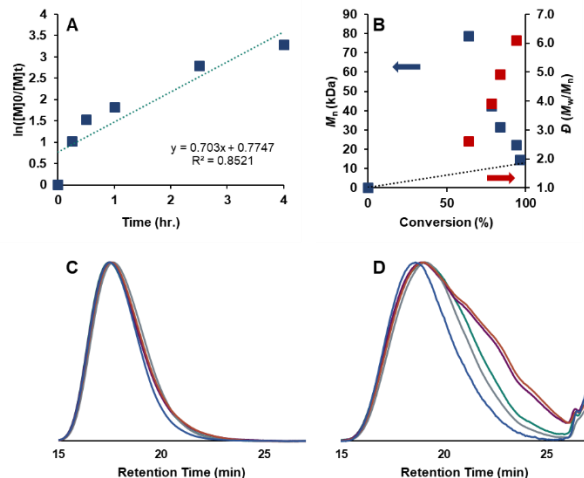
Figure 4.102: First order kinetic plot (a) and plot of M_n (blue) and dispersity (red) versus conversion (b) plotted against the theoretical M_n for O-ATRP of BA using **PC 2** under 365 nm irradiation in batch reactor with corresponding SEC-MALS (c) and dRI (d) GPC traces. Conditions are [1000[:[10]:[1] of [BA]:[DBMM]:[PC] with 1 mL DMAc to 1 mL BA.
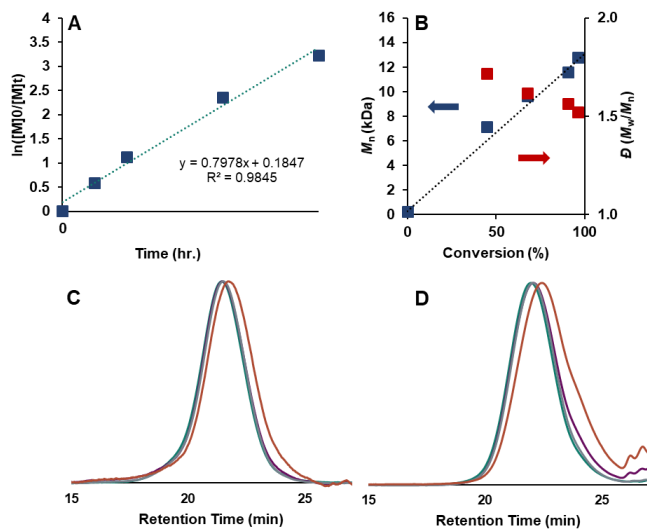

Figure 4.103: First order kinetic plot (a) and plot of M_n (blue) and dispersity (red) versus conversion (b) plotted against the theoretical M_n for O-ATRP of BA using **PC 3** under 365 nm irradiation in batch reactor with corresponding SEC-MALS (c) and dRI (d) GPC traces. Conditions are [1000[:[10]:[1] of [BA]:[DBMM]:[PC] with 1 mL DMAc to 1 mL BA.
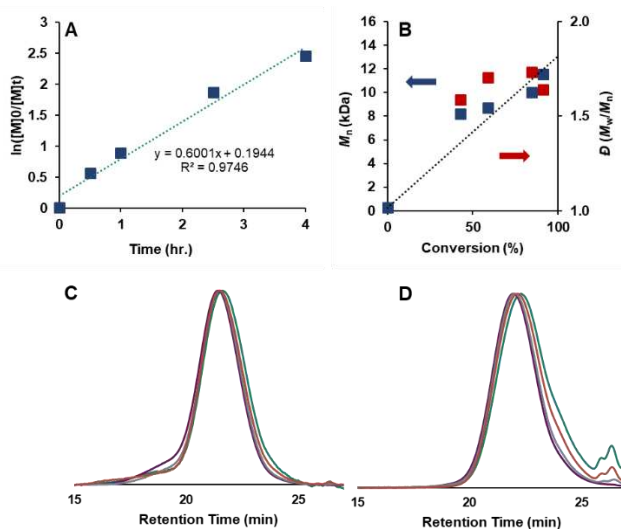
Figure 4.104: First order kinetic plot (a) and plot of M_n (blue) and dispersity (red) versus conversion (b) plotted against the theoretical M_n for O-ATRP of BA using **PC 4** under 365 nm irradiation in batch reactor with corresponding SEC-MALS (c) and dRI (d) GPC traces. Conditions are [1000[:[10]:[1] of [BA]:[DBMM]:[PC] with 1 mL DMAc to 1 mL BA.
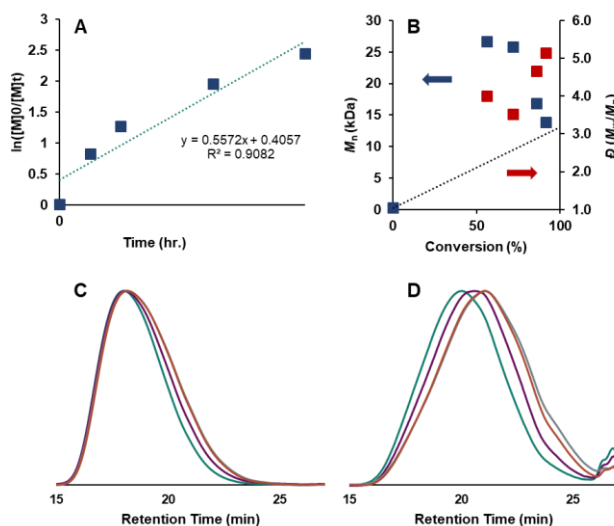

Figure 4.105: First order kinetic plot (a) and plot of M_n (blue) and dispersity (red) versus conversion (b) plotted against the theoretical M_n for O-ATRP of BA using **PC 5** under 365 nm irradiation in batch reactor with corresponding SEC-MALS (c) and dRI (d) GPC traces. Conditions are [1000[:[10]:[1] of [BA]:[DBMM]:[PC] with 1 mL DMAc to 1 mL BA.

Figure 4.106: First order kinetic plot (a) and plot of M_n (blue) and dispersity (red) versus conversion (b) plotted against the theoretical M_n for O-ATRP of BA using **PC 6** under 365 nm irradiation in batch reactor with corresponding SEC-MALS (c) and dRI (d) GPC traces. Conditions are [1000[:[10]:[1] of [BA]:[DBMM]:[PC] with 1 mL DMAc to 1 mL BA.
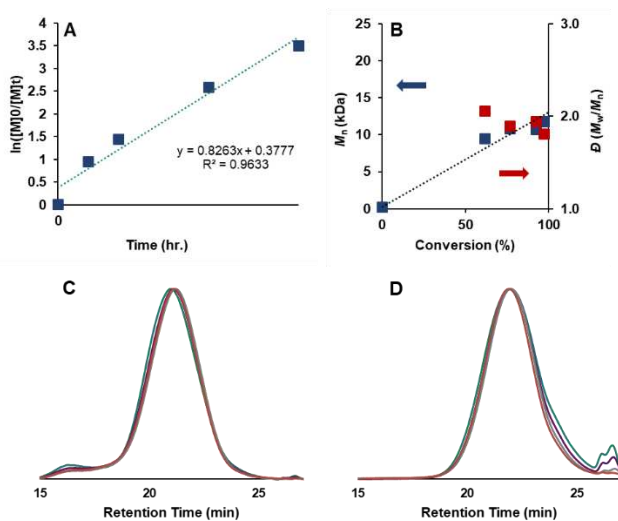

Figure 4.107: First order kinetic plot (a) and plot of M_n (blue) and dispersity (red) versus conversion (b) plotted against the theoretical M_n for O-ATRP of BA using **PC 7** under 365 nm irradiation in batch reactor with corresponding SEC-MALS (c) and dRI (d) GPC traces. Conditions are [1000[:[10]:[1] of [BA]:[DBMM]:[PC] with 1 mL DMAc to 1 mL BA.

Solvent Screen:

Table 4.12: Results of different solvents on the O-ATRP of butyl acrylate using **PC 2** after 60 minutes.[a]

Entry	Solvent	Conv. (%)[b]	$M_{n, calc.}$ (kDa)	$M_{n, theo.}$ (kDa)	Đ (M_w/M_n)	$I*$ (%)
1	DMAc	77	10.6	10.2	1.53	96
2	DMF	67	9.3	8.8	1.58	94
3	DMSO	71	9.7	9.4	2.37	97
4	THF	88	11.2	11.6	2.42	103
5	Benzene	92	24.6	12.1	4.47	49

[a]Conditions are [1000]:[10]:[1] of [BA]:[DBMM]:[PC 2] with 1 eq of solvent to BA by volume. Reactions were irradiated by 365 nm LEDs in batch conditions at ambient temperatures.
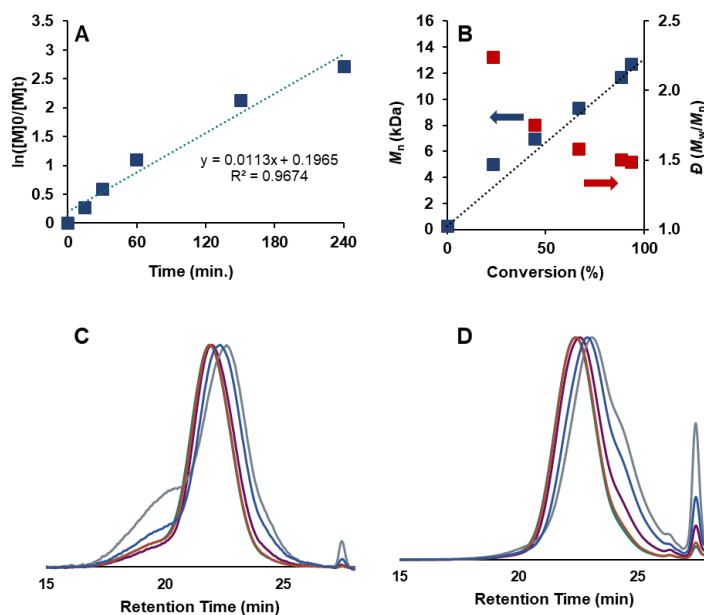

Figure 4.108: First order kinetic plot (a) and plot of M_n (blue) and dispersity (red) versus conversion (b) plotted against the theoretical M_n for O-ATRP of BA using **PC 2** under 365 nm irradiation in batch reactor with corresponding SEC-MALS (c) and dRI (d) GPC traces. Conditions are [1000[:[10]:[1] of [BA]:[DBMM]:[PC] with 1 mL DMF to 1 mL BA.
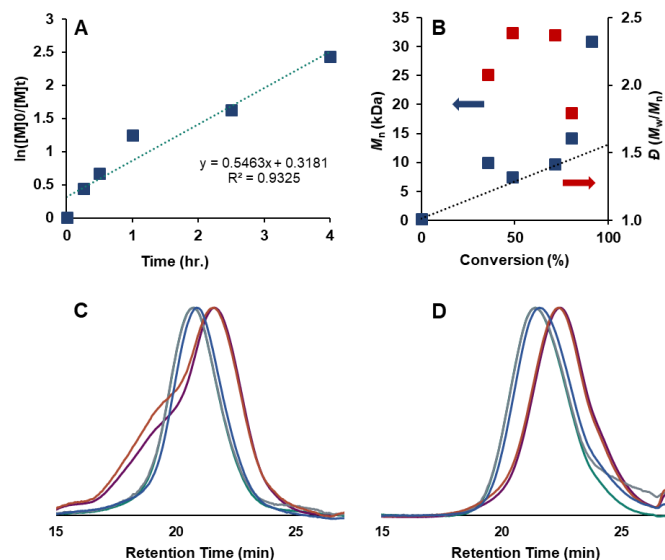
Figure 4.109: First order kinetic plot (a) and plot of M_n (blue) and dispersity (red) versus conversion (b) plotted against the theoretical M_n for O-ATRP of BA using **PC 2** under 365 nm irradiation in batch reactor with corresponding SEC-MALS (c) and dRI (d) GPC traces. Conditions are [1000[:[10]:[1] of [BA]:[DBMM]:[PC] with 1 mL DMSO to 1 mL BA.
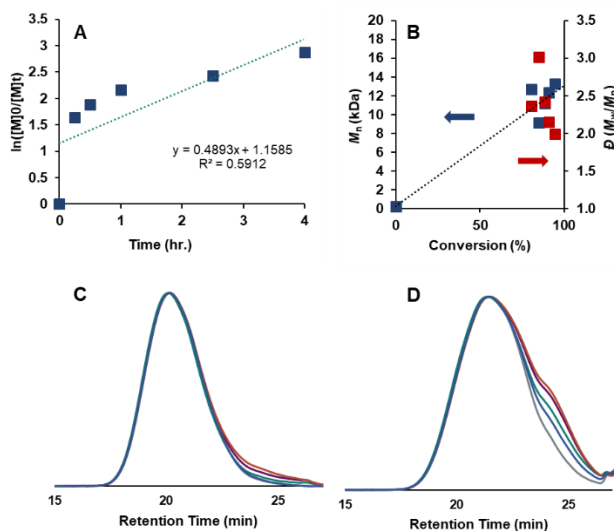

Figure 4.110: First order kinetic plot (a) and plot of M_n (blue) and dispersity (red) versus conversion (b) plotted against the theoretical M_n for O-ATRP of BA using **PC 2** under 365 nm irradiation in batch reactor with corresponding SEC-MALS (c) and dRI (d) GPC traces. Conditions are [1000[:[10]:[1] of [BA]:[DBMM]:[PC] with 1 mL THF to 1 mL BA.
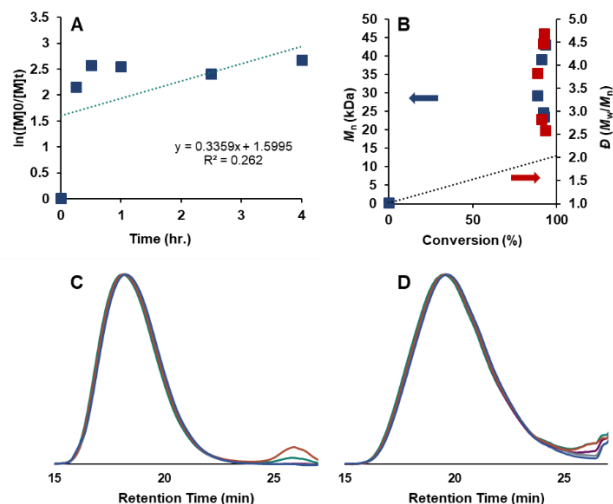
Figure 4.111: First order kinetic plot (a) and plot of M_n (blue) and dispersity (red) versus conversion (b) plotted against the theoretical M_n for O-ATRP of BA using **PC 2** under 365 nm irradiation in batch reactor with corresponding SEC-MALS (c) and dRI (d) GPC traces. Conditions are [1000[:[10]:[1] of [BA]:[DBMM]:[PC] with 1 mL Benzene to 1 mL BA.

Initiator Screen:

Table 4.13: Results of differing alkyl halide initiators on the O-ATRP of BA using **PC 2** after 60 minutes.[a]

Entry	Initiator	Conv. (%)[b]	$M_{n, calc.}$ (kDa)	$M_{n, theo.}$ (kDa)	$Đ$ (M_w/M_n)	I^* (%)
1	DBMM	77	10.6	10.2	1.53	96
2	M2BP	76	17.5	9.9	1.97	57
3	2BrCN	57	8.8	7.5	1.66	85

[a]Conditions are [1000]:[10]:[1] of [BA]:[RX]:[PC 2] with 1 eq DMAc relative to 1 mL BA and were irradiated by 365 nm light in batch reactor conditions with ambient temperature.
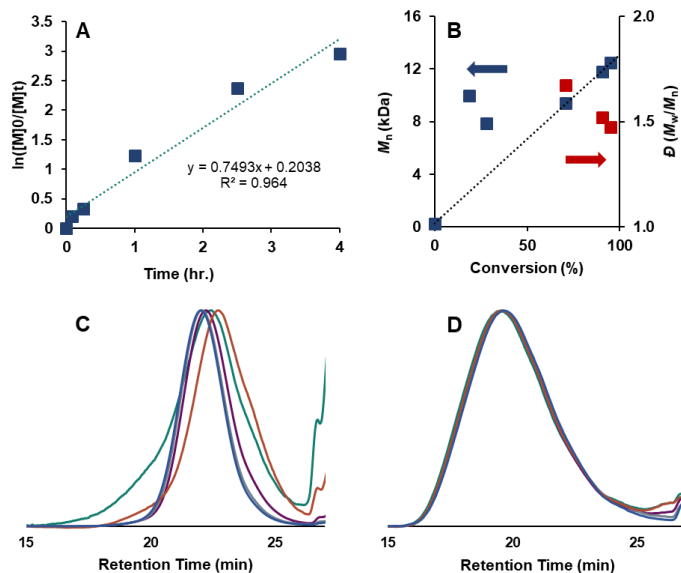
Figure 4.112: First order kinetic plot (a) and plot of M_n (blue) and dispersity (red) versus conversion (b) plotted against the theoretical M_n for O-ATRP of BA using **PC 2** under 365 nm irradiation in batch reactor with corresponding SEC-MALS (c) and dRI (d) GPC traces. Conditions are [1000[:[10]:[1] of [BA]:[DBMM]:[PC] with 1 mL DMAc to 1 mL BA.
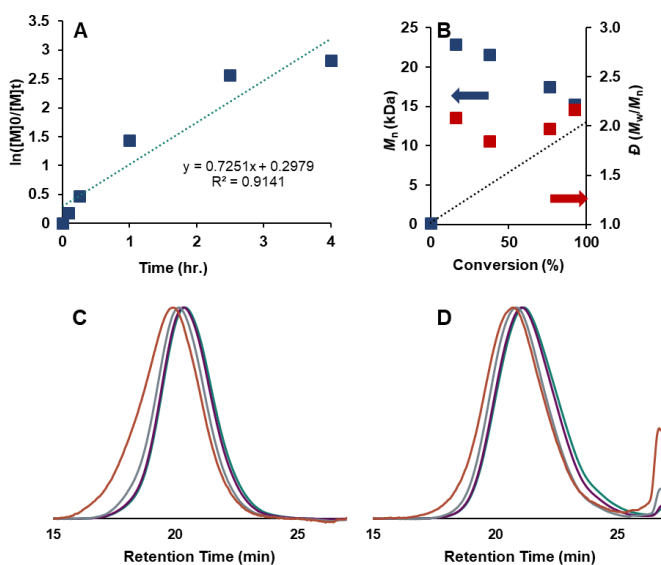

Figure 4.113: First order kinetic plot (a) and plot of M_n (blue) and dispersity (red) versus conversion (b) plotted against the theoretical M_n for O-ATRP of BA using **PC 2** under 365 nm irradiation in batch reactor with corresponding SEC-MALS (c) and dRI (d) GPC traces. Conditions are [1000[:[10]:[1] of [BA]:[M2BP]:[PC] with 1 mL DMAc to 1 mL BA.
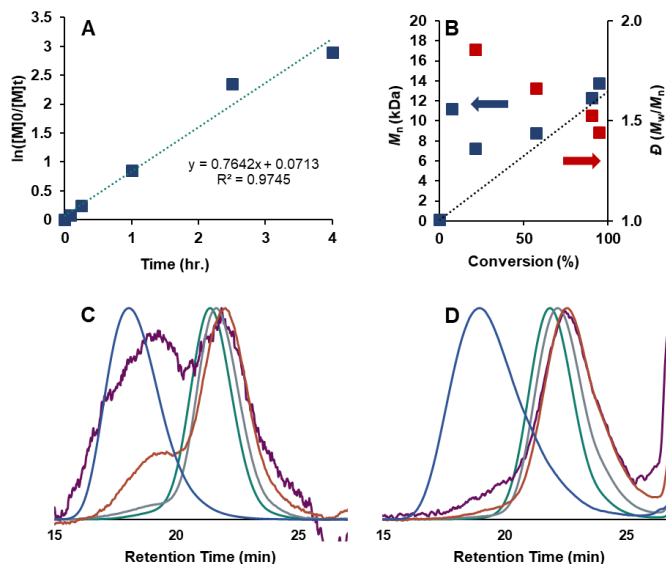
Figure 4.114: First order kinetic plot (a) and plot of M_n (blue) and dispersity (red) versus conversion (b) plotted against the theoretical M_n for O-ATRP of BA using **PC 2** under 365 nm irradiation in batch reactor with corresponding SEC-MALS (c) and dRI (d) GPC traces. Conditions are [1000[:[10]:[1] of [BA]:[2BrCN]:[PC] with 1 mL DMAc to 1 mL BA.

Effect of Reaction Concentration:

Table 4.14: Results of changing reaction concentration on the O-ATRP of BA using **PC 2** after 2.5 hours.[a]

Entry	DMAc:BA (v/v)	Conv. (%)[b]	$M_{n, calc.}$ (kDa)	$M_{n, theo.}$ (kDa)	$Đ$ (M_w/M_n)	$I*$ (%)
1	2:1	90	12/0	11/7	1.43	98
2	1.5:1	89	11.1	11.6	1.52	104
3	1:1	92	10.3	1.52	12.0	117
4	1:2	91	12.7	1.64	12.0	94

[a]Conditions are [1000]:[10]:[1] of [BA]:[DBMM]:[PC 2] and were irradiated by 365 nm light in batch reactor conditions with ambient temperature.
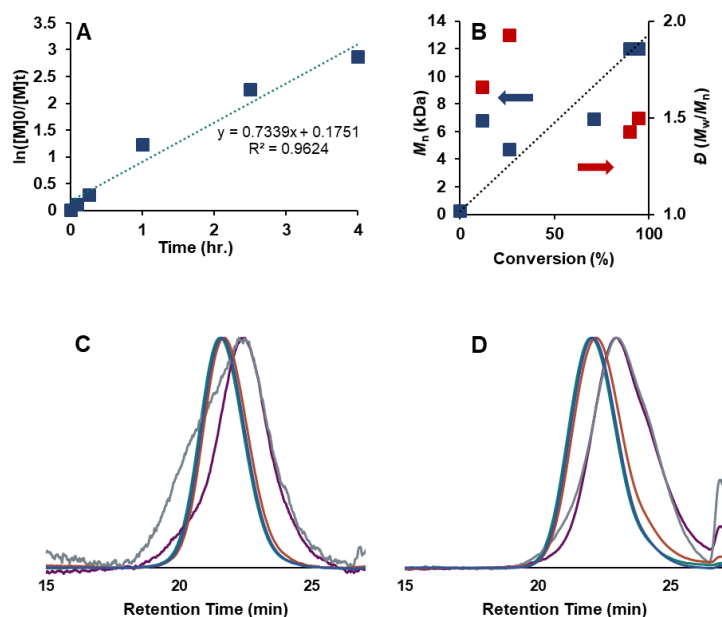
Figure 4.115: First order kinetic plot (a) and plot of M_n (blue) and dispersity (red) versus conversion (b) plotted against the theoretical M_n for O-ATRP of BA using **PC 2** under 365 nm irradiation in batch reactor with corresponding SEC-MALS (c) and dRI (d) GPC traces. Conditions are [1000[:[10]:[1] of [BA]:[DBMM]:[PC] with 2 mL DMAc to 1 mL BA.
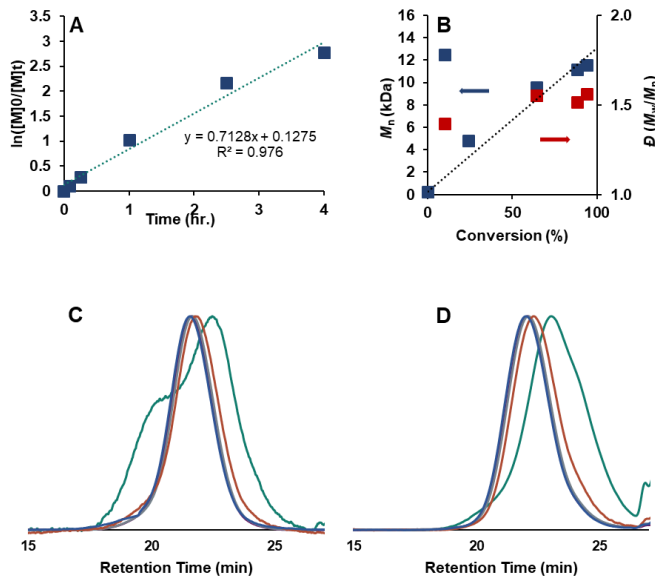

Figure 4.116: First order kinetic plot (a) and plot of M_n (blue) and dispersity (red) versus conversion (b) plotted against the theoretical M_n for O-ATRP of BA using **PC 2** under 365 nm irradiation in batch reactor with corresponding SEC-MALS (c) and dRI (d) GPC traces. Conditions are [1000[:[10]:[1] of [BA]:[DBMM]:[PC] with 1.5 mL DMAc to 1 mL BA.

Figure 4.117: First order kinetic plot (a) and plot of M_n (blue) and dispersity (red) versus conversion (b) plotted against the theoretical M_n for O-ATRP of BA using **PC 2** under 365 nm irradiation in batch reactor with corresponding SEC-MALS (c) and dRI (d) GPC traces. Conditions are [1000[:[10]:[1] of [BA]:[DBMM]:[PC] with 1 mL DMAc to 1.5 mL BA.
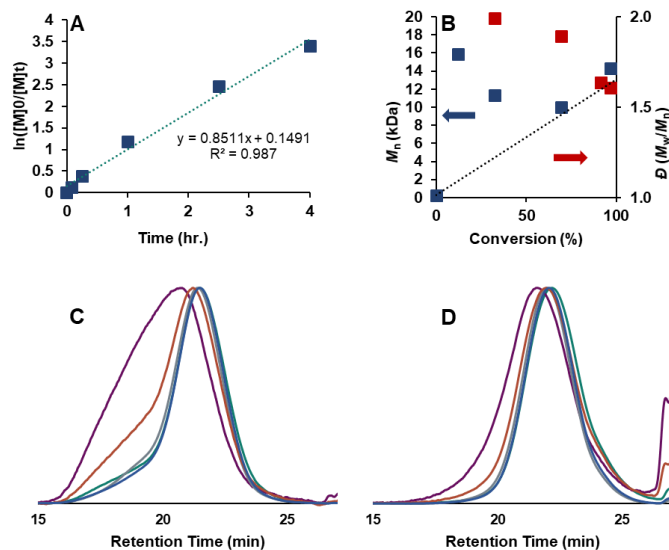
PC loadings:

Table 4.15: Results of O-ATRP of BA after 1 hour testing the effect of **PC 2** loadings.[a]

Entry	Mol % PC 2	Conv. (%)[b]	$M_{n, calc.}$ (kDa)	$M_{n, theo.}$ (kDa)	$Đ$ (M_w/M_n)	I^* (%)
1	0.1	89	11.1	11.6	1.52	104
2	0.075	77	10.2	10.1	1.57	100
3	0.05	77	10.9	10.1	1.55	92
4	0.025	86	10.7	11.2	1.70	104
5	0.01	88	16.3	11.5	2.13	71

[a]Conditions are [1000]:[10]:[X] of [BA]:[DBMM]:[PC 2] with 1.5 equivalents of DMAc to BA by volume. Polymerizations were irradiated by 365 nm light in batch reactor conditions with ambient temperature.
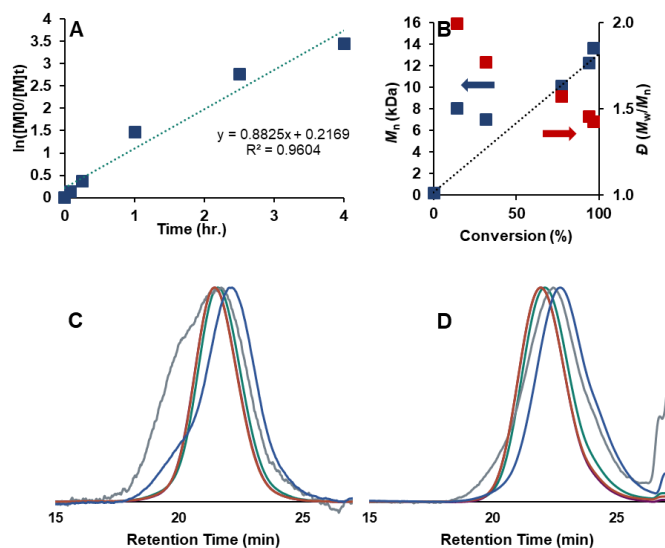
Figure 4.118: First order kinetic plot (a) and plot of M_n (blue) and dispersity (red) versus conversion (b) plotted against the theoretical M_n for O-ATRP of BA using **PC 2** under 365 nm irradiation in batch reactor with corresponding SEC-MALS (c) and dRI (d) GPC traces. Conditions are [1000[:[10]:[0.75] of [BA]:[DBMM]:[PC] with 1.5 mL DMAc to 1 mL BA.

Figure 4.119: First order kinetic plot (a) and plot of M_n (blue) and dispersity (red) versus conversion (b) plotted against the theoretical M_n for O-ATRP of BA using **PC 2** under 365 nm irradiation in batch reactor with corresponding SEC-MALS (c) and dRI (d) GPC traces. Conditions are [1000[:[10]:[0.5] of [BA]:[DBMM]:[PC] with 1.5 mL DMAc to 1 mL BA.
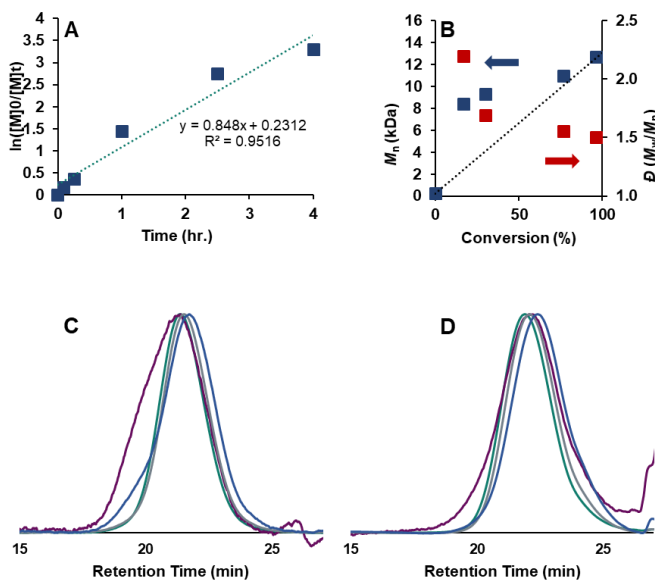
Figure 4.120: First order kinetic plot (a) and plot of M_n (blue) and dispersity (red) versus conversion (b) plotted against the theoretical M_n for O-ATRP of BA using **PC 2** under 365 nm irradiation in batch reactor with corresponding SEC-MALS (c) and dRI (d) GPC traces. Conditions are [1000[:[10]:[0.25] of [BA]:[DBMM]:[PC] with 1.5 mL DMAc to 1 mL BA.
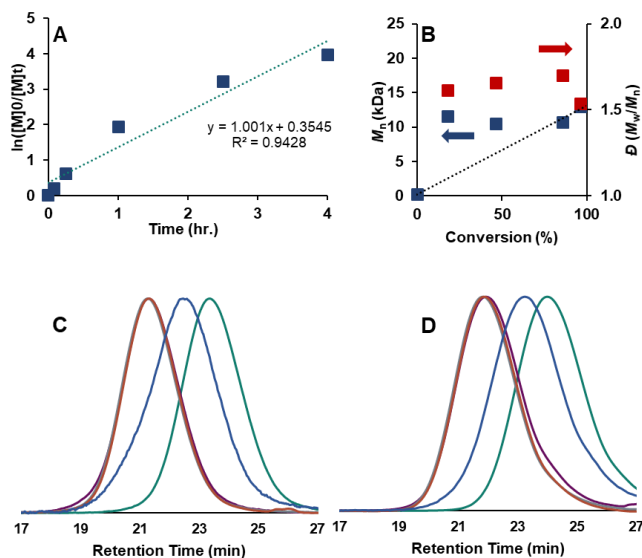

Figure 4.121: First order kinetic plot (a) and plot of M_n (blue) and dispersity (red) versus conversion (b) plotted against the theoretical M_n for O-ATRP of BA using **PC 2** under 365 nm irradiation in batch reactor with corresponding SEC-MALS (c) and dRI (d) GPC traces. Conditions are [1000[:[10]:[0.1] of [BA]:[DBMM]:[PC] with 1.5 mL DMAc to 1 mL BA.
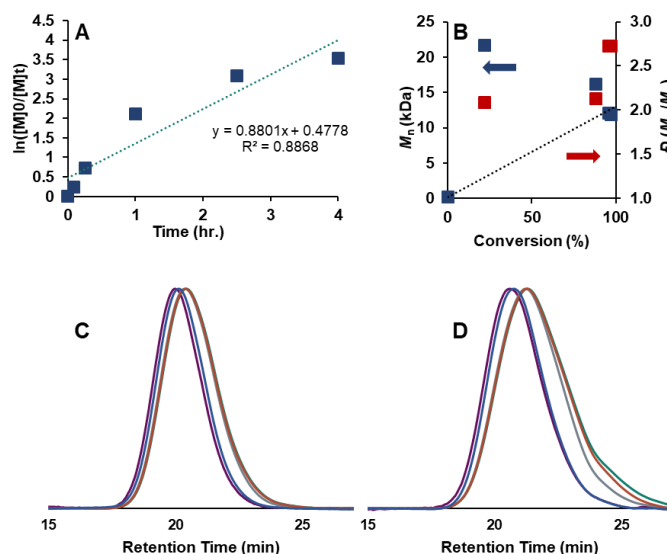
Pulsed Irradiation (On/off) Experiment:

A pulsed irradiation experiment was conducted using the same protocols as a typical batch experiment (described above). After 5 minutes of irradiation by 365 nm LED, an aliquot was taken. Then, the reaction was wrapped in foil and stirred at ambient temperatures for 5 minutes. After that time, another aliquot was taken. This procedure was repeated for intervals of 10, 15, 30, 60, and minutes, followed by an extended "off" period of 16 hours.

Polymerization Results in Flow

Flow Reactor Design:

Flow polymerizations were performed using a Hepatochem Photoredox Temperature Controlled reactor with a 2 mL flow attachment, also purchased directly from Hepatochem and especially configured for this photoreactor. The light source used was a 18 W 365 nm EvoluChem bulb (part no. HCK1012-01-011 from Hepatochem). The flow tubing was 1/16 in O.D. and 0.003 in I.D. with PFA as the tubing material, with inlet and outlet tubing purchased from IDEX Health and Science. All ferrules and fittings were purchased from IDEX Health and Science. The flow rate was controlled using a Pump 11 Elite Syringe Pump from Harvard Apparatus with a 50 Ml stainless steel syringe fitted with chemically resistant Kalrez O-rings.
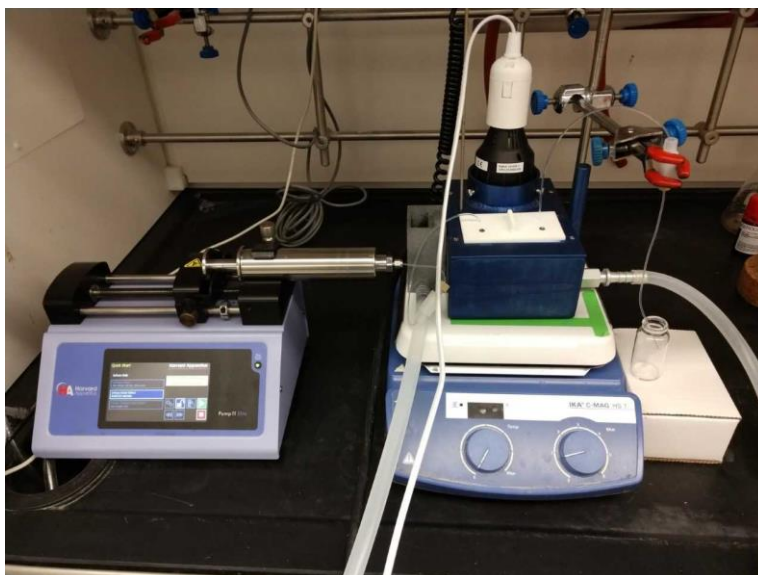
Figure 4.122: Flow reactor setup consisting of syringe pump and stainless-steel syringe (left) and temperature-controlled flow reactor with 18W 365 LED purchased from Hepatochem (right).

General Polymerization Procedure in Flow:

In a typical polymerization experiment, a vial was loaded with 26.7 mg of Acrid-1N-Ome (0.048 µmol, 1 eq.), then brought into a nitrogen-filled glovebox. Under red light irradiation, 7 Ml of DMAc and 7 Ml of butyl acrylate (0.048 mol, 1000 eq.) was then added. Once all catalyst was fully dissolved, 93.3 µL of DBMM (0.488 µmol, 10 eq.) was added using a glass syringe. The reaction mixture was then transferred to a 50 Ml stainless steel syringe and the first section of tubing attached. The syringe was then removed from the glovebox. Excess gas was pushed out of the syringe, then the first section of tubing was quickly connected to the reactor. The reaction was started with the initial flow rate using a syringe pump. The temperature of the reactor was controlled using a 188ecirculatory set to 22 ºC, which recirculated a 1/1 v/v mixture of ethylene glycol and water. The timing for the first equilibration period was set after 1 Ml of initial infusion

188

volume. For all timepoints, an equilibration period of 1.25 times the residence time was performed, followed by 0.125 times of collection time (see Table S8). The resulting polymer was collected directly into a vial containing 1 Ml of BHT-deuterated chloroform. Conversion analysis was performed using ^{1}H NMR and molecular weight analysis was performed using SEC-MALS GPC.

Table 4.16: Example of calculations used for O-ATRP experiments performed in 2 Ml continuous flow reactor. Residence time is determined by flow rate/reactor volume.

Entry	Res. Time (min.)	Flow Rate (Ml/min)	Equilibration Time (min.)	Collection Time (min.)
1	1.5	1.333	1.88	0.1875
2	5	0.400	6.25	0.625
3	15	0.133	18.75	1.875
4	30	0.067	37.50	3.75
5	45	0.044	56.25	5.625
6	60	0.033	75	7.5

Polymerization Optimization in Flow Conditions:

Control Polymerizations:

Table 4.17: Results of control experiments of O-ATRP of butyl acrylate using **PC 2** in flow reactor.[a]

Entry	[BA]:[DBMM]:[PC 2]	Res. Time (min.)	Conv. (%)	$M_{n, calc.}$ (kDa)	$Đ$ (M_w/M_n)
1	[1000]:[0]:[1]	45	86	53	3.15
2	[1000]:[10]:[0]	45	0	--	--
3	[1000]:[0]:[0]	60	0	--	--
4	[1000]:[10]:[1][b]	45	59	9.3	1.65

[a]Conditions are 1:1.5 of BA:DMAc by volume, irradiated by 365 nm LEDs, and performed at 22 ºC. [b]Catalyzed by PhenO.

Dihydroacridine PC Screen:

Table 4.18: Results of O-ATRP of BA using **PCs 1-7** in continuous flow.[a]

Entry	PC	Res. Time (min.)	Conv. (%)[b]	$M_{n, calc.}$ (kDa)[c]	$M_{n, theo.}$ (kDa)[d]	$Đ$ (M_w/M_n)[c]	$I*$ (%)[e]
1	1	45	67	8.9	8.9	1.59	100
2	2	45	81	11.0	10.6	1.35	97
3	3	30	71	13.1	9.5	4.57	72
4	4	45	81	11.1	10.7	1.48	96
5	5	45	79	10.2	10.4	1.48	102
6	6	30	82	11.4	10.7	3.58	94
7	7	45	73	9.6	9.6	1.54	100

[a]Conditions are [1000]:[10]:[1] of [BA]:[DBMM]:[PC] with 1 eq of DMAc to BA by volume. Reactions were performed in continuous flow and irradiated by 18W 365 nm LEDs at 22 ºC.
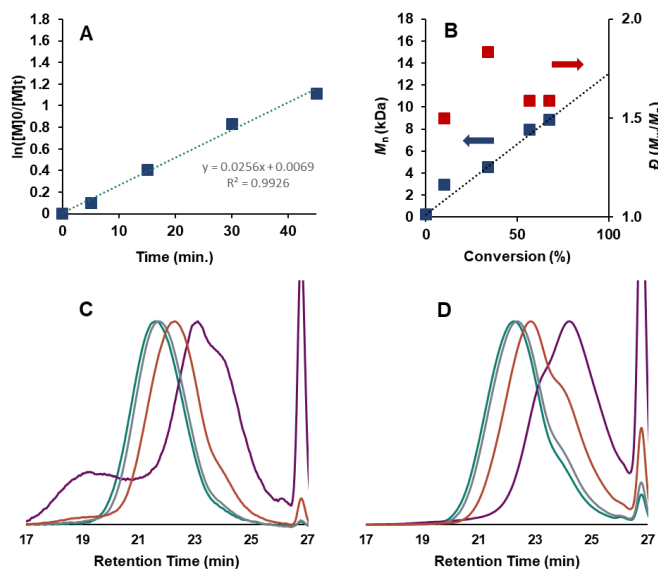

Figure 4.123: First order kinetic plot (a) and plot of M_n (blue) and dispersity (red) versus conversion (b) plotted against the theoretical M_n for O-ATRP of BA using **PC 1** under 365 nm irradiation in flow conditions at 22 º with corresponding SEC-MALS (c) and Dri (d) GPC traces. Conditions are [1000[:[10]:[1] of [BA]:[DBMM]:[PC] with 1 Ml DMAc to 1 Ml BA.
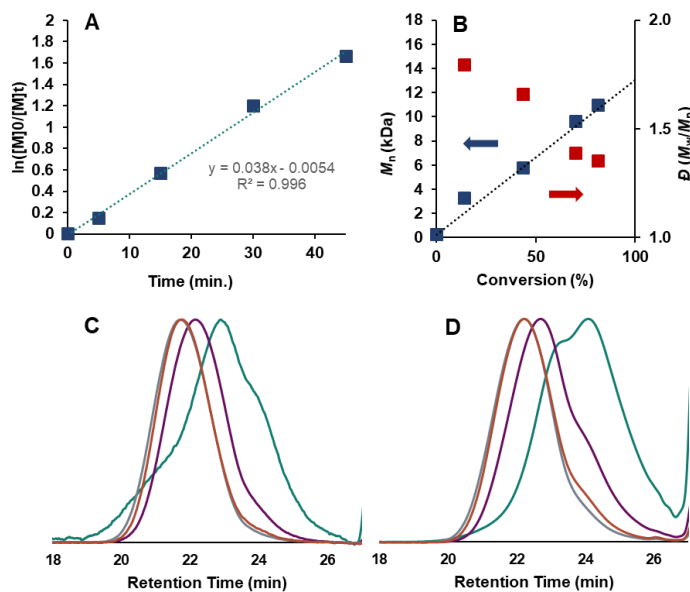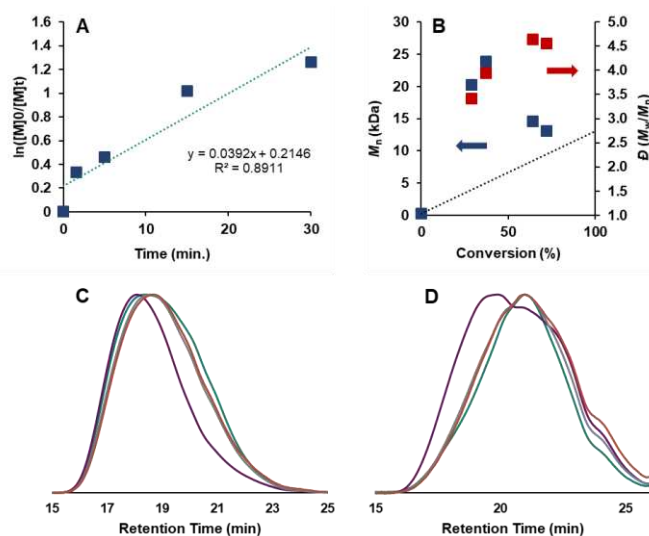
Figure 4.124: First order kinetic plot (a) and plot of M_n (blue) and dispersity (red) versus conversion (b) plotted against the theoretical M_n for O-ATRP of BA using **PC 2** under 365 nm irradiation in flow conditions at 22 ° with corresponding SEC-MALS (c) and Dri (d) GPC traces. Conditions are [1000[:[10]:[1] of [BA]:[DBMM]:[PC] with 1 Ml DMAc to 1 Ml BA.

Figure 4.125: First order kinetic plot (a) and plot of M_n (blue) and dispersity (red) versus conversion (b) plotted against the theoretical M_n for O-ATRP of BA using **PC 3** under 365 nm irradiation in flow conditions at 22 ° with corresponding SEC-MALS (c) and Dri (d) GPC traces. Conditions are [1000[:[10]:[1] of [BA]:[DBMM]:[PC] with 1 Ml DMAc to 1 Ml BA.
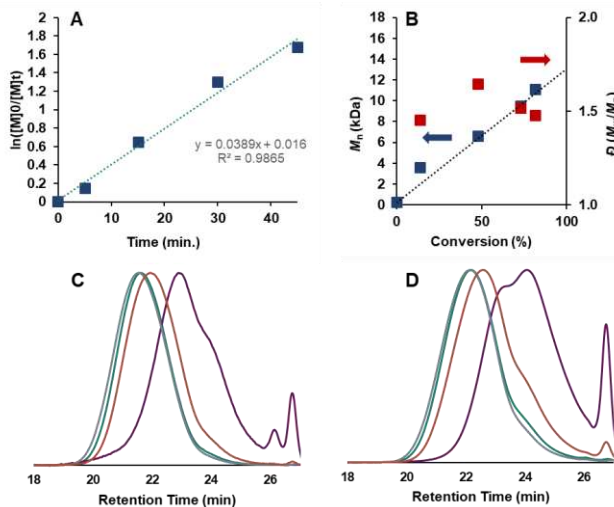
Figure 4.126: First order kinetic plot (a) and plot of M_n (blue) and dispersity (red) versus conversion (b) plotted against the theoretical M_n for O-ATRP of BA using **PC 4** under 365 nm irradiation in flow conditions at 22 ° with corresponding SEC-MALS (c) and Dri (d) GPC traces. Conditions are [1000[:[10]:[1] of [BA]:[DBMM]:[PC] with 1 Ml DMAc to 1 Ml BA.
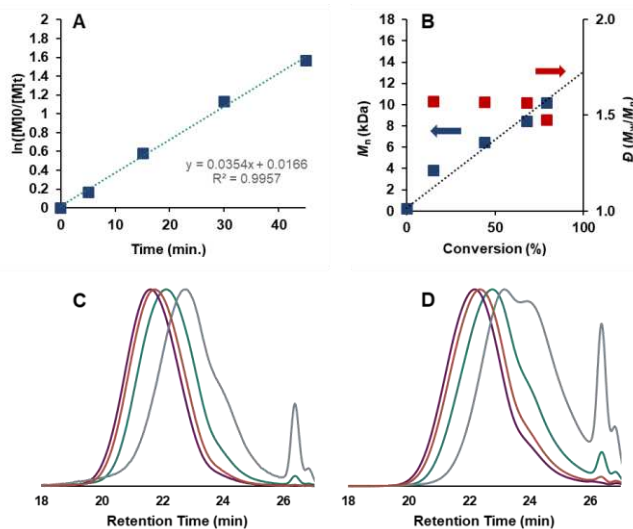

Figure 4.127: First order kinetic plot (a) and plot of M_n (blue) and dispersity (red) versus conversion (b) plotted against the theoretical M_n for O-ATRP of BA using **PC 5** under 365 nm irradiation in flow conditions at 22 ° with corresponding SEC-MALS (c) and Dri (d) GPC traces. Conditions are [1000[:[10]:[1] of [BA]:[DBMM]:[PC] with 1 Ml DMAc to 1 Ml BA.
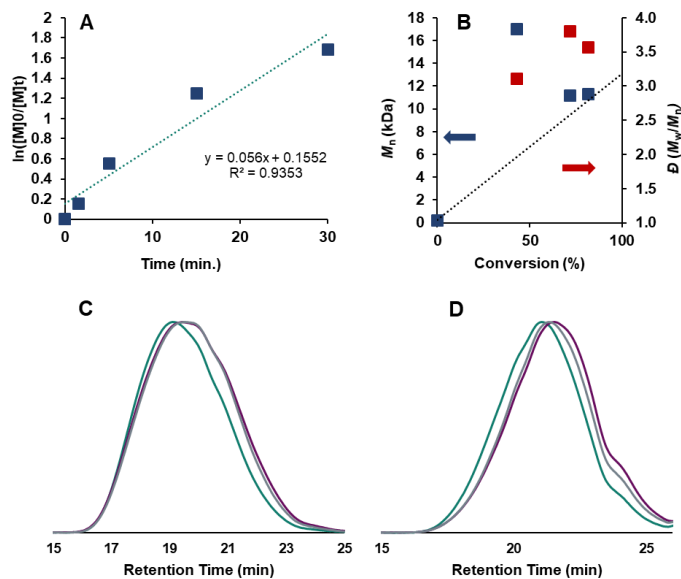
Figure 4.128: First order kinetic plot (a) and plot of M_n (blue) and dispersity (red) versus conversion (b) plotted against the theoretical M_n for O-ATRP of BA using **PC 6** under 365 nm irradiation in flow conditions at 22 ° with corresponding SEC-MALS (c) and Dri (d) GPC traces. Conditions are [1000[:[10]:[1] of [BA]:[DBMM]:[PC] with 1 Ml DMAc to 1 Ml BA.
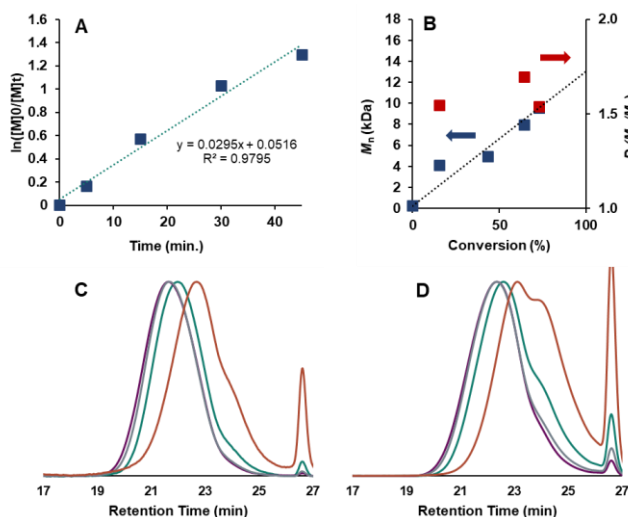

Figure 4.129: First order kinetic plot (a) and plot of M_n (blue) and dispersity (red) versus conversion (b) plotted against the theoretical M_n for O-ATRP of BA using **PC 7** under 365 nm irradiation in flow conditions at 22 ° with corresponding SEC-MALS (c and Dri (d) GPC traces. Conditions are [1000[:[10]:[1] of [BA]:[DBMM]:[PC] with 1 Ml DMAc to 1 Ml BA.

Initiator Screen:

Table 4.19: Results of differing alkyl halide initiators on the O-ATRP of BA in continuous flow using **PC 2** after 45 minutes residence time.[a]

Entry	Initiator	Conv. (%)[b]	$M_{n, calc.}$ (kDa)	$M_{n, theo.}$ (kDa)	Đ (M_w/M_n)	I^* (%)
1	DBMM	81	11.0	10.6	1.35	97
2	MbiB	79	10.8	10.3	1.43	96
3	2BrPN	74	10.8	9.8	1.34	91

[a]Conditions are [1000]:[10]:[1] of [BA]:[RX]:[PC 2] with 1 eq DMAc relative to 1 Ml BA and were irradiated by 365 nm light in continuous flow conditions at 22°.
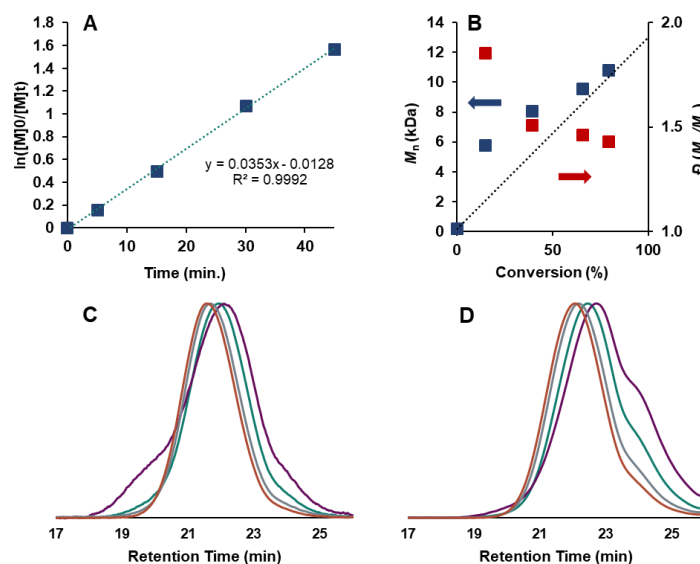

Figure 4.130: First order kinetic plot (a) and plot of M_n (blue) and dispersity (red) versus conversion (b) plotted against the theoretical M_n for O-ATRP of BA using **PC 2** under 365 nm irradiation in flow conditions at 22 ° with corresponding SEC-MALS (c) and Dri (d) GPC traces. Conditions are [1000[:[10]:[1] of [BA]:[MbiB]:[PC] with 1 Ml DMAc to 1 Ml BA.
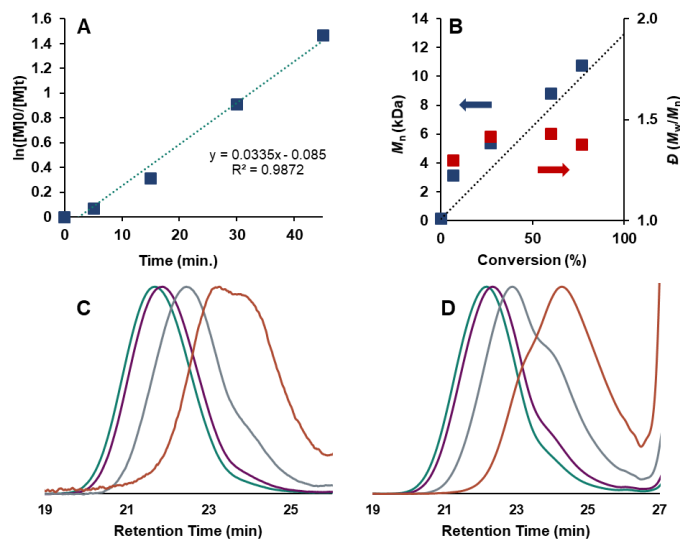
Figure 4.131: First order kinetic plot (a) and plot of M_n (blue) and dispersity (red) versus conversion (b) plotted against the theoretical M_n for O-ATRP of BA using **PC 2** under 365 nm irradiation in flow conditions at 22 ° with corresponding SEC-MALS (c) and Dri (d) GPC traces. Conditions are [1000[:[10]:[1] of [BA]:[2BrPN]:[PC] with 1 Ml DMAc to 1 Ml BA.

Reaction Concentration:

Table 4.20: Results of changing reaction concentration on the O-ATRP of BA using **PC 2** in continuous flow after 45 minutes residence time.[a]

Entry	DMAc:BA (v/v)	Conv. (%)[b]	$M_{n, calc.}$ (kDa)	$M_{n, theo.}$ (kDa)	$Đ$ (M_w/M_n)	$I*$ (%)
1	2:1	87	13.4	11.9	1.31	89
2	1.5:1	80	10.6	10.6	1.37	100
4	1:1	81	11.0	10.6	1.35	97

[a]Conditions are [1000]:[10]:[1] of [BA]:[DBMM]:[PC 2] and were irradiated by 365 nm light in flow conditions at 22 °C.
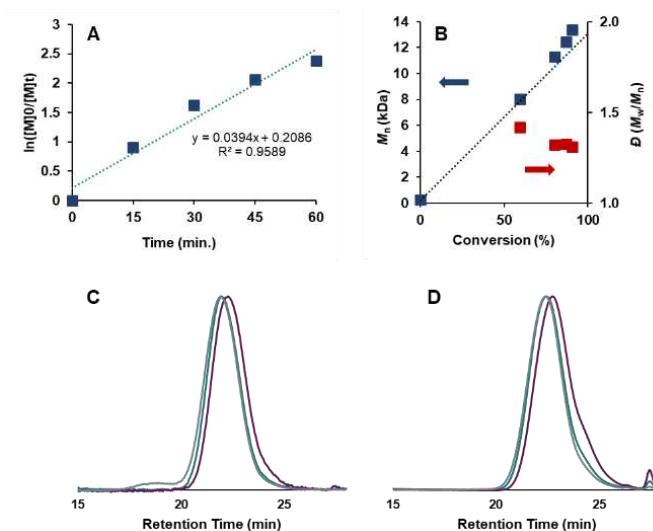
Figure 4.132: First order kinetic plot (a) and plot of M_n (blue) and dispersity (red) versus conversion (b) plotted against the theoretical M_n for O-ATRP of BA using **PC 2** under 365 nm irradiation in flow conditions at 22 ° with corresponding SEC-MALS (c) and Dri (d) GPC traces. Conditions are [1000[:[10]:[1] of [BA]:[DBMM]:[PC] with 2 Ml DMAc to 1 Ml BA.
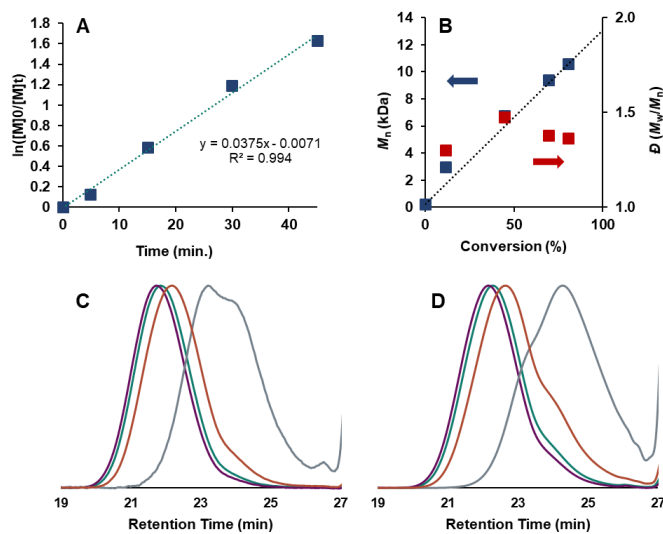

Figure 4.133: First order kinetic plot (a) and plot of M_n (blue) and dispersity (red) versus conversion (b) plotted against the theoretical M_n for O-ATRP of BA using **PC 2** under 365 nm irradiation in flow conditions at 22 ° with corresponding SEC-MALS (c) and Dri (d) GPC traces. Conditions are [1000[:[10]:[1] of [BA]:[DBMM]:[PC] with 1.5 Ml DMAc to 1 Ml BA.

Figure 4.134: First order kinetic plot (a) and plot of M_n (blue) and dispersity (red) versus conversion (b) plotted against the theoretical M_n for O-ATRP of BA using **PC 2** under 365 nm irradiation in flow conditions at 22 ° with corresponding SEC-MALS (c) and Dri (d) GPC traces. Conditions are [1000[:[10]:[1] of [BA]:[DBMM]:[PC] with 1 Ml DMAc to 1 Ml BA.
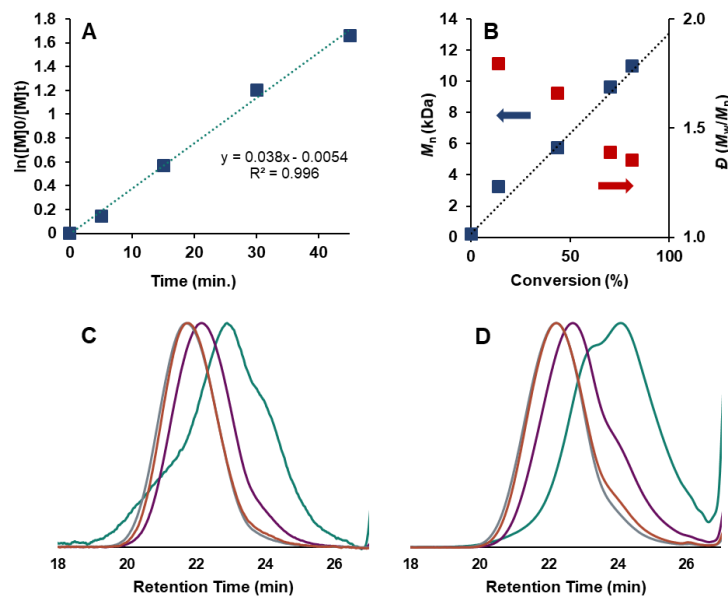
Catalyst Loading:

Table 4.21: Results of O-ATRP of BA in continuous flow after 45 minutes residence time testing the effect of **PC 2** loadings.[a]

Entry	Mol % PC 2	Conv. (%)[b]	$M_{n, calc.}$ (kDa)	$M_{n, theo.}$ (kDa)	$Đ$ (M_w/M_n)	I^* (%)
1	0.1	80	10.6	10.6	1.37	100
2	0.075	80	10.1	10.6	1.43	105
5	0.05	81	10.2	10.6	1.41	104

[a]Conditions are [1000]:[10]:[X] of [BA]:[DBMM]:[PC 2] with 1.5 equivalents of DMAc to BA by volume. Polymerizations were irradiated by 365 nm light in continuous flow reactor conditions at 22 ºC.
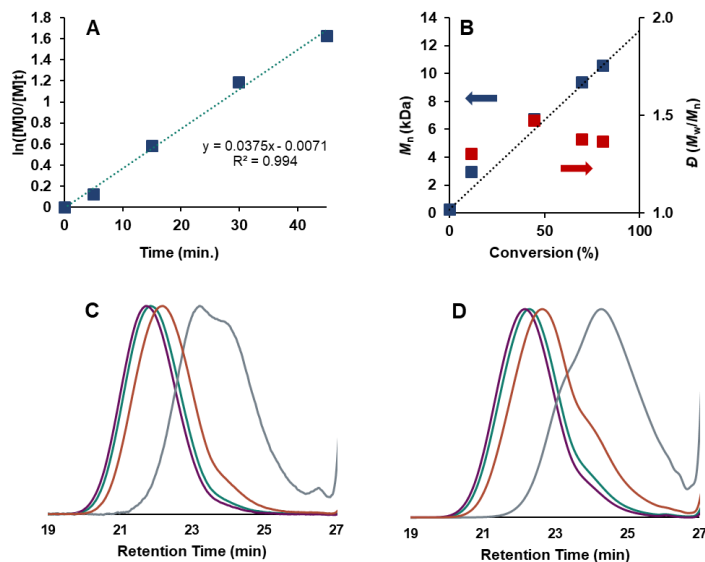
Figure 4.135: First order kinetic plot (a) and plot of M_n (blue) and dispersity (red) versus conversion (b) plotted against the theoretical M_n for O-ATRP of BA using **PC 2** under 365 nm irradiation in flow conditions at 22 ° with corresponding SEC-MALS (c) and Dri (d) GPC traces. Conditions are [1000[:[10]:[1] of [BA]:[DBMM]:[PC] with 1.5 Ml DMAc to 1 Ml BA.
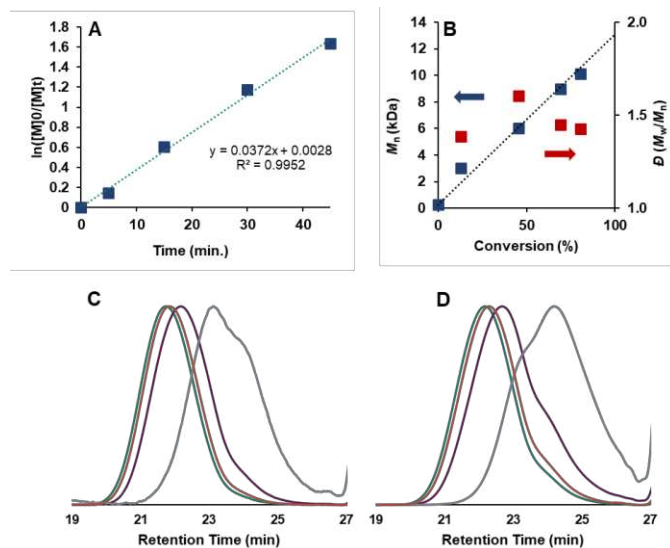

Figure 4.136: First order kinetic plot (a) and plot of M_n (blue) and dispersity (red) versus conversion (b) plotted against the theoretical M_n for O-ATRP of BA using **PC 2** under 365 nm irradiation in flow conditions at 22 ° with corresponding SEC-MALS (c) and Dri (d) GPC traces. Conditions are [1000[:[10]:[0.75] of [BA]:[DBMM]:[PC] with 1.5 Ml DMAc to 1 Ml BA.

Figure 4.137: First order kinetic plot (a) and plot of M_n (blue) and dispersity (red) versus conversion (b) plotted against the theoretical M_n for O-ATRP of BA using **PC 2** under 365 nm irradiation in flow conditions at 22 ° with corresponding SEC-MALS (c) and Dri (d) GPC traces. Conditions are [1000[:[10]:[0.5] of [BA]:[DBMM]:[PC] with 1.5 Ml DMAc to 1 Ml BA.
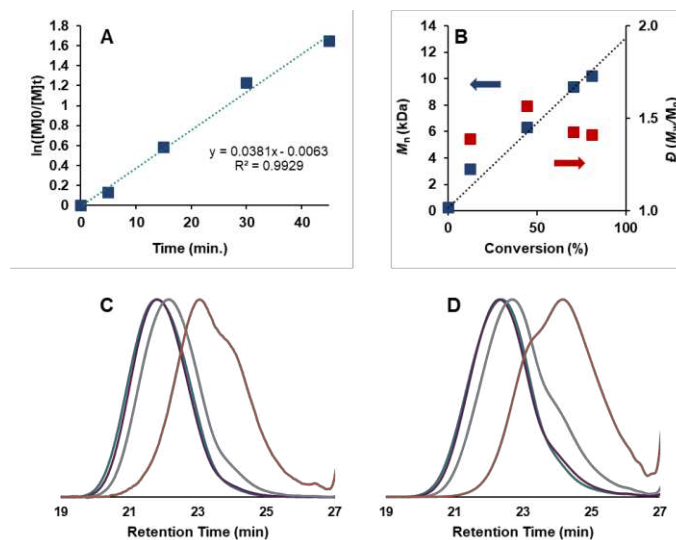
Salt Additives:

Table 4.22: Results of O-ATRP of butyl acrylate using **PC 2** in continuous flow testing the effect of various salt additives on polymerization.[a]

Entry	Salt	Res. Time (min.)	Conv. (%)	k_{app} (s^{-1})	$M_{n, calc.}$ (kDa)	Đ (M_w/M_n)	I^* (%)
1	LiBr	90	79	0.0177	10.0	1.23	104
2	LiBr[b]	60	0	--	--	--	--
3	NaBr	90	81	0.0187	9.2	1.36	116
4	KBr	60	80	0.0278	9.4	1.41	112
5	TBABr	90	82	0.0201	15.0	1.20	72
6	LiCl	60	87	0.0354	27.2	1.98	42
7	LiI	60	0	--	--	--	--
9	LiPF$_6$	60	92	0.0424	14.7	1.31	82

[a]Conditions are [1000]:[10]:[1]:[10] of [BA]:[DBMM]:[PC 2]:[Salt] with 1.5 equivalents of DMAc to BA by volume. Polymerizations were irradiated by 18 W 365 nm light in flow reactor conditions at 22 °C. [b]No DBMM.
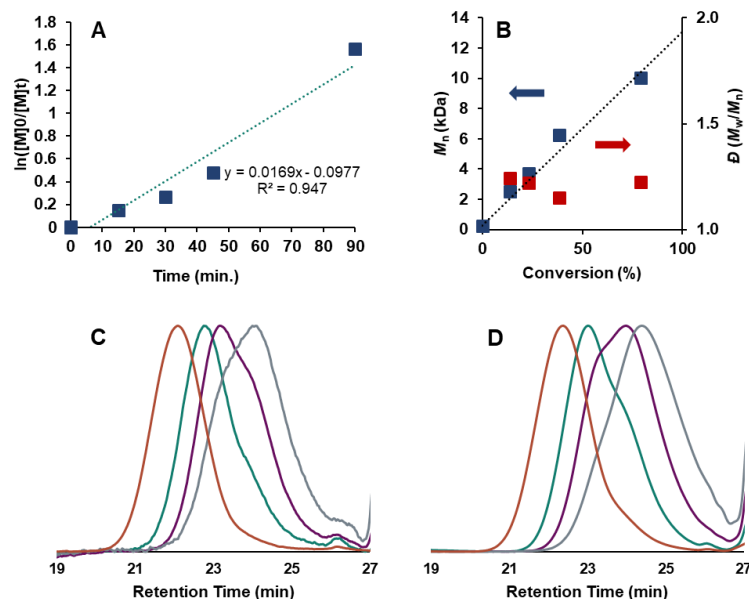
Figure 4.138: First order kinetic plot (a) and plot of M_n (blue) and dispersity (red) versus conversion (b) plotted against the theoretical M_n for O-ATRP of BA using **PC 2** under 365 nm irradiation in flow conditions at 22 ° with corresponding SEC-MALS (c) and Dri (d) GPC traces. Conditions are [1000[:[10]:[1]:[10] of [BA]:[DBMM]:[PC]:[LiBr] with 1.5 Ml DMAc to 1 Ml BA.
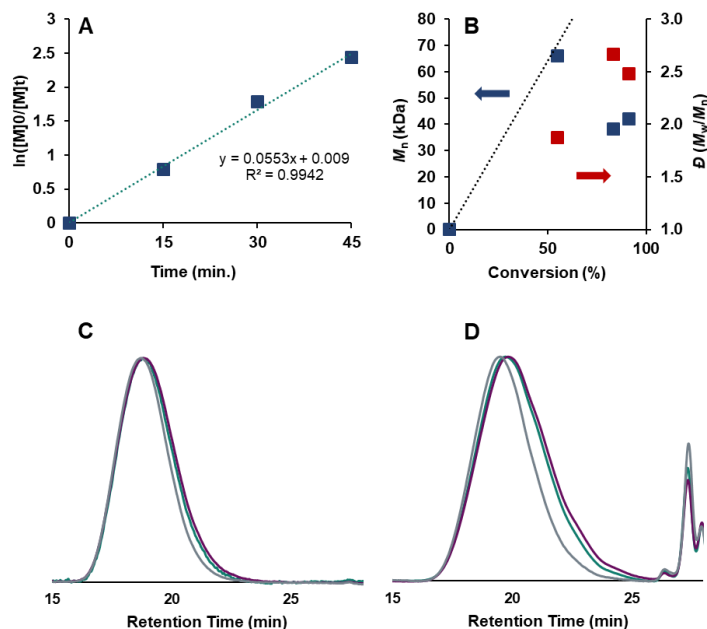

Figure 4.139: First order kinetic plot (a) and plot of M_n (blue) and dispersity (red) versus conversion (b) plotted against the theoretical M_n for O-ATRP of BA using **PC 2** under 365 nm irradiation in flow conditions at 22 ° with corresponding SEC-MALS (c) and Dri (d) GPC traces. Conditions are [1000[:[0]:[1]:[10] of [BA]:[DBMM]:[PC]:[LiBr] with 1.5 Ml DMAc to 1 Ml BA.
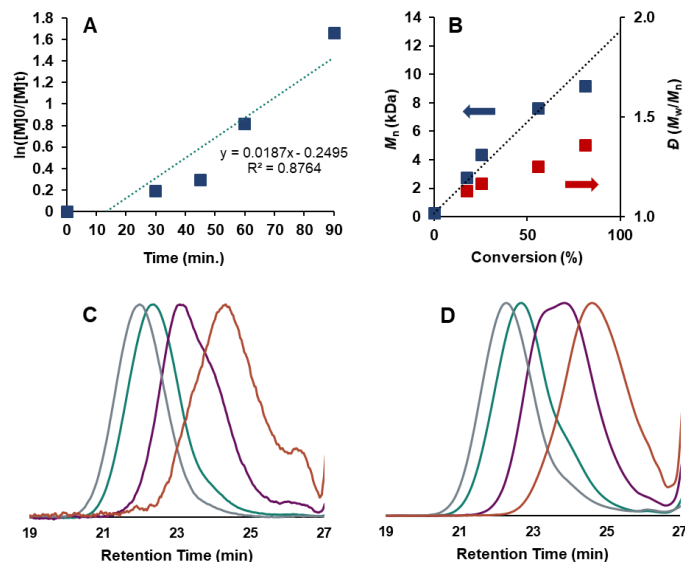
Figure 4.140: First order kinetic plot (a) and plot of M_n (blue) and dispersity (red) versus conversion (b) plotted against the theoretical M_n for O-ATRP of BA using **PC 2** under 365 nm irradiation in flow conditions at 22 ° with corresponding SEC-MALS (c) and Dri (d) GPC traces. Conditions are [1000[:[10]:[1]:[10] of [BA]:[DBMM]:[PC]:[NaBr] with 1.5 Ml DMAc to 1 Ml BA.

Figure 4.141: First order kinetic plot (a) and plot of M_n (blue) and dispersity (red) versus conversion (b) plotted against the theoretical M_n for O-ATRP of BA using **PC 2** under 365 nm irradiation in flow conditions at 22 ° with corresponding SEC-MALS (c) and Dri (d) GPC traces. Conditions are [1000[:[10]:[1]:[10] of [BA]:[DBMM]:[PC]:[KBr] with 1.5 Ml DMAc to 1 Ml BA.
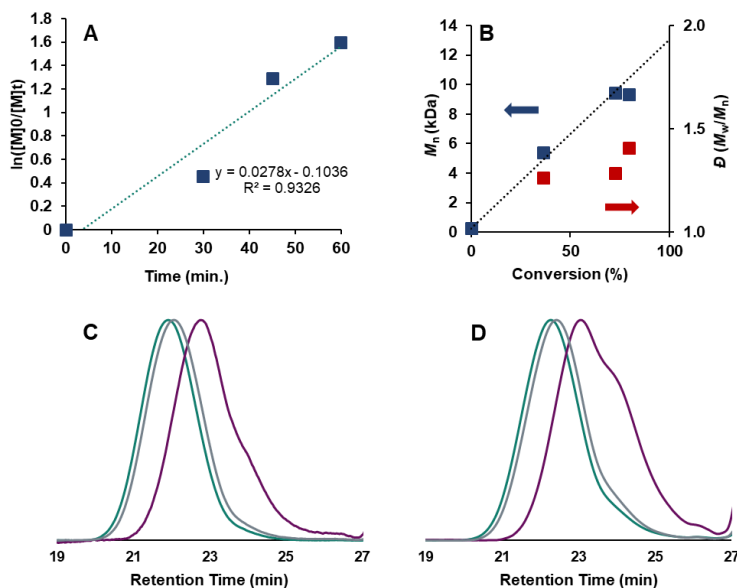
Figure 4.142: First order kinetic plot (a) and plot of M_n (blue) and dispersity (red) versus conversion (b) plotted against the theoretical M_n for O-ATRP of BA using **PC 2** under 365 nm irradiation in flow conditions at 22 ° with corresponding SEC-MALS (c) and Dri (d) GPC traces. Conditions are [1000[:[10]:[1]:[10] of [BA]:[DBMM]:[PC]:[TBABr] with 1.5 Ml DMAc to 1 Ml BA.
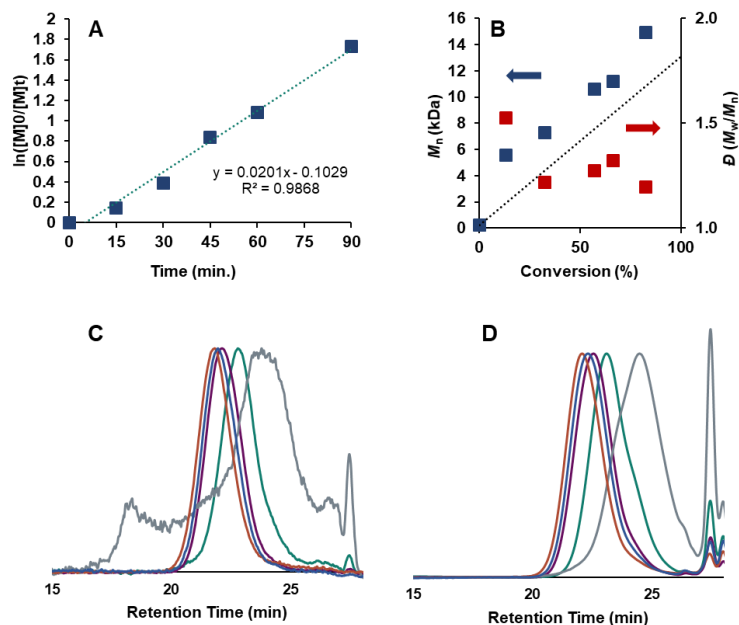

Figure 4.143: First order kinetic plot (a) and plot of M_n (blue) and dispersity (red) versus conversion (b) plotted against the theoretical M_n for O-ATRP of BA using **PC 2** under 365 nm irradiation in flow conditions at 22 ° with corresponding SEC-MALS (c) and Dri (d) GPC traces. Conditions are [1000[:[10]:[1]:[10] of [BA]:[DBMM]:[PC]:[LiCl] with 1.5 Ml DMAc to 1 Ml BA.
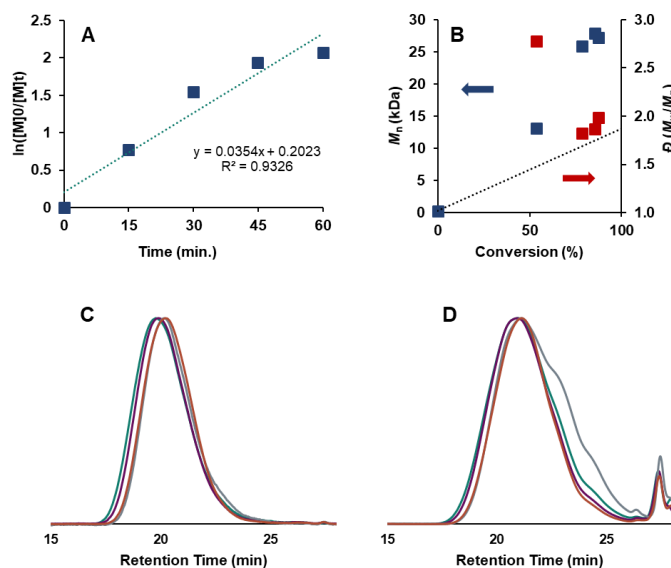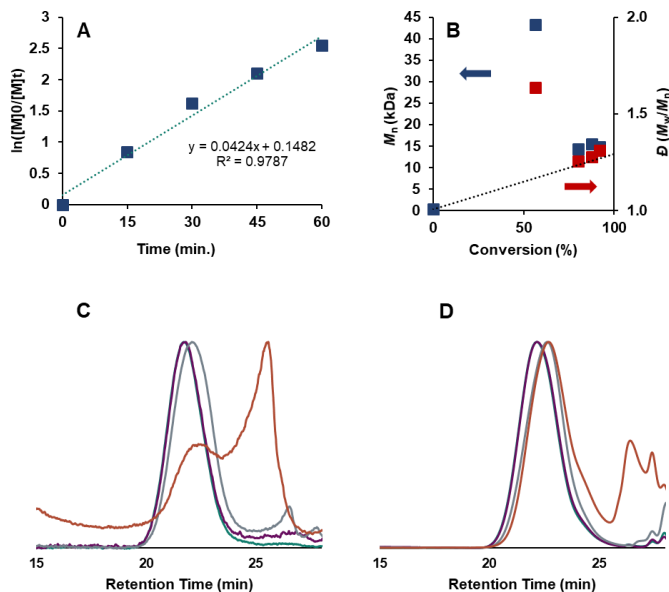
202

Figure 4.144: First order kinetic plot (a) and plot of M_n (blue) and dispersity (red) versus conversion (b) plotted against the theoretical M_n for O-ATRP of BA using **PC 2** under 365 nm irradiation in flow conditions at 22 ° with corresponding SEC-MALS (c) and Dri (d) GPC traces. Conditions are [1000[:[10]:[1]:[10] of [BA]:[DBMM]:[PC]:[LiPF$_6$] with 1.5 Ml DMAc to 1 Ml BA.

LiBr Loadings:

Table 4.23: Results of O-ATRP of BA using **PC 2** in continuous flow testing the effect of LiBr concentration on polymerization.[a]

Entry	[LiBr]:[PC 2]	Res. Time (min.)	Conv. (%)	k_{app} (s^{-1})	$M_{n, calc.}$ (kDa)	Đ (M_w/M_n)	I^* (%)
1	[5]:[1]	60	73	0.0227	9.1	1.30	106
2	[10]:[1]	90	79	0.0177	10.0	1.23	104
3	[20]:[1]	90	60	0.0101	7.7	1.30	104
4	[30]:[1]	120	73	0.0111	9.4	1.20	103
5	[50]:[1]	120	83	10.1	10.9	1.23	108

[a]Conditions are [1000]:[10]:[1]:[X] of [BA]:[DBMM]:[PC 2]:[LiBr] with 1.5 equivalents of DMAc to BA by volume. Polymerizations were irradiated by 18 W 365 nm light in flow reactor conditions at 22 ºC.
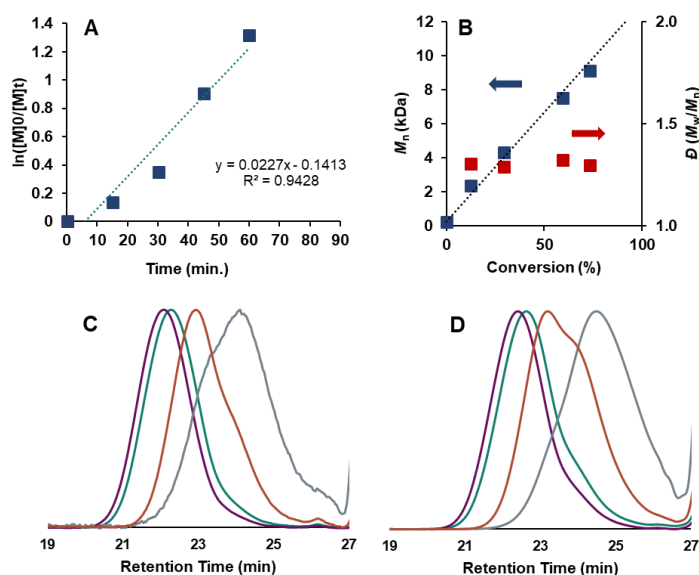
Figure 4.145: First order kinetic plot (a) and plot of M_n (blue) and dispersity (red) versus conversion (b) plotted against the theoretical M_n for O-ATRP of BA using **PC 2** under 365 nm irradiation in flow conditions at 22 ° with corresponding SEC-MALS (c) and Dri (d) GPC traces. Conditions are [1000[:[10]:[1]:[5] of [BA]:[DBMM]:[PC]:[LiBr] with 1.5 Ml DMAc to 1 Ml BA.

Figure 4.146: First order kinetic plot (a) and plot of M_n (blue) and dispersity (red) versus conversion (b) plotted against the theoretical M_n for O-ATRP of BA using **PC 2** under 365 nm irradiation in flow conditions at 22 ° with corresponding SEC-MALS (c) and Dri (d) GPC traces. Conditions are [1000[:[10]:[1]:[20] of [BA]:[DBMM]:[PC]:[LiBr] with 1.5 Ml DMAc to 1 Ml BA.
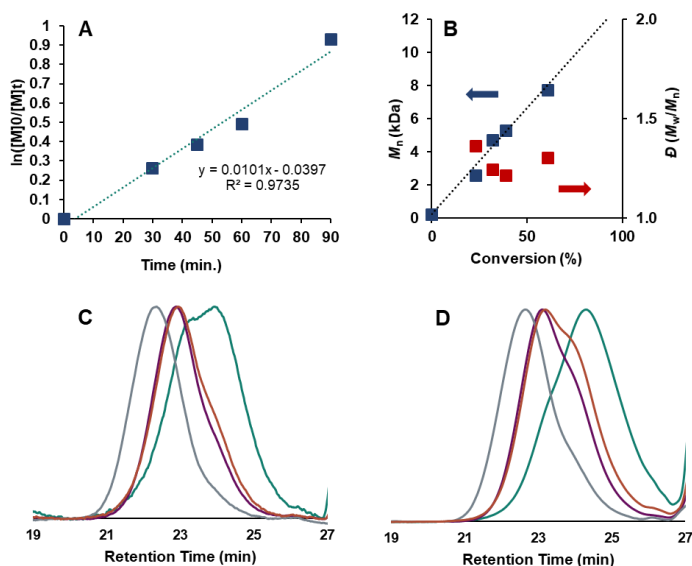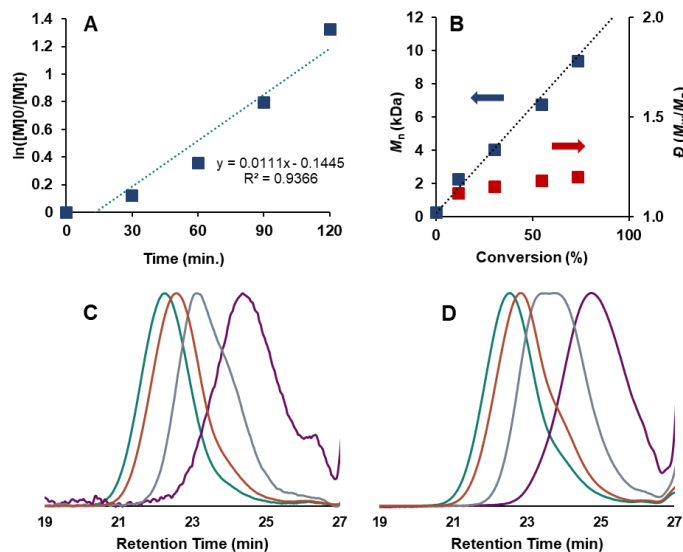
Figure 4.147: First order kinetic plot (a) and plot of M_n (blue) and dispersity (red) versus conversion (b) plotted against the theoretical M_n for O-ATRP of BA using **PC 2** under 365 nm irradiation in flow conditions at 22 ° with corresponding SEC-MALS (c) and Dri (d) GPC traces. Conditions are [1000[:[10]:[1]:[30] of [BA]:[DBMM]:[PC]:[LiBr] with 1.5 Ml DMAc to 1 Ml BA.

Figure 4.148: First order kinetic plot (a) and plot of M_n (blue) and dispersity (red) versus conversion (b) plotted against the theoretical M_n for O-ATRP of BA using **PC 2** under 365 nm irradiation in flow conditions at 22 ° with corresponding SEC-MALS (c) and Dri (d) GPC traces. Conditions are [1000[:[10]:[1]:[50] of [BA]:[DBMM]:[PC]:[LiBr] with 1.5 Ml DMAc to 1 Ml BA.
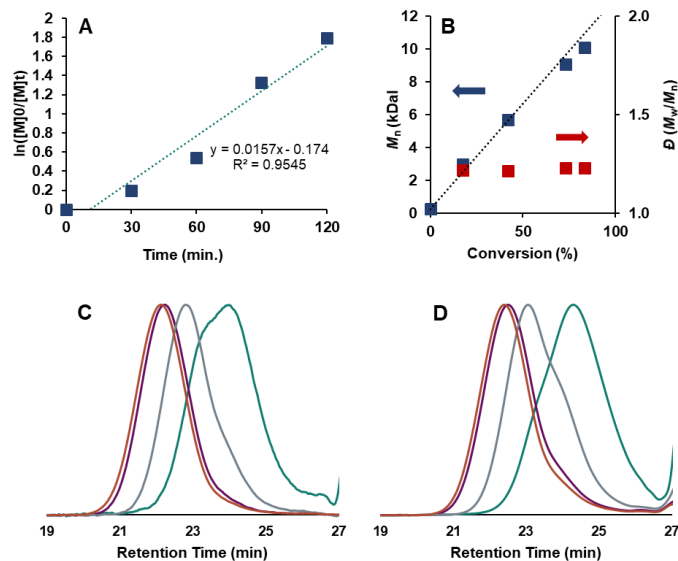
Application of other organic PCs to optimized reaction conditions:

Table 4.24: Results of O-ATRP of butyl acrylate using well-studied organic PCs in continuous flow.[a]

Entry	PC	Res. Time (min.)	Conv. (%)	$M_{n, calc.}$ (kDa)	$M_{n, theo.}$ (kDa)	$Đ$ (M_w/M_n)	$I*$ (%)
1	PhenO	90	77	11.5	10.1	1.35	88
2	PhenO[b]	45	59	9.3	7.8	1.65	84
3	PhenN	120	76	9.2	10.0	1.14	109
4	4-CzIPN	90	0	--	--	--	--
5	4-CzIPN[b]	45	77	40	10.2	2.17	20

[a]Conditions are [1000]:[10]:[1]:[30] of [BA]:[DBMM]:[PC]:[LiBr] with 1.5 equivalents of DMAc to BA by volume. Polymerizations were irradiated by 18 W 365 nm light in flow reactor conditions at 22 ºC. [b]Performed in absence of LiBr.
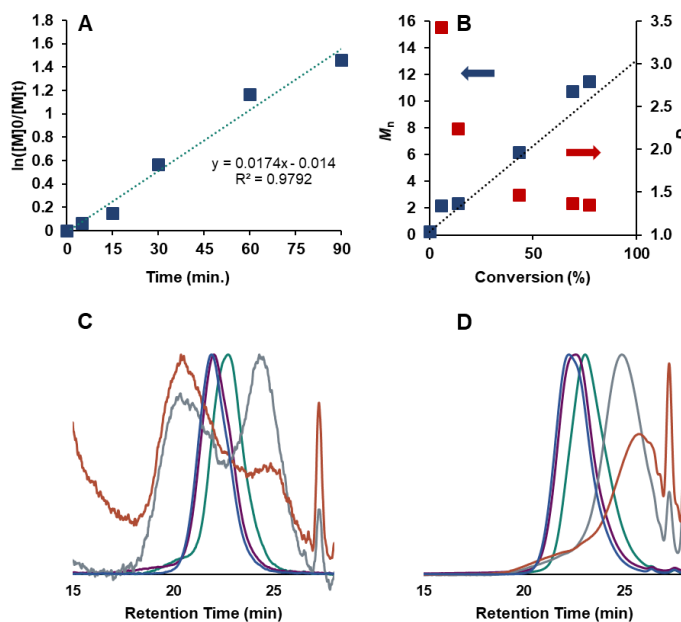

Figure 4.149: First order kinetic plot (a) and plot of M_n (blue) and dispersity (red) versus conversion (b) plotted against the theoretical M_n for O-ATRP of BA using **PhenO** under 365 nm irradiation in flow conditions at 22 º with corresponding SEC-MALS (c) and Dri (d) GPC traces. Conditions are [1000[:[10]:[1]:[30] of [BA]:[DBMM]:[PC]:[LiBr] with 1.5 Ml DMAc to 1 Ml BA.

Figure 4.150: First order kinetic plot (a) and plot of M_n (blue) and dispersity (red) versus conversion (b) plotted against the theoretical M_n for O-ATRP of BA using **PhenO** under 365 nm irradiation in flow conditions at 22 ° with corresponding SEC-MALS (c) and Dri (d) GPC traces. Conditions are [1000[:[10]:[1]:[0] of [BA]:[DBMM]:[PC]:[LiBr] with 1.5 Ml DMAc to 1 Ml BA.
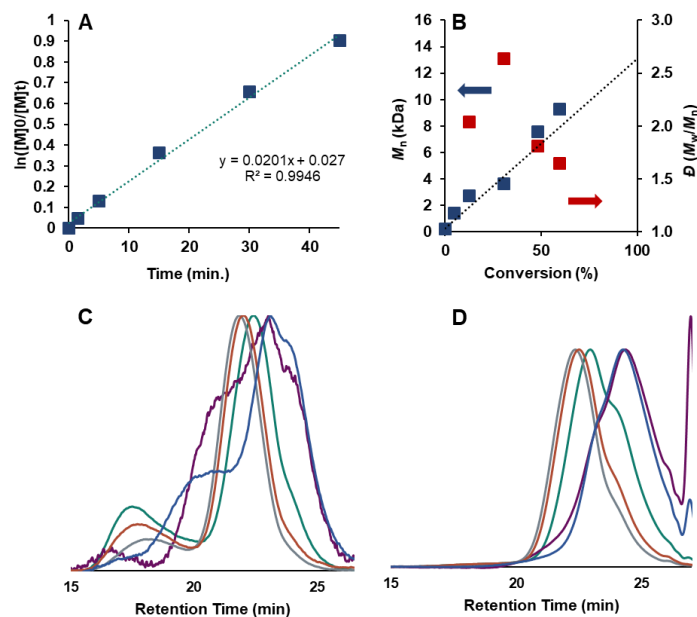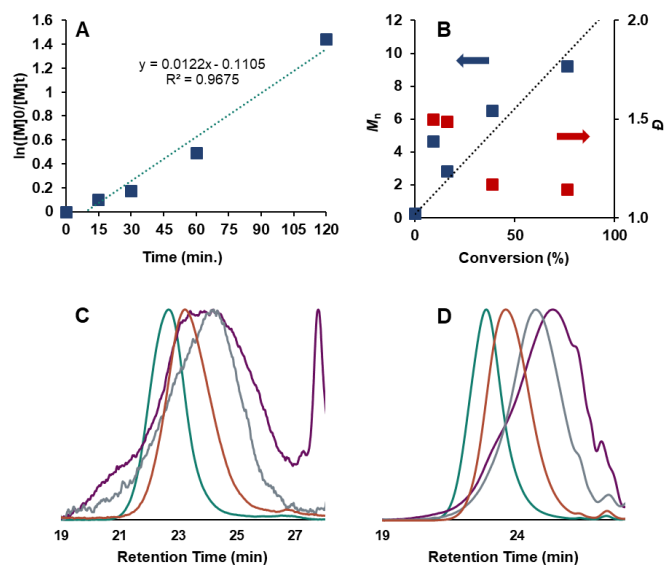

Figure 4.151: First order kinetic plot (a) and plot of M_n (blue) and dispersity (red) versus conversion (b) plotted against the theoretical M_n for O-ATRP of BA using **PhenN** under 365 nm irradiation in flow conditions at 22 ° with corresponding SEC-MALS (c) and Dri (d) GPC traces. Conditions are [1000[:[10]:[1]:[30] of [BA]:[DBMM]:[PC]:[LiBr] with 1.5 Ml DMAc to 1 Ml BA.

Figure 4.152: First order kinetic plot (a) and plot of M_n (blue) and dispersity (red) versus conversion (b) plotted against the theoretical M_n for O-ATRP of BA using **4-CzIPN** under 365 nm irradiation in flow conditions at 22 ° with corresponding SEC-MALS (c) and Dri (d) GPC traces. Conditions are [1000[:[10]:[1]:[0] of [BA]:[DBMM]:[PC]:[LiBr] with 1.5 Ml DMAc to 1 Ml BA.
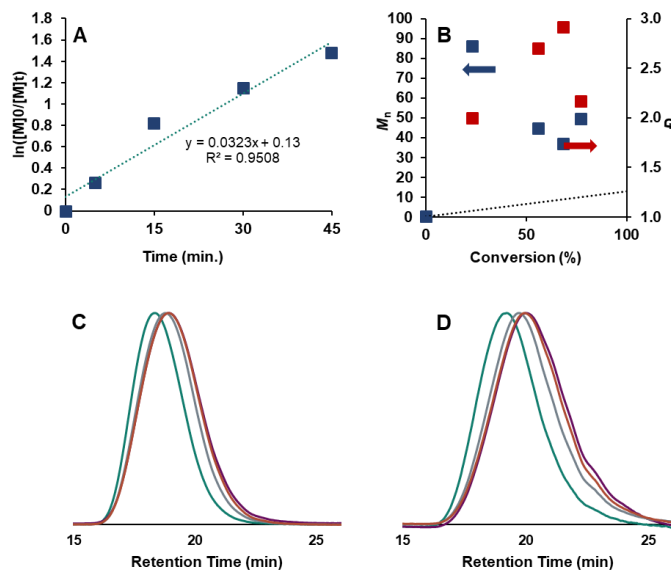
Oxygen Tolerance of PC 2:

General Procedure: The oxygen tolerance of the O-ATRP of BA under the optimized reaction conditions was tested by removing the reagents from the nitrogen-filled glovebox, bubbling compressed air through the DMAc, BA, and DBMM inside the fume hood for 30 minutes. The components, including **PC 2** and LiBr were then mixed together and then loaded into the stainless-steel syringe, where the polymerization was then conducted under the standard procedures, including the same equilibration times. Batch reactions conducted under air did not show any monomer conversion.
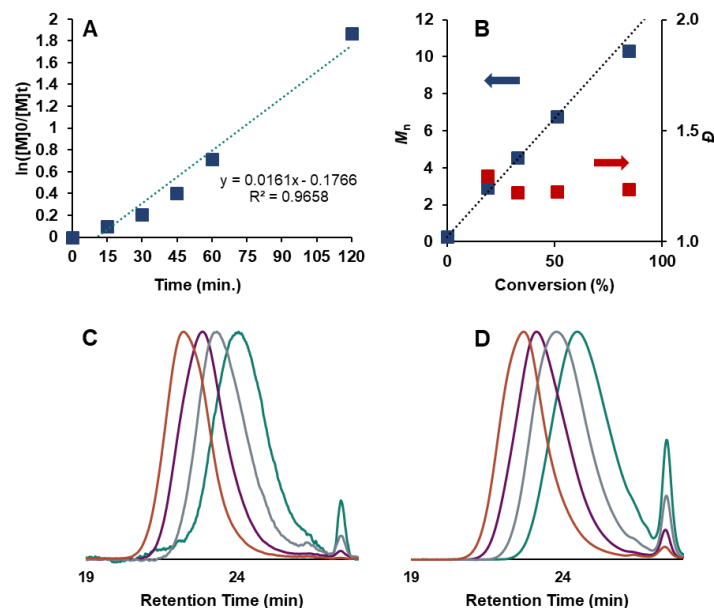
Figure 4.153: First order kinetic plot (a) and plot of M_n (blue) and dispersity (red) versus conversion (b) plotted against the theoretical M_n for O-ATRP of BA using **PC 2** under 365 nm irradiation in flow conditions at 22 ° using reagents sparged with air. Corresponding SEC-MALS (c) and Dri (d) GPC traces are shown. Conditions are [1000[:[10]:[1]:[30] of [BA]:[DBMM]:[PC]:[LiBr] with 1.5 Ml DMAc to 1 Ml BA.

MW Control using PC 2:

Table 4.25: Results of O-ATRP of BA using **PC 2** in continuous flow targeting different MW polymers through adjustment of stoichiometry of monomer and initiator.[a]

Entry	[BA]:[DBMM]	Res. Time (min.)	Conv. (%)	$M_{n, calc.}$ (kDa)	$M_{n, theo.}$ (kDa)	$Đ$ (M_w/M_n)	I^* (%)
1	[1000]:[2.5]	90	89	26.4	45.7	1.35	173
2	[1000]:[5]	120	88	15.2	22.8	1.32	150
3	[1000]:[10]	120	73	9.4	9.7	1.20	103
4	[1000]:[20]	180	80	7.3	5.4	1.19	74
5	[1000]:[40]	180	67	5.4	2.4	1.18	44

[a]Conditions are [1000]:[X]:[1]:[30] of [BA]:[DBMM]:[PC 2]:[LiBr] with 1.5 equivalents of DMAc to BA by volume. Polymerizations were irradiated by 18 W 365 nm light in flow reactor conditions at 22 ºC.
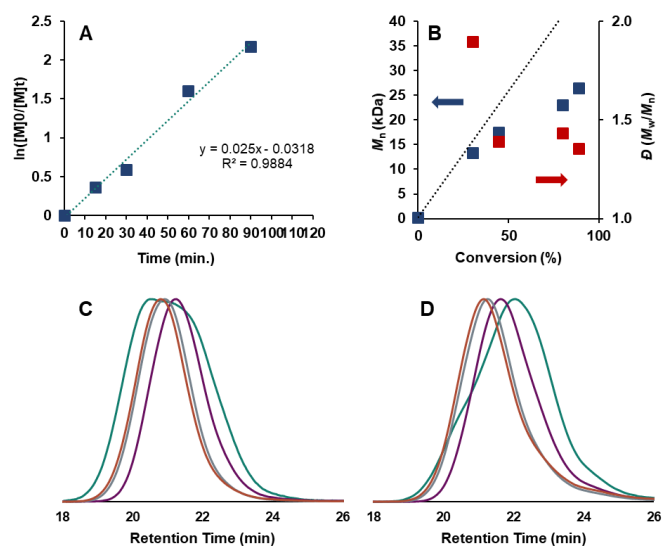
Figure 4.154: First order kinetic plot (a) and plot of M_n (blue) and dispersity (red) versus conversion (b) plotted against the theoretical M_n for O-ATRP of BA using **PC 2** under 365 nm irradiation in flow conditions at 22 ° with corresponding SEC-MALS (c) and Dri (d) GPC traces. Conditions are [1000[:[2.5]:[1]:[30] of [BA]:[DBMM]:[PC]:[LiBr] with 1.5 Ml DMAc to 1 Ml BA.

Figure 4.155: First order kinetic plot (a) and plot of M_n (blue) and dispersity (red) versus conversion (b) plotted against the theoretical M_n for O-ATRP of BA using **PC 2** under 365 nm irradiation in flow conditions at 22 ° with corresponding SEC-MALS (c) and Dri (d) GPC traces. Conditions are [1000[:[5]:[1]:[30] of [BA]:[DBMM]:[PC]:[LiBr] with 1.5 Ml DMAc to 1 Ml BA.
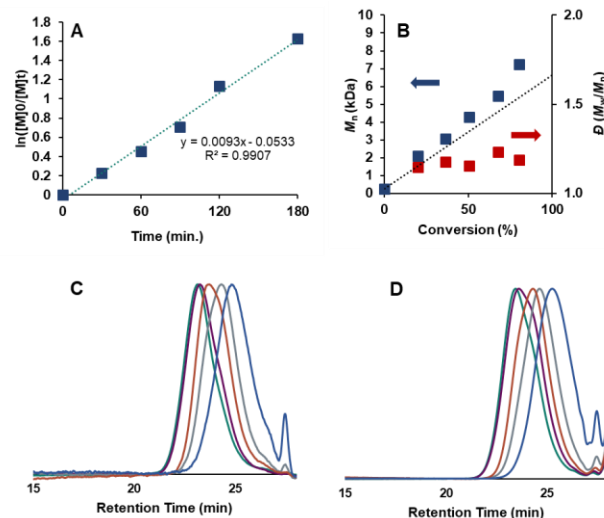
Figure 4.156: First order kinetic plot (a) and plot of M_n (blue) and dispersity (red) versus conversion (b) plotted against the theoretical M_n for O-ATRP of BA using **PC 2** under 365 nm irradiation in flow conditions at 22 ° with corresponding SEC-MALS (c) and Dri (d) GPC traces. Conditions are [1000[:[20]:[1]:[30] of [BA]:[DBMM]:[PC]:[LiBr] with 1.5 Ml DMAc to 1 Ml BA.
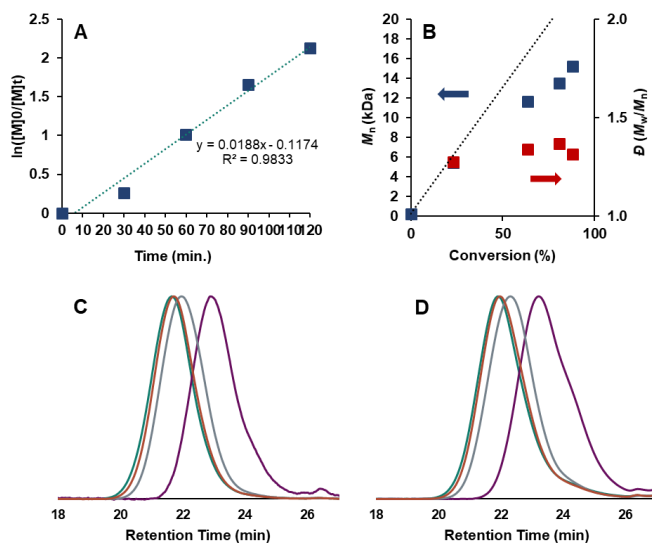

Figure 4.157: First order kinetic plot (a) and plot of M_n (blue) and dispersity (red) versus conversion (b) plotted against the theoretical M_n for O-ATRP of BA using **PC 2** under 365 nm irradiation in flow conditions at 22 ° with corresponding SEC-MALS (c) and Dri (d) GPC traces. Conditions are [1000[:[40]:[1]:[30] of [BA]:[DBMM]:[PC]:[LiBr] with 1.5 Ml DMAc to 1 Ml BA.
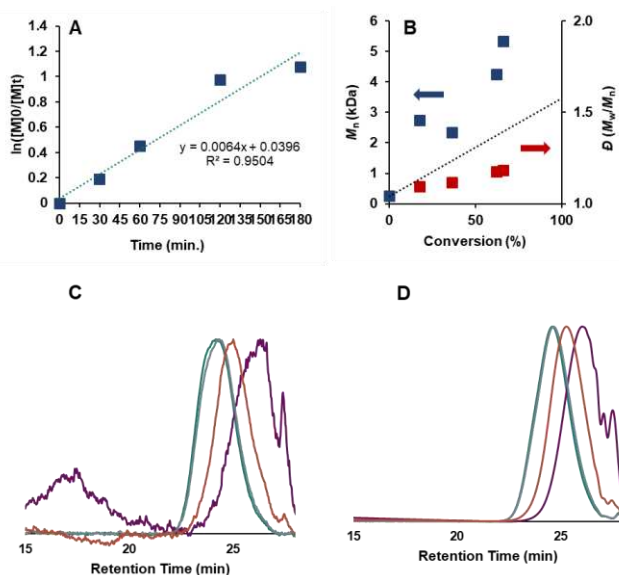
Monomer Scope:

Table 4.26: Results of O-ATRP of acrylate and methacrylate monomers using **PC 2** in continuous flow.[a]

Entry	Monomer	Res. Time (min.)	Conv. (%)	$M_{n, calc.}$ (kDa)	$M_{n, theo.}$ (kDa)	$Đ$ (M_w/M_n)	I^* (%)
1	t-BA	120	92	13.8	12.1	1.23	88
2	MA	90	92	10	8.1	1.30	81
3	EA	90	76	7.5	7.8	1.19	105
4	2-EHA	90	90	16.3	16.8	1.53	104
5	EGMEA	60	92	10.5	12.3	1.37	117
6	MMA	600	72	8.8	7.4	1.17	85

[a]Conditions are [1000]:[10]:[1]:[30] of [Monomer]:[DBMM]:[PC 2]:[LiBr] with 1.5 equivalents of DMAc to BA by volume. Polymerizations were irradiated by 18 W 365 nm light in flow reactor conditions at 22 ºC.

Figure 4.158: First order kinetic plot (a) and plot of M_n (blue) and dispersity (red) versus conversion (b) plotted against the theoretical M_n for O-ATRP of BA using **PC 2** under 365 nm irradiation in flow conditions at 22 º with corresponding SEC-MALS (c) and Dri (d) GPC traces. Conditions are [1000[:[10]:[1]:[30] of [t-BA]:[DBMM]:[PC]:[LiBr] with 1.5 Ml DMAc to 1 Ml BA.
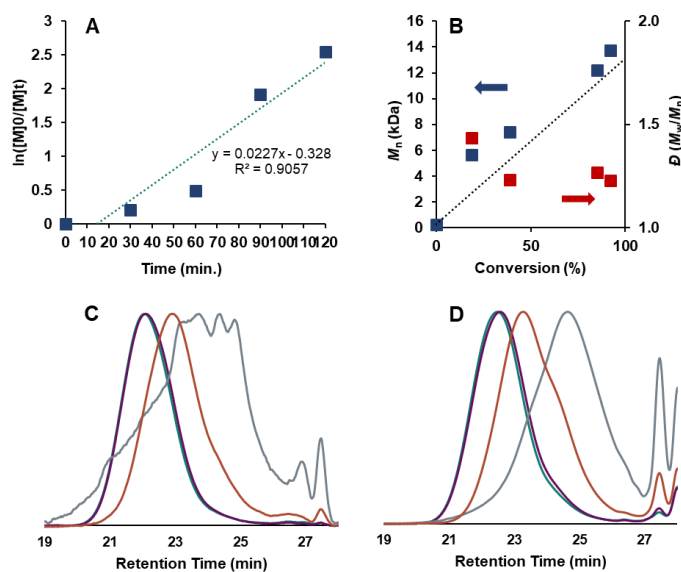
Figure 4.159: First order kinetic plot (a) and plot of M_n (blue) and dispersity (red) versus conversion (b) plotted against the theoretical M_n for O-ATRP of BA using **PC 2** under 365 nm irradiation in flow conditions at 22 ° with corresponding SEC-MALS (c) and Dri (d) GPC traces. Conditions are [1000[:[10]:[1]:[30] of [MA]:[DBMM]:[PC]:[LiBr] with 1.5 Ml DMAc to 1 Ml BA.

Figure 4.160: First order kinetic plot (a) and plot of M_n (blue) and dispersity (red) versus conversion (b) plotted against the theoretical M_n for O-ATRP of BA using **PC 2** under 365 nm irradiation in flow conditions at 22 ° with corresponding SEC-MALS (c) and Dri (d) GPC traces. Conditions are [1000[:[10]:[1]:[30] of [EA]:[DBMM]:[PC]:[LiBr] with 1.5 Ml DMAc to 1 Ml BA.
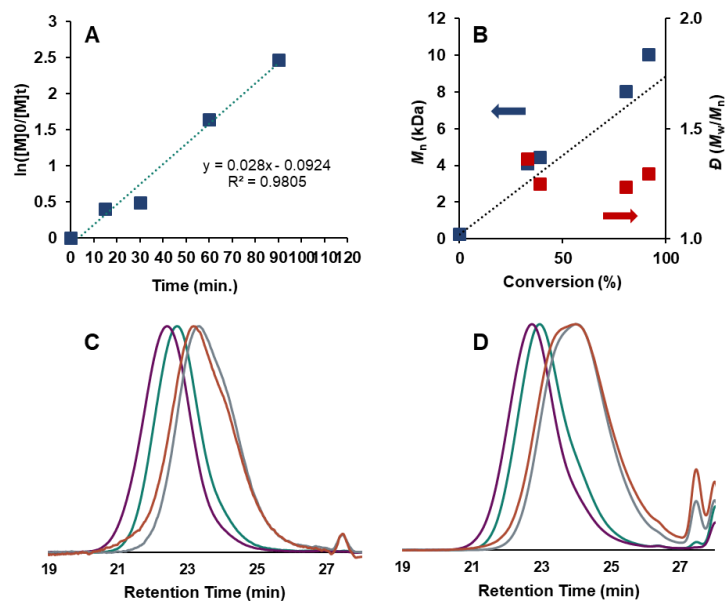
Figure 4.161: First order kinetic plot (a) and plot of M_n (blue) and dispersity (red) versus conversion (b) plotted against the theoretical M_n for O-ATRP of BA using **PC 2** under 365 nm irradiation in flow conditions at 22 ° with corresponding SEC-MALS (c) and Dri (d) GPC traces. Conditions are [1000[:[10]:[1]:[30] of [2-EHA]:[DBMM]:[PC]:[LiBr] with 1.5 Ml DMAc to 1 Ml BA.
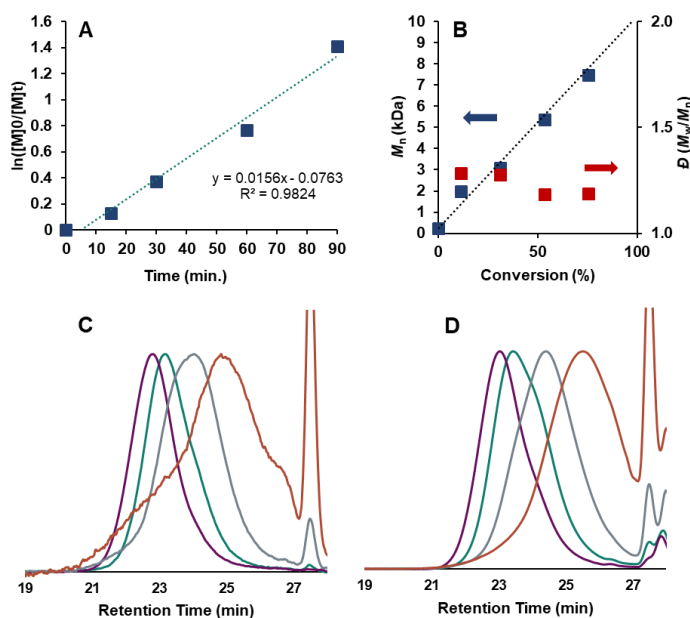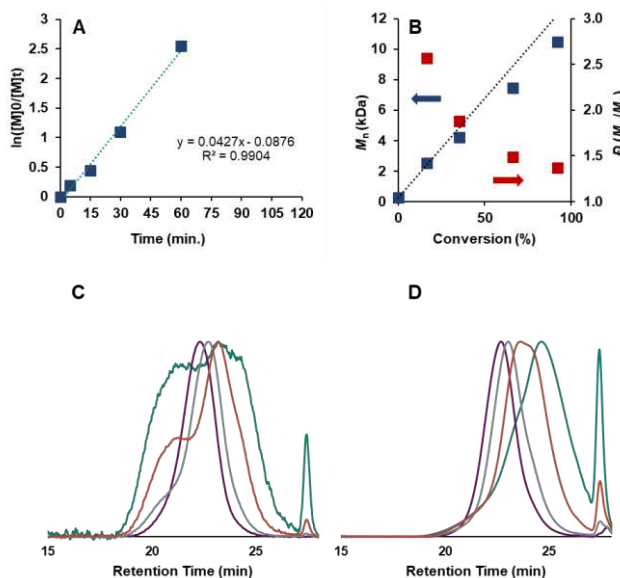

Figure 4.162: First order kinetic plot (a) and plot of M_n (blue) and dispersity (red) versus conversion (b) plotted against the theoretical M_n for O-ATRP of BA using **PC 2** under 365 nm irradiation in flow conditions at 22 ° with corresponding SEC-MALS (c) and Dri (d) GPC traces. Conditions are [1000[:[10]:[1]:[30] of [EGMEA]:[DBMM]:[PC]:[LiBr] with 1.5 Ml DMAc to 1 Ml BA.
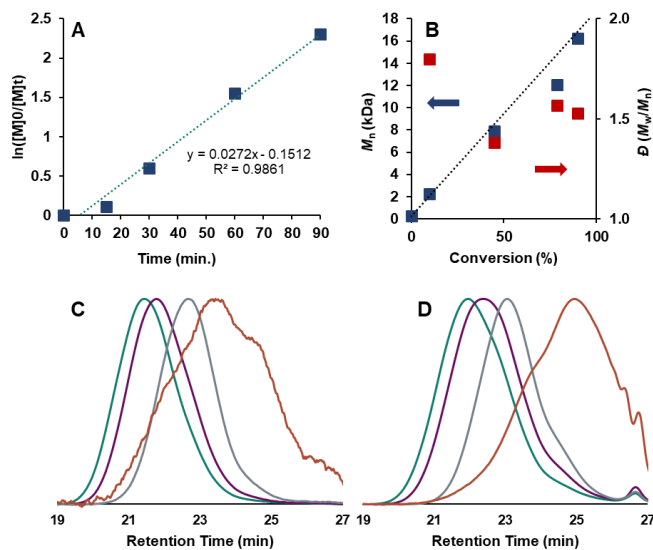
Figure 4.163: First order kinetic plot (a) and plot of M_n (blue) and dispersity (red) versus conversion (b) plotted against the theoretical M_n for O-ATRP of BA using **PC 2** under 365 nm irradiation in flow conditions at 22 ° with corresponding SEC-MALS (c) and Dri (d) GPC traces. Conditions are [1000[:[10]:[1]:[30] of [MMA]:[DBMM]:[PC]:[LiBr] with 1.5 Ml DMAc to 1 Ml BA.
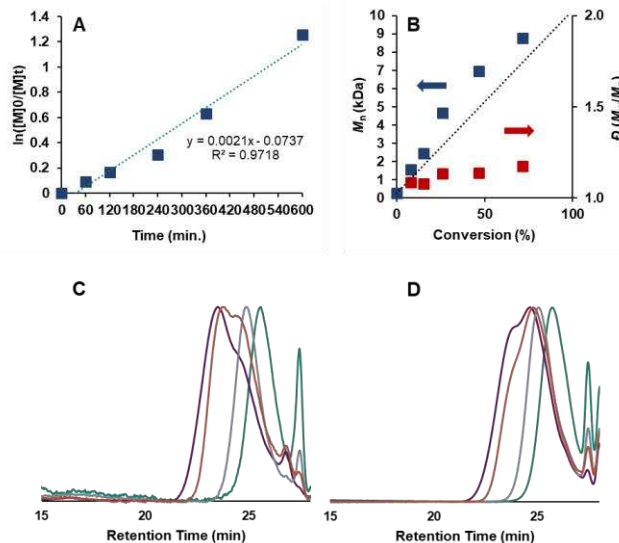
Chain Extension Experiments
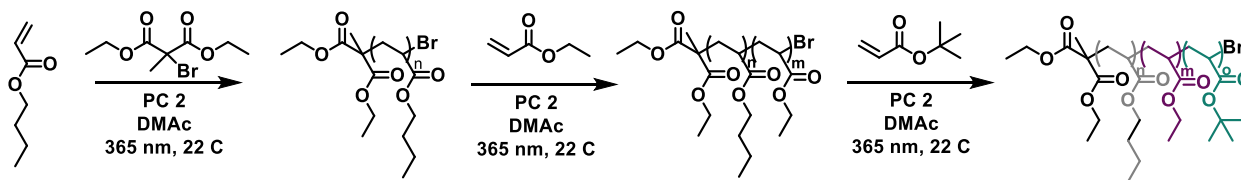
Figure 4.164: Synthetic route for the synthesis of triblock copolymers using a chain-extension approach.

Macroinitiator Synthesis:

A p(BA) macroinitiator was synthesized using optimized O-ATRP conditions. Inside a nitrogen-filled glovebox, 107.4 mg (1.24 mmol, 30 eq.) of LiBr was dissolved in 9 Ml of DMAc. Then, the solution was transferred to a vial with 22.8 mg (0.041 mmol, 1 eq.) of PC 2. 6 Ml of BA (41.7 mmol, 1000 eq.) was added, followed by 79.6 µL DBMM (0.41 mmol, 10 eq.). The solution was then transferred to a stainless-steel syringe, which was then fitted with the first section of PFA

215

tubing. The syringe was taken out of the glovebox and quickly connected to the flow reactor, which was set to a 30 minute residence time. After equilibration for 1.25 x residence time, the product was collected for 2 hours. Monomer conversion was measured at 27.5%. After precipitation in cold methanol/water, the polymer was dried to constant weight under vacuum at 50 °C to give 1.32 g with $M_n = 4.57$ kDa, $Đ = 1.26$, and $I* = 83\%$.
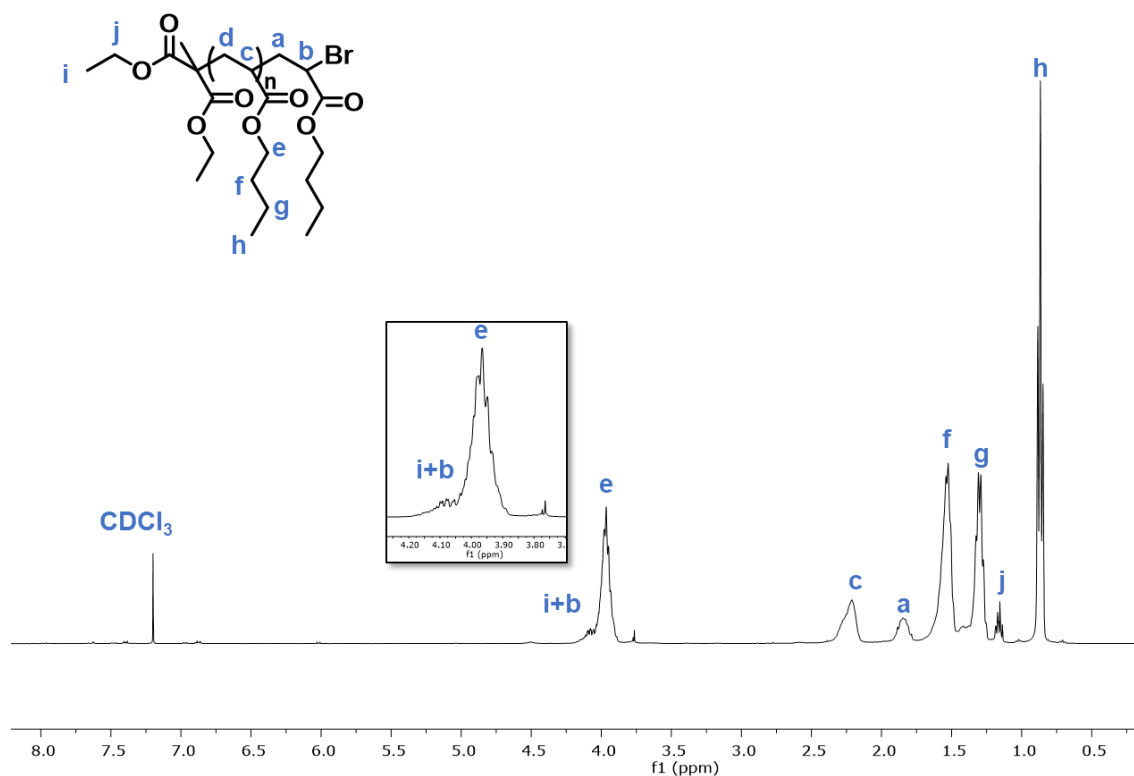

Figure 4.165: ^{1}H NMR spectrum of p(*n*-BA) in CDCl$_3$.

Block Copolymer Synthesis:

A p(BA)-c-p(EA) block copolymer was synthesized using a [200]:[1]:[0.1]:[3] ratio of [EA]:[Pba]:[PC 2]:[LiBr]. 22.6 mg LiBr (0.262 mmol) was dissolved in 3.72 Ml of DMAc. The solution was then transferred to a vial with 4.79 mg PC 2 (0.0087 mmol), which was then

transferred to a vial with 400 mg of p(BA) macroinitiator (0.087 mmol). After the polymer was dissolved, 1.86 Ml of EA (17.5 mmol) was added. The solution was then transferred to a stainless-steel syringe, which was then fitted with the first section of PFA tubing. The syringe was taken out of the glovebox and quickly connected to the flow reactor, which was set to a 60 minute residence time. After equilibration for 1.25 x residence time, the product was collected for 1 hour. After precipitation in cold methanol/water, the polymer was dried to constant weight under vacuum at 50 °C to give 0.45 g with $M_n = 12.6$ kDa, $Đ = 1.16$.

Figure 4.166: ^{1}H NMR spectrum of p(n-BA)-b-p(EA) in CDCl$_3$.

Triblock Copolymer Synthesis:

A p(BA)-c-p(EA)-c-(*t*-BA) triblock copolymer was synthesized using a [200]:[1]:[0.1]:[3] ratio of [t-BA]:[block copolymer]:[PC 2]:[LiBr]. 8.2 mg LiBr (0.095 mmol) was dissolved in 2.80 Ml of DMAc. The solution was then transferred to a vial with 1.7 mg PC 2 (3.18 µmol), which was then transferred to a vial with 400 mg of p(BA)-c-p(EA) macroinitiator (0.032 mmol). After the polymer was dissolved, 0.93 Ml of *t*-BA (6.4 mmol) was added. The solution was then transferred to a stainless-steel syringe, which was then fitted with the first section of PFA tubing. The syringe was taken out of the glovebox and quickly connected to the flow reactor, which was set to a 60 minute residence time. After equilibration for 1.25 x residence time, the product was collected for 30 minutes. After precipitation in cold methanol/water, the polymer was dried to constant weight under vacuum at 50 ℃ to give 0.2 g with M_n = 20 kDa, $Đ$ = 1.44.
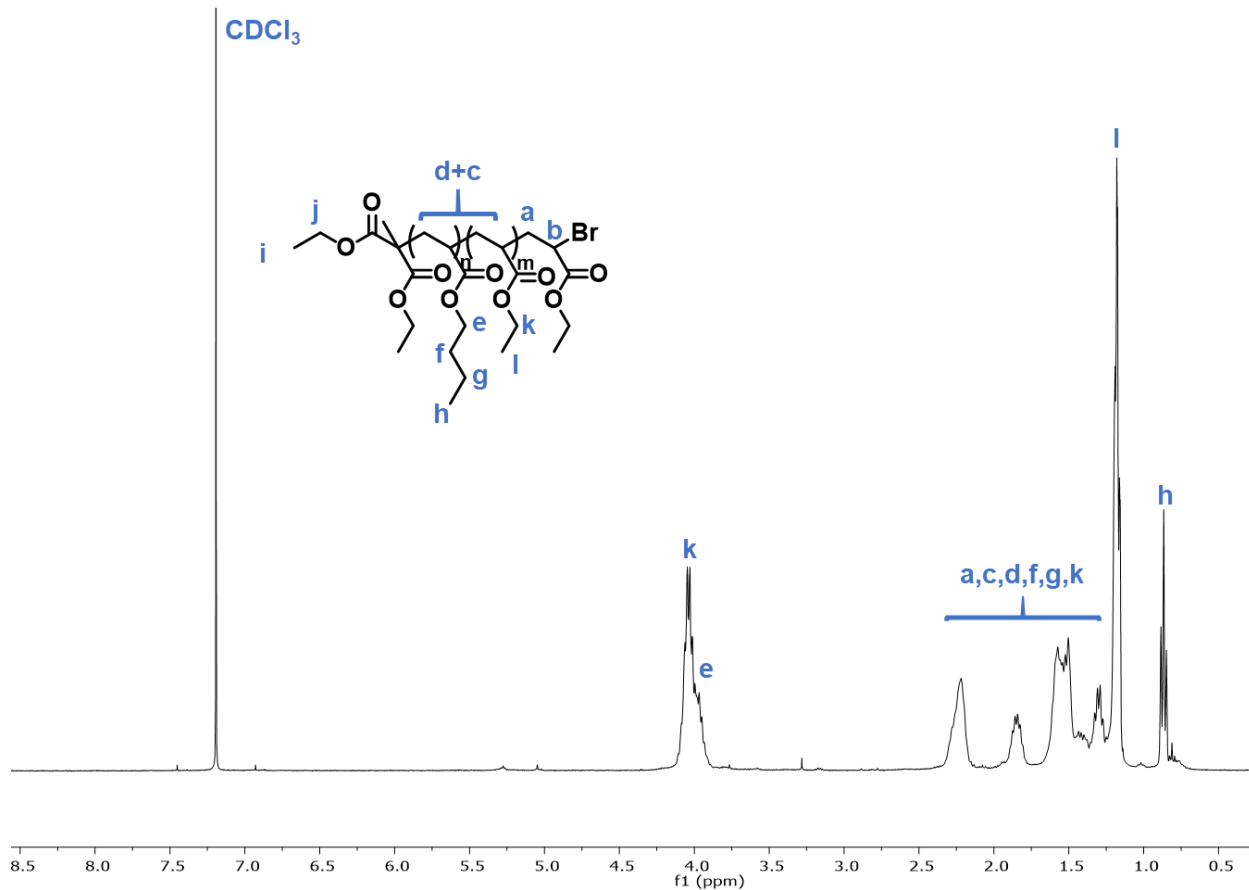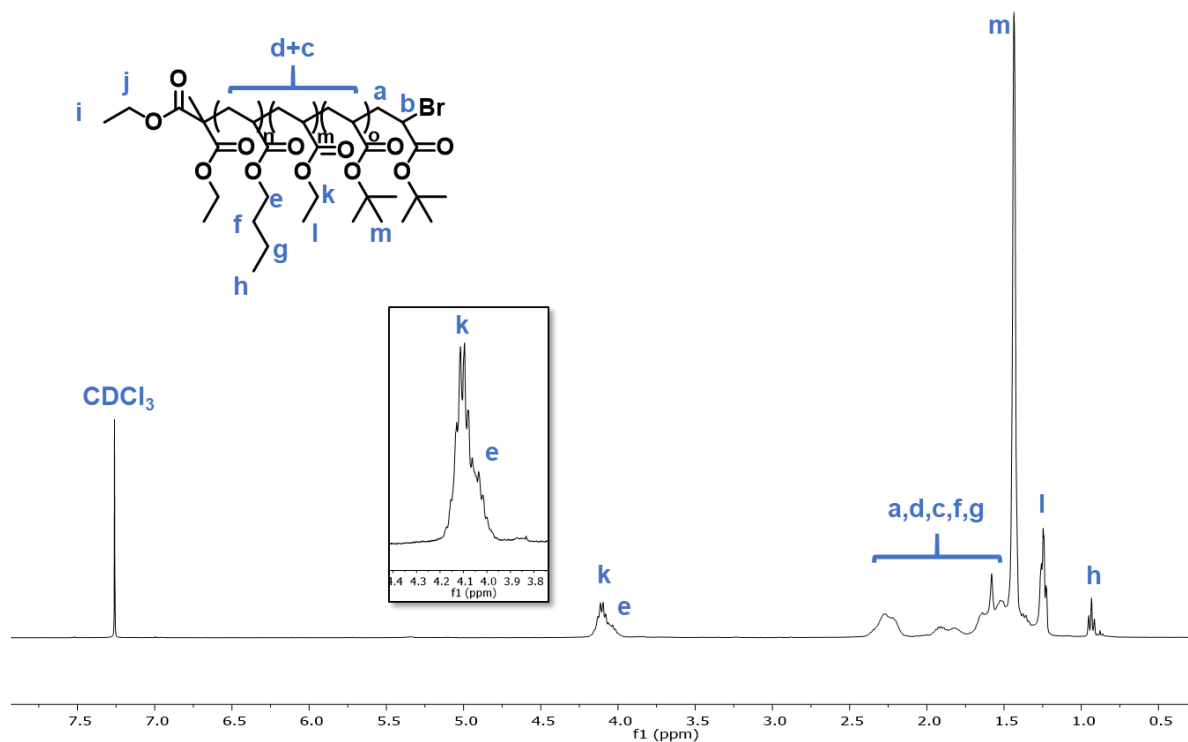
Figure 4.167: ^{1}H NMR spectrum of p(n-BA)-b-p(EA)-b-p(t-BA) in CDCl$_3$.

MALDI-MS Analysis

MALDI-TOF MS analysis was performed on a Bruker Microflex LRF Instrument using NaTFA as ionization agent and trans-2-[3-(4-tert-Butylphenyl)-2-methyl-2-propenylidene]malononitrile as matrix. Two polymers were selected for analysis, both synthesized in continuous-flow. Conditions are [1000]:[10]:[1]:[X] of [BA]:[DBMM]:[PC 2]:[LiBr] with 1.5 eq. DMAc.
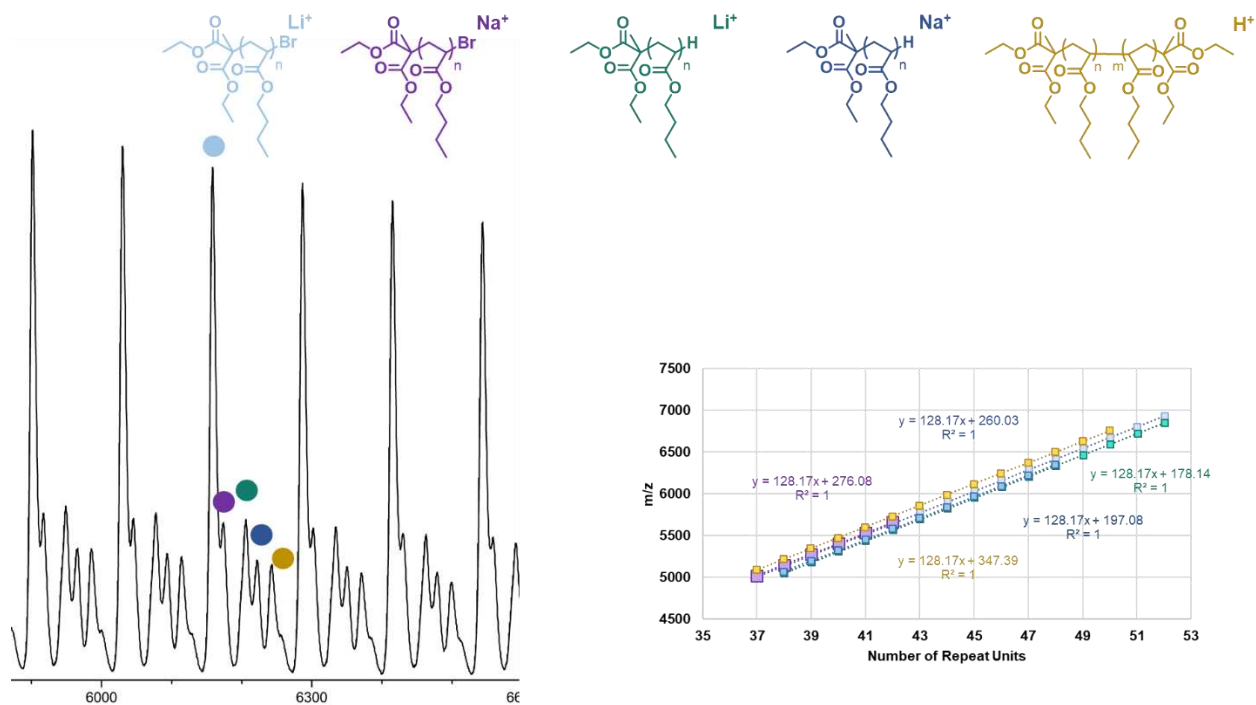
Figure 4.168: MALDI-TOF analysis of p(BA) synthesized in continuous-flow with 30 eq. of LiBr.

Figure 4.169: MALDI-TOF analysis of p(BA) synthesized in continuous-flow with no LiBr additives.

References

1. a) Romero, N. A.; Nicewicz, D. A. *Chem. Rev.* **2016,** *116,* 10075-10166. b) Prier, C. K.; Rankic, D. A.; MacMillan, D. W. C. *Chem. Rev.* **2013,** *113,* 5322-5363. c) Narayanam, J. M. R.; Stephenson, C. R. J. *Chem. Soc. Rev.* **2011,** *40,* 102-113. d) Buzzetti, L.; Crisenza, G. E. M.; Melchiorre, P. *Angew. Chem. Int. Ed.* **2019,** *58,* 3730-3747. e) Corrigan, N.; Shanmugam, S.; Xu, J.; Boyer, C. *Chem. Soc. Rev.* **2016**, *45*, 6165-6212.
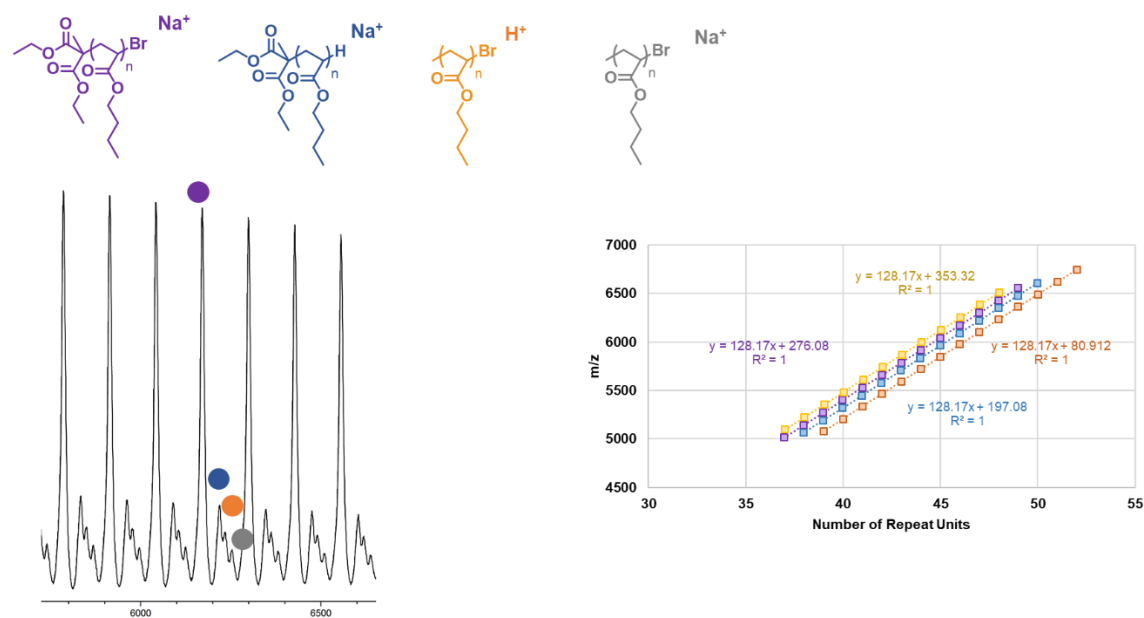
2. a) Leibfarth, F. A.; Mattson, K. M.; Fors, B. P.; Collins, H. A.; Hawker, C. J. *Angew.Chem. Int. Ed.* **2012,** *52,* 199-210. b) Chen, M.; Zhong, M.; Johnson, J. A. *Chem. Rev.* **2016,** *116,* 10167-10211. c) Corrigan, N.; Yeow, J.; Judzewitsch, P.; Xu, J.; Boyer, C. *Angew. Chem. Int. Ed.* **2019**, *131*, 5224-5243.

3. a) Matyjaszewski, K. *Adv. Mater.* **2018,** *30,* 1706441. b) Ribelli, T. G.; Lorandi, F.; Fantin, M.; Matyjaszewski, K. *Macromol. Rapid Commun,* **2019,** *40,* 1800616. c) Ouchi, M.; Terashima, T.; Sawamoto, M. *Chem. Rev.* **2009,** *109,* 4963-5050.

4. a) Yang, Q.; Dumur, F.; Morlet-Savary, F.; Poly, J.; Lalevee, J. *Macromolecules* **2015,** *48,* 1972-1980. b) Zhang, G.; Song, I. Y.; Ahn, K. H.; Park, T.; Choi, W. *Macromolecules,* **2011,** *44,* 7594-7599. c) Fors, B. P.; Hawker, C. J. *Angewandte Chemie* **2012,** *51,* 8850-8853.

5. Shanmugam, S.; Boyer, C. *Science* **2016,** *352,* 1053-1054

6. Yilmaz, G.; Yagci, Y. *Polym. Chem.* **2018,** *9,* 1757-1762.

7. Theriot, J. C.; McCarthy, B. G.; Lim, C. -H.; Miyake, G. M. *Macromol. Rapid Commun.* **2017,** *38,* 1700040.

8. Roth, H. G.; Romero, N. A.; Nicewicz, D. A. *Synlett* **2016**, *27,* 714-723.

9.   a) Miyake, G. M.; Theriot, J. C. *Macromolecules* **2014,** *47,* 8255-8261. b) Treat, N. J.; Sprafke, H.; Kramer, J. W.; Clark, P. G.; Barton, B. E.; Alaniz, J. R.; Fors, B. P.; Hawker, C. J. *J. Am. Chem. Soc.* **2014,** *136,* 16090-166101

10.   a) Theriot, J. C.; Lim, C. -H.; Yang, H.; Ryan, M. D.; Musgrave, C. B.; Miyake, G. M. *Science* **2016,** *352,* 1082-1086.

11.   a) Pearson, R. M.; Lim, C. -H.; McCarthy, B. G.; Musgrave, C. B.; Miyake, G. M. *J. Am. Chem. Soc.* **2016,** *138,* 11399-11407.

12.   a) Singh, V. K.; Yu, C.; Badgujar, S.; Kim, Y.; Kwon, Y.; Kim, D.; Lee, J.; Akhter, T.; Thangavel, G.; Park, L. S.; Lee, J.; Nandajan, P. C.; Wannemacher, R.; Milian-Medina, B.; Luer, L.; Kim, K. S.; Gierschner, J.; Kwon, M. S. *Nature Catalysis,* **2018,** *1,* 794-804. b) Discekici, E. H.; Anastasaki, A.; Read de Alaniz, J.; Hawker, C. J. *Macromolecules* **2018** *51*, 7421–7434.

13.   a) Narupai, B.; Page, Z. A.; Treat, N. J.; McGrath, A. J.; Pester, C. W.; Discekici, E. H.; Dolinski, N. D.; Meyers, G. F.; Read de Alaniz, J.; Hawker C. J. *Angewandte Chemie* **2018**, *57*, 13433–13438. b) Discekici, E. H.; Pester, C. W.; Treat, N. J.; Lawrence, J.; Mattson, K. M.; Narupai, B.; Toumayan, E. P.; Luo, Y.; McGrath, A. J.; Clark, P. G.; Read de Alaniz, J.; Hawker C. J. *ACS Macro Lett.* **2016**, *5*, 258–262.

14.   Pan, X.; Fang, C.; Fantin, M.; Malhotra, N.; So, W. Y.; Peteanu, L. A.; Isse, A. A.; Gennaro, A.; Liu, P.; Matyjaszewski, K. *J. Am. Chem. Soc.* **2016,** *138,* 2411-2425.

15.   a) McCarthy, B. G.; Pearson, R. M.; Lim, C. -H.; Sartor, S. M.; Damrauer, N. H.; Miyake, G. M. *J. Am. Chem. Soc.* **2018,** *140,* 5088-5101. b) Cole, J. P.; Federico, C. R.; Lim, C. -

H.; Miyake, G. M. *Macromolecules* **2019,** *52,* 747-754. c) Koyama, D.; Dale, H. J. A.; Orr-Ewing, A. J. *J. Am. Chem. Soc.* **2018,** *140,* 1285-1293.

16.   Corbin, D. A.; Lim, C. -H.; Miyake, G. M. *Aldrichimica Acta.* **2019,** *52,* 7-21.

17.   a) Ryan, M. D.; Pearson, R. M.; French. T. A.; Miyake, G. M. *Macromolecules,* **2017,** *50,* 4616-4622. b) Ryan, M. D.; Theriot, J. C.; Lim, C. -H.; Yang, H.; Lockwood, A. G.; Garrison, N. G.; Lincoln, S. R.; Musgrave, C. B.; Miyake, G. M. *J. Polym. Sci. Part A: Polym. Chem.* **2017,** *55,* 3017-3027. c) Ramsey, B. L.; Pearson, R. M.; Beck, L. R.; Miyake, G. M. *Macromolecules* **2017,** *50,* 28-2674. d) Buss, B. L.; Beck, L. R.; Miyake, G. M. *Polym. Chem.* **2018,** *9,* 1658-1665. e) McCarthy, B. G.; Miyake, G. M. *ACS Macro. Lett.* **2018,** *7,* 1016-1021. f) Du, Y.; Pearson, R. M.; Lim, C. -H.; Sartor, S. M.; Ryan, M. D.; Yang, H.; Damrauer, N. H.; Miyake, G. M. *Chem. Euro. J.* **2017,** *23*, 10962-10968. g) Rao, H.; Lim, C. -H.; Bonin, J.; Miyake, G. M.; Robert, M. *J. Am. Chem. Soc.* **2018,** *140,* 17830-17834.

18.   a) Pan, X.; Lamson, M.; Yan, J.; Matyjaszewski, K. *ACS Macro Lett.* **2015,** *4,* 192-196. b) Chen, D. -F.; Boyle, B. M.; McCarthy, B. G.; Lim, C. -H.; Miyake, G. M. *J. Am. Chem. Soc.* **2019,** *141,* 13268-13277. c) Ramakers, G.; Krivkov, A.; Trouillet, V.; Welle, A.; Mobius, H.; Junkers, T. *Macromol. Rapid Commun.* **2017,** *38,* 1700423.

19.   Destarac, M. *Polym. Chem.* **2018,** *9,* 4947-4967.

20.   Beuermann, S.; Buback, M.; *Prog. Polym. Sci.* **2002,** *27,* 191-254.

21.   Tang, W.; Matyjaszewski, K. *Macromolecules* **2007,** *40,* 1858-1863.

22. Anastasaki, A.; Nikolaou, V.; Zhang, Q.; Burns, J.; Samanta, S. R.; Waldron, C.; Haddleton, A. J.; McHale, R.; Fox, D.; Percec, V.; Wilson, P.; Haddleton, D. M. *J. Am. Chem. Soc.* **2014,** *136,* 1141-1149.

23. Treat, N. J.; Fors, B. P.; Kramer, J. W.; Christianson, M.; Chiu, C. -Y.; Read de Alaniz, J.; C. J. Hawker, C. J. *ACS Macro. Lett.* **2014,** *3,* 580-584.

24. a) Wong, M. Y.; Zysman-Colman, D. *Advanced Materials* **2017,** *29,* 1605444. b) Li, W.; Li, B.; Cai, X.; Gan, L.; Xu, Z.; Li, W.; Liu, K.; Chen,D.; Su, S. -J. *Angew. Chem. Int. Ed.* **2019,** *58,* 11301-11305.

25. Lim, C. -H.; Ryan, M. D.; McCarthy, B. G.; Theriot, J. C.; Sartor, S. M.; Damrauer, N. H.; Musgrave, C. B. Miyake, G. M *J. Am. Chem. Soc.* **2017,** *139,* 348-355.

26. Sartor, S. M.; McCarthy, B. G.; Pearson, R. M.; JMiyake, G. M.; Damrauer, N. H. *J. Am. Chem. Soc.* **2018,** *140,* 4778-4781.

27. a) Hartman, R. L.; McMullen, J. P.; Jenson, K. F. *Angew. Chem. Int. Ed.* **2011,** *50,* 7502-7519. b) Buss, B. L.; Miyake, G. M. *Chem. Mater.* **2018,** *30,* 3931-3942. c). Junkers, R.; Wenn, B. *React. Chem. Eng.* **2016,** 1, 60. d) Tucker, J. W.; Zhang, Y.; Jamison, T. F.; Stephenson, C. R. J. *Angew. Chem. Int. Ed.* **2012,** *51,* 4144-4147.

28. a) Simakova, A.; Averick, S. E.; Konkolewicz, D.; Matyjaszewski, K. *Macromolecules* **2012,** *45,* 6371-6379. b) Fantin, M.; Isse, A. A.; Gennaro, A.; Matyjaszewski, K. *Macromolecules* **2015,** *48,* 6862-6875.

29. Gaussian 09, R. D., Frisch, M. J.; Trucks, G. W.; Schlegel, H. B.; Scuseria, G. E.; Robb, M. A.; Cheeseman, J. R.; Scalmani, G.; Barone, V.; Mennucci, B.; Petersson, G. A.; Nakatsuji, H.; Caricato, M.; Li, X.; Hratchian, H. P.; Izmaylov, A. F.; Bloino, J.; Zheng,

G.; Sonnenberg, J. L.; Hada, M.; Ehara, M.; Toyota, K.; Fukuda, R.; Hasegawa, J.; Ishida, M.; Nakajima, T.; Honda, Y.; Kitao, O.; Nakai, H.; Vreven, T.; Montgomery, J. A., Jr.; Peralta, J. E.; Ogliaro, F.; Bearpark, M.; Heyd, J. J.; Brothers, E.; Kudin, K. N.; Staroverov, V. N.; Kobayashi, R.; Normand, J.; Raghavachari, K.; Rendell, A.; Burant, J. C.; Iyengar, S. S.; Tomasi, J.; Cossi, M.; Rega, N.; Millam, J. M.; Klene, M.; Knox, J. E.; Cross, J. B.; Bakken, V.; Adamo, C.; Jaramillo, J.; Gomperts, R.; Stratmann, R. E.; Yazyev, O.; Austin, A. J.; Cammi, R.; Pomelli, C.; Ochterski, J. W.; Martin, R. L.; Morokuma, K.; Zakrzewski, V. G.; Voth, G. A.; Salvador, P.; Dannenberg, J. J.; Dapprich, S.; Daniels, A. D.; Farkas, Ö.; Foresman, J. B.; Ortiz, J. V.; Cioslowski, J.; Fox, D. J. Gaussian, Inc., Wallingford CT, 2009.

30.   He, H.; Zapol, P.; Curtiss, L. A. *The Journal of Physical Chemistry C* **2010**, *114*, 21474.

31.   Tossell, J. A. *Computational and Theoretical Chemistry* **2011**, *977*, 123.

32.   Winget, P.; Cramer, C. J.; Truhlar, D. G. *Theoretical Chemistry Accounts: Theory, Computation, and Modeling (Theoretica Chimica Acta)* **2004**, *112*, 217.

33.   Zhao, Y.; Truhlar, D. *Theoretical Chemistry Accounts* **2008**, *120*, 215.

34.   Yanai, T.; Tew, D. P.; Handy, N. C. *Chemical Physics Letters* **2004**, *393*, 51-57

CHAPTER 5

Summary

The work presented in this dissertation focused on the expansion of the scope and relevance of organocatalyzed atom transfer radical polymerization (O-ATRP) through exploration of scalability, application to higher-order polymeric architectures, and the successful polymerization of acrylate monomers through development of new organic photocatalysts (PCs). Notably, in all three publications discussed in detail, the promotion of PC photoexcitation through more efficient reaction irradiation contributed to improvement in polymerization performance.

There still remains today some key challenges in O-ATRP, centered on application to vinyl monomers with high rates of propagation, such as acrylamides, and those with challenging functional groups, such as acids and amines. Furthermore, application in non-polar solvents and with chloride initiators remains elusive. As in the current progress in O-ATRP, future advancements in this technology are dependent on continued development and understanding of these photocatalysts. In particular, greater elucidation of the photophysical nature of these PCs through ultra-fast spectroscopy will influence our understanding of electron transfer in these systems, given that PC irradiation and substrate activation has been demonstrated to play a central role in polymerization control.

Currently, PC development relies on density functional theory to predict key PC properties, but there remains minimal understanding on the relationship between PC properties and performance in O-ATRP. Of great importance in the continued advancement of O-ATRP is the development of predictive metrics for PC performance using a variety of monomers, solvents, and other reaction conditions. As such, incorporation of machine learning and a design-of-experiments

approach for rapid data generation could provide important insights into structure-property-performance relationships.

Ultimately, the development of O-ATRP and other organic photoredox-catalyzed processes is a rapidly growing arena, encompassing scientists from diverse fields of study. With continued efforts, robust collaborations, and fresh ideas, the outlook of organic photoredox catalysis is bright and primed for widespread adoption.

APPENDIX I

List of Publications

1. <u>Buss, B.</u>; Lim, C.-H.; Miyake, G. Dimethyl dihydroacridines as photocatalysts for the organocatalyzed atom transfer radical polymerization of acrylate monomers, *Angewandte Chemie,* **2020,** *59,* 3209-3217. **Article Featured on Cover.**

2. <u>Buss, B.</u>; Price, M.; Miyake, G. Organic photoredox catalyst design to enable transformative chemistry, *to be submitted.*

3. <u>Buss, B.</u>; Lim, C.-H.; Kudisch, M.; Miyake, G. Carbazole and acridine photoredox catalysts for small molecule and macromolecular transformations, U.S. Provisional Pat. filed 3/20/2019.

4. <u>Buss, B.</u>; Miyake, G. Photoinduced controlled radical polymerizations performed in flow: methods, products, and opportunities. *Chemistry of Materials,* 2018, *30,* 3931-3942.

5. <u>Buss, B.</u>; Beck, L.; Miyake, G. Synthesis of star polymers using organocatalyzed atom transfer radical polymerization through a core-first approach. *Polymer Chemistry* 2018, *9,* 1658-1665.

6. <u>Ramsey (Buss), B.</u>; Pearson, R.; Beck, L.; Miyake, G. Photoinduced Organocatalyzed Atom Transfer Radical Polymerization Using Continuous Flow. *Macromolecules* 2017, *50(7),* 2668-2674.